Application of Cold Metal Transfer Technology for Cladding of ER70S-6 Alloy on AA 6061-T6 Aluminum Alloy

A Thesis Submitted in Partial Fulfillment of the Requirements for the Degree of

DOCTOR OF PHILOSOPHY

by

Bappa Das

(Roll No. 206103008)

Department of Mechanical Engineering

Indian Institute of Technology Guwahati

Guwahati 781039

INDIA

September 2023

Department of Mechanical Engineering,
Indian Institute of Technology Guwahati,
Guwahati-781039, INDIA

CERTIFICATE

It is certified that the work contained in the thesis entitled "**Application of Cold Metal Transfer Technology for Cladding of ER70S-6 Alloy on AA 6061-T6 Aluminum Alloy**" is submitted by **Mr. Bappa Das** to the Indian Institute of Technology Guwahati for the award of the degree of Doctor of Philosophy. The work has been carried out under my supervision in the Department of Mechanical Engineering, Indian Institute of Technology Guwahati. This work has not been submitted elsewhere for the award of any other degree or diploma.

Dr. Uday Shanker Dixit
Professor
Department of Mechanical Engineering,
Indian Institute of Technology Guwahati,
Guwahati-781039, INDIA

Dr. Biranchi Narayan Panda
Assistant Professor
Department of Mechanical Engineering,
Indian Institute of Technology Guwahati,
Guwahati-781039, INDIA

Date: September 11, 2023

DECLARATION

I declare that,

a. The work contained in this thesis is original and has been done by me under the guidance of my supervisors.
b. The work has not been submitted to any other institute for any degree or diploma.
c. I have followed the guidelines provided by the institute in preparing the thesis.
d. I have confirmed the norms and guidelines given in the ethical code of conduct of the institute.
e. Whenever I used materials (data, theoretical analysis, figure and text) from other sources, I have given due credit to them by citing them in the text of the thesis and giving their detail in references.

Bappa Das

Dedicated to My Parents, Teachers and Friends

Acknowledgement

I am privileged to take this opportunity to express my respect towards all who have supported me during the tenure of my PhD programme at IIT Guwahati. The first persons I would like to express my sincere gratefulness is my supervisors **Prof. Uday Shanker Dixit** and **Dr. Biranchi Narayan Panda**. I feel fortunate for getting the opportunity to work under them as a research scholar. Their endless support, encouraging interactions and constructive criticism was a great driving force for me to carry out this research work.

I express my sincere gratitude to my doctoral committee members **Prof. S. Senthilvelan**, **Prof. R. Ganesh Narayanan** and **Prof. V. Manivannan** for their encouragement and suggestions throughout the study. I express my sincere thanks to the former and present heads of the Department of Mechanical Engineering, Prof. S.K. Dwivedy, Prof. S. Senthilvelan and Prof. KSR Krishna Murthy**.** I would also like to thank the staff members of the Department office and Central Workshop for their support and cooperation. A special thanks to Mr. Ritam Sharma for helping me in carrying out experiments. Also, the financial support provided by the Ministry of Education (MoE), India is greatly acknowledged.

The experiment facility used was provided by the Material Science Lab of Mechanical Department, NECBH and CIF of the Indian Institute of Guwahati (IITG), and the CMT Machine was procured from grant number DST/NMICPS/TIH12/IITG/2020 from the IITG Technology Innovation and Development Foundation, which is part of the NMICPS. I greatly acknowledge this help.

I express my sincere thanks to Dr. Faladrum Sharma, Dr. Amit Raj, Mr. Abhijeet Dhulekar, Mr. Kaustabh Chatterjee, Mr. Nilkamal Mahanta, Mr. Nitish Bhardwaj, Mr. G. Safiur Rahiman, Mr. Bhanu Prakash Bonthala, and Mr. Amritesh Kumar. Special thanks to all my mates who made my stay enjoyable and memorable.

I am always indebted to my parents for generously encouraging me and providing moral support during every footstep of my life. My father Mr. Jagannath Das, my mother Mrs. Benu Majumdar and my brother Mr. Biplob Das deserve my wholehearted thanks. I will be grateful to them for sharing every responsibility in my family during my Ph.D. Finally, I would like to express my special thanks to all those who have helped me in various ways directly and indirectly during the tenure of my Ph.D. work. I shall always be grateful to the entire fraternity of IIT Guwahati for their encouragement and wishes.

Bappa Das

IIT Guwahati

Abstract

The Cold Metal Transfer (CMT) process is an advanced welding technique used for cladding and coating, which involves applying a layer of metal onto a base material. In fact, CMT cladding is an efficient additive manufacturing technology that finds application in the automotive, defence, and power plant sectors. As Additive Manufacturing evolves, new welding methods have emerged, including CMT, an advanced version of Metal Inert Gas (MIG) welding known for reduced spatter and low heat input. CMT-based cladding processes have gained attention for improved aesthetics and lower heat input. Utilizing a wire as feedstock and a robotic arm for deposition enables precise material deposition in complex shapes, with heat input determined by process parameters like voltage, current, wire feed speed, and stand-off distance.

In this thesis, the motivation is implementing the cost-effective method of surface modification of AA 6061-T6 aluminum alloy. For this, CMT process was used. The CMT cladding was conducted by depositing filler material to the aluminum substrate. Fe-based ER70S-6 filler material was selected due to automatic welding, stable arc, low sputter, cost-effectiveness, and high deposition efficiency. In order to investigate the proper deposition different cladding bead was deposited and the best was selected on the basis of visual inspection. The formation of good metallurgical bond was observed between the former and latter. The formation of good bonding of added materials with aluminum substrate played a great role in improving surface properties such as microhardness, wear, tensile and shear strength.

The cladding layer corrosion behavior was studied through longer-duration immersion tests in 2.0% of H_2SO_4 acid solution, revealing considerable surface damage caused primarily by localized pitting corrosion. The pits grew more rapidly laterally than in the depth direction. Moreover, the corrosion test led to a decrease in the average micro-hardness due to the removal of hard materials and the introduction of porosity, resulting in a reduced load-bearing area at specific locations.

The impact of heat treatment on the cladded layer was investigated using four distinct methods. The first method involved heating the sample to 600 °C for 1 h holding time followed by furnace cooling. The second method utilized water quenching after heating the sample to 600 °C after 1 h hold. The third approach entailed artificial age hardening, which included heating the sample to 175 °C, holding it for 24 h, and slowly

cooling it in a furnace over 6 h. Lastly, the deep cryo-treatment in liquid nitrogen (–196 °C) for 1 h. The cryogenic treatment exhibited the most significant improvement in the properties of the steel cladded parts manufactured using CMT technology. Water quenching was second in terms of effectiveness, while furnace cooling demonstrated enhanced ductility but had a detrimental impact on tribological properties.

To study the effectiveness of layer thickness, cladding layers of 1.5, 2.5 and 3.5 mm were deposited on the substrate. The cladded layer of 0.5 mm was milled to remove uneven surface. Among these thicknesses, the 1 mm cladding layer yielded the most favourable results in terms of bead quality, exhibiting minimal dilution, reduced porosity, a low bead contact angle, and a relatively smoother surface. The 1 mm cladding layer also provided a fine grain structure, featuring enhanced low angle grain boundaries. The presence of a higher number of such boundaries in the 1 mm cladding layer led to a higher dislocation density, which, in turn, contributed to improved mechanical properties such as hardness and wear resistance.

Overall, this research highlights the potential of CMT-based cladding processes for surface modification and the importance of selecting appropriate heat treatment methods to enhance the properties of cladded materials for various industrial applications.

Contents

List of figures

List of Tables

Nomenclature

Roman letters

D_V	Volumetric dilution
a	Lattice parameter
b	Burger vector
d	Average grain diameter
D	Crystallite size
E	Young's modulus
E_{eq}	Equivalent modulus
Fe_C	Weight percentage of iron in cladding
Fe_S	Weight percentage of iron in substrate
F_n	Normal load
H	Hardness
I	Current
K	Constant
k	Lancaster wear coefficient
N	Number of revolution/min
Q	Heat input
R_a	Surface roughness
s	Sliding distance
S	Welding speed
V	Material loss
V	Voltage
W_{dry}	Dry wright
W_{sat}	Weight of the saturated sample
W_{susp}	Weight of the suspended sample in water
Y_{eq}	Equivalent yield strength
ρ_c	Density of the cladding
ρ_s	Density of the substrate

Greek letters

ρ	Dislocation density
η	Efficiency
δ	Elongation
β	Full width half maxima
ε	lattice strain
λ	Wavelength
σ_i	Lattice friction stress
σ_y	Yield stress

List of abbreviations

AFM	Atomic force microscopy
AM	Additive manufacturing
BC	Band contrast
BCC	Body- centered cubic
CMT	Cold metal transfer
CoF	Coefficient of friction
EBSD	Electron backscatter diffraction
EDS	Energy dispersive spectroscopy
FB	Fusion boundary
FCC	Face-centered cubic
FESEM	Field emission scanning electron microscope
FWHM	Full width half maxima
FZ	Fusion zone
GMAW	Gas metal arc welding
GNDs	Geometrically necessary dislocations
HAGBs	High-angle grain boundaries
HAZ	Heat affected zone
IMC	Intermetallic compound
IPF	Inverse pole figure
JCPDS	Joint committee of powder diffraction standard
KAM	Kernel average misorientation
LAGBs	Low-angle grain boundaries
LVDT	Linear variable differential transducer

MIG	Metal inert gas
PAGBs	Prior austenite grain boundaries
PMZ	Partially melted zone
PTA	Plasma Transferred Arc
SAED	Selected area electron diffraction
SCR	Steel catenary riser
SSCC	Sulfide stress corrosion cracking
TEM	Transmission electron microscopy
TIG	Tungsten inert gas
UTM	Universal testing machine
UTS	Ultimate tensile strength
WEDM	Wire cut electron discharge machine
XPS	X-ray photoelectron spectroscopy
XRD	X-ray diffraction
YS	Yield strength

Chapter 1

Background, Motivation and Scope

1.1 Overview

Surface treatment of materials including cladding is of paramount importance for imparting functional properties and surface protection from corrosive media, wear and temperature. The surface treatment involves processes such as surface cleaning, electroplating, conversion coating and vacuum coating. Surface modifications using techniques such as laser treatment, ion implantation, and heat treatment are employed to enhance surface properties and functionality. New processes are being regularly introduced. Existing processes are continuously adapted to the engineering of material surfaces and becoming increasingly important for new types of design. Surface treatment technologies for light metals, ceramics, and amorphous/nano-structured materials are advancing rapidly. It is important to consider the metallurgical (interfacial bonding, redistribution of elements, porosity, defects and cracks), manufacturing (non-contact, fast and flexible treatment), environmental (green and benign treatment) and health (non-hazardous materials and processing) aspects during surface treatment.

1.2 Overlay Welding

Weld overlay is a type of cladding that uses a fusion welding process to deposit one material on another material. When the cladded layer thickness is small, it is called coating. Although there is no clear-cut definition of coatings from the thickness point of view, they generally have thickness of less than 1 mm. On the other hand, claddings can be several millimetres thick, and hence the cladding technology can be used for additive manufacturing (AM), which is popularly known as 3D printing. Weld overlay is a popular method for cladding to improve the surface properties like hardness, wear resistance and corrosion resistance. The negative side effects of cladding may include change in the composition of the substrate and formation of the heat affected zone (HAZ). These phenomena may sometimes affect the strength and ductility of the substrate adversely (Selvi et al. 2018).

The cladding and coating of materials have been achieved through various processes such as cold spraying, plasma spraying and laser cladding. Nevertheless, these methods have limitations in terms of deposition thickness per pass. On the other hand, weld overlay cladding techniques allow for thicker deposition in a single pass using a

welding setup. Fusion welding overlay techniques like plasma transferred arc welding, gas tungsten arc welding and gas metal arc welding (GMAW) have been utilized for weld deposition. However, one of the critical challenges is the dilution of the cladding composition that occurs when melting the substrate. For instance, when traditional GMAW technology is used to clad low melting point materials such as aluminium, there is high dilution due to the high heat input.

The welding or cladding of two dissimilar metals is very challenging due to their different thermal-physical characteristics and melting temperatures. The prime issue lies with the development of hard, brittle intermetallic compound (IMC) layers and phases at the cladded interface, which may impair the mechanical properties of the resulting dissimilar joint (Li et al. 2023). The observed weak miscibility between the dissimilar alloys during the fusion process results in inadequate weld metallurgical compatibility, which is further aggravated by non-identical thermal and physical characteristics. The temperature and cooling time of the welding and cladding process have a significant impact on the development of intermetallic compound phases (Lee et al. 2007). Low and regulated heat input throughout the process can be used to limit the formation of the IMC layer thickness and phases (Murakami et al. 2003, Mathieu et al. 2006). In recent times, various joining techniques were adopted for the joining of Al and steel alloys. However, the main issue was the abundant development of brittle IMC at the interface due to the unregulated heat supply and molten metal transfer. Because of the high thermal conductivity and low melting point of substrate material, it is hard to produce cladding layer using the traditional fusion technique. A low heat input is desired for the cladding on Al and other low melting point materials. Recently, industries have started to replace traditional welding and cladding with the Cold Metal Transfer (CMT) process, which requires less heat input. CMT provides better quality than other traditional joining process, due to which it has become an exemplary process for the industrial application (Meco et al. 2013, Selvi et al. 2018).

CMT, a modified form of GMAW welding technique based on the short-circuit transfer process developed by Fronius Austria in 2004, uses low temperature metal transfer to deposit materials with enhanced bead quality, controlled droplet separation, low heat input, low porosity and low smoke (Selvi et al. 2018). CMT technology, which is also referred to as mechanically assisted droplet deposition, controls the short circuit by pulling the wire. The robotic arm utilized in CMT allows for deposition on complex paths with ease. The amount of heat used to melt the wire during this process is

determined by various process parameters such as voltage, current, wire feed speed, and stand-off distance. Process parameters in CMT affect the microstructural and mechanical properties of the part. Although the CMT is essentially a GMAW type process, it differs in the drop transfer mechanism. The controlled current in the CMT process ensures low heat input in the weld bead, causing less distortion and increased productivity (Luchtenberg et al. 2019). The major advantage of CMT over GMAW is enhanced computer control of welding technology. The low heat input during the CMT process also minimizes tensile residual stresses on the surface. Reduced heat energy prevents development of intermetallic phases, which improves the cladded joint quality. These benefits of CMT process enable it a suitable process for the joining of thin sheet of similar and dissimilar metals.

The heat transfer that occurs during and after deposition impacts the microstructure and mechanical properties of the coated or cladded material. It has been established that CMT cladding has a significant advantage over traditional techniques as it employs lower processing temperatures, thus having a smaller thermal impact on the materials being processed (Selvi et al. 2018). It is particularly beneficial for claddings that are vulnerable to oxidation at high temperatures.

1.3 CMT process

During CMT processes, the digital process control of the system causes the wire-feed servomotor of the welding gun to reverse its direction when the electrode wire tip contacts the molten weld pool. Retraction of the wire causes short circuit mode of metal transfer as shown in Fig. 1.1(a); it is also known as mechanically assisted droplet deposition (Kah et al. 2013). The current is reduced to almost zero value during the metal transfer, thus preventing spatter. The arc is restarted after one cycle of metal transfer, and the wire is then fed forward once more with a predetermined reflow of welding current (Furukawa, 2006).

The current and voltage waveform is shown in Fig. 1.1(b). Each cycle of metal transfer comprises three phases as follows:

I. **Peak current phase**: The welding arc ignites in the first phase of operation due to applied voltage and low resistance causing a high pulse of current; the wire electrode is heated and droplet is produced.
II. **Background current phase**: This phase corresponds to a reduced current to prevent the small liquid droplet that has formed on the wire tip from spreading outward. This

phase continues till droplet touches the weld pool.

III. **Short-circuiting phase**: During this phase, the arc voltage (and hence current) is reduced to zero. The wire feeder receives the return signal at the same moment, which causes the wire to retract back. At this stage, droplet is transferred into the welding pool. The cycle continues to deposit the material at another location.

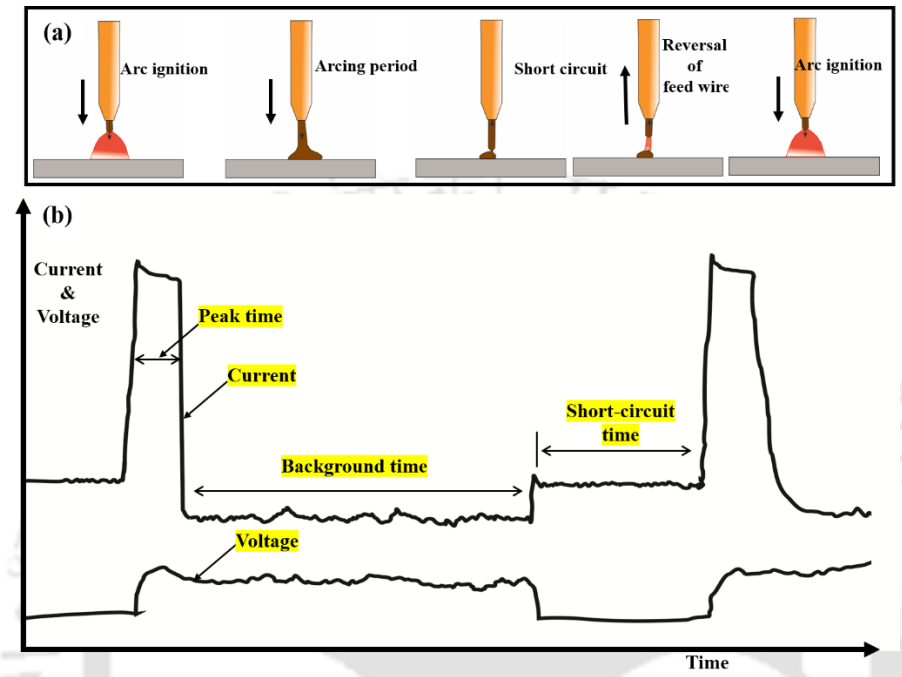

Figure 1.1 Cold metal transfer technology: (a) droplet formation mechanisms and (b) typical current and voltage waveform versus time

1.4 Key principles of CMT process

The key principles of the CMT are listed as follows:

- **Controlled Short-Circuiting:** At the core of CMT is a controlled short-circuiting process. Unlike traditional GMAW, where the wire continuously feeds and arcs, in CMT, the wire is repeatedly fed forward and then retracted during each short-circuit phase. This controlled movement of the wire helps regulate the heat input into the workpiece.
- **Heat Regulation:** By controlling the short-circuiting action, CMT technology allows for precise control over the amount of heat transferred to the weld joint. This prevents overheating of the material and minimizes the potential for distortion, especially on thin or heat-sensitive materials.
- **Droplet Detachment:** During each short-circuit phase, a small, precisely controlled droplet of molten metal forms at the end of the welding wire. This droplet is then detached from the wire and transferred to the weld pool with minimal force, reducing

the likelihood of spatter and ensuring better control over the weld bead.

- **Pulsed Current:** CMT utilizes a pulsed current waveform, where the current alternates between higher and lower levels. This pulsing helps regulate the heat input and also contributes to the controlled transfer of the molten droplet from the wire to the weld pool.

1.5 Benefits of the CMT process

The CMT process is widely used in the manufacturing industry due to its various benefits. Some important benefits of CMT process are listed as follows:

- **Reduced Heat Input:** CMT utilizes a controlled short-circuiting process, where the welding wire is fed forward and retracted during each short circuit. This controlled movement of the wire helps to regulate heat input, preventing excessive heating of the workpiece and minimizing distortion, especially on thin materials.
- **Lower Spatter:** The controlled short-circuiting action in CMT minimizes spatter compared to traditional GMAW techniques. This results in cleaner welds and less post-weld clean-up.
- **Enhanced Weld Quality:** The precise control of the welding process in CMT helps produce high-quality welds with good fusion and minimal defects. This makes it suitable for applications where weld quality is critical.
- **Versatility:** CMT can be used for a wide range of materials, including steel, aluminum, and other alloys. It is particularly well-suited for joining dissimilar metals.
- **Reduced Distortion:** The low heat input and controlled process of CMT contribute to reduced distortion and warping of the workpiece, making it suitable for applications where maintaining the shape and dimensional accuracy is important.
- **Automation and Robotics:** CMT technology can be integrated into automated and robotic welding systems, allowing for consistent and repeatable weld quality.
- **Energy Efficiency:** The reduced heat input of CMT results in lower energy consumption compared to traditional welding methods.

1.6 Aluminum in manufacturing

Aluminum stands as the most abundant metallic element on earth and ranks third among all elements. Its versatility makes aluminum alloys widely used, second only to steel. However, aluminum does not occur freely in nature; it is found in compound form within ores such as bauxite, kaolinite, nepheline, and cyolite. The demand and production

of aluminum have been consistently increasing, with the global demand reaching about 112 million metric tons and the supply meeting 115 million metric tons in the year 2016 (Aluminum Association, 1998).

One notable advantage of aluminum products is their ease of remanufacturing to create components for the same or different purposes. Recycling aluminum products incurs only about 5–10% of the energy consumption compared to primary aluminum production (Bergsdal et al., 2004). Pure aluminum exhibits softness, corrosion resistance, and excellent electrical and thermal conductivity. Cladding aluminum with different metals enhances its mechanical properties, rendering it suitable for structural applications. The strength-to-weight ratio of aluminum alloys often surpasses that of steel. Key attractive properties of aluminum alloys include high formability, lightweight nature, good corrosion resistance, high thermal and electrical conductivity, and recyclability (Hatch, 1984). Nevertheless, due to its strong chemical affinity to oxygen, aluminum primarily exists in ore form, necessitating significant energy consumption during extraction.

Aluminum alloys find extensive use in manufacturing components for automobiles, aircraft, and shipbuilding industries due to their lightweight characteristics. Moreover, they are employed in various household items like kitchen utensils and packaging materials. The lightweight and excellent electrical conductivity of aluminum make it a preferred choice for electrical transmission lines.

1.7 Cladding materials

The assortment of suitable coating materials depends on the application and the environment. Choosing the right materials can significantly increase the life of the part, and vice versa. Steel, nickel (Ni), and cobalt (Co)-based alloys are used when wear resistance is required. Hardened alloys with an austenitic structure (steels) are employed when impact strength is a property that needs reinforcement. Heat and corrosion resistance are also essential considerations when choosing coating materials. Co and Ni-based alloys have outstanding heat and corrosion resistance compared to martensitic and manganese alloy steels, which corrode quickly in corrosive environments (Dearnley, 1988).

1.8 Motivation and Scope

The increasing attention given to the use of CMT in manufacturing, both in research and industry, stems from its unique advantages that can only be achieved

through CMT properties. Two primary features that contribute to this interest are the ease of controlling heat input to the material during processing and the ability to precisely focus CMT deposition during welding and surface modifications. A noteworthy benefit of the CMT process is its capability to minimize distortion of the processed material. This thesis is motivated by the desire to explore CMT for the surface modification of aluminum, as it provides an easy and cost-effective method to achieve enhanced microhardness and improved wear resistance of the aluminum material. Furthermore, the melting-based CMT surface modification method proves to be economically friendly and efficient.

The primary objective of this thesis is to study the performance of CMT based cladding process of steel based on aluminum alloy. The influence of CMT process parameters, viz., current, voltage, stand-off distance and welding speed have great influence on the accuracy and efficiency of the process. This study is mainly focused on CMT cladding of Fe-based (ER70S-6) alloy on aluminum (AA 6061-T6) alloy. Steel was selected since the material cost is less and it is widely available compared to other alloys. Besides this the properties like hardness and wear resistance of aluminum is less compared to steel and it needs surface improvement. This thesis explores efficient technique to deposit thick cladding with good surface quality, bonding and minimum porosity. For this purpose, CMT technique has been employed as it generates low heat during the cladding process. CMT cladded aluminum alloy by Fe-based alloy has good mechanical strength and tribological characteristics. It can be used to make bimetallic strips and body requiring high surface hardness.

1.9 Organization of the Thesis

This thesis comprises eight chapters. This chapter has provided a brief introduction of surface treatment and cladding process. Introduction of CMT process and its application for surface modification are explained. The aluminum in manufacturing and cladding materials are also discussed. The remaining chapters in the thesis are organized as follows:

- In Chapter 2, a literature review on recent developments in cladding and coating using cold metal transfer technology are discussed.
- Chapter 3 presents the details of experimentations used in the thesis.
- Chapter 4 presents microstructure and mechanical properties of ER70S-6 alloy cladding on aluminum using a cold metal transfer process.

- Chapter 5 presents corrosion behavior and its effect on mechanical properties of ER70S-6 cladding on AA 6061-T6 alloy using a cold metal transfer process.
- Chapter 6 presents effects of heat-treatment on the mechanical properties of Fe-based ER70S-6 cladding on aluminum substrate using CMT process.
- Chapter 7 presents effect of layer thickness in cold metal transfer cladding of Fe-based ER70S-6 alloy on AA 6061-T6 aluminum alloy
- In Chapter 8, the conclusion and scope of future work are discussed.

Chapter 2

Literature Survey and Detailed Objectives

2.1 Introduction

Cladding and coating using the Cold Metal Transfer (CMT) process is an advanced welding technique used to apply a layer of metal onto a base material. In fact, CMT cladding is an efficient additive manufacturing technology and finds application in the automotive, defence and power plants sectors. It is commonly used for repairing worn components, adding corrosion-resistant layers, or modifying the surface properties of parts. The process's ability to provide precise and controlled deposition makes it a valuable tool for various manufacturing and maintenance scenarios. Several combinations of base metal and cladding material have been covered in detail with particular emphasis to microstructure and mechanical properties. It surpasses several cladding techniques as per literature. There are several issues worth researching in cladding and coating by CMT for enhancing the overall sustainability of the processes.

This survey critically analyses CMT cladding techniques and applications. Several reports have been published on CMT welding from 2004 to 2023. However, this survey offers a unique and significant contribution by thoroughly examining CMT as a cladding and coating methods that enhance surface characteristics. To conduct the research, various sources such as Scopus, Elsevier, and Google Scholar were used to select appropriate bibliographic references. The literature search was conducted using keywords like “CMT welding,” “cladding through CMT welding,” “coating through CMT welding,” and “weld overlay through CMT welding.” Further, some cross-references were also examined. The search produced over 400 documents; however, only representative papers have been discussed resulting in ~100 reports.

A review on cladding through CMT technology, is discussed in this chapter. The chapter is organized into different sections as follows —Section 2.2 discusses the performance indicators of CMT cladding. Section 2.3 discusses the effect of process variables. Section 2.4 presents a review of cladding between similar filler and substrate alloys. Section 2.5 presents a review of CMT cladding of dissimilar filler and substrate alloys. Section 2.6 presents the post processing towards the enhancement of deposition characteristics. Section 2.7 presents the comparison of CMT with other GMAW process.

Section 2.8 presents the challenging issues for future research and Section 2.9 concludes the chapter.

2.2 Performance indicators of CMT cladding and coating

An ideal cladding or coating process should deposit the material on the substrate in the following manner:

(i) There should not be diffusion of cladding material to substrate material and vice versa. The purpose of the cladding and coating is to improve the surface properties of the product without affecting the substrate. Hence, diffusion of cladding material to substrate is the wastage of expensive material at the least. Additionally, it may affect the overall mechanical and metallurgical properties adversely. The reverse diffusion, i.e., the diffusion of substrate to cladded layer is equally undesirable as it will mitigate the protective power of the cladded layer.

(ii) There should be strong bonding between the cladded layer and substrate. This requirement is in conflict with the first requirement, as without any diffusion between cladding material and substrate, a strong metallurgical bond cannot be produced. Hence, there is a need of trade-off between these two conflicting requirements.

(iii) The mechanical and metallurgical properties of the cladded layer should be as good as possible.

(iv) Surface roughness of the top surface of cladded layer should be as low as possible, unless there is a requirement of special texture on the surface.

Requirement (i) is measured by a parameter called dilution. The dilution of the substrate by cladding materials is one of the most vital aspects of the cladding or coating process. The researchers have defined dilution in several ways. As per one definition, the dilution (%) is the percentage of the total cross-sectional area of the bead, which lies below the surface of the substrate as shown in Fig. 2.1 (Rajeev et al. 2014). Mathematically,

$$\text{Dilution}(\%) = \left(\frac{\text{Area A}}{\text{Area A} + \text{Area B}} \right) \times 100. \tag{2.1}$$

Some researchers have focused on the diffusion of Fe from the substrate to cladding and defined volumetric dilution as (Varghese et al. 2019, Hasson and Otterloo, 1997, Zhao et al. 2022)

$$D_V = \left[1 + \frac{\rho_S}{\rho_C} \left(\frac{Fe_S}{Fe_C} - 1 \right) \right]^{-1}. \tag{2.2}$$

where ρ_S and ρ_C are the densities of the substrate and cladding, respectively. Fe_S and Fe_C represent the weight percentage of iron in substrate and cladding, respectively. The similar formula can be employed for measuring the dilution by other elements such as Cr.

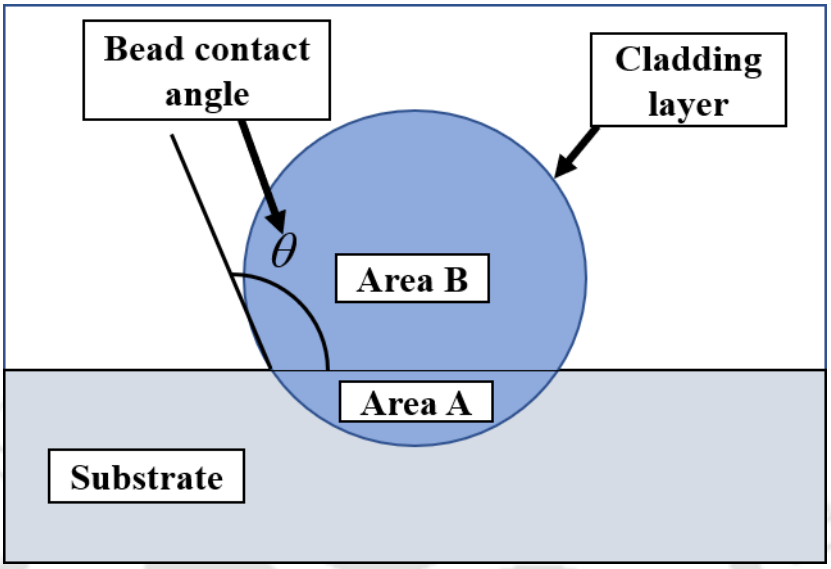

Figure 2.1 Schematic for dilution calculation and bead contact angle

Apart from dilution, surface roughness, porosity, microhardness, wear resistance and corrosion resistance are other performance indicators of cladding. Invariably, the cladded surface has high roughness. Hence, some machining is required. During some cladding processes, the formation of pores in the clad layer can occur. Porosity should be avoided as it weakens the material, reduces the corrosion resistance, and leads to defects. Cladded surface has enhanced microhardness, which directly enhances the wear resistance. However, it may have some adverse effect on the overall tensile strength and percentage elongation. Cladding can provide a protective layer that enhances the corrosion resistance, provided a proper cladding material is chosen.

2.3 Effect of process variables

Process parameters viz., welding current, voltage, welding travel speed, polarity, diameter of filler wire, length of the free wire, overlapping of weld beds, angle of the nozzle and shielding gas are the important parameters of overlay coating, which affect the dilution of the weld. Process parameters can be divided into two parts— non-numeric machine-independent parameters (types of filler wire and shielding gas) and numeric machine parameters (welding current, arc voltage and welding speed). It is easier to choose non-numeric parameters as the choice is limited. For example, only a few filler wires may be available and one may have to choose a wire of suitable diameter and

composition based on desired cladding geometry and composition. On the other hand, there is a lot of scope to fine-tune numeric machine parameters.

Several studies have been conducted to study the influence of numeric machine parameters. The influence of current, voltage and welding speed in the efficient cladding process has been discussed by a few researchers (Kumar et al. 2016, Varghese et al. 2019, Rajeev et al. 2014, Ghelichi et al. 2014, Meng et al. 2022) and is presented in Table 2.1. Table 2.1 indicates that heat input is the most crucial parameter affecting the properties of the cladded layer. The heat input Q in kJ/mm during cladding can be calculated as (Evangeline and Sathiya, 2019),

$$Q = \eta\left(\frac{VI}{S}\right). \tag{2.3}$$

where η is the efficiency, V the voltage, I the current and S is the welding speed. Excessive line energy causes the dilution of the cladding. The heat input corresponding to current voltage and welding speed are reported by a few authors (Kumar et al. 2016, Varghese et al. 2019, Rajeev et al. 2014). The dilution (in %) was proportional to the heat input, albeit not in a linear fashion. The 1.6 mm diameter of AA6061 filler wire was deposited on the substrate of the same composition, with argon as the shielding gas at a flow rate of 18 l/min at three different welding currents (50 A, 60 A and 70 A) and welding speeds (400 mm/min, 500 mm/min and 600 mm/min) (Kumar et al. 2016). Welding voltage remained in the range of 11–14.2 V. The current and voltage in CMT process are usually expressed in root mean square form; however, barring a few researchers, authors have not explicitly mentioned it. The wire feed rate is also not mentioned, which is an important parameter. A combination of high current and high welding speed provided sound weld. The highest dilution of 62.8% was reported at the highest heat input of 0.138 kJ/mm. A narrow HAZ and low intermetallic phase were obtained. The deposition of Inconel 617M coating on 316L steel was employed at three different variable inputs viz., current inputs (80, 90 and 100 A), voltage (11.5, 12 and 12.5 V) and welding speed (300, 400 and 600 mm/min) (Varghese et al. 2019). The lowest volumetric dilution in cladding (6.3%) was obtained at the lowest heat input (0.125), while the highest heat input (0.184) yielded the highest volumetric dilution (32.2%). The volumetric dilution of the cladded layer was estimated at 100 μm from the interface.

During the coating of Ai-Si-Mn alloy on commercially pure aluminum (Rajeev et al. 2014), three different beads were produced at three different welding speeds (384 mm/min, 510 mm/min and 636 mm/min). The other parameters were as follows: voltage 12.5 V, current 80 A, wire feed rate 4.8 m/min and nozzle to plate distance 5 mm. The lowest dilution of 7.7% was obtained at the lowest heat input 0.94 kJ/min, while the highest heat input 0.157 kJ/min yielded the highest dilution of 23%. The minimum bead contact angle of 67° and maximum Vickers hardness of 57 HV was observed at the welding speed of 10.6 mm/s; the welding speed of 6.4 mm/s provided a bead contact angle of 101° and the hardness of 52 HV.

During the cladding of Ni201 filler wire onto 304 stainless steel substrate (Zhao et al. 2022). The highest volumetric dilution of 24.5% was observed at highest heat input of 0.55 kJ/mm, compared to 0.3% at 0.28 kJ/mm. In the deposition process of Inconel 625 nickel-based alloy on ductile cast iron using CMT wire-arc welding (Meng et al. 2022), the level of dilution increased with higher heat input. At low heat input interface bonding was similar to a brazed joint but at high input it had the characteristics of a weld-braze joint. In the deposition process of Inconel 718 on the SS304 base substrate using CMT (Gejendhiran et al. 2023), sinewave weaving with 30% overlap demonstrated lower dilution (13.46%) compared to the stringer (i.e. straight line) technique. Fine equiaxed grains were developed in the straight beads due to the lower thermal conductivity of IN718. However, the overlap region exhibited a boundary between randomly oriented dendrites and formed a homogenous microstructure with fine equiaxed grains due to higher thermal gradient occurring between the two weld bead layers. The homogeneous microstructure in the overlap beads also enhanced hardness compared to straight beads. The ultimate tensile strength was also greater than the base substrate.

The influence of CMT welding speed on microstructure of AZ31 magnesium cladding was reported by Zhang et al. (2015). The welding speed was the best in the range 10–12 mm/s. Both feedstock and substrate used for the CMT process are of similar compositions. Zhang et al., 2015 correlated the welding speed with cooling rate and heat input values. Enhanced cooling rates gave the precipitates less time for nucleation and therefore produced less precipitates in the final product. Less heat input leads to a narrow HAZ.

The bead contact angle also plays an important role in the cladding process when the cladding is developed by side-by-side overlapping beads. A lower bead contact angle is desired to avoid lack of fusion while developing overlap cladding layers (Evangeline and Sathiya, 2019). As discussed, dilution is proportional to heat input, but the bead contact angle can have positive (Rajeev et al. 2014) or negative correlation (Kumar et al. 2016) with it depending on other factors.

Another important parameter is the welding speed. A high-speed welding with the same line energy provides high cooling rate, which tends to produce finer and consequently harder structure. Welding speed affects the amount of material that can be deposited per unit time. Increasing the welding speed can result in a thinner and more even coating, while reducing the speed can result in a thicker and less even coating. The optimal welding speed is typically determined by the size of the substrate and the desired coating thickness.

The welding current and welding gun traverse speed also have significant influence on mechanical properties. The welding current affects the penetration depth of the weld, which in turn affects the mechanical properties of the cladding. Higher welding currents result in deeper penetration, which can lead to better bonding between the cladding and substrate. However, too high a current can cause defects in the cladding, such as porosity, and reduce the mechanical strength. The welding speed also affects the grain structure of the cladding, which in turn affects the mechanical properties. Exact influence depends on several factors including type of materials, temperature and shielding gas. Other important controllable parameters are length of the free wire, travel angle of the nozzle, path planning, voltage and wire feed rate. Modelling and simulation can throw better light on this aspect.

Table 2. 1 Different process parameters and output in the CMT cladding

Reference, Filler material and substrate	Current (A)	Voltage (V)	Welding speed (mm/min)	Heat input (kJ/mm)	Dilution (%)	Bead contact angle (°)
Kumar et al. (2016), AA6061 filler wire and AA6061 alloy	50	11.0	600	0.055	4.9	118.8
		11.2	500	0.067	5.6	112.6
		11.7	400	0.087	6.67	111.5
	60	12.0	600	0.072	27.6	61.3
		13.2	500	0.095	34.8	61
		14.2	400	0.127	42.9	59.7
	70	13.7	600	0.095	58.3	40
		13.3	500	0.111	60.8	37.5
		13.2	400	0.138	62.8	38.7
Varghese et al. (2019), Inconel 617M and 316L steel	100	12.5	600	0.125	6.3	
	90	12	400	0.162	14.6	–
	80	11.5	300	0.184	32.2	
Rajeev et al. (2014), Al-Si-Mn alloy and pure Al	80	12.5	636	0.094	7.7	67
			510	0.118	8.3	89
			384	0.157	23	101
Zhao et al. (2022), Ni201 wire and 304 stainless steel	120	26		0.28	0.3	
	140	30		0.37	4.7	–
	160	35	600	0.46	18.2	
	180	38		0.55	24.5	
Meng et al. (2022), ERNiCrMo-3(Inconel 625) wire and ductile iron QT500-7	95	16.6	–	0.47	~2.2	–
	110	18.1		0. 59	~4.3	
	125	19.2		0. 72	~8.6	
	140	19.9		0. 83	~13.7	
	155	20.5		0. 95	~13.9	
	170	21.2		1.08	~13	

2.4 CMT cladding/coating of similar filler and substrate alloys

Since the advent of CMT in 2004, many comparable alloys have been successfully cladded using CMT process. The following discussion focuses on similar metal clad produced with CMT for several alloys.

2.4.1 Aluminum-based alloy

Aluminum alloys are preferred for a range of engineering applications due to their light weight, high ductility, and exceptional corrosion resistance. However, the wear resistance of these alloys is typically low, and their parts can suffer from a shortened lifespan as a result of damage. To address this issue, surface cladding and coating are commonly employed to improve the lifespan of these parts. Weld overlay cladding is particularly popular for repairing damaged parts. Nonetheless, cladding aluminum alloys using fusion welding remains a challenge due to their low melting temperature. The resulting weld metal oxidizes immediately, leading to the development of a brittle intermetallic layer that adversely impacts the mechanical properties of the product. The use of low heat input CMT technology can help overcome these issues and enhance the surface mechanical properties of aluminum alloys.

Several studies have been conducted to study the influence of Al-based filler alloy cladding on substrate of similar alloy. Al-based ER2319 filler wire was deposited on 19 mm thick AA2291 Al alloy sheet (Cong et al. 2016). Spherical-shape bead geometry with lower dilution was achieved and the porosity was significantly eliminated in the deposited beads due to use of CMT pulsed technology. ER4043 filler wire was deposited on 6061 aluminum alloy in a hybrid TIG-CMT process (Liang et al. 2017). The TIG was used to preheat the base metal to improve the wettability of liquid metal, which had a significant effect on the contact angle and dilution of the weld bead. In the microstructure morphology shown in Fig. 2.2, the partially melted zone (PMZ) displays fine equiaxed grains, whereas the HAZ shows coarser equiaxed grains. An increase in heat input resulted in the increase of PMZ and developed the coarser columnar dendrites.

Low dilution cladding of 2024 Al alloy with 2319 Al and 4043 Al wires was also reported by Pickin et al. (2011). The limits for cladding were established based on the contact angle of the weld bead with the base material. It was observed that an angle of less than 90° can lead to non-uniform bead shape deposition, and the development of voids between successive cladding weld passes.

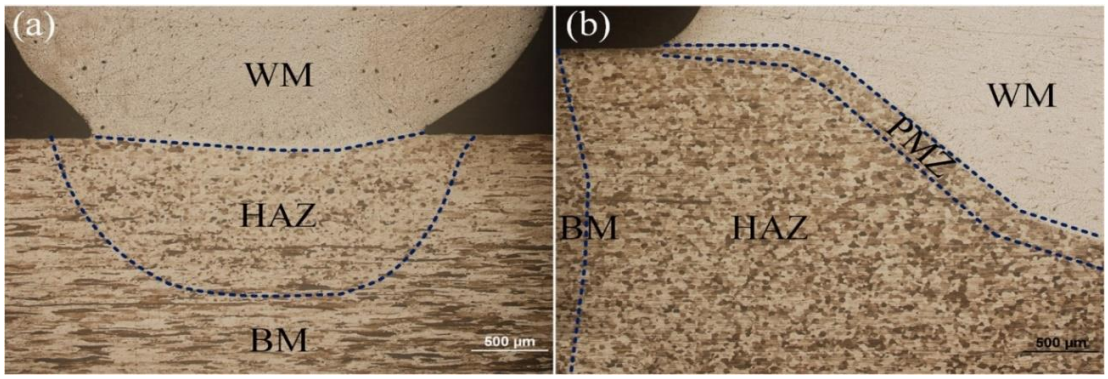

Figure 2.2 Microstructures of joints: (a) conventional CMT; (b) TIG-CMT. With permission from Liang et al., 2017. Copyright Elsevier

2.4.2 Nickel-based alloy

Inconel 718 filler wire was deposited on 7.5 mm thick substrate of similar composition (Benoit et al. 2011). The microstructural observation indicated good quality weld with no lack of fusion between the filler and substrate material. Compared to the traditional metal inert gas (MIG) welding, the HAZ was less in size. The developed tensile residual stresses were less than those compared to traditional welding techniques.

2.4.3 Steel-based alloy

The utilization of the CMT process has emerged as a viable option for depositing grade 309 and 310 austenitic stainless-steel alloys on 16Mo3 steel pipes (Gornikowaka et al. 2021). Three distinct zones were identified– composite, intermediate (transition), and heat-affected. The composite zone consisted mainly of austenitic microstructure with a minor amount of ferrite, 7% for the 309-steel and less than 0.5% for the 310-steel cladding. The dendrite cores in the 309-steel cladding exhibited enrichment with Cr and depletion of Ni, while the solidification process in the 310-steel cladding led to significant micro-segregation of Cr, Mn, and Fe. The interdendritic region of the 310-steel cladding showed notable enrichment with Cr and Mn and depletion of Fe with a relatively uniform distribution of Ni. Both types of cladded pipes demonstrated increased hardness at the interface between the substrate and the cladding layer. The microstructural evolution was studied in the transition zone of a 310 austenitic steel cladding layer on 16Mo3 unalloyed steel using CMT (Gornikowaka et al. 2023). The transition zone exhibited a complex structure, with the region near the fusion boundary consisting of martensite and the remaining region austenite. The zone containing martensite had a narrow width of only 600 nm.

The ER2209 steel wire was deposited on S32205 steel plate using CMT process (Luchtenberg et al. 2019). During deposition the current and voltage were maintained at constant values of 215 A and 20 V, while welding speeds were 360, 300, 230 and 150 mm/min, corresponding to welding line energy of 0.53, 1.01, 1.27 and 1.74 kJ/mm, respectively. The line energy of 1.27 kJ/mm provided the highest corrosion resistance, while the worst corrosion resistance was at line energy of 1.74 kJ/mm. The high energy input during the process resulted in the formation of intergranular and Widmanstätten austenite at the expense of ferrite and partially transformed austenite. Widmanstätten austenite exhibits a lath-like (rather than a plate-like) shape.

Ahsan et al. (2016) deposited Fe-based ER70S-3 filler wire on 2.3 mm galvannealed steel sheet. They reported optimized welding conditions to reduce porosity for two heat range inputs— low (200–250 J/mm) and high (350–550 J/mm). During low heat input, solidification started early, resulting in small porosities near the weld root. High heat input combined with high vapour pressure and poor viscosity of the molten metal at high temperature helped the bubbles grow. The bubbles could, however, escape from the weld pool and a porosity-free weld bead was produced as a result of the delayed initiation of solidification. In comparison to low heat input conditions, the medium heat input conditions produced a low viscosity weld pool and a high vapour pressure, which allowed the bubbles to grow. However, the temperature of the weld pool was not as high as under conditions of high heat input, delaying the start of solidification until all the bubbles had been completely vented from the weld pool. Consequently, most of the time, there were significant porosities discovered close to the surface of weld beads.

Additionally, the study found that the welding parameters, such as wire feed speed and welding current, can also affect porosity formation. Specifically, a higher wire feed speed and lower welding current were found to reduce the formation of porosity.

2.4.4 Magnesium-based alloy

An additional issue regarding fusion welding of Mg alloys is that the localized melting occurs in the high hazard zone. Under varied welding speeds, however, there was a small variation in microhardness. It is because, when welding speed was reduced, an extra granular phase developed in fusion zone (FZ) and HAZ as a result of increased heat input, partially offsetting the influence of grain coarsening upon micro-hardness drop. Grain agglomeration, localized melting, and liquidation fractures are common in HAZ, making it the most susceptible part of cladding. As a result, controlling the breadth of

HAZ is critical for better cladding quality (Zhang et al. 2015, Zhu et al. 2006). Magnesium alloys provide better specific strength, relatively low density, good castability, ideal electromagnetic wave shielding, and good thermal conductivity, and therefore are easily recyclable. They have the potential to be used as lighter-weight structural components in vehicles like cars and planes. Grain coarsening, Mg oxidation and vaporization, thermal stress, as well as hot cracking are indeed concerns when welding magnesium alloys (Liu et al. 2014). During restoration welding or cladding procedures, it is critical to repair parts without sacrificing weld quality or endangering the structure's mechanical characteristics. As a result, improving existing repair procedures and developing new creative restoration processes are critical. It is widely acknowledged that CMT results in decreased heating rate for the same current while maintaining the same fusion rate, making it a viable cladding alternative. Regarding Mg-alloys, the reduced heat input of the CMT method may assist to mitigate issues like droplet eruption, large grain development, hot cracking, thermal stress, and other issues that may emerge during welding (Liu et al. 2014). Furthermore, the retraction of the electrode wire may help with spatter free droplet transmission.

Overall, in cladding or coating with CMT, it is generally recommended to use filler wire that is similar in composition to the substrate or base metal. This helps to ensure good bonding between the two materials and prevent any potential issues with metallurgical incompatibility. In general, the choice of filler wire will depend on the specific application and the properties that are desired in the final product. It is important to consider factors such as the mechanical properties, corrosion resistance, and thermal conductivity of both the substrate and the filler wire when selecting materials for CMT cladding or coating.

2.5 CMT cladding of dissimilar filler and substrate alloys

Fusion welding of dissimilar filler and substrate alloys presents a challenge due to their incompatible materials properties. This can lead to the development of a brittle intermetallic layer that has an adverse impact on the mechanical properties of the product. Traditional GMAW technology intensify this issue, as the high heat input involved promotes a high degree of dilution. Low heat input CMT can be a viable solution for cladding. A summary of some studies is provided in the following paragraphs.

2.5.1 Nickel and steel-based alloy

The Inconel 625 alloy was deposited on carbon-manganese steel through CMT processes by Lorenzin et al. (2009). The parameters were 1.2 mm wire diameter, argon gas and weld speed of 250 mm/mm. The coating produced was of less dilution and defect free. Increasing dilution affects the coating composition, which can have a detrimental effect on the final products. The properties like hardness, corrosion resistance and strength will deteriorate with higher dilution. A low dilution also indicates less heat input, which causes minimal changes in microstructure and geometric shapes. During the deposition of Inconel 625 superalloy on 316L steel (Evangeline and Sathiya, 2019), the microstructure of the clad bead was found to be primarily made of columnar dendrites that were cellular in nature and spaced apart by secondary dendrite arms. The cladded and the interface regions had enhanced hardness and corrosion resistance due to the development of equiaxed dendrite. In a study conducted by Tang et al. (2020), both Ni-based and Fe-based coatings were produced on AISI 304 stainless steel substrate. The results showed that the Fe-based coating had good wear resistance, whereas the Ni-based coating exhibited good corrosion resistance.

Various methodologies can be used to protect boiler parts from high temperatures and corrosive environments, including pottery cladding, thermal spraying, as well as reinforced tubes. Due to the extremely high cost of nickel, applying Ni-based metals and alloys for tubes in drain incinerator walls is impractical. As a result, these alloys are commonly employed as coating materials, particularly for clad protective coatings on tubes made of lower corrosion-resistant structural steel (Solecka et al. 2015, Solecka et al. 2018). Inconel 625 was deposited on 16Mo3 boiler tubes (Solecka et al. 2015, Solecka et al. 2018). The microstructure of cladded layers had cellular-dendritic characteristic. The formed dendrites solidify in the same direction of heat transfer. The difference in solidification rates had resulted in micro segregation of different elements (Ni, Cr and Fe) in the dendritic regions shown in Fig. 2.3. In comparison to the dendritic region, the hardness increased significantly because of the high segregation of Mo and Nb to the interdendritic regions. The corrosion resistance enhanced due to cladding.

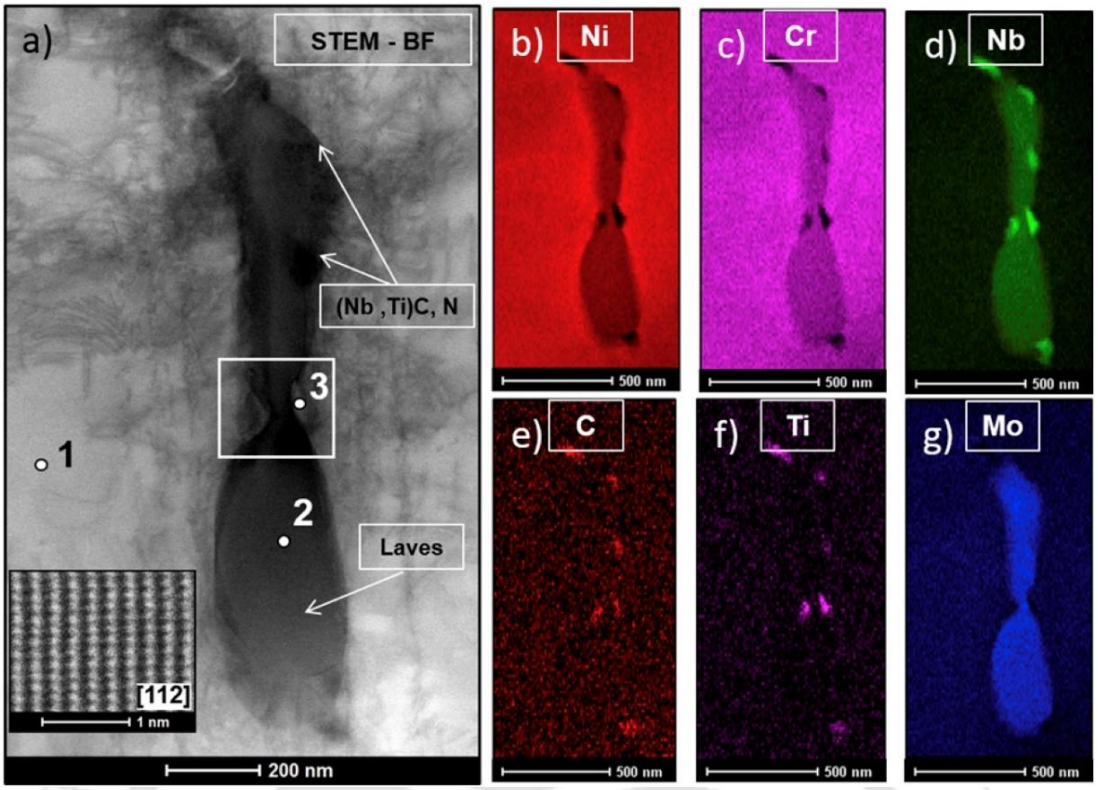

Figure 2.3 TEM morphology: (a) Phases with an eutectic morphology visible in the interdendritic areas - Laves phase surrounded by (Nb, Ti) C, N precipitates and (b–g) EDS maps of selected elements. With permission from Solecka et al.,2018. Copyright Elsevier

Gornikowska et al. (2014) studied the CMT coating of Inconel 625 on ferritic-perlite steel. They mentioned that one requirement for Ni-based coating was an Fe content less than 5 wt.%. The filler Inconel 625 had an Fe content of approx. 0.3% by weight and the applied coating had an Fe content of 2–3%, which indicates a slight dilution. The Fe content keeps on reducing with distance from the interface toward the coated surface and was higher in the partially mixed zone compared to FZ, which is the farthest from the interface. The micro segregation of a few elements (Ni, Fe, Cr, Nb and Mo) was also observed in the zone before FZ of cladded layer due to weld overlay solidification. Similar phenomenon is also reported by Pawel et al., 2015 deposited Inconel 625 on P235GH boiler steel. The dilution zone in the substrate was very narrow; Fe content near the interface of substrate and cladded layer was about 2%, which abruptly reduced towards the top surface of the cladded layer. The chemical composition of the dendrite cores and interdendritic gaps differed significantly as a result of the solidification process.

Nickel-based thick hardface coatings are crucial in nuclear power plants for their superior wear and high-temperature resistance. However, conventional techniques like Plasma Transferred Arc (PTA) and Metal Inert Gas (MIG) often result in crack-prone coatings with high dilution. A study on the wear behavior of Ni-Cr-B-Si hardface coatings deposited on 316LN stainless steel using the CMT welding process reported a higher the specific wear rate of the coating than the specific wear rate of the coating developed using traditional welding techniques (Mishra et al. 2022). The wear process was primarily abrasive in essence. During the wear tests, wear debris analysis revealed that the mating surfaces had oxidized. The coating exhibited a micro-hardness of 531.24 ± 73.15 HV0.5 and contained precipitates such as borides and carbides. The investigation highlights CMT as a viable method for depositing crack-free, low-dilution, and wear-resistant coatings in nuclear industries.

Ni-based alloys were deposited on 304 stainless steel substrate by Zhao et al. (2022). They used ERNiCrMo-3 (Inconel 625) and ERNiCrNo-4 (Hastelloy C-276) as cladding materials. Both types of cladding layers were uniform and dense. The Inconel 625 layer had a γ-phase matrix dominated by NbC precipitates causing solid solution strengthening. The Hastelloy C-276 coating had a γ-phase matrix and Mo-rich P phase. Both claddings displayed high corrosion and cavitation erosion resistance. Among these two claddings, Hastelloy C-276 was superior. The wear resistances of the Inconel 625 and Hastelloy C-276 cladding were approximately 1.3 and 1.5 times that of the 304 substrate, respectively. Monel K500 coatings were applied to the 304 stainless steel substrate using the CMT process, including single-layer, double-layer, and a transition layer with Ni201 (Zhao et al. 2023). All coatings had the FCC-γ phase with minor dispersed γ'-Ni3(Al,Ti) precipitates. The Fe element content varied along the thickness of the layer, with the transition layer coating having the lowest Fe content (0.72 wt.%) and the highest corrosion resistance. In 3.5 wt.% NaCl artificial seawater, the Monel K500 coating with the Ni201 transition layer showed the highest corrosion resistance. Additionally, this coating exhibited higher microhardness (211.6 ± 0.2 HV) due to its smaller average grain size, stronger anisotropy, and higher alloying element content. The coefficients of friction (CoF) for the three Monel K500 coatings were measured as 0.68, 0.67, and 0.61.

Additive manufacturing (AM) with low heat input is a vital technology for the online maintenance of long-distance oil and gas transmission pipelines. Recent studies (Dong et al. 2022, Ning et al. 2021, Wu et al. 2023, Toguyeni et al. 2013) have

extensively tested steel alloys using two AM methods: laser and cold metal transfer (CMT) arc, with a custom filler wire and low heat input. The CMT process emerged as a viable option for depositing nickel-based alloys (Inconel 325) on X80 carbon steel pipelines due to its limited dilution capabilities (Dong et al. 2022). However, dissimilar weld joints face challenges with sulfide stress corrosion cracking (SSCC). To tackle this, a study focused on the microstructure and SSCC behavior of an Inconel 625/X80 weld overlay fabricated through the CMT process, with emphasis on the tempering effect. The heat-affected zone (HAZ) displayed distinct features; the non-overlap zone exhibited lath structures and prior austenite grain boundaries (PAGBs) containing Martensite-austenite (M-A) constituents, while the overlap zone showed granular bainite, fine ferrite, pearlite, and a small amount of fine blocky M-A islands. SSCC preferentially occurred at lath martensite/bainite and PAGBs in the fusion boundary (FB) region. The tempering effect in the overlap zone resulted in lower residual strain, fewer high angle boundaries, and a more homogenized microstructure, leading to a higher resistance to SSCC compared to the non-overlap zone. Reversed austenite acted as a strong hydrogen trapping site, mitigating susceptibility to cracking in the FB region.

Two methods —laser and cold metal transfer (CMT)— were used to deposit EAMW16MND5 wire on X80 steel (Ning et al. 2021). Neither method softened the HAZ in the substrate. The laser-prepared additive manufactured parts (AMPs) had microhardness values 140% of the substrate and impact energies of 53% at room temperature. The CMT-prepared AMPs had microhardness values 119% of the substrate and impact energies of 67%. Both AMPs exhibited anisotropic mechanical properties, with the laser-based AMPs showing more significant anisotropy.

A steel catenary riser (SCR) connects a subsea wellhead to a floating platform and faces substantial loads from waves, currents, and winds causing fatigue damage. The appearance of SCR weld joints, especially the weld root, requires strict standards. A new gas metal arc welding/pulse gas tungsten arc welding (GMAW/GTAW-P) double-sided root welding process was proposed for SCRs to achieve a nearly smooth root geometry (Wu et al. 2023). The GMAW/GTAW-P double-sided simultaneous welding process improved fatigue strength by reducing root stress concentration, making it suitable for pipelines with high fatigue life requirements in deep-water environments under complex alternating loads.

The use of high-strength steel, Grade X80, offers benefits like reduced pipeline weight, cost savings in material and fabrication, and easier installation by existing pipelay

vessels. Reel-lay is a cost-effective offshore installation method for high-strength steel pipe. A seamless quenched and tempered Grade 555 linepipe, designed for offshore reel-lay, has been successfully developed and qualified using GMAW-CMT/PGMAW process (Toguyeni et al. 2013).

2.5.2 Aluminum and steel-based alloy

Cladding between aluminum and steel-based alloys is often done to combine the beneficial properties of both materials. As, steel is strong and has good wear resistance, while aluminum is lightweight and offers excellent corrosion resistance. The CMT process is particularly suitable for aluminum and steel-based alloy cladding because of its low heat input and ability to control the cladding parameters precisely. The low heat input minimizes the risk of distortion or thermal damage to the base materials.

The Al 4043 alloy was deposited on galvanized steel using CMT process and a good wettability and contact angle of 38° were reported between the deposition bead and substrate (Zhou and Lin, 2014). The joint surface was obtained with metallic characteristic rather than oxidized characteristic. Cao et al. (2014) deposited AA6061-T6 filler wire to boron steel with different coatings. It was discovered that a zinc coating on the steel substrate is crucial. Under the arc, a pure Zn coating on galvanized boron steel melted, which improved the wetting of molten aluminium filler metal onto the solid steel substrate. As a result, low reinforcing and smooth-appearing welds were produced. Again, with Fe-Zn coating to galvannealed boron steel, due to high melting temperature the molten Al barely wet to the steel substrate under an applied arc. This led to the production of poor-quality welds. However, during CMT joining of AA6061-T6 galvanized boron steel, element zinc was evaporated. The development of brittle Fe-Al intermetallics between the aluminium weld metal and the steel substrate was low as a result of the weld pool's temperature being lowered due to heat dissipation from the evaporation of the Zn. They also reported, due to significant development of the brittle $FeAl_3$ intermetallic during the welding process, the CMT arc welding technique was unable to produced joints between AA6061-T6-bare boron steel and AA6061-T6-Al-Si-coated boron steel.

2.5.3 Cobalt and steel-based alloy

Rajeev et al. (2019) reported deposition of Stellite 21 coating on H13 steel by CMT and traditional plasma transferred arc welding (PTAW) process. Compared to the PTAW technique, the CMT approach produced the coating with a finer microstructure

and less dilution. The increase in microhardness was achieved as a result of the CMT coating's finer structure and reduced dilution. Rajeev et al. (2017) also conducted a study where they deposited Stellite 21 coating on H13 substrate. The deposition was carried out in both annealed as well as quenched and tempered (Q&T) conditions, and at both ambient and 400 °C preheat conditions. They observed that under-bead cracking occurred in the Q&T substrate with and without preheat, as well as in the annealed substrate without preheat (see Fig. 2.4, AWPH: annealed with preheat; AWOPH: annealed without preheat; Q&TWPH: quenched and tempered with preheat; Q&TWOPH: quenched and tempered without preheat). This cracking was caused by the formation of brittle martensite upon rapid cooling, which led to the development of high tensile residual stresses at the bead toe. However, the annealed substrate with a preheat of 400 °C showed the least tendency for cracking and resulted in improved mechanical properties. The Co-based Stellite 12 was deposited on martensitic stainless steel using CMT process (Tapiola et al. 2023). The deposition was uniform, thick (>2.5 mm) with less number cracks and pores.

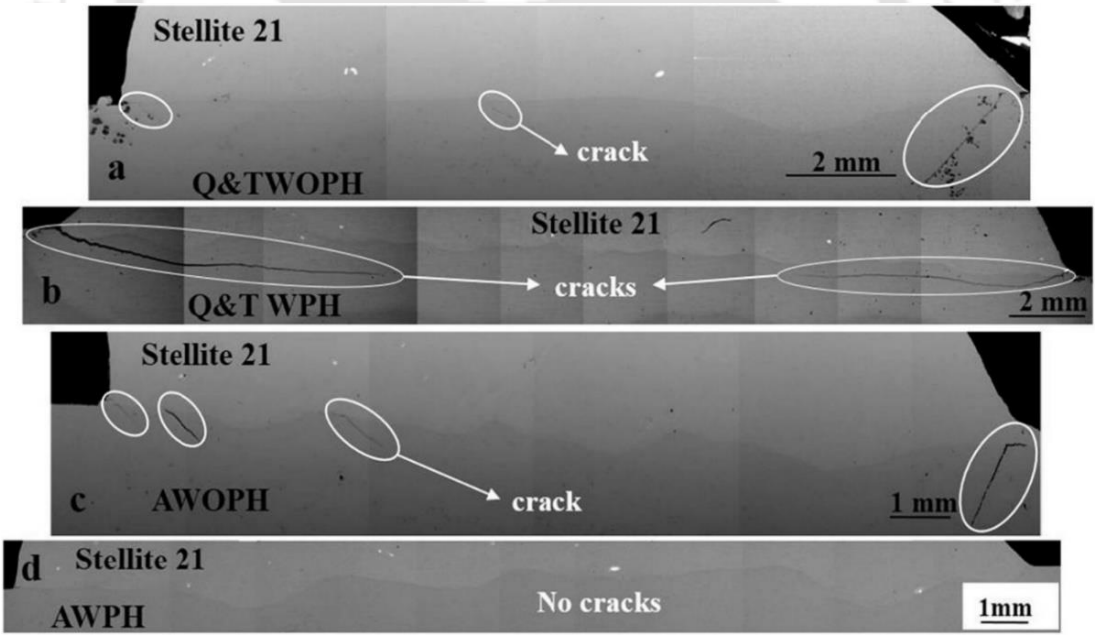

Figure 2.4 Micrograph of the cross section of Stellite 21 coating on H13 substrate under different conditions: (a) Q&T without preheat (b) Q&T with preheat (c) annealed without preheat, and (d) annealed with preheat. With permission from Rajeev et al. (2019). Copyright Elsevier

2.6 Post processing towards the enhancement of deposition characteristics

The heat treatment after the CMT coating process has an enhanced effect in microstructure, mechanical properties and bond strength. The heat treatment also has an influence on the relaxation of residual stress and strain in the final products. In general, the microstructure and mechanical strength of the final products change after overlay welding because the parent metal melts during the welding process. It leads to weakness. To overcome this problem, heat treatment is carried out to obtain the required mechanical properties and reduce the stresses of the joint.

The effects of various heat treatment methods, including solution treatment, aging, and a combination of both was compared for the deposition of ER4043 filler wire on AA 2024 Al sheet (Prakash et al. 2018). The results showed that the CMT welding process produced a fine and homogenous microstructure with a uniform distribution of intermetallic particles in the weld zone. However, the HAZ exhibited a coarser microstructure due to the thermal cycling during the welding process. The solution treatment resulted in the dissolution of the intermetallic particles and the formation of a supersaturated solid solution. Aging the material after solution treatment resulted in the precipitation of the intermetallic particles and an increase in strength, while reducing ductility. The combination of solution treatment and aging resulted in a good balance of strength and ductility. The post-weld heat treatment significantly affected the microstructure and mechanical properties of the AA6061 aluminum alloy welded joint (Ahmad and Baskar, 2011). After post-weld heat treatment, the microstructure of the welded joint was observed to transform from a dendritic structure to a more uniform and equiaxed grain structure. The heat treatment also led to the dissolution of the precipitates and resulted in the formation of a more homogeneous microstructure. Additionally, the heat treatment reduced the hardness and improved the tensile strength of the welded joint. Furthermore, the heat treatment also improved the ductility and fracture toughness of the welded joint. The fracture surface of the welded joint after heat treatment exhibited a more uniform and finer dimple pattern, indicating improved toughness. The post-weld heat treatments were performed at two different temperatures, 170 °C and 320 °C, for 1 h each for the deposition of ER 4043 filler wire on AA 6061-T6 alloy (Yang et al. 2013). The peak load during the tensile test of the welds subjected to the post-weld heat treatment at 170 °C was improved as compared to the as-welded welds. This improvement was attributed to the increased number of precipitates formed during the longer post-weld heat treatment time, which was longer than the thermal cycle

experienced during CMT welding. However, the tensile load of the welds decreased significantly when subjected to the post-weld heat treatment at 320 °C for 1 h. The reduction in peak load was ascribed to a decrease in the density of needle-shaped precipitates and an increase in the amount of β′ precipitate.

Overall, the heat treatment process improved the microstructural properties of the cladding, leading to the formation of a more uniform and refined structure. It is also found that the mechanical properties of the cladding improved significantly after heat treatment. These findings have significant implications for the development of high-performance cladding materials for various industrial applications.

2.7 Comparison of CMT with other GMAW process

In GMAW based fusion techniques, the feedstock materials are melted by an arc heat source and deposited on the substrate metal surface. Therefore, it is necessary to consider metal transfer patterns as they have a great influence on the microstructure, surface profile and properties of the manufactured part. In order to obtain a reproducible material application for manufacturing in the quality area, the influence of arc and metal transfer mode must be considered in the analysis. The parameters during overlay welding that affect the type of metal transfer are current, voltage, arc length, wire feed rate and type of shielding gas. The influence of current is having a significant role owing to greater influence on droplet size, metal transfer frequency and the droplet acceleration in the arc region. Globular metal transfers are ensured at low currents and high voltages with a diameter almost twice the diameter of the electrode. The CMT evolved from a GMAW process. However, it has a peculiar the drop transfer mechanism. The controlled electrode in the CMT process ensures low heat effect in the weld bed. It leads to the development of less distortion and increased productivity. The CMT process has become popular in recent years owing to low current at the short-circuit point; which develops a low heat input. The process is controlled by pulling the wire out of the short circuit; hence, it is known as mechanical assisted droplet deposition. Several studies have been conducted to study the comparison of CMT process with other fusion process. The influence of current, voltage and welding speed in the efficient cladding process has been discussed by a few researchers (Rajeev et al. 2019, Varghese et al. 2019, Kun et al. 2022, Mishra et al. 2023, Meng et al. 2023, Han et al. 2022); it is summarized in Table 2.2.

During the hardfacing of Stellite 21 on H13 steel through CMT and plasma transferred arc welding (PTAW); the CMT process provided enhanced microstructure

and mechanical characteristics compared to PTAW (Rajeev et al. 2019). The microstructure morphology of CMT process sample showed a finer and homogeneous microstructure with smaller carbide particles compared to the PTAW process, which had larger carbide particles and some porosity in the microstructure. The CMT process had lower dilution levels in spite of developing a thick layer (Table 2.2), which is desirable for hardfacing applications, compared to the PTAW process. The wear behavior analysis showed that both processes produced similar wear behavior, with the CMT process having slightly lower wear rates in some cases.

The CMT process used for applying an Inconel 617M overlay coating on type 316L stainless steel provided enhanced characteristics compared to traditional Gas Tungsten Arc Welding (GTAW) process (Varghese et al. 2019). The CMT process provided a more uniform and consistent overlay coating compared to GTAW for same thick layer, with minimal volumetric dilution of the Inconel 617M with the stainless-steel substrate. The maximum dilution of 50.1% was observed in GTAW, as shown in Table 2.2. Furthermore, the CMT process resulted in a lower heat input during the welding process, which reduced the risk of distortion and improved the mechanical properties of the coated material. The average penetration depth of the cladding material into the substrate was more in GTAW (900 μm) than that in CMT (404 μm) process.

The cladding of Inconel 625 on X80 pipeline steel shows that the CMT process produced a finer microstructure with smaller dendrites and a more uniform distribution of precipitates compared to the TIG process, thanks to the lower heat input and higher cooling rate associated with the CMT process (Kun et al. 2022). Again, from electron backscatter diffraction (EBSD) analysis of the microstructure (Fig. 2.5), it is seen that fine grains are formed near the interface region, possibly due to the high cooling rate and a large number of heterogeneous nucleation sites (Ni et al. 2020). The region adjacent to the fine grains in the CMT cladding showed a large number of equiaxed grains, while the TIG cladding exhibited coarse elongated grains in the same area. The corrosion behavior of Inconel 625 cladding deposited through both processes using electrochemical polarization and immersion tests in a 3.5% NaCl solution. The enhanced corrosion resistance was observed in the CMT process compared to the TIG process.

Crack-free Ni-Cr-B-Si hardface coatings were deposited on the 316LN stainless steel substrate using CMT and PTAW processes (Mishra et al. 2023). However, CMT process provided a crack-free hardface coating with superior wear behaviour when

compared to PTAW. The hardface coating produced by the CMT process has higher average hardness (502.96 ± 55.89 HV0.5) compared to the coating produced by the PTAW process (385.56 ± 67.1 HV0.5). The CMT coating exhibited a distinct interface with minimal dilution, while the PTAW coating had a diffused zone with relatively higher dilution.

The ERNiCrMo-3 wire (Inconel 625) was cladded on HT250 (steel) using CMT and plasma arc welding process (Meng et al. 2023). The dilution rate of plasma arc deposited layers was significantly higher compared to CMT process. The fatigue behavior of API X65 pipeline steel joints by ER70S-6 filler wire with CMT and GMAW process was compared (Han et al. 2022). The fatigue life of CMT-joints improved by approximately 67% compared to GMAW-joints due to the combined effect of reduced stress concentration at the weld root and the fine microstructure.

Overall, the CMT process is a viable alternative to traditional welding processes for applying overlay coatings on different substrate alloys, offering improved control, consistency, and mechanical properties.

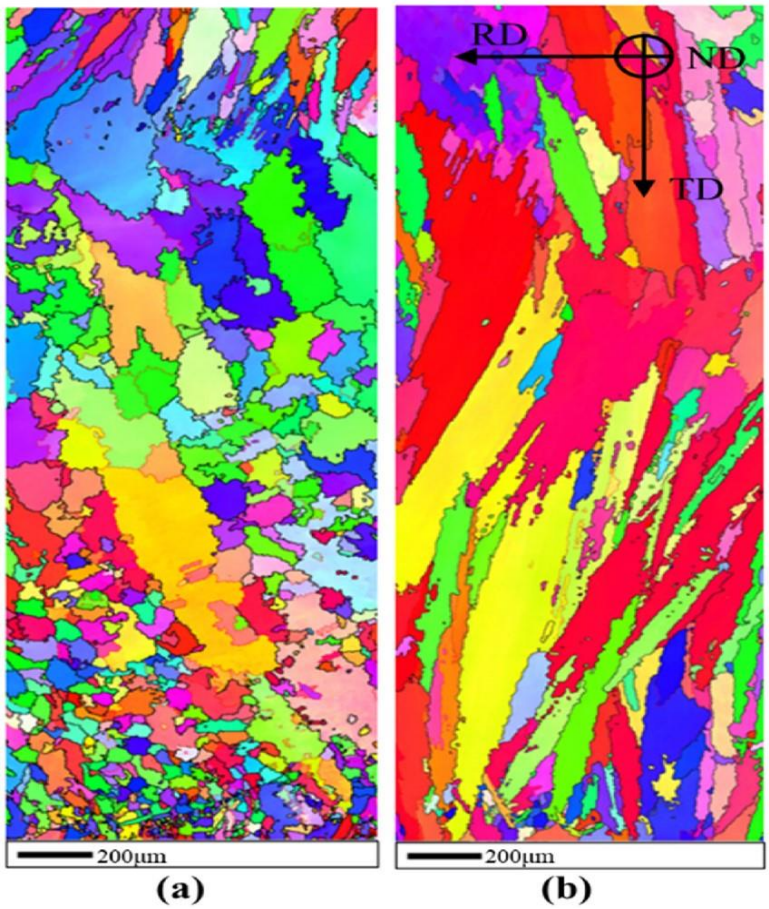

Figure 2.5 EBSD crystal orientation maps of the cross-section: (a) CMT cladded layer and (b) TIG cladded layer. With permission from Kun et al. (2022). Copyright Elsevier

Table 2. 2 Comparison of CMT with other traditional process

Reference	Process	Current (A)	Voltage (V)	Welding speed (mm/min)	Heat input (kJ/mm)	Volumetric dilution%
Rajeev et al. (2019)	CMT	117	9.6	127	0.53	10
	PTAW	155	16	193	0.77	13.5
Varghese et al. (2019)	CMT	80	11.5	300	0.18	32.2
		90	12	400	0.16	14.6
		100	12.5	600	0.12	6.3
	TIG	100	10.5	110	0.57	50.1
He at al. (2022)	CMT	245	16.9	600	0.41	–
	TIG	140	12	300	0.33	–
Mishra et al. (2023)	CMT	160–170	15–20	280	0.61	–
	PTAW	120	25.1–28.4	100	1.90	–
Meng et al. (2023)	CMT	95–170	16.6–21.2	200	0.47–1.08	≤16.91
	PAW	120–200	19.5–22.9	200	0.72–1.37	≤77.10
Han et al. (2022)	CMT	190	12	420	0.33	–
	GMAW	169	19	500	0.44	–

2.8 Major Gaps in the Literature

In the recent years, the welding industry has witnessed progress with the development of dissimilar welding and non-conventional welding techniques. Dissimilar welding has exhibited remarkable potential in reducing manufacturing expenses and time, particularly in the automotive and shipbuilding sectors. Nevertheless, there is still considerable scope for research in optimizing welding parameters, filler materials, base metals, and other critical factors involved in dissimilar welding. CMT welding process has gathered considerable attention due to its numerous advantages over conventional welding techniques. Some possible future directions for research in CMT welding process with respect to cladding and coating are as follows:

- Although there have been some investigations on applying CMT for cladding, there is no reported research on cladding of Al alloy by steel. Some researchers did coat Al alloys by metallic powders using spray techniques but observed a lot of porosity. Moreover, metallic powders are usually expensive.
- The research on corrosion immersion tests and their utility in evaluating the corrosion effects on CMT-cladded Fe-based layers is less. Furthermore, there is a need to investigate the impact of corrosion on surface roughness, hardness, and wear properties.
- A less amount of work has been reported on the post-processing of the CMT cladding. Heat treatment can be used to improve the mechanical properties of the cladding by relieving residual stresses and enhancing grain refinement. The type of heat treatment used would depend on the material of the substrate and the desired mechanical properties of the cladding.
- Surface finishing techniques such as milling, grinding and polishing can be used to improve the surface roughness and aesthetics of the cladding. Proper surface finishing techniques can also improve the wear and corrosion resistance of the cladding.
- The effects of different cladding thickness on the bead contact angle, dilution and porosity level in the cladded samples was less explored.
- The effect of cladding thickness on the hardness and wear needs to be investigated.

2.9 Objective of the thesis

Based on the literature survey, the following objectives are decided:

1. To investigate the application of CMT for cladding of AA6061-T6 by ER70S-6 alloy in welding-electrode form and compare the performance of cladding using CMT with the existing cladding techniques using powder.
2. To analyze the corrosion behavior of the Fe-based cladding on the Al substrate. Focusses on the surface roughness, microhardness and wear before and after corrosion.
3. To study the effect of different heat treatment (annealing, water quenching, artificial age hardening and deep cryo-treatment) on the cladded layer.
4. Studying the effect of cladding layer thickness on the mechanical properties of cladded layer.

The overall plan of the thesis is shown in the flowchart in Fig. 2.6.

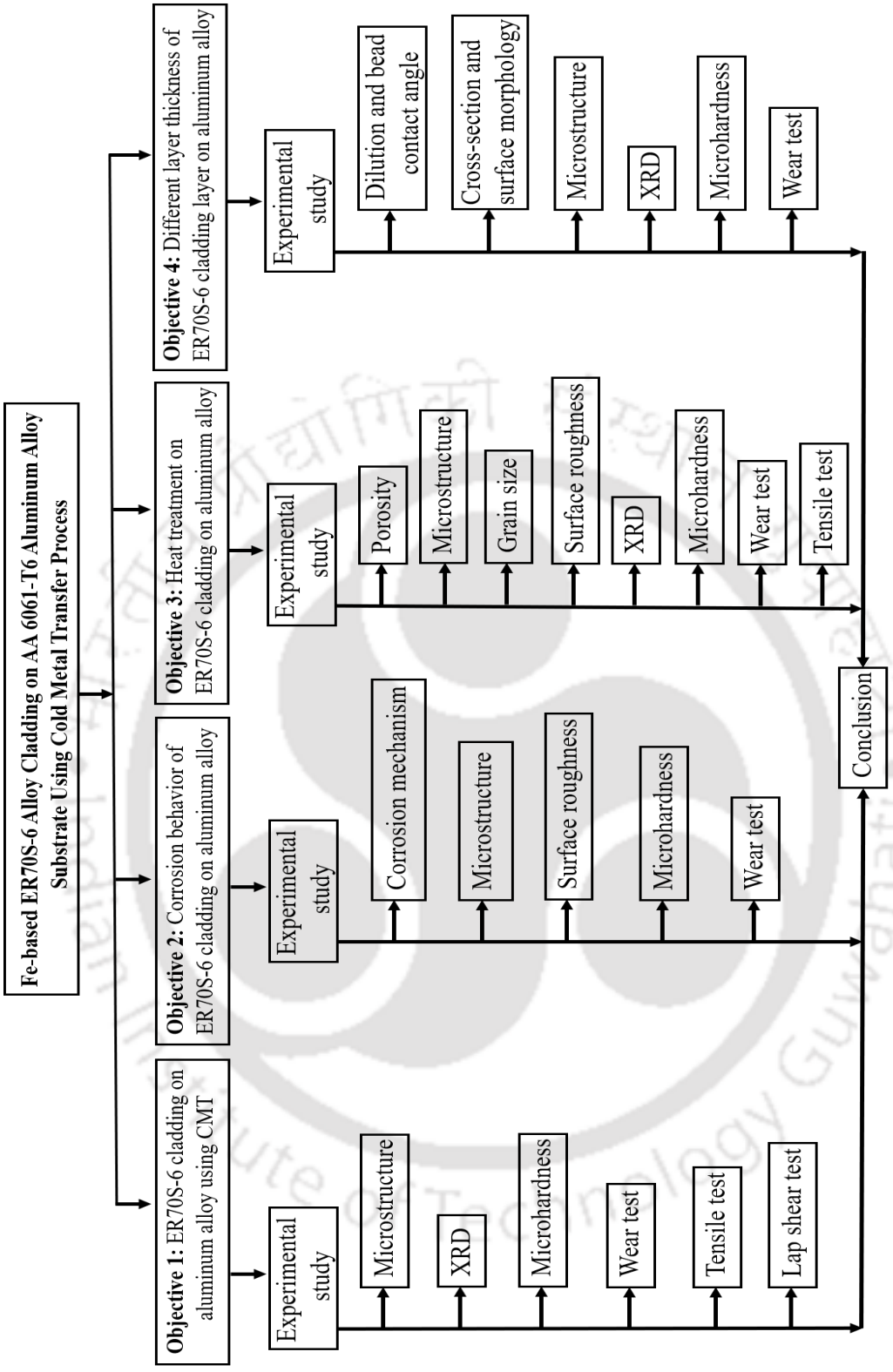

Figure 2.6 Flow chart of the thesis

Chapter 3

Details of Experimentation

3.1 Introduction

This chapter discusses all experimental setups and equipment's used for experimental work. Details of the experimental setup, working procedure and methods, workpiece types and dimensions, cladding parameters, type of working material has been discussed. This chapter only focus on methodology; the research findings are reported in the subsequent chapters.

3.2 Details on CMT Machine and other Instruments

A CMT machine was used for the experimental work for the cladding process. The steel based ER70S-6 filler wire of 1.2 mm diameter was used as a cladding material. The AA 6061 T-6 alloy plate was used as substrate material throughout the experiments.

3.2.1 CMT Machine

The CMT machine setup consists of a six-axis robotic arm (Fanuc robot ARC mate 100iD) integrated with Fronius TPS 400i GMAW as shown in Fig. 3.1. The robotic arm severs as a deposition head of wire arc additive manufacturing. The deposition head is used as an end effector of the robotic arm, which holds the consumable electrode and maintains an arc between substrate and electrode. The whole setup consists of a two-parts motion module and a deposition module. The motion module consists of a robot controller which controls the motion of joints as a result controls deposition velocity, and the deposition module consists of a deposition power source, shielding gas, and material spool which controls the weld bead parameters by using cold metal transfer type of material transfer process. The specification of the CMT machine is given in Appendix A.

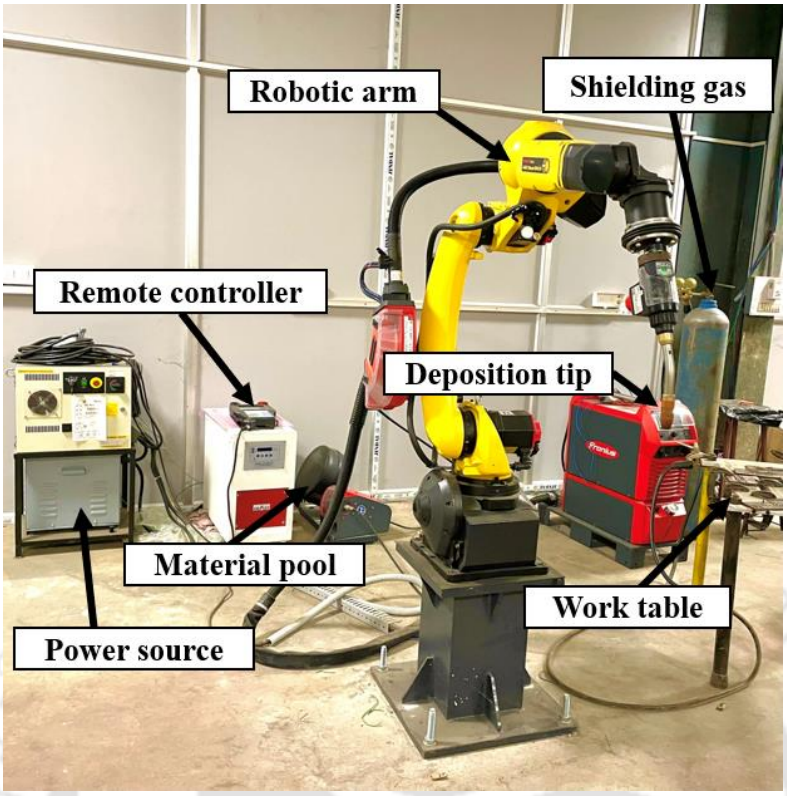

Figure 3.1 CMT machine setup for cladding process

3.2.2 Milling Machine

The milling machine as shown in Fig. 3.2, was used for face milling the cladded metal after the cladding layer deposition. The face milling was carried out to remove the uneven surface. The milling was conducted for about ~1 mm.

Figure 3.2 Milling machine

3.3 Study on Metallographic Sample Preparation and Examination

Figure 3.3 shows the basic steps followed for the preparation of samples for finding microstructure and mechanical properties. Different instruments were used in the whole operation (metallographic sample preparation and examination). They are explained in the following sub-sections. The results of microstructure and mechanical characteristics have been discussed in the Chapter 4, 5, 6 and 7.

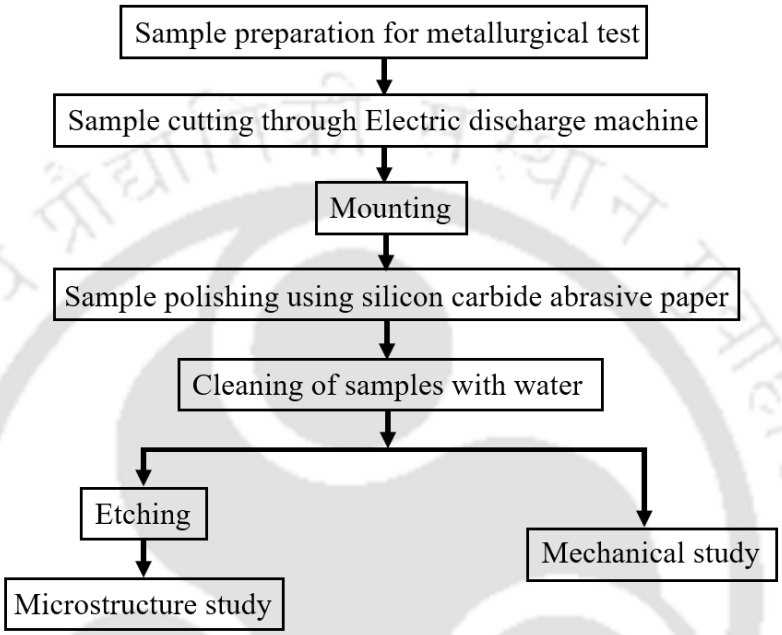

Figure 3.3 Basic steps for microstructure and mechanical sample preparation

3.3.1 Electron Discharge Machine

The wire cut electron discharge machine (WEDM) was used for precise and deformation-free cutting. It produced samples that were in perfect condition for the next step. The Fig. 3.4. shows WEDM machine that generates less heat with less cutting time due to integrated flood coolant delivery system. It produces very less depth of damage with minimum material loss.

Figure 3.4 Wire cut electrical discharge machine

3.3.2 Polishing Machine

After mounting the samples with phenolic polymer, all samples for microstructure and mechanical properties evaluation were polished by using double disc polishing (Make: Metco, India (P) LTD.); Model: Bainpol). The photograph of polishing machine is shown in Fig. 3.5. It has smooth speed variation of the grinding wheel with soft start and stop. Polishing machine was used to avoid surface effects in microstructure and mechanical testing. The sample holder was held by operator and desired grinding depth was also manage by operator. All samples were polished by silicon carbide abrasive paper having 80–2000 grit size and finally polished on velvet cloth using MicroPolished alumina particles of the size ~1 μm.

Figure 3.5 Polishing machine

3.4 Study on Metallurgical Examination

For metallographic study, the polished samples were washed with water and dried properly. After drying the samples, etching was done using standard Killer's reagent (95 ml of HNO_3, 1.5 ml of HCl and 1 ml of HF) and Nital reagent (5 ml of HNO_3 and 95 ml of CH_3OH). Etching was conducted for 10 s at room temperature. Etching with Nital reagent provided a good metallographic property.

3.4.1 Optical Microscope

The polished and etched samples were examined using an optical microscope (Make: Leica microsystem, Schweiz; Model: Leica DM750M) and stereo zoom microscope ((Make: Nikon corporation, Japan; Model: Nikon SMZ25) as shown in the Fig. 3.6(a) and Fig. 3.6(b), respectively. The polished and etched samples were examined at different magnifications, viz., 5×, 10×, 20×, 50× and 100×. Using ImageJ software and the random line intercept approach, the samples grain size was calculated. Intercept lines were positioned such that at least 10 grains are intercepted by the lines. The specification of the microscopes is given in Appendix B.

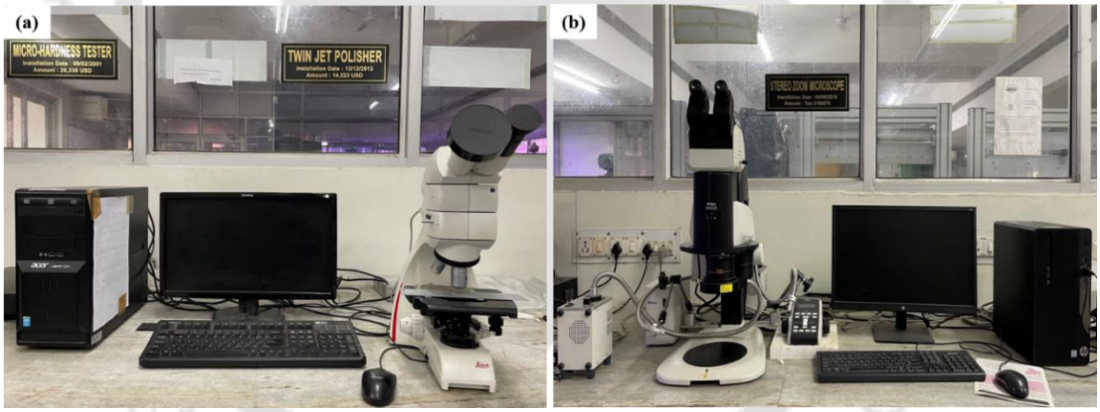

Figure 3.6 Optical microscope: (a) Leica DM750M and (b) Nikon SMZ25

3.4.2 Scanning Electron Microscope (SEM)

The surface morphology milled cladded surface was obtained through field emission scanning electron microscope (FESEM) (Model: Sigma 300; Make: Zeiss) and (Model: Gemini 300; Make: Zeiss). Fig. 3.7(a) and 3.7(b) shows the photographs of Sigma 300 and Gemini 300, respectively. Furthermore, the detailed examination of grain size, grain distribution and grain misorientation was accomplished using electron backscatter diffraction (EBSD) (Model: Quanta 3D FEG; Make: FEI). Different phases and structure were observed using transmission electron microscope (TEM) (Model: 2100F; Make: JEOL). Fig. 3.8 shows the photograph of TEM machine. The specification of the microscopes is given in Appendix C.

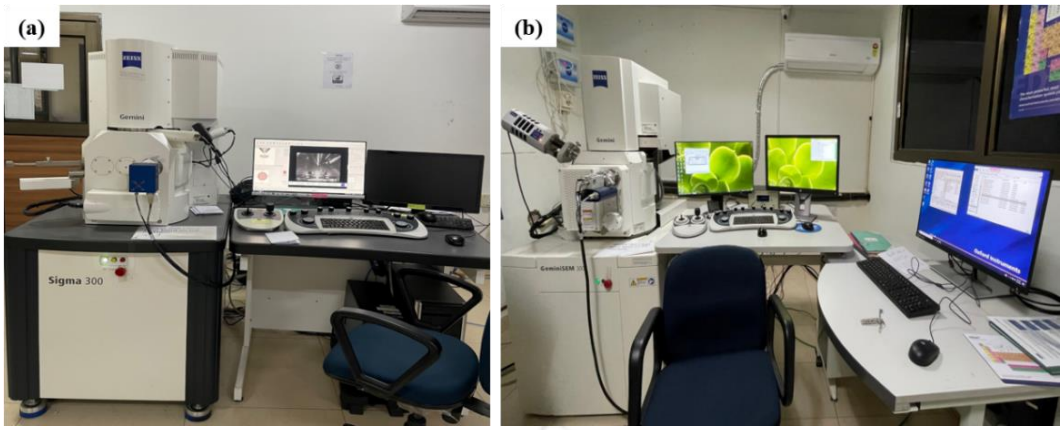

Figure 3.7 FESEM Machine: (a) Sigma 300 and (b) Gemini 300

Figure 3.8 TEM Machine

3.4.3 X-Ray Diffractometer (XRD)

The X-ray diffraction (XRD) study of the different samples was carried out using Rigaku X-ray diffractometer (Make: Rigaku; Model: SmartLab) with Cu-Kα1 radiation (λ=1.54056Å). To identify the phases contained in the samples, X-ray diffraction investigation were conducted. The solid sample was placed on a sample holder with dimensions of 20×25×2 mm^3. The measurements were carried out at an applied voltage of 45 kV, grazing incidence angle of 1° and a current of 200 mA while the samples were

scanned at a rate of 20 °/min with steps of 0.05° in the diffraction angle (2θ) range of 20°–100°. The X-ray diffractogram produced by the experiment demonstrates the connection between relative intensity and diffraction angle. The inter-planar spacing *d* corresponding to each peak is utilized for identifying the various phases of the material. By comparing experimental *d*-values with standard reference cards from the Joint Committee of Powder Diffraction Standard (JCPDS) file, the phases contained in the samples were determined. Fig. 3.9 shows the photograph of XRD machine.

Figure 3.9 XRD machine

3.4.4 X-Ray Photoelectron Spectroscope (XPS)

The development of different compounds and their activation energy on the cladding layer surface was analysed using X-ray photoelectron spectroscope (XPS) (Model: PHI 5000 Versa Probe III; Make: Φ Ulvac-PHI, Inc.). The process involves bombarding a material's surface with X-ray photons, which eject electrons from inner energy levels. The emitted electrons' energies reveal elemental composition, oxidation states, and chemical bonding. By measuring the energy difference between incident X-rays and emitted electrons, XPS determines core-level binding energies unique to each element, providing insight into surface chemistry. Fig. 3.10 shows the photograph of XPS machine.

Figure 3.10 XPS machine

3.4.5 Non-Contact Profilometer

The surface roughness of the cladded layer before and after the corrosion tests were measured using 3D optical non-contact surface profilometer (Make: Tylor Hobson®; Model: CCI-Lite). Three measurements were made per sample at different regions. The average of 3 measurements was reported. The 3D optical non-contact surface profilometer is shown in Fig. 3.11. The specifications are listed in Appendix D.

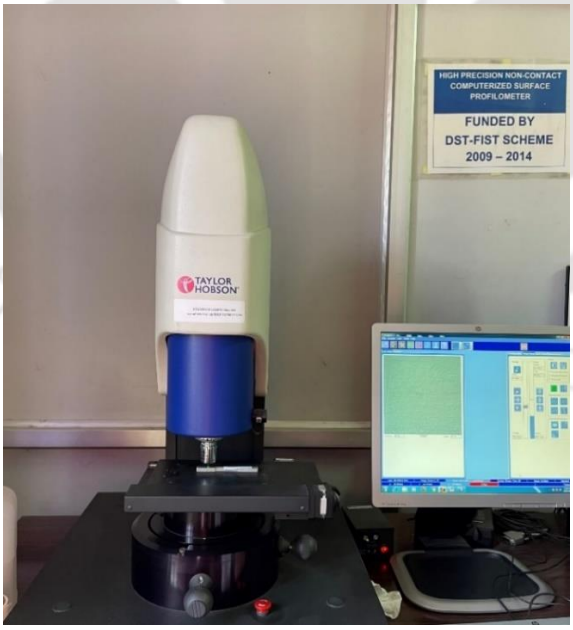

Figure 3.11 Non-contact profilometer

3.4.6 Atomic force microscope (AFM)

The surface quality achieved through both conventional and non-conventional machining methods holds significance, as a smoother surface diminishes susceptibility

to wear and corrosion-induced surface deterioration. Similarly, the excellence of components produced through CMT cladding influences the surface's wear and corrosion protection performance. In this work, sample size of 10×10×2 mm^3 was scanned through a non-contact atomic force microscopy (AFM) to examine the surface roughness of the cladded layer (Model: Cypher S; Make: Oxford Instruments) in tapping mode along the cladding direction of wire path. The test was conducted on the surface of the cladded layer before surface milling i.e., as-cladded condition. The average scan data of three different scanning test of 10×10 μm^2 is reported. Fig. 3.12 shows the atomic force microscope.

Figure 3.12 Atomic force microscope machine

3.5 Study on Mechanical properties of sample

3.5.1 Porosity analysis

The porosity of the different samples was calculated according to Archimedes' principle. Sectioned sample of 10×10×8 mm size was properly cleaned and weighted for the dry weight. The same sample was dipped in the distilled water for 24 h, which was dried with tissue paper to remove the water before weighing for the saturated weight. It was then dipped in water and weighted for the suspended weight. The accuracy of the weight measurement was 0.01 mg on a digital weight machine. According to Archimedes' principle, the porosity is given by

$$\varepsilon = \frac{W_{sat} - W_{dry}}{W_{sat} - W_{susp}}, \tag{3.1}$$

where W_{dry} is the dry wright, W_{sat} is the weight of the saturated sample i.e., weight after soaking in distilled water for 24 h and W_{susp} is the weight of the suspended sample in water.

3.5.2 Vickers microhardness tester

Vickers microhardness of samples were conducted using MVH-II (Make: Omni Tech, India; Model: MVH-II) microhardness tester. The hardness analysis has been conducted at the base metal and at different regions of the cladded layer. In the microhardness testing machine, the loads of 1–2000 g force can be applied. Using a 136° square-based Vickers diamond pyramid, an indentation was created with a 200 g load and 20 s dwell period. The samples were polished such that their opposing surfaces were parallel to each another. Ten indentations were carried out on each sample, and the average microhardness hardness value and standard deviations are reported. It was ensured that the indentations were at a distance that was at least twice the preceding indentation's diagonal length. The microhardness tester used for the present study is shown in Fig. 3.13. Microhardness tester specifications are listed in Appendix E.

Figure 3.13 Microhardness tester

3.5.3 Pin-on-disc tribometer

Friction and wear study were conducted using a pin-on-disc test on a tribometer (Make: Ducom, India; Model: TR-201). The sliding occurred between the stationary pin specimen and a rotating disc. The normal load, rotational speed and wear track diameters were fixed according to the need. The frictional force and wear were measured using sensors. The machine loading capacity was up to 100 N and the speed from 100–1000 rpm. The machine is applicable for sliding wear test in a dry condition. The minimum

and maximum wear track diameters were 10 and 80 mm, respectively. The specimen samples were prepared in a cylindrical geometry and placed inside the specimen holder.

The linear variable differential transducer (LVDT) measures the wear between the wear pin specimen and hardness disc. The friction between pin and disc is also measured by a load cell. A bam type load cell has a capacity of 5 kg, which measure frictional force up to 100 N. The load cell was fixed on sliding plate and moves with it for fixing the wear track diameter. The tribometer is shown in Fig. 3.14.

Figure 3.14 Wear test machine

3.5.4 Universal testing machine

Tensile and shear lap test was conducted using universal hydraulic tensile testing machine (Make: Instron; Model: 881J4051) with a capacity of 100 kN. The tensile test specimen was prepared according to ASTM E8M-11 standard. The complete setup of the tensile machine is shown in Fig. 3.15. The specifications are listed in Appendix F.

Figure 3.15 Universal testing machine

3.5.5 Electric furnace

The heat treatment was carried out using an electric muffle furnace. The muffle furnace is typically made of a refractory material that can withstand high temperatures and is designed to isolate the heating elements from the sample being heated. This setup prevents direct contact between the heating elements and the sample, ensuring a controlled and contamination-free heating environment. The samples were properly cleaned with acetone before the heat treatment process to remove the undesired oils and dirt during the cutting process using WEDM as well as milling. The electric muffle furnace is shown in Fig. 3.16.

Figure 3.16 Electric muffle furnace

3.6 Corrosion testing

The corrosion analysis is conducted for CMT cladded samples. The electrochemical result of an external environment on a metallic surface is corrosion. One of the main problems that leads to the breakdown of crucial engineering components is surface corrosion of metal components. The corrosion test on the cladding layer was carried out following the cladding process. For corrosion test, a sample of CMT cladded alloy was tested in a solution of 2.0% H_2SO_4 for 200 h according to ASTM standard: G31. The corrosion immersion test should run for a longer duration of time. As per ASTM standard G31, test durations typically range from 48 to 168 h. Where the corrosion rate is less than 0.5 mm/year, the test should be conducted for at least 200 h. On alloys that generate passive films, short-time testing can also produce false findings. To allow for the breakdown of the passive film and a subsequent more rapid attack in borderline conditions, a long duration test may be necessary. As a result, tests that are done for extended periods of time are much more realistic than tests that are run for short duration. However, the corrosion should not advance to the point where the original specimen size, the exposed area, or the metal is perforated. Considering these factors, in the present work the test was conducted for 200 h. The CMT cladded sample was mounted in a corrosion resistant cold mount with top surface area of 100 mm^2 exposed to acidic solution at room temperature. To calculate the weight loss, the corroded sample was weighed with an accuracy of 0.1 mg. A non-contact optical surface profilometer was used

to measure the corrosion pits height and surface roughness. The upright optical microscope and FESEM were used to investigate the sample's morphology.

3.7 Conclusion

In this chapter, details of experiment used in the research of Fe-based alloy cladding on AA 6061-T6 alloy substrate are presented. Photographs of the machines have been used to present the experiment. The substrate and cladding material used in the experiment are also discussed accordingly. All the machines are available in Indian Institute of Technology Guwahati.

Chapter 4

Microstructure and mechanical properties of ER70S-6 alloy cladding on AA 6061-T6 aluminum alloy

4.1 Introduction

Aluminum (Al) alloys find wide application in aircraft, railway vehicles, automobiles, and weapons due to their lightweight nature, high corrosion resistance, and good ductility. One particular type of Al alloy, known as aluminum-magnesium-silicon (Al-Mg-Si) alloys, has gained popularity for structural purposes due to its favorable weldability and formability (Hu et al., 2019). However, these alloys exhibit low wear resistance, which can lead to shortened part lifespans. To address this issue, surface cladding techniques are employed to enhance part longevity. Weld overlay cladding, in particular, is a popular method for repairing damaged components. Nonetheless, achieving successful fusion welding between steel and Al alloys poses challenges due to the incompatible properties of these materials. The weld metal quickly oxidizes and forms a brittle intermetallic layer, negatively impacting the mechanical properties of the final product. Processes like high-velocity oxygen fuel coating, cold spraying and plasma spraying have been utilized for depositing coatings on Al and its alloys (Bakshi et al. 2008, Mindivan et al. 2010). Laha et al. (2005) synthesized a bulk nanostructured aluminum alloy component through a vacuum plasma spray technique. However, the thermal spray coating processes provide low deposition thickness in a single pass and several passes may be required to prepare a thick cladding (Laha et al. 2005). On the other hand, weld overlay cladding techniques can achieve higher deposition thickness in a single pass (Rajeev et al. 2019). Plasma transferred arc welding, gas metal arc welding (GMAW) and gas tungsten arc welding are a few fusion welding overlay techniques used for weld deposition (Murugan and Parmar, 1994, Deng et al. 2015, Gurumoorthy et al. 2006). One of the important concerns in the surfacing layer is the dilution of the cladding composition due to the melting of the substrate (Rajeev et al. 2019, Kumar et al. 2016). When using traditional GMAW technology for Al surfacing, the heat input is extremely high, which promotes a high degree of dilution (Elrefaey, 2015). Thus, due to high thermal conductivity and low melting point of aluminum alloys, it is hard to clad them using traditional fusion techniques. It is desirable to clad Al alloys using a process

providing high production rate but low heat input; one such process is cold metal transfer (CMT).

A few studies on joining of pure Al sheets using CMT indicate that this technology can be used for thin-sheet-welding due to low heat input during the process; CMT provides good bonding and mechanical strength (Feng et al. 2009, Ahmad and Bakar, 2011). The CMT process has also been utilized for dissimilar metal joining. Zhang et al. (2009) obtained strong lap joints of Al and zinc-coated steel using CMT. Shang et al. (2012) joined 6061 Al alloy and AZ31B Mg alloy with Cu as a filler wire using CMT resulting in good bonding strength of 34.7 MPa. CMT was used to join titanium and Al alloy and the tensile strength of the joint was high (Cao et al. 2013).

The CMT was used for surface modification by a few researchers. Rajeev et al. (2017) reported crack-free hard-facing of satellite 21 on H13 steel with preheating the substrate at 400 °C in the process. The dilution of the coating by Fe content was less than 4 %, which helped in getting a wear-resistant coating. Varghese et al. (2019) deposited Inconel 617 M on 316 L stainless steel; a typical grain morphology of columnar dendritic microstructure along with fine inter-dendritic precipitates was obtained. Ola et al. (2014) used CMT for the cladding of 718 Inconel by the similar material. Luchtenberg et al. (2019) carried out ER2209 cladding on duplex stainless-steel substrate and observed the enhancement in wear and corrosion resistance. Tang et al. (2020) produced Ni as well as Fe-based coatings on AISI 304 stainless steel substrate. Iron based coating provided good wear resistance, whilst the nickel-based coating provided good corrosion resistance.

A few researchers also reported the surface coating of Al using steel powders as a strategy to improve the wear and hardness. Sova et al. (2013) deposited 316 L stainless steel powder on Al surface using a cold spray technique but there was significant porosity between the deposited layers. Application of post heat treatment reduced the porosity (from ~8% to <1%). Villa et al. (2013) deposited 316 L stainless powder on Al-7075-T6 alloy and reported high abrasive wear resistance of the coating surface compared to the substrate. Zhou et al. (2020) deposited 316 L stainless powder on an Al alloy sheet with high-speed particle injection at a spraying temperature of approximately 400 °C. Coating provided high microhardness (HV>400) and enhanced wear resistance at high temperature.

In the present study, the motivation for selecting Fe-based ER70S6 as cladding materials is due to its suitability for automatic welding with excellent welding properties, stable arc, low sputter, low cost and high deposition efficiency (Ermakova et al. 2021).

The review of literature reveals that although there have been some investigations on applying CMT for cladding, there is no reported research on cladding of Al alloy by steel. Some researchers did coat Al alloys by metallic powders using spray techniques but observed a lot of porosity. Moreover, metallic powders are usually expensive. In view of it, this study aimed to investigate the application of CMT for cladding of AA6061-T6 by ER70S-6 alloy in welding-electrode form. ER70S-6 is a mild steel containing Mn and Si and is less expensive compared to steel powders. Main objective is to compare the performance of cladding using CMT with the existing cladding techniques using powder.

4.2 Experimental procedure

The experiment was carried out on an AA 6061-T6 plate with a dimension of 180×100×6 mm^3. This material is widely used in many engineering structures. On AA 6061-T6 substrate, cold metal transfer of ER70S-6 was accomplished. The composition of the substrate was 0.1% Ti, 0.3% Fe, 0.3% Zn, 0.7% Si, 0.7% Cu, 0.7% Cr, 1% Mg by weight and the rest Al, as identified by energy dispersive spectroscopy (EDS). The filler wire of ER70S-6 was obtained from ESAB, India. The typical weld metal analysis as supplied by ESAB was 0.01% Al, 0.075% C, 1.45% Mn, 0.85% Si, 0.30% Cu, traces of Cr, Mo, Ni, P, S and V with balance Fe. In-house EDS provided Al (0.1% max.), Mn (1.4% max.) and Si (1.4% max.) on the milled cladded surface. The AA 6061-T6 substrate was properly cleaned with acetone to remove unwanted dirt, oxides and oil before the cladding. The cladding layer was deposited using a Fronius CMT TPS400i machine with a filler wire of 1.2 mm diameter. The variation of cladding path and speed was controlled by a 6-axis FANUC Arc Mate 100iD robot. Process parameters were regulated by the remote-controlled unit of the CMT system. Argon was used as a shielding gas with a flow rate of 20 l/min. The voltage was the main variable input in the cladding process. CMT power source is designed such that, it automatically fixes the other welding parameters, once the input is set. The observed current and wire feed rate during the cladding was of 95–105 A and 8–10 m/min, respectively. The interlayer dwell time was maintained at 300 s. The variable processes parameters used in the CMT process and obtained bead dimensions are shown in Table 4.1. Fig. 4.1 shows cladding layers and face milled samples. Fig. 4.2 shows the optical micrograph of the bead cross-section and bead contact angle. The cross-sectional area and hence, the volume of the bead increases with increasing voltage. It is recommended to have a lower bead contact angle, which causes less porosity and the deposition will be proper in multi-pass cladding

layer with overlap (Elrefaey, 2015, Rajeev et al. 2014, Zhou and Lin, 2014). For the present study, the bead contact angle of Bead A is the lowest and that of Bead B is the highest. Bead C has a higher volume deposition of metals compared to Bead A. The visual inspection also ascertained that bead C was the best; hence, further study was carried out with the parameters chosen for Bead C. The cladding layer was face milled for about 1 mm depth before extracting different samples for characterization. The final thickness of the cladding layer was 2 mm.

Table 4.1 Trial parameters and dimensions for different beads

Bead	Voltage (V)	Welding speed (mm/min)	Width (mm)	Height (mm)
A	8	400	2	1.5
B	9	400	2.5	2.5
C	10	400	3	3

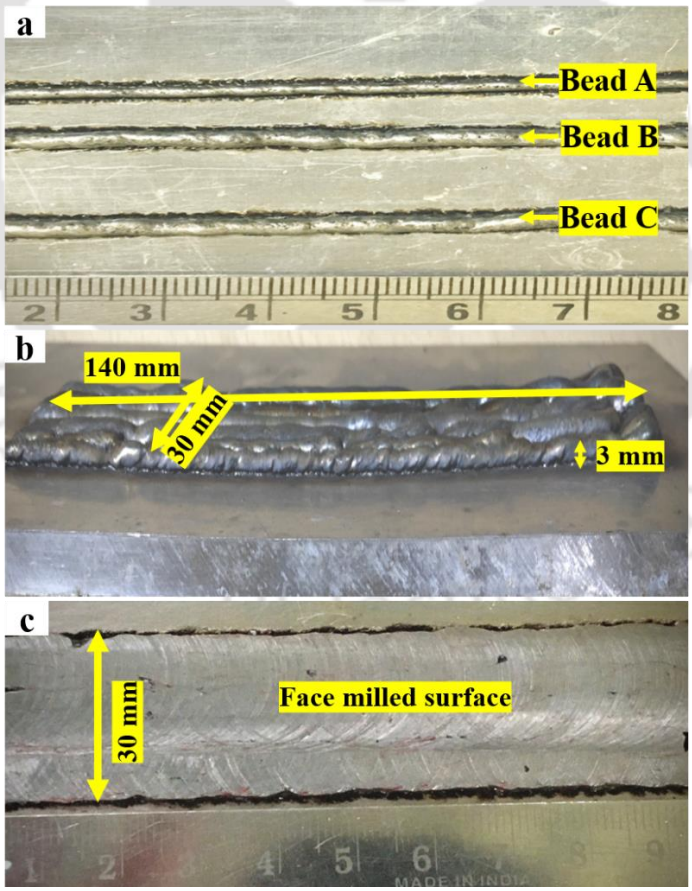

Figure 4.1 Cladding layer produced by cold metal transfer technology: (a) three types of beads, (b) as-deposited bead Type C and (c) machined bead Type C

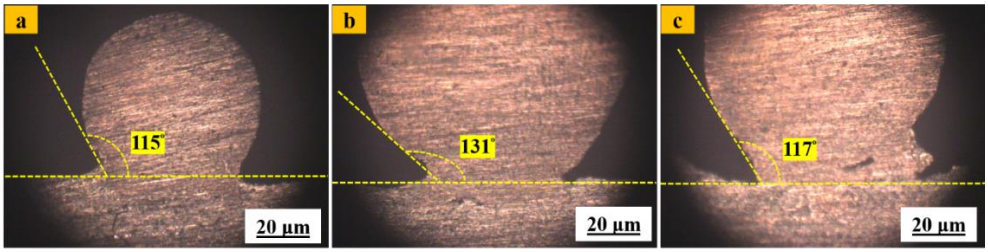

Figure 4.2 Optical cross-sectional micrograph (X10 magnification): (a) Bead A, (b) Bead B and (c) Bead C

For microstructural and hardness measurement, the samples were sectioned for observing the variation across thickness using electric discharge machining (EDM). The samples were polished on a polishing machine (Model: Bainpol; Make: Metco, India) using different grits of silicon carbide emery papers. The polished samples were etched just before optical microscopy in Keller's reagent for about 10 s. The Keller's reagents contained 95 ml of H_2O, 2.5 ml of HNO_3, 1.5 ml of HCI and 1 ml of HF. The micrographs of the samples were obtained using an upright optical microscope (Model: Axiocam MRc; Make: Carl Zeiss). The X-ray diffraction (XRD) analysis was carried out on the surface of the polished solid sample using an X-ray diffractometer (Model: SmartLab; Make: Rigaku). The parameters used for the XRD study are 20 °/min scan rate, 0.05° step size, 20º to 100º diffraction angle (2θ) range and Cu-$K_{\alpha 1}$ radiation (λ=1.54056 Å). The results of the XRD have been verified with Joint Committee on Powder Diffraction Standards (JCPDS) data. The Vickers microhardness was measured with a microhardness tester (Model: MVH-II; Make: Omni Tech, India) for 20 s dwell time with 200 gf applied load.

The wear study was conducted using a pin-on-disc test on a tribometer (Model: TR-201, Make: Ducom, India) with 70 mm track diameter for 30 minutes at 350 rpm and 20 N applied load on hardened steel disc (84 HRC), following the ASTM: G99 standard. The worn-out surface and wear debris morphology was observed using Field emission scanning electron microscopy (FESEM) (Model: Sigma 300; Make: Zeiss). The tensile specimen was cut out using a wire cut EDM machine as per ASTM E8M-11 standard and then polished using a series of emery papers. The tensile test was carried out on universal testing machine (UTM) (Model: 8801; Make: Instron) (100 kN) machine at room temperature maintaining an average strain rate of 0.001 s^{-1}. The lap shear test was conducted using a UTM machine (Model: 8801; Make: Instron) at room temperature maintaining an average displacement control of 0.1 mm/min. The experimental setup and geometry of shear lap test are shown in Fig. 4.3.

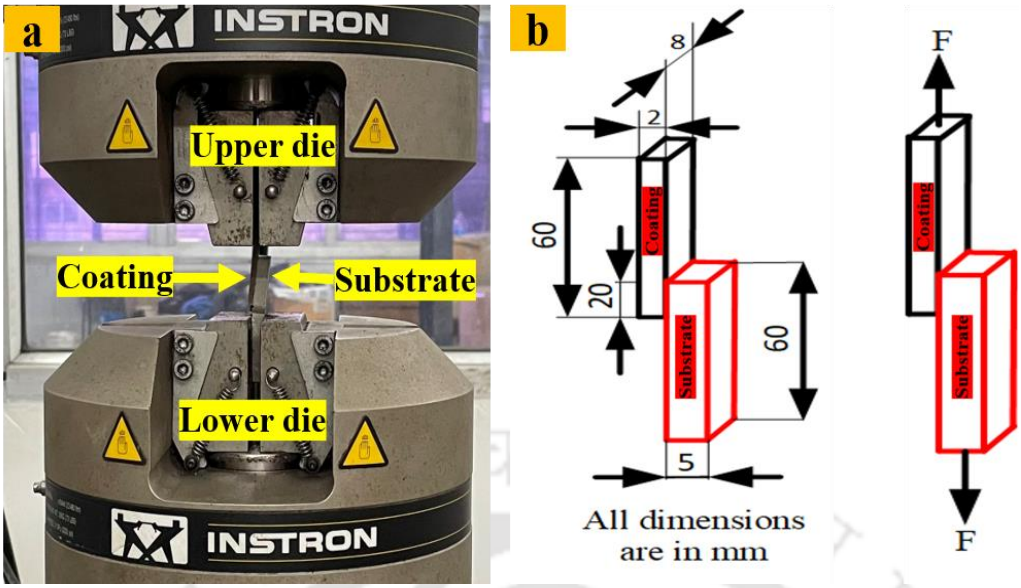

Figure 4.3 Lap shear test: (a) experimental setup and (b) specimen geometry

4.3 Results and discussion

This section describes the results of experimental investigation. Microstructure, XRD, microhardness and tribological observations are discussed. Finally, the load-displacement behavior and lap shear tests are discussed.

4.3.1 Microstructural study

Figure 4.4 shows the micrographs of Bead A at various locations. Solidified structure is greatly influenced by the rate of cooling (Ola et al. 2014). During CMT based cladding, the cooling rate is high at the weld-substrate interface due to high thermal conductivity of the substrate. Therefore, near the weld-substrate interface a fine equiaxed structure is obtained. However, at the top surface of the clad, cooling takes place due to natural convection, which is quite slow. Therefore, the columnar grain structure without any secondary branch structure was observed away from the weld-substrate interface.

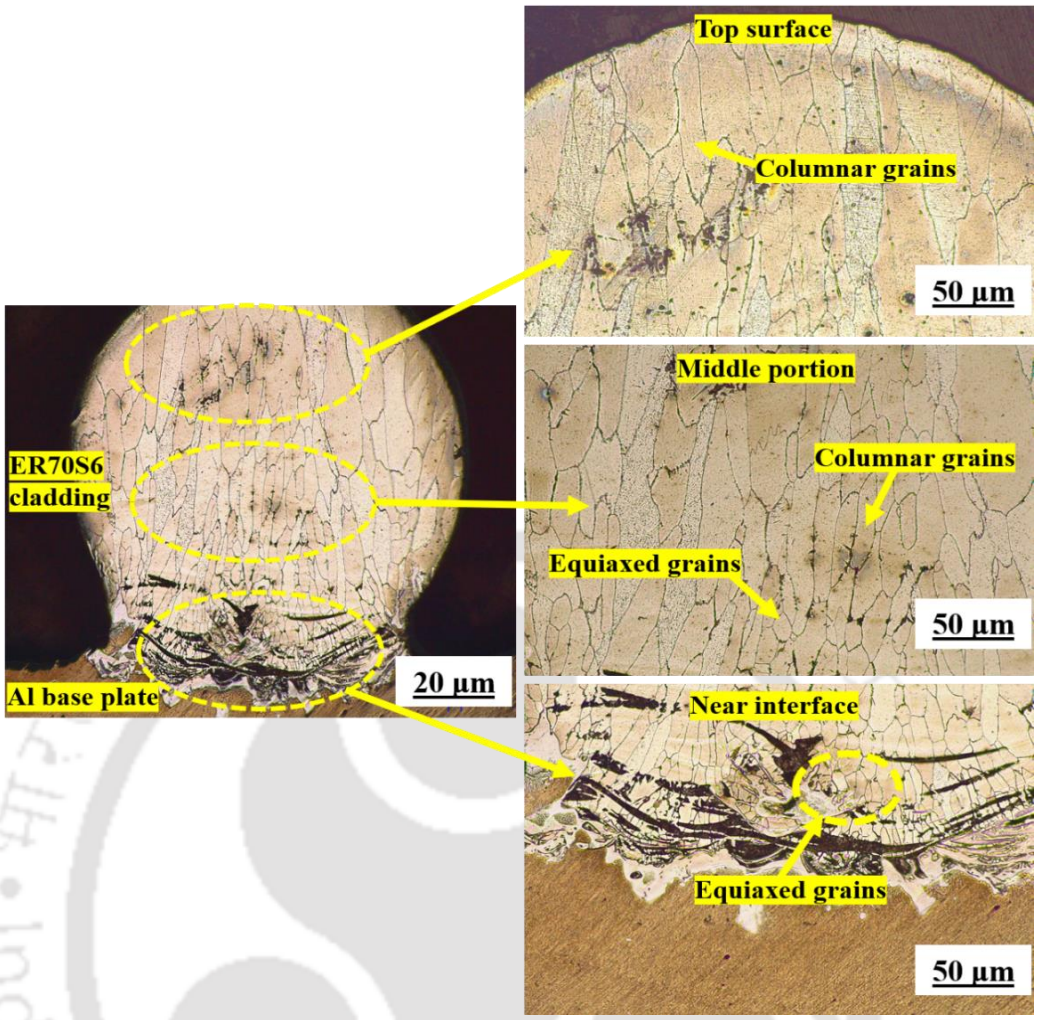

Figure 4.4 Optical micrograph (X10) for Bead A along with magnified (X20) micrographs of three regions

Figure 4.5 shows the micrographs of Bead C at various locations; due to large size of the specimen integrated micrograph could not be obtained in this case. Bead C is larger than Bead A. Therefore, the temperature gradient away from the boundaries of weld-metal is lower than that in Bead A. Due to this, the microstructure of the middle portion of the cladding layer has a dendritic grain structure. The dendritic growth of grain-structure appears to be random and non-uniform because of non-uniform temperature-distribution. The structure obtained in the present study is similar to the structure obtained in CMT based manufacturing processes (Varghese et al. 2019, Evangeline and Satiya, 2019). No significant porosity is observed in micrographs, which is a positive characteristic of CMT processes (Zhang et al. 2019). On the other hand, cold spray deposition of stainless steel on Al substrate displayed significant porosity in FESEM image (Sova et al. 2013).

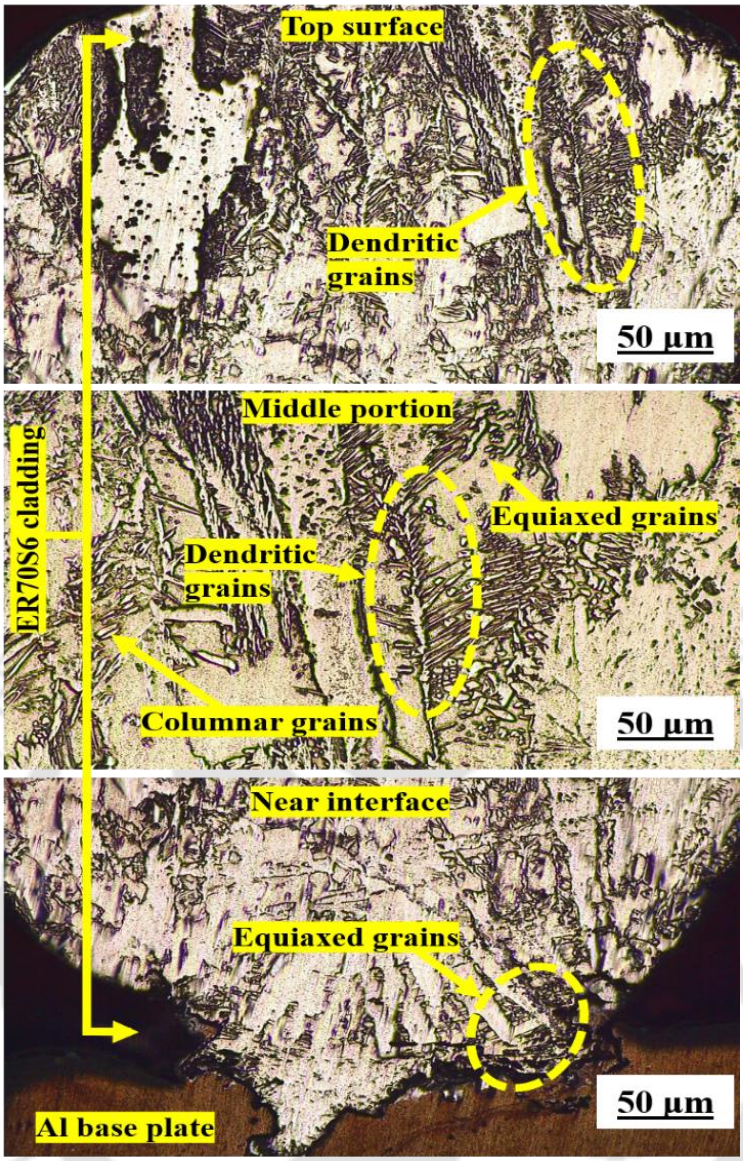

Figure 4.5 Optical micrograph (X20) for Bead C

The cross-sectional microstructures of the cladding layer and base metal are depicted in Fig. 4.6 (a and b). A well-defined substrate-cladding interface are observed. The bonding between cladding layer and substrate is dense and crack-free. Melting temperature and densities of the substrate and cladding material as well as cooling rate during cladding affect the distribution of strengthening elements (Chiareli et al. 1994). The melting temperature of AA 6061 is about 650 °C, whereas the melting temperature of ER70S-6 is about 1450 °C (Liu et al. 2014). There is a dilution of cladding layer material into the base metal due to low melting temperature of the latter as well as difference in densities of the two materials; this makes the bond stronger.

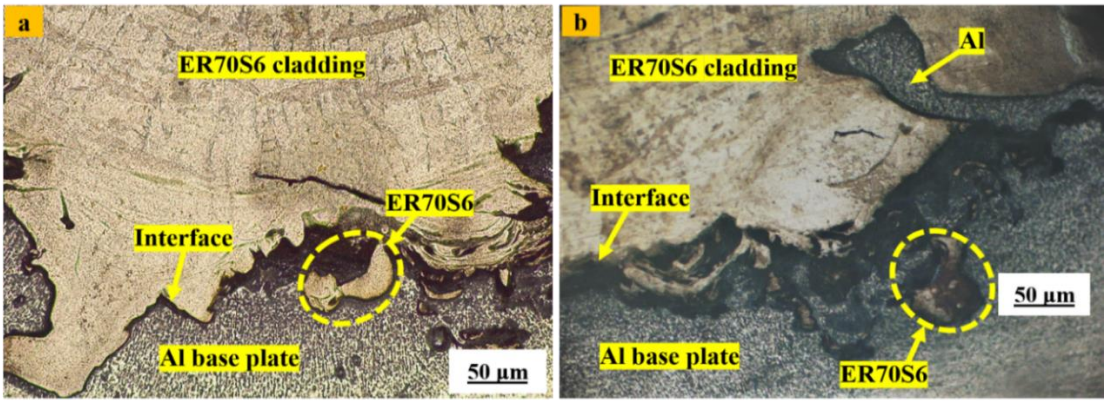

Figure 4.6 Interface optical micrographs (X20 magnification) of cladding layer and the substrate produced by the CMT process: (a) location 1 and (b) location 2

Figure 4.7 (a) shows the FESEM micrograph of substrate and cladding layer. Fig. 4.7 (b and c) show the magnified FESEM micrographs of cladding layer region and weld-substrate interface. Fig. 4.7 (d and e) show the line EDS analysis in the cladding layer and weld-substrate interface region, respectively. During the cooling of molten zones, the alloying elements form strengthening precipitates with parent element (Zhang et al. 2019). The line EDS analysis at the weld-substrate depicts dilution of alloying elements due to changes in cooling rate. The weld-substrate interface region has also the presence of oxides due to oxidation during cladding.

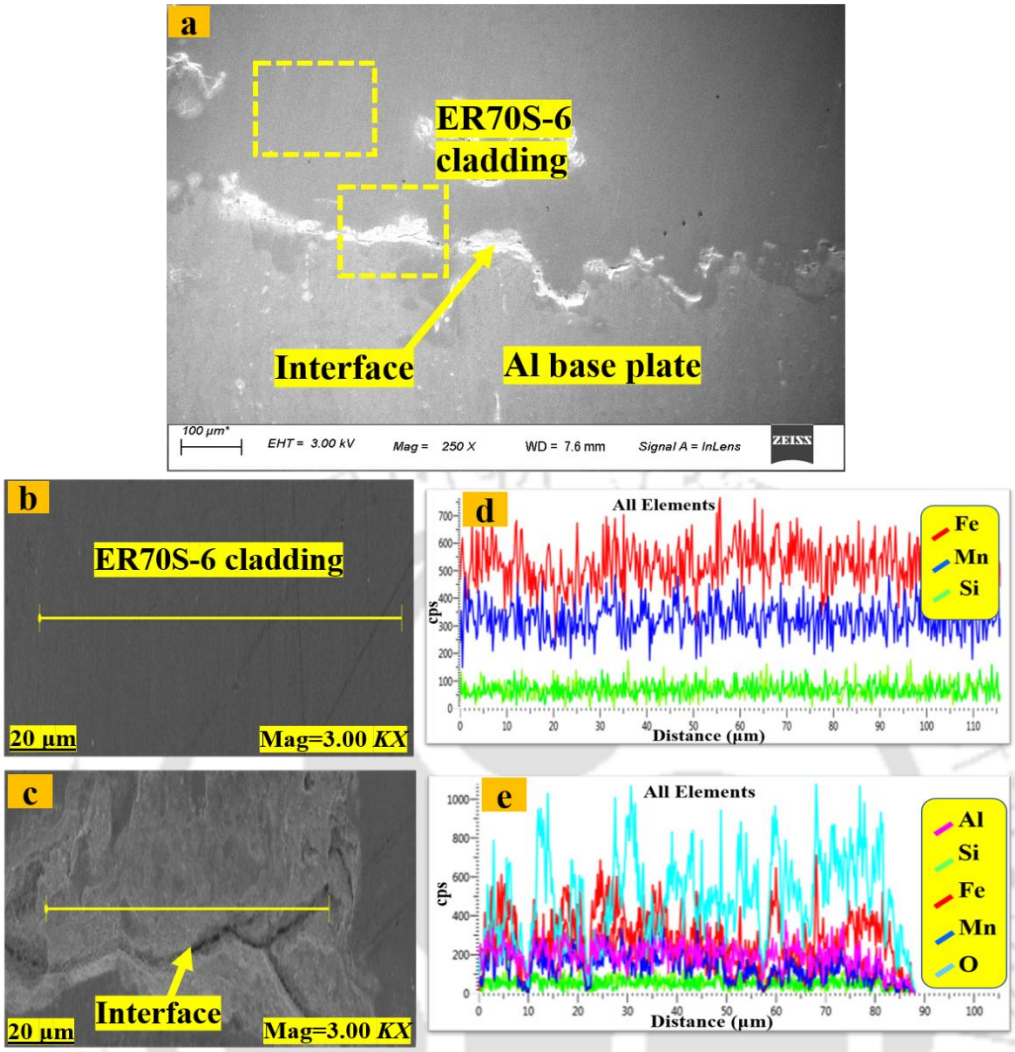

Figure 4.7 FESEM morphology: (a) cladding layer interface (X250), (b) cladding layer region as marked in 'a' (X3000), (c) weld-substrate interface as marked in 'a' (X3000), (d) line EDS elemental spectra of cladding layer region and (e) line EDS elemental spectra of weld-substrate interface

Figure 4.8 shows the FESEM morphology of ER70S-6 cladded surface after milling (i.e., after the removal of about 1 mm material). The cladded surface shows globular and dendritic grain structure as the columnar structure got removed during milling. The microstructure of cladded surface shows the presence of ferrite, carbide and martensite. However, the structure is not homogenous as evident from differing structures at two locations in Fig. 4.8 (a and b). Fig. 4.8(c), i.e., area EDS elemental distribution confirms it. A typical area on the cladded surface was chosen for obtaining the elemental maps. FESEM image of the area is shown in Fig. 4.8 (c); the elemental maps of Fe, Mn and Si of the area are depicted in Fig. 4.8 (d, e and f, respectively). The uneven distribution of these elements throughout the cladded area is revealed.

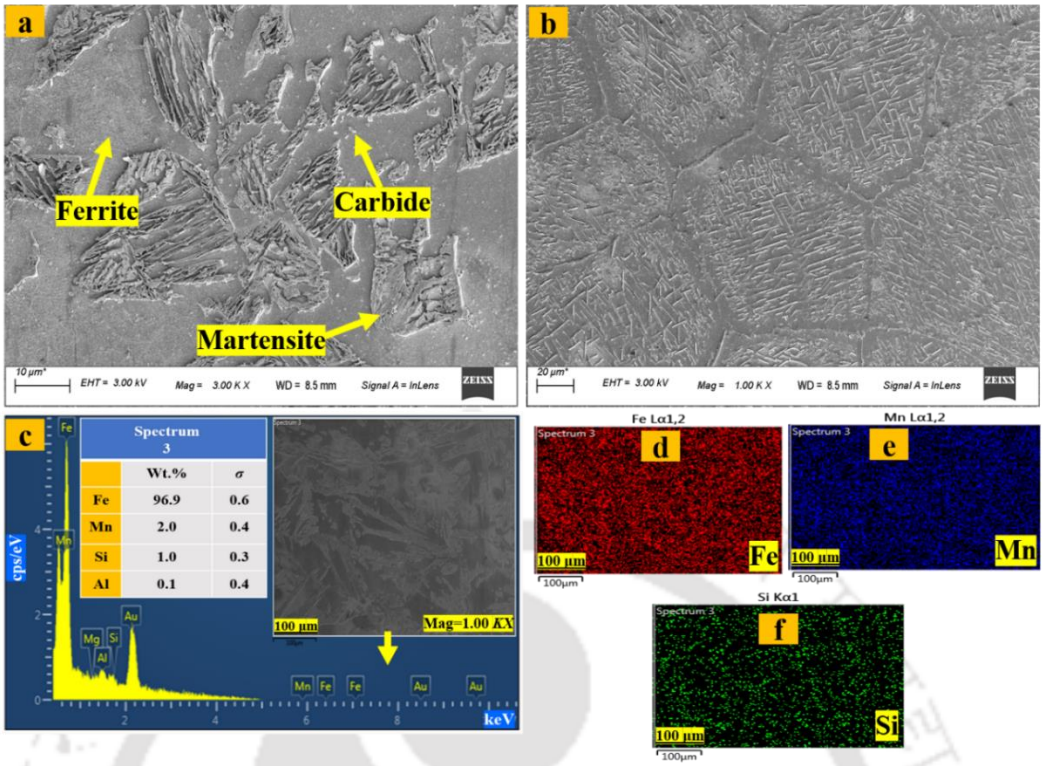

Figure 4.8 FESEM morphology of cladded surface: (a) location 1 (X3000), (b) location 2 (X1000), (c) area EDS elemental distribution, (d) map of Fe, (e) map of Mn and (f) map of Si

4.3.2 XRD analysis

Figure 4.9 shows the X-ray diffraction (XRD) patterns obtained from the substrate, cladding layer beads and cladded milled surface (in parts a, b and c, respectively). The XRD patterns reveals the presence of face-centered cubic (FCC) lattice Al as major peaks corresponding to 2θ value of 38.34º, 44.58º, 64.8º, 77.88º and 82.06º as per JCPDS-96-900-8461. The pattern also reveals a few traces of Si and Mg in the substrate. Similarly, intense peaks of body-centered cubic (BCC, ferrite) lattice of α–Fe phase are dominant in the coating surface due to its composition corresponding to 2θ value of 44.22º, 64.36º, 81.86º as per JCPDS-96-901-3477. The XRD pattern showed the absence of face centred cubic (FCC, austinite) lattice of γ–Fe phase, confirming that no retained austinite had formed in the deposited bead or that its volume fraction was too low. However, the presence of γ–Fe phase was reported by Ron et al. (2019). The XRD pattern also reveals the alloying between Mn and Fe during solidification at the clad surface due to their close similarity in atomic radius. A few peaks of Mn and Si are also revealed in the cladded region.

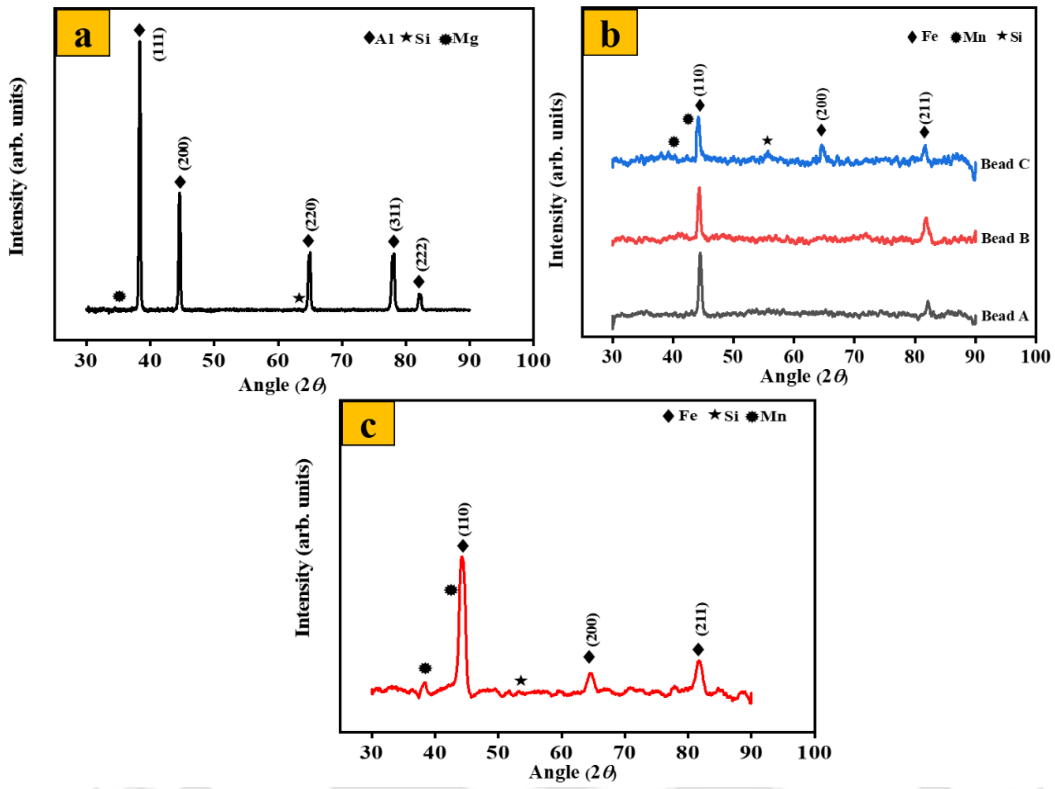

Figure 4.9 XRD patterns: (a) substrate metal, (b) cladding layer beads and (c) ER70S-6 milled cladded surface

4.3.3 Hardness study

Figure 4.10 shows the microhardness of the cladded piece as a function of the depth from the base metal to the cladded surface. It is evident from the figure that the microhardness increased from 88 HV in the base to 235 HV in the cladding layer. Sova et al. (2013) reported the mean hardness value of steel powder coating on Al using cold spray as ~150 HV. Here also, the mean hardness is almost of the same order. The variation in microhardness values across different regions is due to the non-uniform microstructural development due to different cooling rates (Evangeline and Sathiya, 2019). There is an increased hardness of 121 HV nearer to the interface region compared to 88 HV at the base due to the heating effect and strain accumulation at the time of cladding. Thus, the heat affected zone in the substrate influences the hardness variation. The main reason for the sudden rise in the hardness value in the cladding region is due to the chemical composition of ER70S-6 and the higher content of Mn, Ni, Si and C (Mishra et al. 2022).

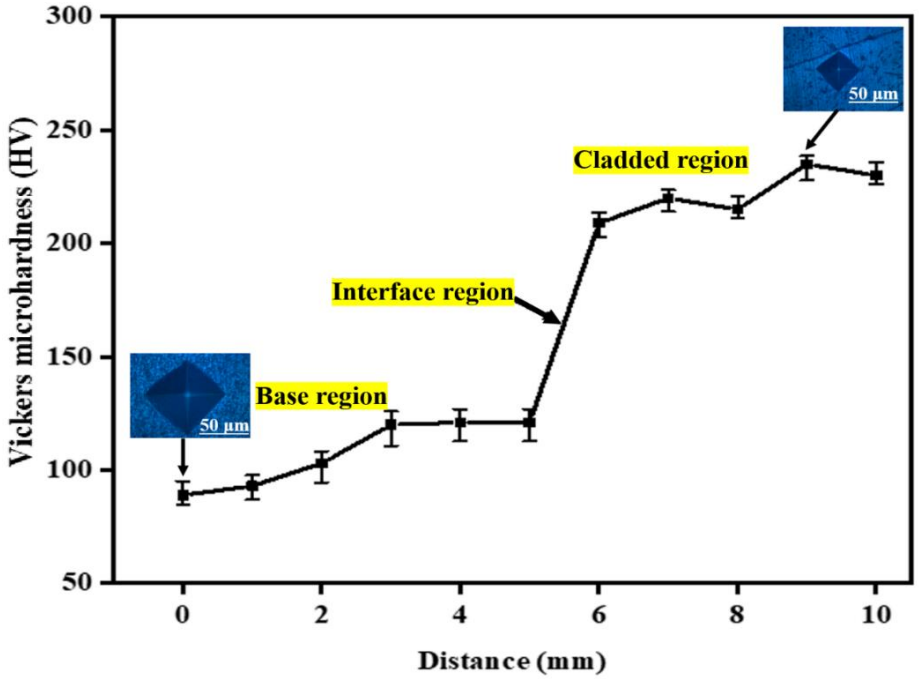

Figure 4.10 Variation of microhardness profile of ER70S-6 cladded aluminum by CMT

The heterogeneity of grain-structure also affects the microhardness values. As seen in Fig. 4.4 and 4.5, the microstructure near the interface was equiaxed. However, away from the interface, the microstructure of the cladding layer was a mixture of equiaxed, columnar and dendritic grains. The FESEM micrograph (Fig. 4.8) also revealed the formation of hard phases in the cladded surface. Therefore, the hardness increased significantly from the interface to the cladding layer. Similar observations were reported during the CMT coting process by other researchers (Rajeev et al. 2014, Evangeline and Sathiya, 2019). Fig. 4.10 also shows the indent sizes at the base and in the cladding layer after applying a load of 200 gf for 20 s.

4.3.4 Wear study

Figure 4.11 shows the variation of wear depth as a function of sliding time. The wear depth increases linearly with the sliding time. The wear depth of CMT cladded Al is less than that of the as-received Al sample. Developing the ER70S-6 cladding layer on the AA 6061-T6 base plate reduced the wear depth significantly. The mean wear depth of as-received Al and cladded Al are 75 µm and 37 µm, respectively. The materials properties, such as hardness, strain hardening and strength, affect the wear resistance. Generally, as the hardness increases the wear resistance also increases. As the cladding layer is harder than the substrate, wear resistance of the cladded sample was higher as evident from Fig. 4.11(a and b). Similar observations were also reported by a few researchers during steel powder coating (Zhou et al. 2020, Ermakova et al. 2021).

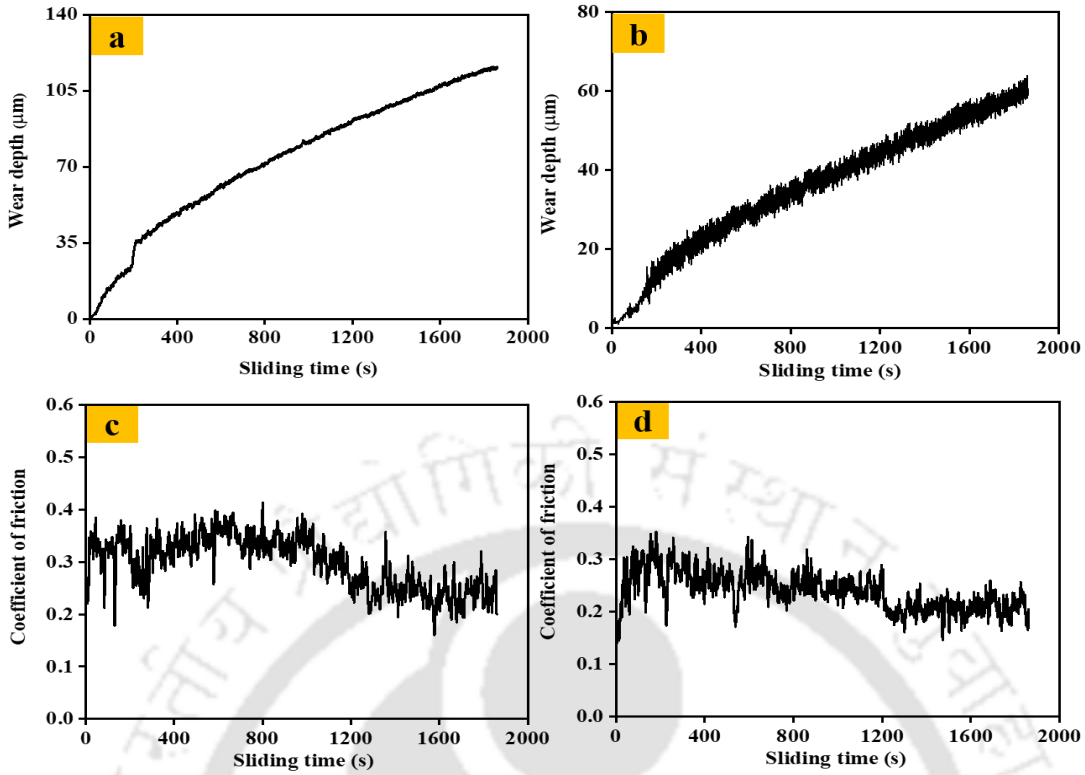

Figure 4.11 Variation of tribological parameters with sliding time: (a) wear depth of AA 6061-T6, (b) wear depth of ER70S-6 cladding layer, (c) coefficient of friction for AA 6061-T6 and (d) coefficient of friction for ER70S-6 cladding layer

Fig. 4.11(c and d) also depicts the variation of the friction coefficient with sliding time. The fluctuation in the coefficient of friction is more in as-received AA 6061-T6 compared to the cladded sample. The mean coefficient of friction between the cladded sample and hardened steel disc was 0.23; it was 0.29 between the base metal and hardened steel disc. Cladding also reduced fluctuation in the coefficient of friction. These results are consistent with the theoretical knowledge about friction. Generally, a harder surface exhibits a lower frictional coefficient because a harder surface develops less contact area with a constant applied load (Sun et al. 2008).

Lancaster, (1967) used the following equation for the estimation of wear rate:

$$k = \frac{V}{F_n s} \tag{4.1}$$

where V is the material volume loss, F_n is the applied normal load and s is the sliding distance. Many researchers prefer it to call it wear coefficient rather than the wear rate (Pirso et al. 2004, Pirso et al. 2009). In the subsequent discussion, it will be referred as Lancaster wear coefficient. Table 4.2 shows the comparison of the wear volume and Lancaster wear coefficient for the specimens. The Lancaster wear coefficient was lower

for cladding layer compared to substrate; it was 1.01×10^{-5} mm^3/Nm for cladding layer and 1.45×10^{-5} mm^3/Nm for substrate. Tang, (2020) applied Fe-based 4Cr18 coating on AISI 304 stainless steel substrate using the CMT process and reported the wear coefficient of 5.32×10^{-5} mm^3/Nm for the coating. However, they did not specify the load and sliding distance. It is to be noted that Lancaster wear coefficient does depend on the load and sliding distance.

Table 4.2 Measured wear data of AA 6061-T6 and ER70S-6 cladding layer

Sample	Applied load (N)	Sliding distance (m)	Wear volume (mm^3) $\times10^{-3}$	Lancaster wear coefficient (mm^3/Nm) $\times10^{-5}$
AA 6061-T6	20	2309	0.67	1.45
Cladding layer	20	2309	0.47	1.01

Fig. 4.12 shows FESEM micrograph of the worn surface of Al and Al cladded samples. The Al sample without cladding layer consists of pits, micro-cracks, plowing and spallation in the worn surface morphology. Thus, delamination and abrasion mechanisms have occurred during the wear. Abrasive wear indicators, such as plowing, spallation and pits, are visible on the worn surface micrograph. The worn-out asperities are harder than specimen. The hard fragments cause the removal of the substrate material due to abrasion (Shanthi et al. 2007). It is evident from Fig. 4.12 that the surface with cladding layer contains shallower spallation, indicating milder abrasion wear.

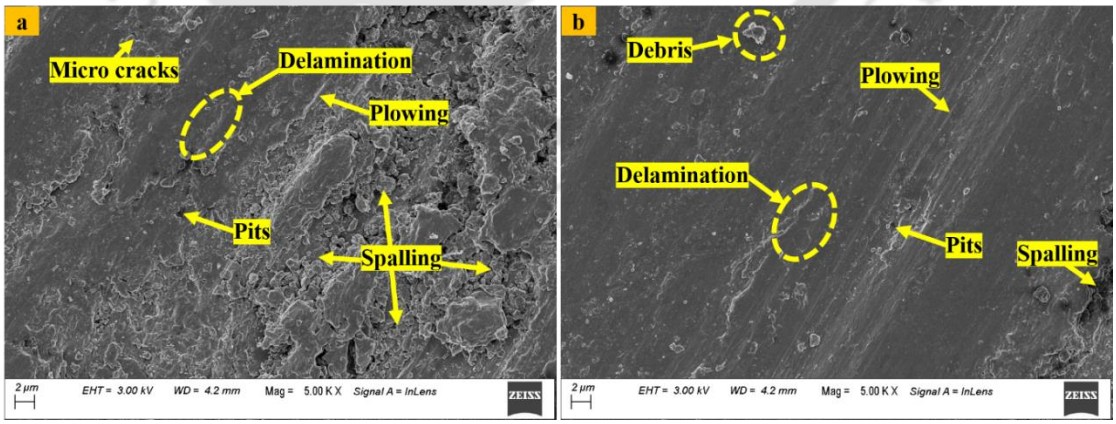

Figure 4.12 FESEM wear micrograph: (a) aluminum substrate and (b) cladded surface

The FESEM micrograph of worn-out debris produced from the wear of the samples is shown in Fig. 4.13. In the case of the Al sample without cladding layer, the plate-like debris morphology shown in Figs. 4.13(a and b) indicated that delamination had

occurred. The ribbon shape morphology of the worn-out debris indicates that the materials were removed by cutting, which is an abrasive mechanism. The serrated side of ribbon shape debris has several parallel fringes. These features are considered to be a sign of shear band formation and are also evident in Fig. 4.13(b). The worn-out debris of the cladded surface is of smaller size indicating a higher wear resistance as shown in Fig. 4.13(c). The FESEM observation of debris and worn surfaces revealed that the Al samples without cladding layer had severe delamination and predominance of abrasion wear mechanism as compared to cladded Al sample.

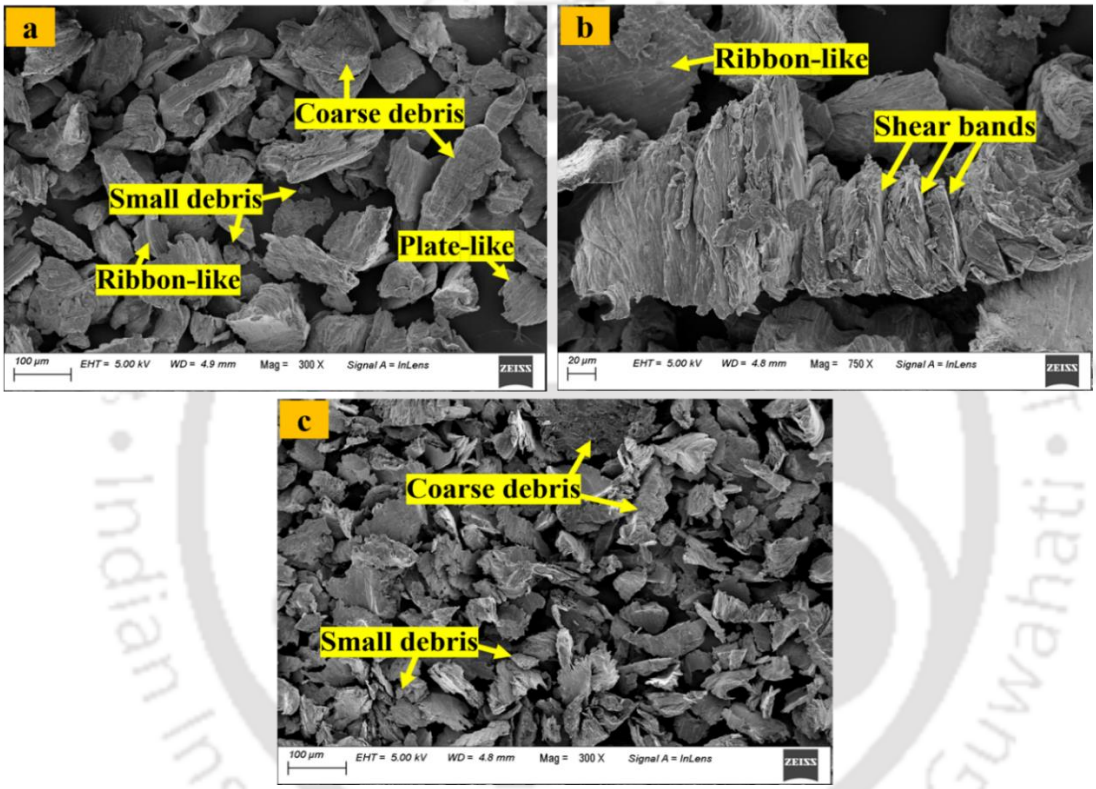

Figure 4.13 FESEM micrograph of wear debris: (a, b) aluminum substrate and (c) cladded surface

4.3.5 Tensile study

Figure 4.14 shows the true stress versus strain curve of the tensile test performed at a strain rate 0.001 s^{-1}. The yield strength (YS) and the ultimate tensile strength (UTS) has improved due to cladding on the Al sample. For example, the YS and UTS of the cladded Al sample were 300 MPa and 360 MPa, respectively. Corresponding values for the non-cladded sample were 236 MPa and 249 MPa. However, there was an overall loss of ductility as evident from the reduction of total elongation.

The increase in strength can be analysed from a simple model based on strength of materials. Composite tensile test sample of Al and ER70S6, shares the total load F. Let the load shared by Al portion be F_1 and that shared by ER70S-6 be F_2, i.e.,

$$F_1 + F_2 = F. \tag{4.2}$$

Assuming the bonding to be perfect, elongation δ of the sample of length L is given by

$$\delta = \frac{F_1 L}{A_1 E_1} = \frac{F_2 L}{A_2 E_2}, \tag{4.3}$$

where A and E denote the cross-section area and Young's modulus, respectively; subscripts 1 and 2 denote Al alloy and ER70S-6, respectively. Eqs. (4.2) and (4.3) lead to

$$\delta = \left(\frac{L}{A_1 E_1 + A_2 E_2} \right) F, \tag{4.4}$$

and

$$F_1 = \left(\frac{A_1 E_1}{A_1 E_1 + A_2 E_2} \right) F. \tag{4.5}$$

From Eq. (4.4), equivalent modulus E_{eq} of composite sample can be defined as

$$E_{eq} = \frac{A_1 E_1 + A_2 E_2}{A_1 + A_2}. \tag{4.6}$$

It is assumed that the yielding of the entire sample starts once the stress in the Al alloy portion reaches its yield strength Y_1. At the occurrence of yielding,

$$F_1 = Y_1 A_1, \tag{4.7a}$$

$$F = Y_{eq} \left(A_1 + A_2 \right), \tag{4.7b}$$

where Y_{eq} is the equivalent yield strength of the sample. Using Eqs. (4.5, 4.6, 4.7a and 4.7b), Y_{eq} is obtained as

$$Y_{eq} = \left(\frac{E_{eq}}{E_1} \right) Y_1. \tag{4.8}$$

Taking E_1 as 68 GPa and E_2 as 190 GPa, for the given sample (substrate thickness of 6 mm and cladding layer thickness as 2 mm), Y_{eq} is obtained as 342 MPa against

experimental value of 300 MPa; which is in error by 14%. This overestimation is due to inherent assumptions of uniform strain at the point of yielding. In actual case, before the yielding starts in Al alloy, cracks are initiated in the ER70S-6, thus lowering the equivalent modulus of the sample.

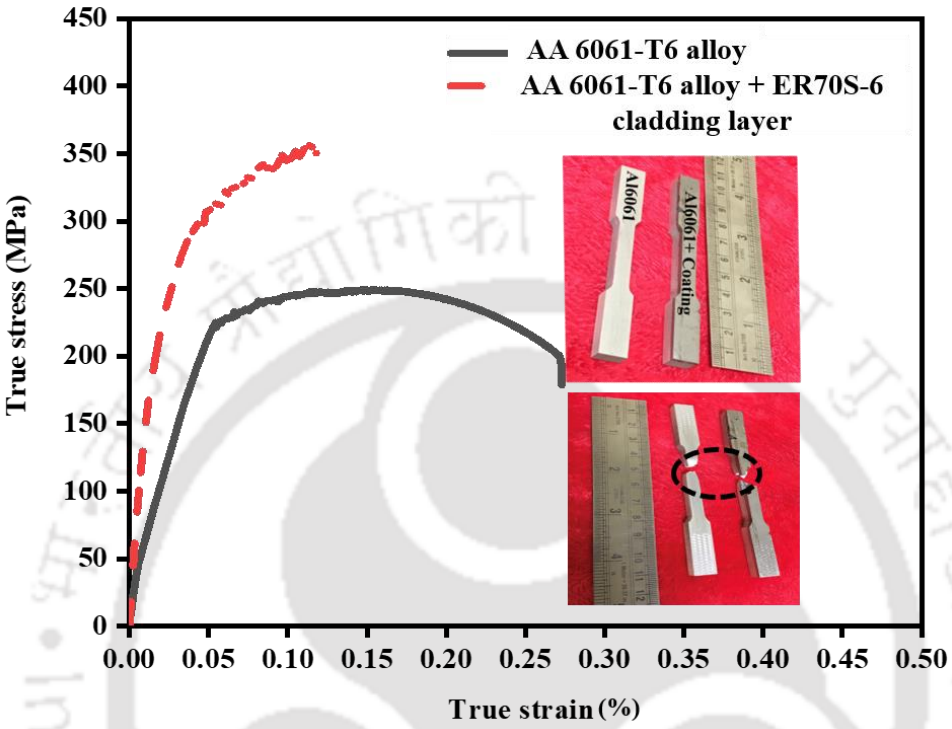

Figure 4.14 True stress versus strain curve of tensile test for aluminum and ER70S6 cladded aluminum by CMT

Fig. 4.15 shows the typical fracture appearance of the ruptured surface of the investigated samples. A combination of large and small shaped dimples is observed in the fractography of Al samples (Fig. 4.15a and Fig. 4.15b), indicating a ductile fracture. Fig. 4.15(c) shows the fracture surface of cladded portion. A large flat area is seen in the ER70S-6 portion, which is a characteristic of the brittle failure. Fig. 4.15(d) depicts the EDS of cladded side, showing high percentage of iron.

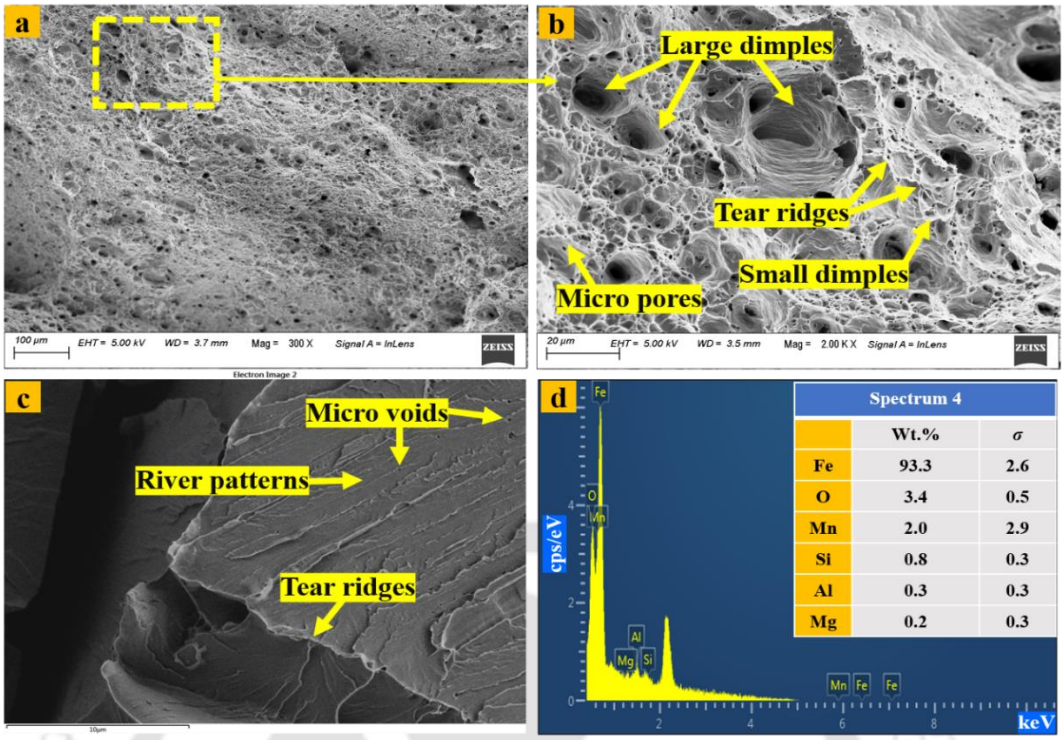

Figure 4.15 Fracture surface morphology: (a, b) of aluminum sample, (c) ER70S-6 cladded portion and (d) EDS elemental distribution of cladded portion

4.3.6 Lap shear study

Figure 4.16 shows the load versus displacement curve for the lap shear test for aluminum and ER70S-6 cladded aluminum by CMT. The cladded specimen was tested for the shear bond strength between the cladding layer and substrate material. The tensile load is applied gradually until the breakage occurs by bond failure. The maximum load, i.e., shear force required to maintain the bond is measured to be 4.87 kN. This amounts to an average shear stress of 74 MPa, which is a reasonable bond strength. However, this bond strength is less than the shear strength of substrate and cladding layer. Hadad, (2007) obtained a bond strength in the range of 43–68 MPa for Al_2O_3 coating on steel for a coating thickness of 330 μm. In the present work, the bond strength was 74 MPa, even when the finished cladding layer thickness was 2 mm. Hadad, (2007) used thermal spray coating and also noted that for bond strength was about 90 MPa for a coating thickness of 140 μm. Bond strength of thinner cladding layer produced by CMT out of the scope of the present work.

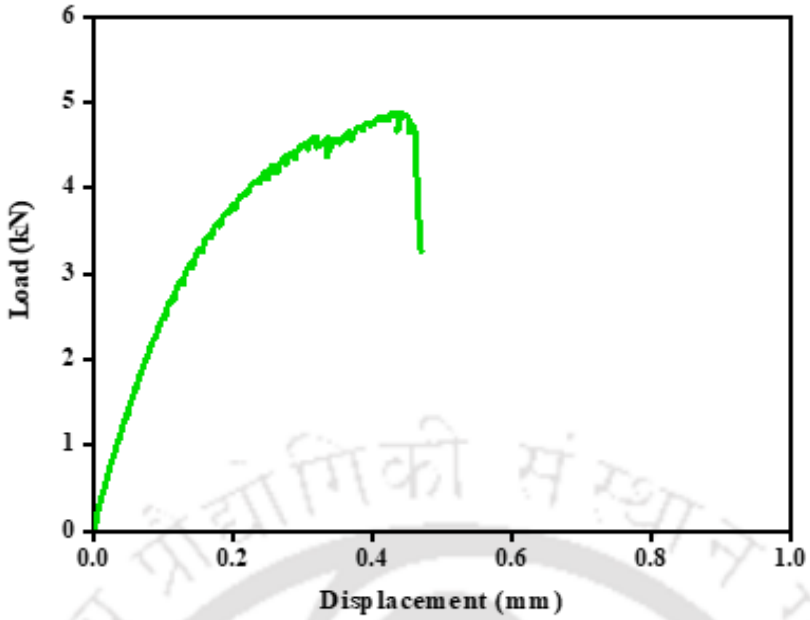

Figure 4.16 Load versus displacement curve of lap shear test for aluminum and ER70S-6 cladded aluminum by CMT

4.4 Conclusions

The ER70S-6 alloy was deposited on AA 6061-T6 substrate using the CMT process and the metallurgical, mechanical tests were evaluated. Following conclusions are drawn:

- A single-pass of CMT could produce about 3 mm thick cladding layer. Usually, the thermal spray process does not provide such thick cladding layer in one pass.
- Tribological study was carried out with hardened steel as the disk and sample as the pin. Cladding layer provided high wear resistance compared to substrate; the Lancaster wear coefficient was 1.01×10^{-5} mm^3/Nm for cladding layer and 1.45×10^{-5} mm^3/Nm for substrate. The coefficient of friction reduced from 0.29 to 0.23 due to increased hardness of the cladding layer. FESEM of worn out surface indicated the abrasion as the dominant mechanism of the wear.
- Improved yield strength of 300 MPa for the cladded sample was observed, compared to 236 MPa yield strength for the base metal. A simple model based on strength of materials over-predicted the yield strength of the cladded sample with 14% error. The maximum shear bond shear strength of 74 MPa was observed during the lap shear test, which indicated good bonding between the substrate and cladding layer, when compared with the similar data in literature

Chapter 5

Corrosion behavior and its effect on mechanical properties of ER70S-6 cladding on AA 6061-T6 alloy

5.1 Introduction

Aluminum (Al) and its alloys have low density and good ductility, making it one of the widely used materials in the aircraft and automobiles industries. However, due to their low hardness and wear resistance, it is not suitable for certain sensitive applications. Many scientists are trying to improve the surface properties of Al by cladding/coating and surface alloying with different metallic and ceramic powders. Generally, Al has good corrosion resistance; however, in the acidic medium, the protective layer breaks and corrosion starts. Corrosion has a profound effect on the strength and stability of structures and has received much attention in engineering.

Corrosion is a serious problem in components of gas and diesel engines, aircraft components and heat exchangers. The salt and acid solutions are harsh working environment that corrode metals. Chemicals like H_2SO_4 attack metals like copper (Cu), stainless steel and their alloys. Fouad, (2017) reported the corrosion behavior of Cu and stainless steel in an acidic medium of H_2SO_4. The rate of corrosion was high for copper as compared to stainless steel. Moorthy and Srinivas, (2016) reported corrosion of mild steel, aluminum, copper, and other metals because of base coolants used in automobiles during a 14-days corrosion test. One of the easiest and most direct ways to assess corrosion of any kind is weight loss measurement in a corrosion immersion test.

In the chapter, an Fe-based electrode was cladded on Al substrate using CMT process. The primary objective of this chapter is to analyse the corrosion behavior of the Fe-based cladding on the Al substrate. The work focusses on the surface roughness, microhardness and wear before and after corrosion.

5.2 Experimental procedures

The experiments were conducted on Al plate with dimension of 180×100×6 mm^3. On AA 6061-T6 alloy substrate, cladding of ER70S-6 was accomplished. The cladded layer was deposited with a Fronius CMT TPS400i machine. The shielding gas used was argon at 20 l/min constant flow rate. The parameters for CMT process were 105 A current, 400 mm/min welding speed, 10 m/mm wire feed speed, 300 s interlayer dwell time and 10 V voltage. The final height of the cladding achieved was 3 mm in single

pass. Fig. 5.1 shows the extracted characterization sample after milling. The cladded layer was milled to a depth of approximately 1 mm to remove the uneven surface prior to sample extraction for characterization.

For microstructural, corrosion and mechanical characterization, the sample was sectioned through electric discharge machining after milling. The sample was polished on various grits (sizes: 80, 400, 800, 1000, 1500, 2000) of silicon carbide emery papers followed by cloth and diamond polishing. For corrosion test, a sample of CMT cladded alloy was tested in a solution of 2.0% H_2SO_4 for 200 h according to ASTM standard: G31. The CMT cladded sample was mounted in a corrosion resistant cold mount with top surface area of 100 mm^2 exposed to acidic solution at room temperature. To calculate the weight loss, the corroded sample was weighed with an accuracy of 0.1 mg. A non-contact optical surface profilometer was used to measure the corrosion pits height and surface roughness. The upright optical microscope and FESEM were used to investigate the sample's morphology. A microhardness tester was used to test the Vickers microhardness 20 s as dwelling period while applying a 200 gf load. The pin-on-disk wear test was conducted on a tribometer for 30 min with 20 N load at 350 rpm. Cladded material in the form of 10 mm diameter pin traversed on 70 mm track diameter on hardened steel disc according to ASTM standard: G99.

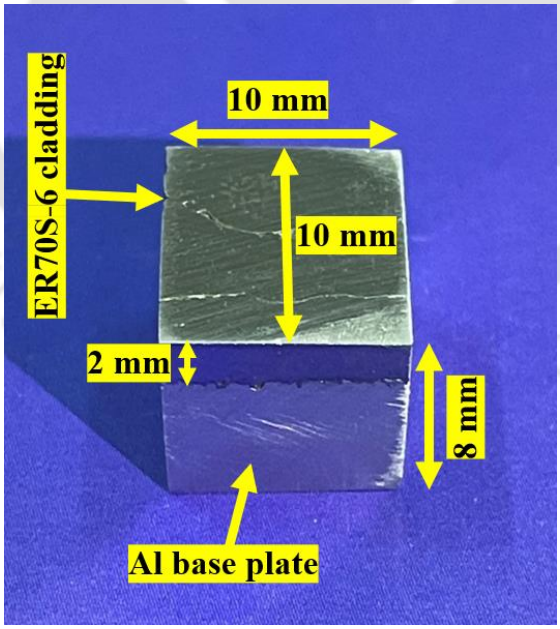

Figure 5.1 Cladded extracted sample for characterization after milling

5.3 Results and discussion

This section discusses a few findings. First the microstructure is described. Next, the surface roughness due to corrosion is discussed. Finally, the microhardness and wear results before and after the corrosion test are described.

5.3.1 Corrosion mechanism and microstructural study

Understanding the mechanism of corrosion is essential to comprehending the physics of corrosion. The mechanisms of steel corrosion in aqueous solution is reported by a few authors (Kahyarian et al. 2017, Hou et al. 2018). The corrosion mechanisms of steel in presence of oxygen is follows:

Anodic reaction:

$$Fe \rightarrow Fe^{2+} + 2e^{-} \tag{5.1}$$

Cathodic reaction:

$$O_2 + 4e^{-} + 2H_2O \rightarrow 4OH^{-} \tag{5.2}$$

$$O_2 + 4e^{-} + 2H_2O \rightarrow 4OH^{-} \tag{5.3}$$

$$4Fe(OH)_2 + O_2 \rightarrow 2Fe_2O_3 + 4H_2O \tag{5.4}$$

Panossian, (2012) reported the corrosion of steel in H_2SO_4 medium in absence of oxygen. Steel is immediately attacked by the creation of hydrogen gas and ferrous ions when it comes into contact with a dilute H_2SO_4 medium, as follows:

Anodic reaction: As per Eq. (5.1)

Cathodic reaction:

$$2H^{+} + 2e^{-} \rightarrow H_2 \tag{5.5}$$

Therefore, the global corrosion reaction can be written as follows:

$$Fe + 2H^{+} \rightarrow Fe^{2+} + H_2 \tag{5.6}$$

The composition of the steel, particularly the amount of carbon, has a significant impact on the rate of corrosion of carbon steels in diluted acids. As a result, the oxidation reaction ($Fe \rightarrow Fe^{2+} + 2e^{-}$) occurs in the ferrite phase whereas the cathodic reduction reaction of H_2 occurs at cementite phase. When the steel comes in contact with the H_2SO_4 medium, the latter reduced to form H_2 and Fe oxidized to form ferrous sulfate ($FeSO_4$), as follows:

$$Fe + H_2SO_4 \rightarrow FeSO_4 + H_2 \tag{5.7}$$

The $FeSO_4$ adheres to the steel surface and acts as a barrier. This $FeSO_4$ layer protects the steel surface from further corrosion attacks in the acid medium during a long-term process. As a result, the maintenance of the $FeSO_4$ layer determines the durability of steel products.

Figure 5.2 shows cross-sectional micrographs and EDS analyses of the cladded layer after the CMT process. The morphology depicts a well-defined and crack-free cladded layer deposited on Al base plate. The presence of different elements in the cladded layer and substrate region was confirmed by EDS analysis (Figs. 5.2(c, d)). The optical and FESEM images are shown in Fig. 5.3 to establish the interaction of H_2SO_4 with the metal surface in the cladding layer. The micrograph morphology shows the features of cladded surface before and after 200 h of corrosion in 2.0% H_2SO_4. The FESEM images depicts that the cladded surface after corrosion is covered with corrosion products and appears to be full of pits and cavities. The corrosion cracks are also visible in a few places in the corroded surface. The weight loss after the corrosion test was 0.089 g. As the exposed area was 100 mm^2, this amounts to a weight loss of 8.9×10^{-4} g/mm^2.

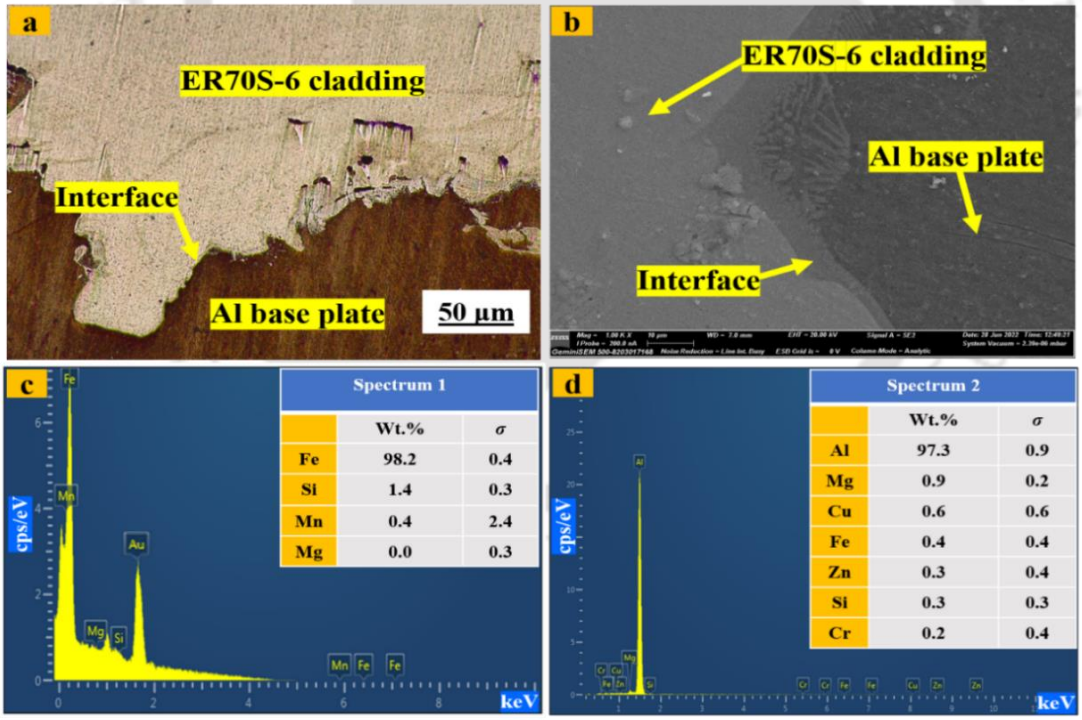

Figure 5.2 Micrograph after cladding: (a) optical (X20), (b) FESEM (X2000); EDS elemental distribution of (c) cladded and (d) base plate region

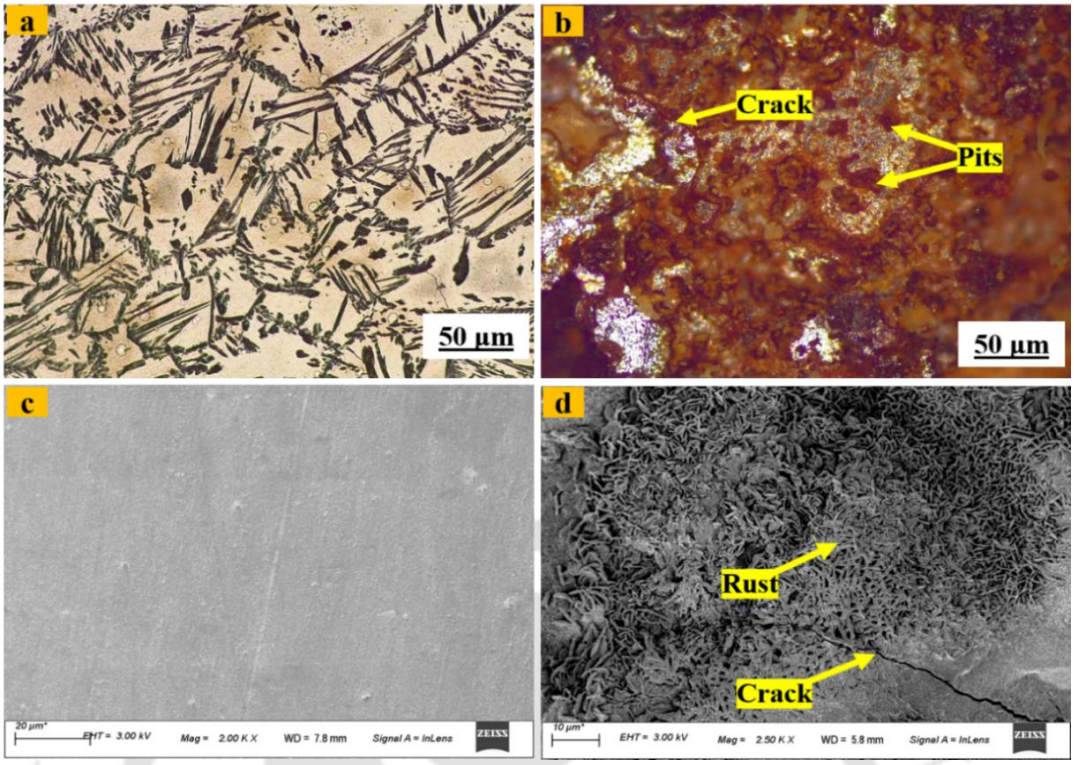

Figure 5.3 Morphology of cladded layer: 1. optical micrograph (X20): (a) before corrosion, (b) after corrosion, 2. FESEM micrograph: (c) before corrosion (X2000), (d) after corrosion (X2500)

5.3.2 Surface roughness

The non-contact optical surface profilometer was used for measuring the surface roughness after the corrosion test. Fig. 5.4 shows the 3D morphology after corrosion immersion test. The corrosion product iron oxide (Fe_2O_3) is observed in Fig. 5.4(b). The average surface roughness value (R_a) before the corrosion test was 0.429 µm, which became 3.10 µm after corrosion test. Mean height before the corrosion was 0.391 µm and 5.46 µm after 200 h corrosion test.

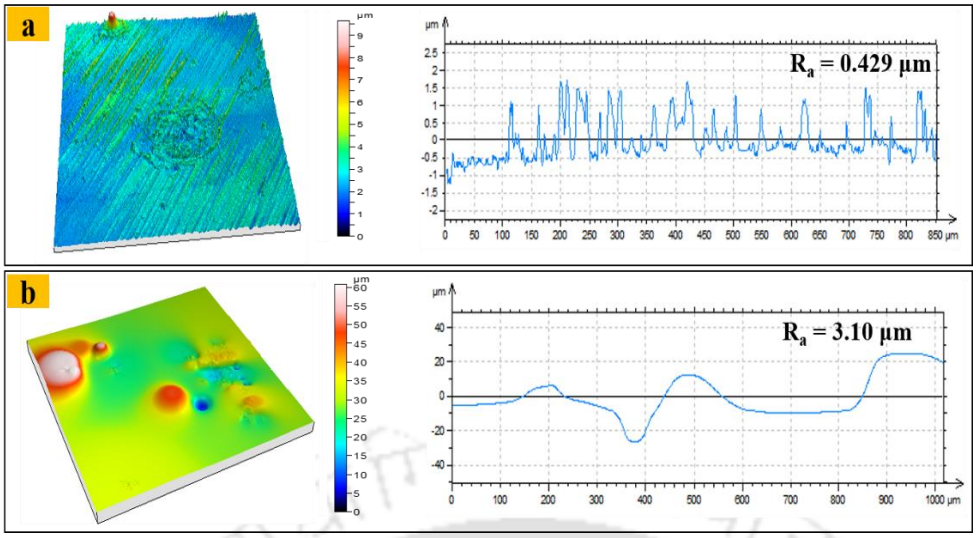

Figure 5.4 3D images and corresponding roughness plot of cladded layer: (a) before corrosion test and (b) after corrosion test

5.3.3 Hardness study

Figure 5.5 show the average microhardness value of cladded layer before and after the corrosion test. Corrosion removes the hard layer of metal and reduces the hardness. The average microhardness value before corrosion was 237 HV, but after the corrosion test, the hardness reduced to 213 HV. The decrease in the microhardness value indicates that some depth of the corrosion-resistant alloy zone has been removed. This reduction attributes to the dissolution of metal ions and hard iron oxide layer in the corrosive medium (Jiru et al. 2019). The microhardness also decreased due to increased pitting corrosion, thus reducing the load-bearing area at certain places.

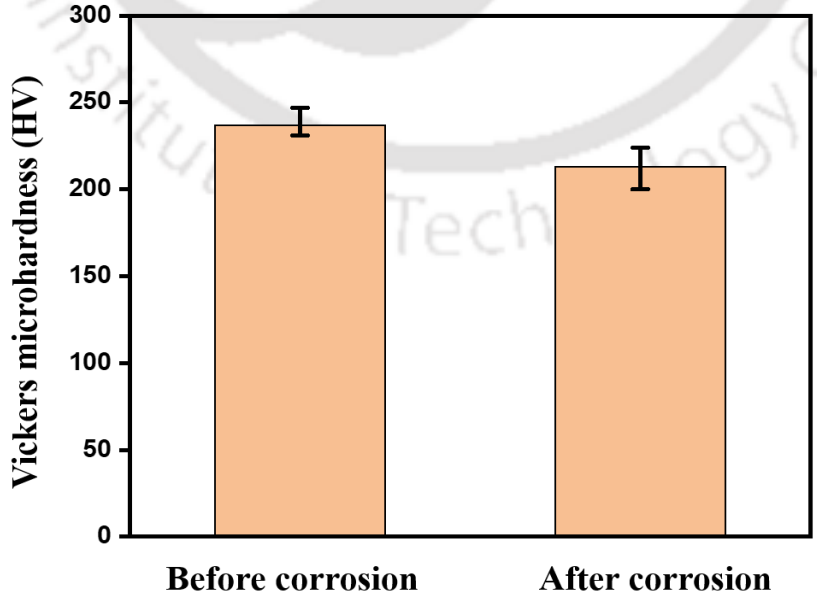

Figure 5.5 The effect of corrosion on microhardness of the cladded layer

5.3.4 Wear Study

Figure 5.6 shows the wear data after the corrosion test. The average wear depth was 51.61 µm; which was 37 µm before corrosion test for the same test condition. This 39.5% increase in wear depth after corrosion was due to the removal of hard particles from the upper most section of the cladding layer. The fluctuation of the wear depth data also increased due to the presence of corrosion pits in the cladding layer. The morphology of worn out surface of cladding layer in Fig. 5.6(b) also shows indications of abrasive wear. The spallation of the hard-cladding layer is comparatively spread over a larger region.

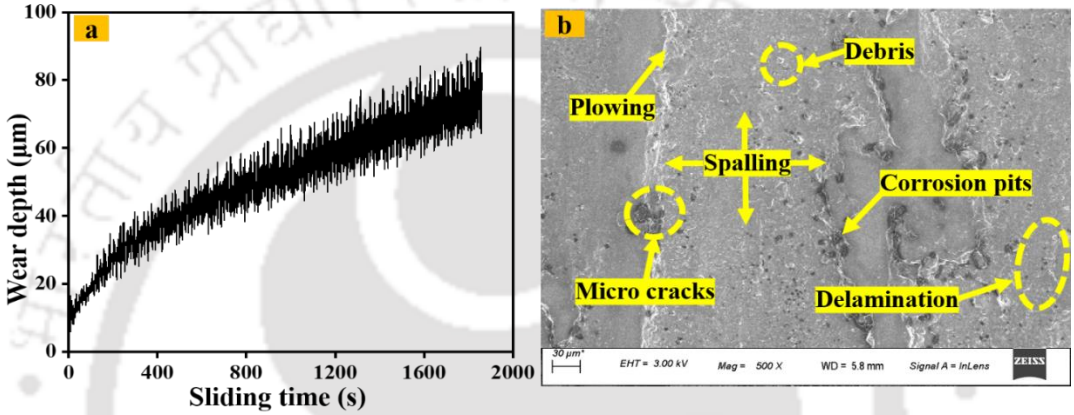

Figure 5.6 Wear analysis of the cladded layer after corrosion test: (a) wear depth with sliding distance and (b) FESEM (X500) morphology

5.4 Conclusion

The cladding of Fe-based filler wire was carried out on Al substrate with CMT technology. After cladding, the corrosion, hardness and wear were studied. Following are the salient conclusions:

- The major surface damage in the cladding layer is due to localized pitting corrosion. The growth of the pit is faster in the lateral direction compared to depth direction. The shapes of the pits were irregular. After 200 h of corrosion test, the weight loss was 8.9×10^{-4} g/mm^2.
- The average micro-hardness after the corrosion test reduced by 10% due to removal of hard materials and introduction of porosity, thus reducing the load-bearing area at certain places.
- The wear depth increased by 39.5% in the cladded region after 200 h corrosion test due to the presence of corrosion pits and removal of hard layer of metal.

Chapter 6

Heat treatment of ER70S-6 cladding on AA 6061-T6 aluminum alloy

6.1 Introduction

The CMT can be used for depositing the material on the substrate to enhance the targeted microstructural and mechanical properties, which is called cladding process. Both heat input during deposition and heat transfer after deposition affect the properties of the cladded or coated material (Selvi et al. 2018). The greatest distinguishing feature of CMT cladding over conventional thermal spray is the lower processing temperature of the former, which has a correspondingly smaller thermal impact on the processed materials (Pickin et al. 2011). Therefore, CMT cladding is especially useful for coatings that are susceptible to oxidation at high temperature. CMT cladding has been employed for cladding cobalt (Rajeev et al. 2019, Rajeev et al. 2019, Thiagaran and Ponnusamy, 2021), nickel (Evangeline and Sathiya, 2019, Ola and Doern, 2014, Kun et al. 2022, Solecka et al. 2018, Tang et al. 2020), aluminum (Rajeev et al. 2014, Bowen et al. 2019) and ferrous alloys (Tang et al. 2020, Luchtenberg et al. 2019). Dense claddings with reduced oxidation provide superior mechanical, thermal, and electrical properties (Li et al. 2006, Gartner et al. 2006). On the negative side, it also results in residual tensile stresses as a result of differential thermal expansion (Gartner et al. 2006), although some kinetic processes may tend to produce residual compressive stresses on the surface (Luzin et al. 2011, Ghelichi et al. 2014). A reduction in ductility after cladding is also not uncommon. To mitigate the negative effect of the CMT cladding heat treatment may be employed. Heat treatment is in vogue for CMT welding (Prakash et al. 2018, Ahmad and Baskar, 2011, Shanglu et al. 2013). The improved strength and hardness of the aged AA 2024 joint could be obtained thanks to refined grain structure (Prakash et al. 2018). The heat treatment resulted in enhanced tensile strength and hardness of AA6061 welded joint because of fine and homogenous distribution of precipitates (Ahmad and Baskar, 2011). The heat treatment could restore the weld strength of aluminum to zine-coated low carbon steel, which had reduced due to heat affected zone softening (Shanglu et al. 2013). The microstructure and the mechanical properties of cold sprayed copper (Li et al. 2006, Gartner et al. 2006, Sudharshan et al. 2007), aluminum (Hengyong et al. 2011), stainless steel (Xian-Ming et al. 2011, Al-Mangour et al. 2014), titanium (Molak et al. 2017) and Inconel 718 (Wong et al. 2013) coatings could be altered by heat treatment. The thermal

and electrical properties of the cold sprayed coatings enhanced as a result of improved particle-to-particle contact but the hardness reduced owing to the absence of work hardening from heat treatment (Li et al. 2006, Sudharshan et al. 2007). Additionally, heat treatment could reduce the porosity of cold-sprayed coatings (Mangour et al. 2014) and even in bulk materials (Gartner et al. 2006).

Fe based ER70S-6 electrode was cladded on aluminum (Al) substrate using CMT technique. In the chapter, the effect of heat treatment on the cladded layer is studied. Following four types of heat treatment were used: (1) sample heated up to 600 °C followed by a 1 h holding and furnace cooling in 24 h, (2) sample heated up to 600 °C followed by a 1 h holding and water quenching, (3) artificial age hardening by heating the sample up to 175 °C, holding it for 24 h and then furnace cooling in 6 h and (4) deep cryo-treatment by dipping the sample in liquid nitrogen (–196 °C) for 1 h and then bringing to ambient temperature. A detailed comparative study of these types is presented.

6.2 Materials and methods

In this chapter, the substrate material was taken in the form of 180 mm×100 mm×6 mm size plates of AA 6061-T6 alloy. This aluminum alloy is frequently employed in structural applications due to its high specific strength and good corrosion resistance. ER70S-6 filler wire of 1.2 mm diameter was used for cladding. The composition of the substrate and filler wire are reported in chapter 4. A Fronius make TPS400i CMT machine was used for the cladding. The speed and route of the cladding layer were changed using a 6-axis FANUC make Arc Mate 100iD robot.

6.2.1 Cladding process

The cladding was carried out in the room temperature. Prior to the cladding procedure, the substrate plate was thoroughly cleaned with acetone. The heat input Q during cladding was 142.5 J/mm, calculated as per equation 2.3. Cladded layer thickness was about 3 mm.

6.2.2 Sample preparation

Cladded portion was milled to make the thickness of the cladding as 2 mm. Different samples were cut into sections using a wire-cut electrical discharge machine (WEDM) for microstructure and mechanical characterization purpose. Fig. 6.1 shows the sectioned sample for the characterization.

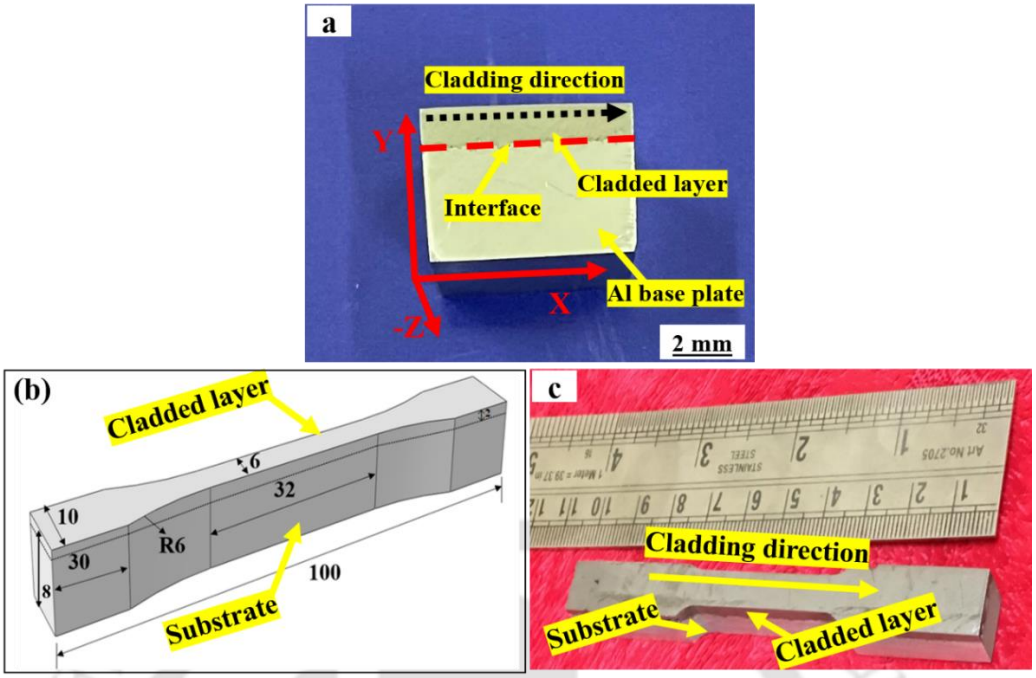

Figure 6.1 Deposition of cladding layer using CMT technology: (a) sectioned wire cut and milled sample for different characterization prior to heat-treatment; tensile specimens**:** (b) schematic diagrams and (c) sectioned wire cut sample for tensile characterization

6.2.3 Heat treatment process

The samples were properly cleaned with acetone before the heat treatment process to remove the undesired oils and dirt during the cutting process using WEDM. The heat treatment was carried out using an electric muffle furnace. The post heat-treatment used on the extracted samples was of four types— (1) sample heated up to 600 °C followed by a 1 h holding and furnace cooling in 24 h, (2) sample heated up to 600 °C followed by a 1 h holding and water quenching, (3) artificial age hardening by heating the sample up to 175 °C, holding it for 24 h and then furnace cooling in 6 h and (4) deep cryo-treatment by dipping the sample in liquid nitrogen (–196 °C) for 1 h and then bringing to ambient temperature.

6.2.4 Porosity analysis

The porosity of the different samples was calculated according to Archimedes' principle. Sectioned sample size of 10×10×8 mm^3 was for the porosity analysis. The calculation details are provided in the chapter 3.

6.2.5 Microstructural analysis

Using silicon carbide sheets with grit sizes ranging from 80 to 2000 to polish the sectioned samples, cloth and diamond polish were applied. The polished samples were etched into Nital reagent for 15 s in order to observe the microstructure. The Nital reagent contains 5 ml of nitric acid (HNO_3) and 95 ml of alcohol (CH_3OH). The upright optical microscope was used to produce the optical micrographs. Field emission scanning electron microscopy (FESEM) was used to examine the surface, worn-out debris and fracture morphology at operating voltage of 20 kV. A gold sputtered coating was applied to the samples before FESEM. Using ImageJ software and the random line intercept approach, the samples grain size was calculated. Intercept lines were positioned such that at least 10 grains are intercepted by the lines.

6.2.6 Surface roughness analysis

The sample size of 10×10×2 mm^3 was scanned through a non-contact atomic force microscopy (AFM) to examine the surface roughness cladded layer (Model: Cypher S; Make: Oxford Instruments) in tapping mode. The test was conducted on the surface of the cladded layer before surface milling i.e., as-cladded condition. The average scan data of three different scanning test of 10×10 μm is reported.

6.2.7 XRD analysis

To identify the phase changed due to different heat treatment X-ray diffraction investigations were conducted on the sample top surface. The solid sample was placed on a sample holder with dimensions of 20×25×2 mm^3. The measurements were carried out at an applied voltage of 45 kV and a current of 200 mA while the samples were scanned at a rate of 10 °/min with steps of 0.05° in the diffraction angle (2θ) range of 30°–90°. Crystallite size and lattice strain are estimated from the peak position and peak broadening is measured from the XRD pattern. By adopting a precise lattice parameter computation method, the lattice parameter is computed from the X-ray diffraction pattern.

6.2.8 Hardness analysis

Vickers microhardness of samples were conducted using MVH-II (Make: Omni Tech) microhardness tester. Using a 136° square-based Vickers diamond pyramid, an indentation was created with a 200 g load and 20 s dwell period.

6.2.9 Wear analysis

Pin-on-disc dry sliding wear tests were performed on steel discs with a hardness of 64 HRC in pin-on-disc with applied loads of 20 N and a fixed sliding speed of 350 rpm. The hardened steel was 100 mm in diameter and 10 mm thick. The steel disc surface was properly cleaned with acetone to remove any foreign particles which may acts as a hard impurity against pin surface. The exposed surface area of the pin-shaped cladded layer was 25 mm^2. The weight loss, wear volume and coefficient of friction (CoF) were calculated as follows:

$$W_{loss} = W_1 - W_2, \tag{6.1}$$

where W_1 and W_2 is the weight of the sample before and after wear, respectively,

$$\text{Wear volume loss} = \frac{W_{loss}}{\text{density of cladded layer}}, \tag{6.2}$$

$$\text{CoF} = \frac{\text{frictional resistance}}{\text{normal load}}. \tag{6.3}$$

The sliding speed is given by

$$\text{sliding speed} = \frac{\pi DN}{60}, \tag{6.4}$$

where D=70 mm is the track diameter and N=350 rpm is the number of revolution/min by the pin on hardened steel surface. Product of sliding speed and time provides sliding distance. For a 30 min of wear test, the sliding distance was 2309 m.

The load is imparted to the sample during sliding via a cantilever mechanism, and the specimens are brought into close proximity to the rotating disc at a track diameter of 70 mm. Prior to and following each test, the samples were weighted using a digital microbalance to an accuracy of 0.01 mg. The wear rate was calculated from the weight loss information in terms of volume loss per unit sliding distance. Based on the applied load and the observed frictional force, the coefficient of friction was calculated. The worn surface 3D morphology and roughness was analysed by AFM at 3 different areas of squares 30 μm side and the average value is reported. On the steel disc, sticking of the dislodged material from the specimen surface was also observed. The worn debris from the steel surface was also collected for the characterization purpose.

6.2.10 Tensile property analysis

The tensile specimen was sectioned according to the ASTM E8M–11standard. The test was conducted using Autograph AGX-V universal testing machine with 0.1×10^{-3} s^{-1} strain rate. The test was conducted at room temperature. For the fracture morphology, height of ~2 mm just below the fracture spot was sectioned.

6.3 Results and discussion

In this section, effects of heat treatment are reported. The term as-cladded means samples obtained after milling the cladded samples for about 1 mm depth. Heat treatment was also carried out on cladded and milled samples. However, while studying the effect of heat treatment on surface roughness, milling was not carried out.

6.3.1 Porosity study

Figure 6.2 shows the porosity percentage of the as-cladded and heat-treated samples. The as-cladded sample had the maximum porosity of 2.56%. The porosity in the cladded samples reduced to 0.48–1.21% after heat treatment. Type 1 heat treatment provided 1.35% porosity, the least among all samples due to sintering effect. Bin-you, (2009) also reported 19% reduction in porosity during annealing at 600 °C of Fe-based 1 mm cladding layer through spray technique. In the present study the porosity has reduced by 47% at similar annealing temperature and the cladding layer thickness of 2 mm.

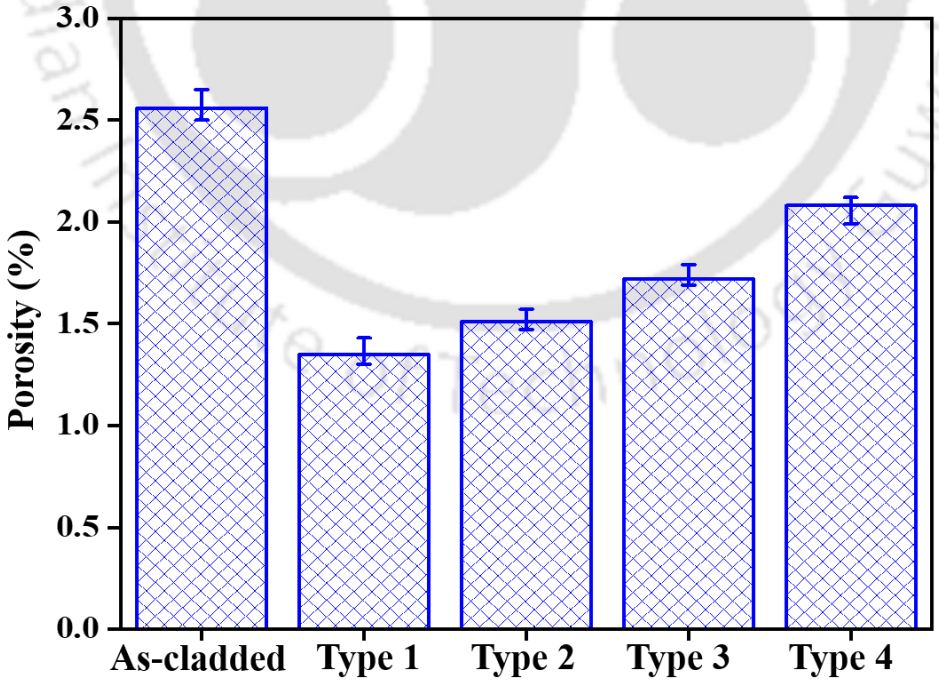

Figure 6.2 Porosity of the sample before and after heat treatment process

Fig. 6.3 shows typical cross-sectional optical micrographs of the cladding layer for various samples. The micrographs were obtained from the plane containing thickness and cladding directions, i.e., from the front view of the sample. The micrographs depict the high dense nature of the claddings with uneven infiltration of cladding materials into base metal due to differences in density. The as-cladded layer depicts presence of small oxide strings and microcracks. However, in case of heat-treated samples pores and micro-cracks reduced.

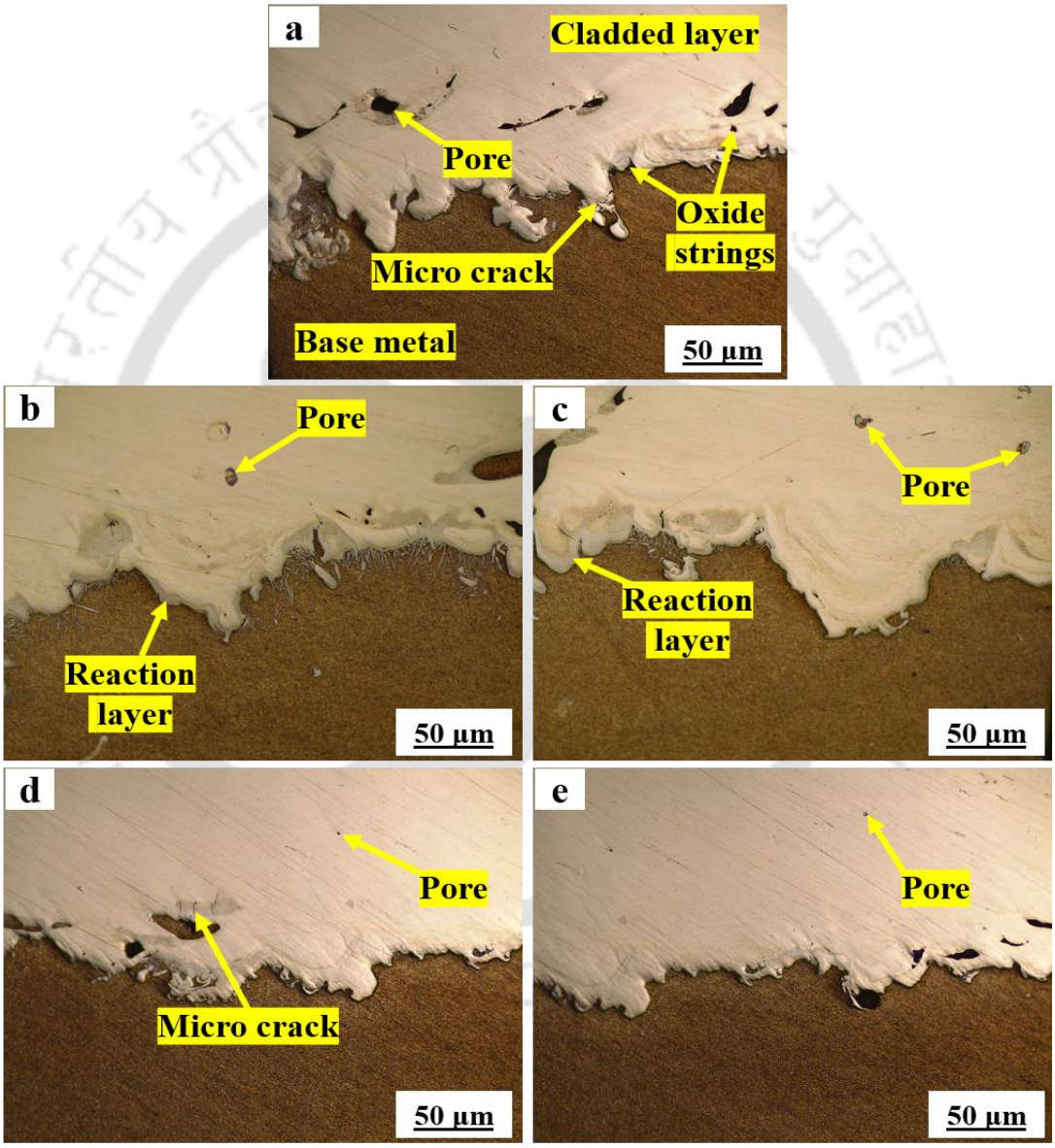

Figure 6.3 Cross-section morphology (front view) of cladded (and milled) layer and substrate: (a) As-cladded, (b) Type 1, (C) Type 2, (d) Type 3 and (e) Type 4

6.3.2 Microstructural study

The FESEM morphology of the cladded layer after cladding depicts development of different phases such as ferrite, martensite and distribution of carbides discussed in chapter 4. The different phases occurred due to the fast heating and cooling involved in CMT cladding process. The cladding layer cools in a manner analogous to quenching, where martensite transformation takes place at various places in the structure. However, due to application of different types of heat treatment to the cladded layer the proportion of the developed phase in the heat-treated layer has been changed to some extent as compared to as-cladded layer. The proportion of martensite transformation during the heat treatment process was calculated by image area method. The martensitic phase at the as-cladded layer was ~32%, which reduced to ~20% in Type 1 heat treatment and ~26% in Type 3 heat treatment. However, in Type 2 and Type 4 heat treatment, the martensitic phase transformation increased to ~43% and ~56%, respectively. The results are also relatable in the visible observation of the surface morphology in the X-Y plane (Fig. 6.4b, d, f, h). The martensite phase is densely distributed in the Type 4 heat treated sample compared to all others Type of heat-treated sample.

Distinct grain boundary is visible in the X-Z plane morphology (Fig. 6.4c, e, g, i). The ferritic phase and distribution of coarse carbide is dominant in Type 1 and Type 3 heat treated sample. During Type 1 heat treatment, the high temperature causes the primary alloy carbides to dissolve more thoroughly, adding additional carbon and alloying components. This led to the formation of a network of tiny course carbide precipitate at the grains during cooling. However, the proportion is low in Type 3 owning to heat treatment at lower temperature. At a few region pearlite and cementite phases were also developed in Type 1 and Type 3 heat treated sample due to slow cooling. The proportion of ductile ferritic phase is dominated by brittle acicular martensite phase in the Type 2 and Type 4 heat treated sample. Some retained austenite structure was observed in Type 2 heat treated sample. However, in the Type 4 heat treatment no such phase was observed. Type 4 heat treatment also reduced the proportion and distribution of carbide precipitates. Harish, (2009) also observed the same in cryogenic treating of EN 31 bearing steel.

Fig. 6.5 shows the EDS analysis of Type 1 heat treated sample. The cross-section micrograph (Fig. 6.5(a)) depicts good bonding between cladded layer and substrate without any visible porosity. The area EDS elemental distribution (Fig. 6.5(b)) shows the

presence of elements throughout the sample. The line EDS analysis (Fig. 6.5(c)) in the interface region shows only slight hike in the oxygen present, which is indicative of less oxidation during cladding using CMT process. The elemental maps depict uneven distribution of elements in the cross-section (Fig. 6.5d).

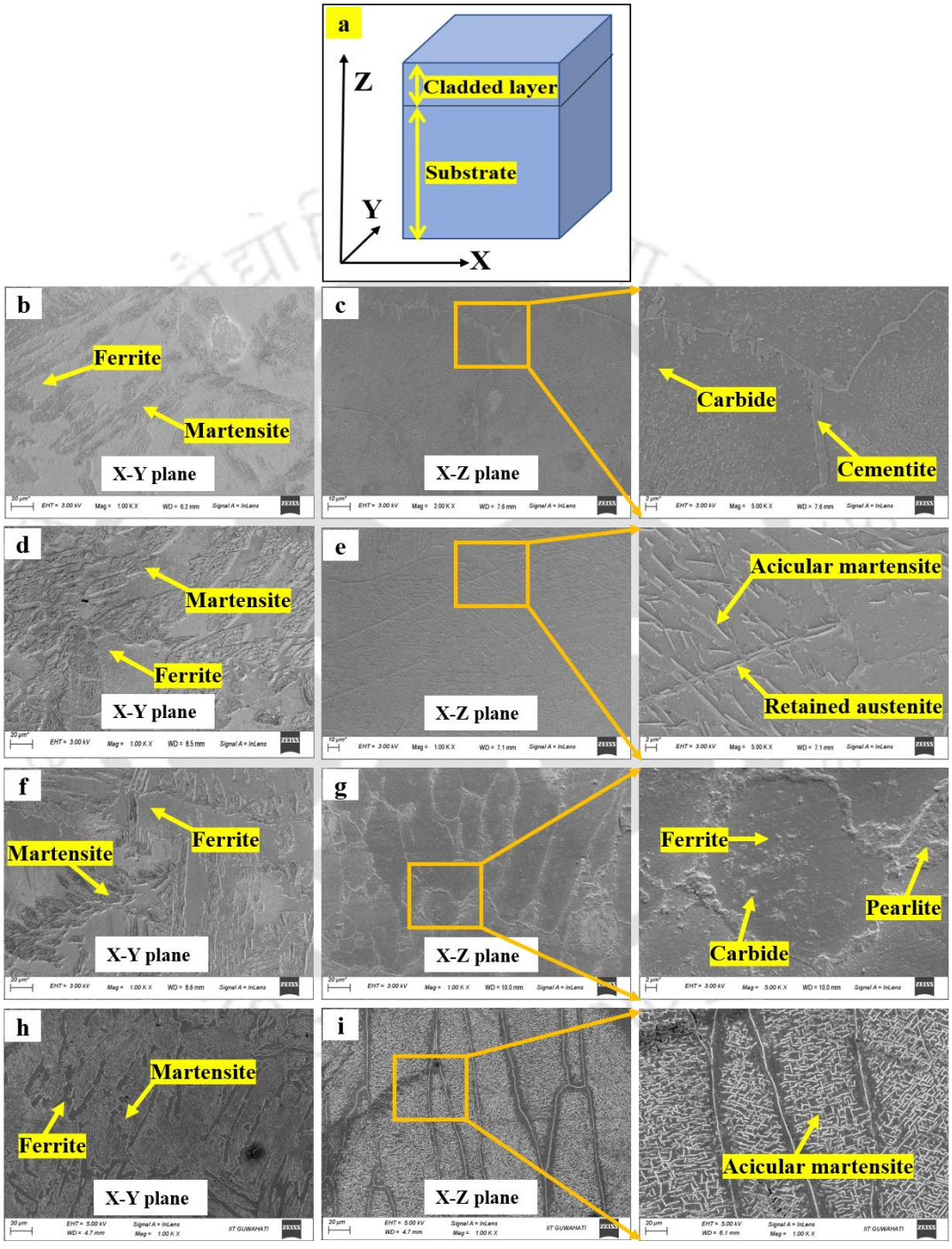

Figure 6.4 Morphology at the top surface (X–Y plane) and at the cross-section (X–Z plane) of cladded (and milled) layer: (a) schematic showing X-Y-Z axes, (b, c) Type 1, (d, e) Type 2, (f, g) Type 3 and (h, i) Type 4. X and Z axes are along cladding and thickness directions, respectively

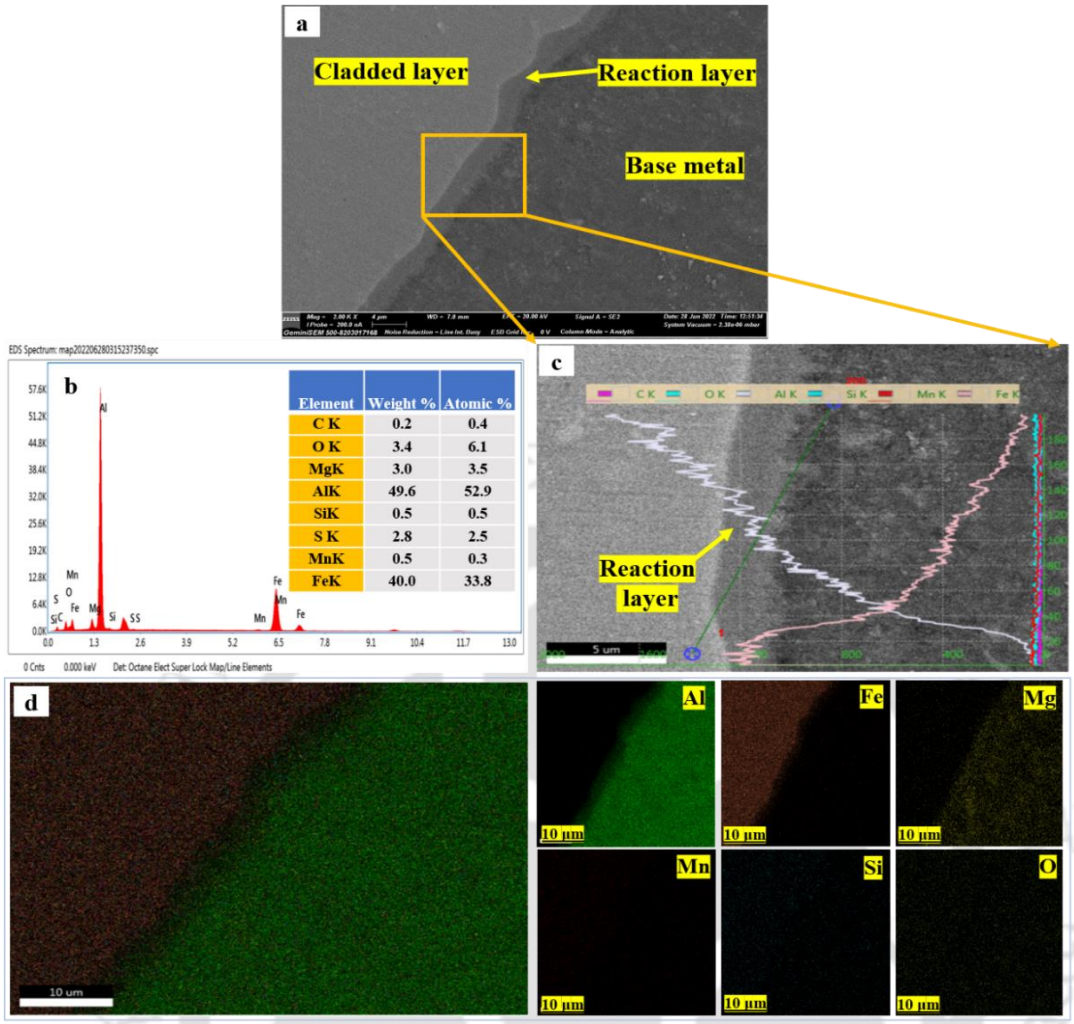

Figure 6.5 EDS analysis of Type 1 heat treated cladded (and milled) layer: (a) cross-section morphology, (b) elemental distribution, (c) cross-section interface elemental graphs and (d) maps of present elements

6.3.3 Grain size analysis

Figure 6.6 shows the microstructure of the as-cladded and heat treated samples. Grains contain mostly matensite along with other phases. Some grains contain traces of the retained austenite. The heat treatment type had a significant impact on the grain size. With the increasing temprerature the grains size also increased. The average grain size increased during Type 1 and Type 3 heat treatment, which was 30 and 29 µm, respectively, against 27 µm in the as-cladded sample. Low temperatures result in irregular grain shapes and curved grain boundaries, whereas high temperatures result in roughly hexagonal grain shapes and flat grain boundaries (Chen et al. 2017). The similar observation is also observed in Fig. 6.6. The maximum reduction in the average grain size was observed in case of Type 4 heat treatment; the average grain size was 20 µm. It is because carbon content has a significant impact on the movement and dissolution of

components during the modification of microstructure. Due to the migration and dissolution of the carbon during Type 4 heat treatment, the phase modification (martensite) in the steel cladding occured. The stress developed by the lattice shrinkage of martensite during cryogenic treatment encourage the migration of moveable dislocations, which results in grain refinement (Manjunatha et al. 2018). Yuhua, (2020) also reported that cryo-treatment effects significantly the low-angle and high-angle grains boundary and their average influences reasults in grain refinement. Fig. 6.7 shows the distribution of the grain size of the as-cladded and heat treated samples. Significant amount of samll size grains (<20 μm) are observed in Type 4 heat treatment unlike all others types of heat treatment.

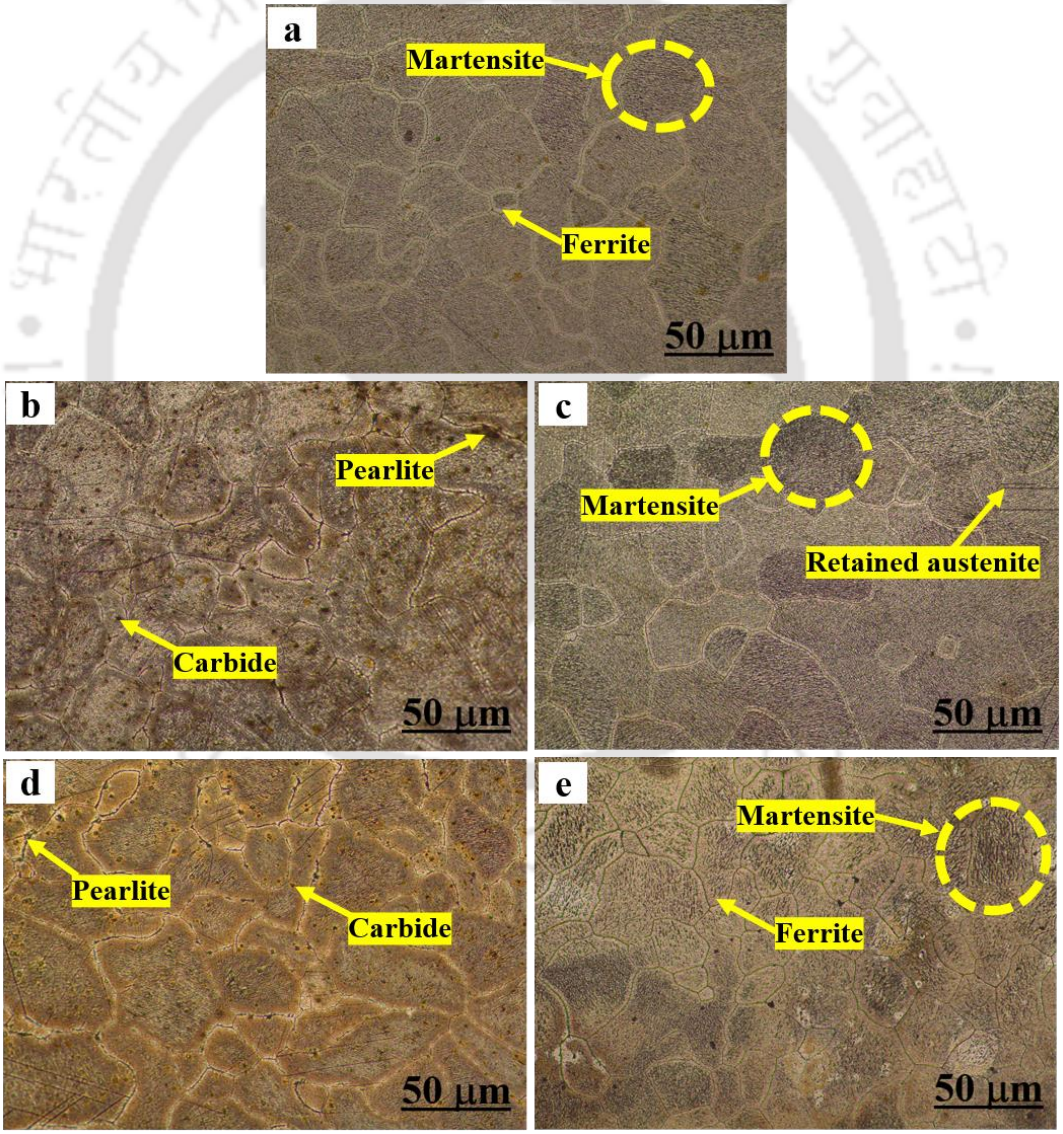

Figure 6.6 Optical micrograph at the top surface of cladded (and milled) layer (X20): (a) as-cladded, (b) Type 1, (C) Type 2, (d) Type 3 and (e) Type 4

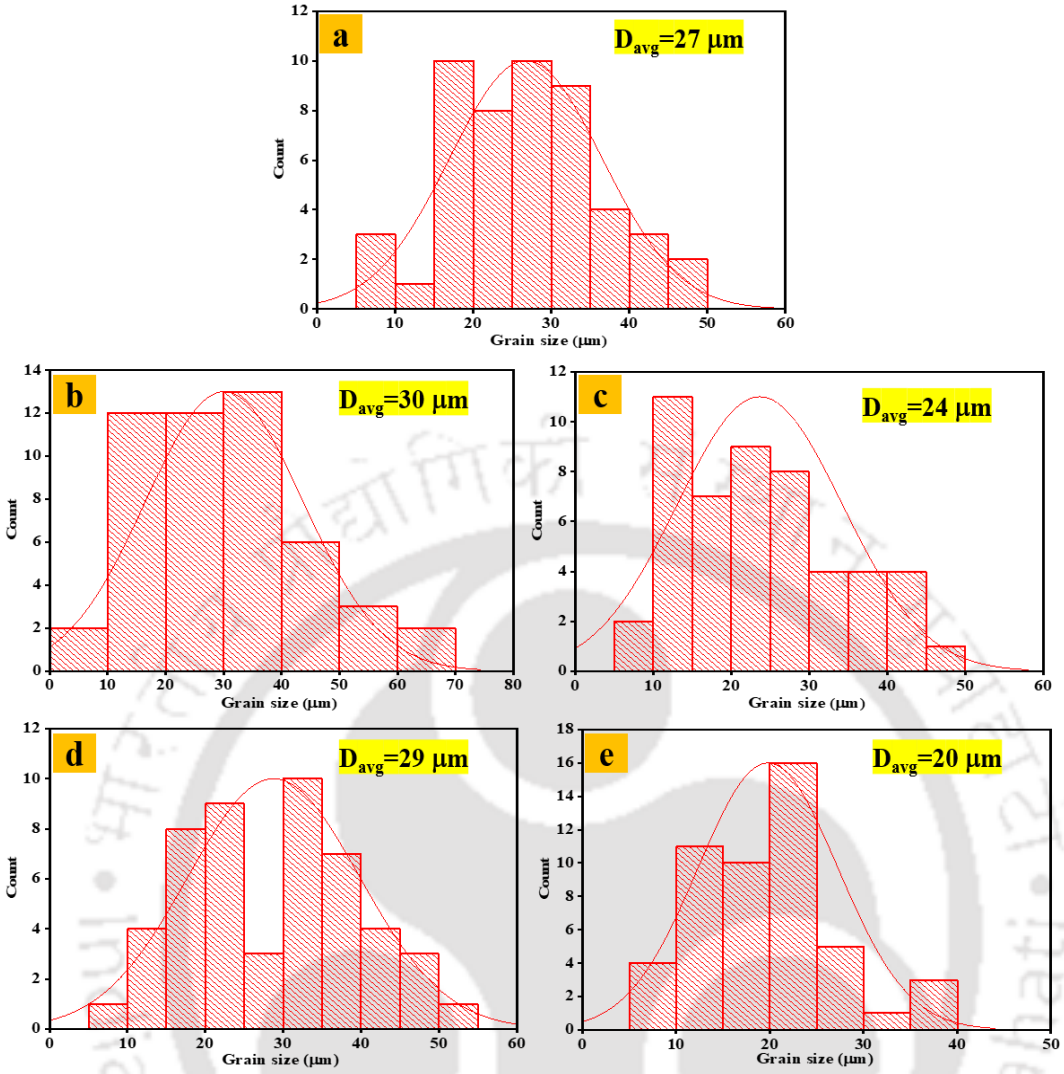

Figure 6.7 Grain size plot of cladded (and milled) layer (based on top surface): (a) as-cladded, (b) Type 1, (C) Type 2, (d) Type 3 and (e) Type 4

6.3.4 Surface roughness study

Figure 6.8 shows 3D surface profile of as-cladded (without milling) and heat-treated (without milling) samples. The surface roughness value increased to 75 nm in Type 1 heat treated sample, compared to 46 nm in the as-cladded sample. The increase in surface roughness value for Type 1 heat treated sample is mainly due to the increased grain size. At high temperature, the formation of coarse carbide and the oxide layer has major role in enhancing roughness value. However, during Type 4 heat treatment, the formation of fine carbide, absence of oxidation and grain refinement led to minimum surface roughness, which was 25 nm. However, the surface roughness value is dependent on surface area and cutoff length (Wen-Ruey et al. 2004). The present scan surface area was 100 $(\mu m)^2$.

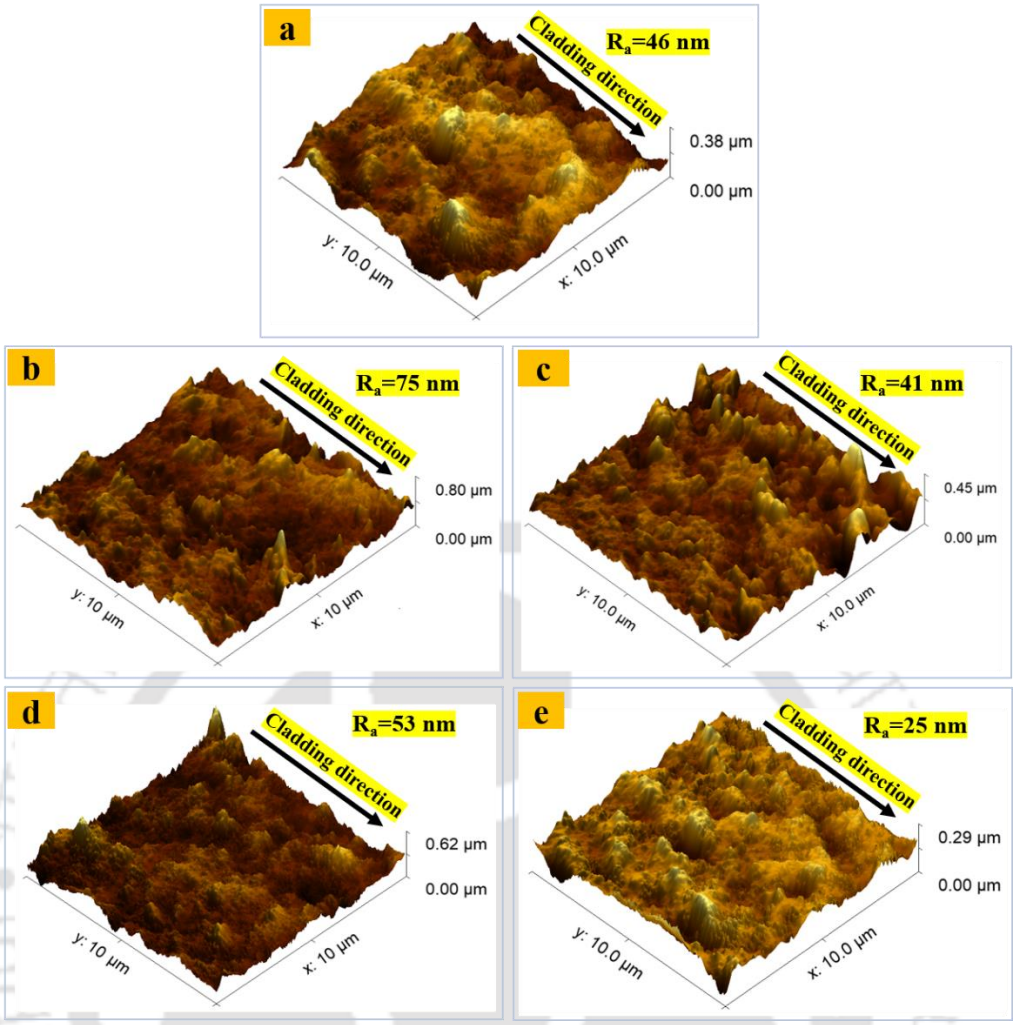

Figure 6.8 AFM 3D surface micrograph of cladded (without any post-processing) layer prior to milling: (a) as-cladded, (b) Type 1, (C) Type 2, (d) Type 3 and (e) Type 4

6.3.5 XRD study

The phases developed in the cladded layer under various heat treatment conditions have been investigated using XRD analysis, and the results are shown in Fig. 6.9. The plots depict the development of crystalline and amorphous phases in the cladded layers. The pattern shows the presence of α-Fe (ferrite, BCC) phase as dominant phase and a few traces of γ-Fe (retained austenite, FCC) phase, which is consistent with the FESEM micrograph observed in Fig. 6.7. The intensity of the γ-Fe reduced in Type 4 heat treated sample, confirming the transformation of retained austenite to martensite. Additionally, as evident from Fig. 6.9, the heat treatment changes the intensity of the peaks across all crystallographic planes and angles. After heat treatment, the big hump pattern diminished and the peaks moved in the direction of an increasing angle. This confirms the change in the matrix structure and strain state as a result of heat treatment (Bin-you et al. 2009).

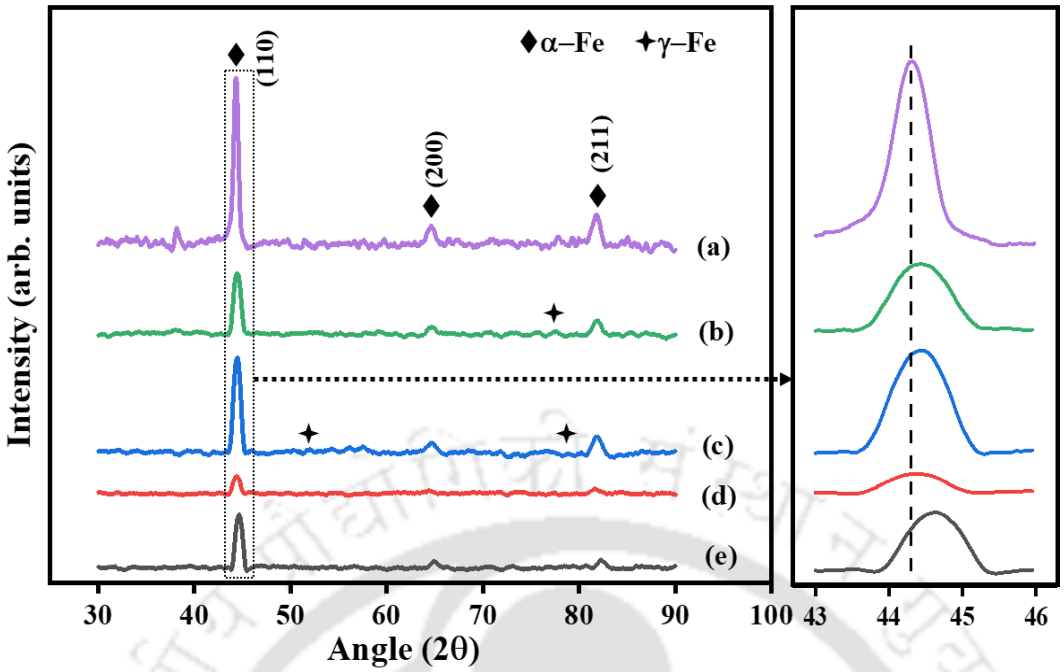

Figure 6.9 XRD plot at the top surface of cladded (and milled) layer: (a) as-cladded, (b) Type 1, (C) Type 2, (d) Type 3 and (e) Type 4

Fig. 6.10 (a, b) shows the crystallite size and lattice strain of the as-cladded and different heat-treated samples. The crystallite size and the lattice strain are calculated using Williamson-Hall equation (Jenkins and Snyder, 1996):

$$\beta = \beta_G + \beta_S \tag{6.5}$$

$$\beta_G = \frac{K\lambda}{D\cos\theta} \tag{6.6}$$

$$\beta_S = 4\varepsilon \sin\theta \tag{6.7}$$

where β is the full width half maxima (FWHM), β_G is the contribution due to crystallite size, β_S is the contribution due to lattice strain, K=0.9 is the constant, λ is the wavelength, D is the crystallite size and ε is the lattice strain. The lattice strain ε was calculated by rearranging the Williamson-Hall equation as

$$\beta\cos\theta = \frac{K\lambda}{D} + 4\varepsilon\sin\theta. \tag{6.8}$$

Crystallite size and lattice strain are determined from intercept and slope of the linear plot of 4sinθ and βcosθ. Fig. 6.11(a) shows a linear plot of Type 4 heat treated sample. The maximum crystallite size of 47.16 nm was observed in case of Type 1 heat treated sample while the minimum was 30.53 nm in Type 4 treated sample against 38.94 nm in the as-cladded layer. In Type 1 samples, heat treatment was carried out at higher temperature. Higher temperatures facilitate atomic vibration and diffusion, forming

grains with lower surface energy (Joydip et al. 2011); critical sizes of the nuclei rises (Rashidi and Amadeh, 2009).

Fig. 6.10(c) shows the dislocation density of the a as-cladded and different heat-treated samples. The dislocation density (ρ) is calculated as (He et al. 2016):

$$\rho = \frac{2\sqrt{3}\varepsilon}{Db} \tag{6.9}$$

where b is burger vector, for BCC structure $b = (a\sqrt{3})/2$, where a is the lattice parameter. It was computed from three highest XRD peaks of different samples using the Nelson-Riley extrapolation method. For each peak, the fraction error is given by the product of a constant K and a trigonometric function called Nelson-Riley function (Jenkins and Snyder, 1996). Thus,

$$\frac{\Delta a}{a} = K\left(\frac{\cos^2\theta}{\sin\theta} + \frac{\cos^2\theta}{\theta}\right). \tag{6.10}$$

The error will be zero when the value of Nelson-Riley function is zero. In that case, the value of lattice parameter calculated on the basis of Bragg's law will be the exact value. However, there is no data for zero value of Nelson-Riley function. It is customary to extrapolate the value of a for zero value of Nelson-Riley function. For this purpose, a is plotted against the value of Nelson-Riley function with a linear fit. The point of intersection of the fitted line with the axis corresponding to a provides the actual lattice parameter value, which is shown Fig. 6.11(b) for Type 4 treated sample; it is 2.865 Å.

Following the aforesaid procedure, the maximum dislocation density of $10.78\times10^{16}/m^2$ was observed in case of Type 4 heat treated sample while the minimum was $4.15\times10^{16}/m^2$ in Type 1 treated sample. For as-cladded samples, dislocation density was $6.08\times10^{16}/m^2$. The dislocation density is related to crystallite size. The dislocation density increases with decrease in crystallite size. However, thermal expansion also plays a major role in dislocation density of Fe-C alloys by changing the concentration of carbon content (Zhao et al. 2001). With the decrease in the temperature, differential local thermal expansion causes localized stress to rise, which multiplies dislocations (Huang at al. 2003). Since the distribution of carbon inside the microstructure is heterogeneous, it is proposed that this will cause local lattice strain and dislocation multiplication during Type 4 heat treatment. The crystallite size, lattice strain and dislocation density of the electrode (acting as filler wire) were 56.82 nm, 0.13 and $3.41\times10^{16}/m^2$, respectively. The

maximum crystallite size and minimum dislocation density observed in the filler wire owes to non-occurrence of any mechanical alteration to the property.

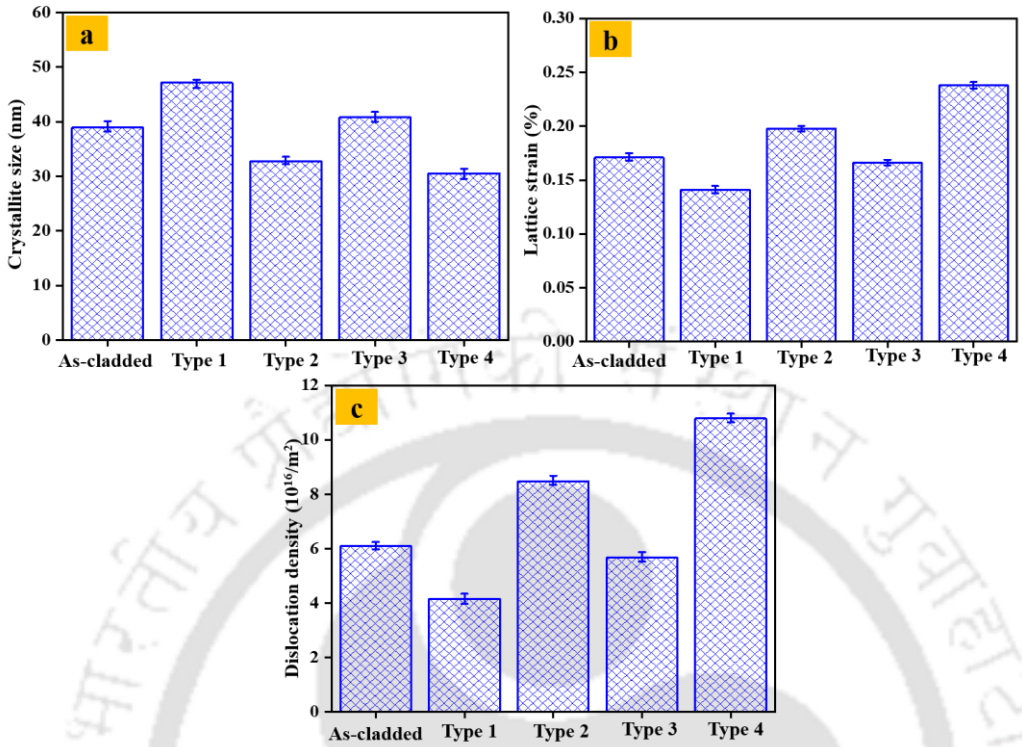

Figure 6.10 XRD analysis of cladded (and milled) layer: (a) crystallite size, (b) lattice strain and (c) dislocation density

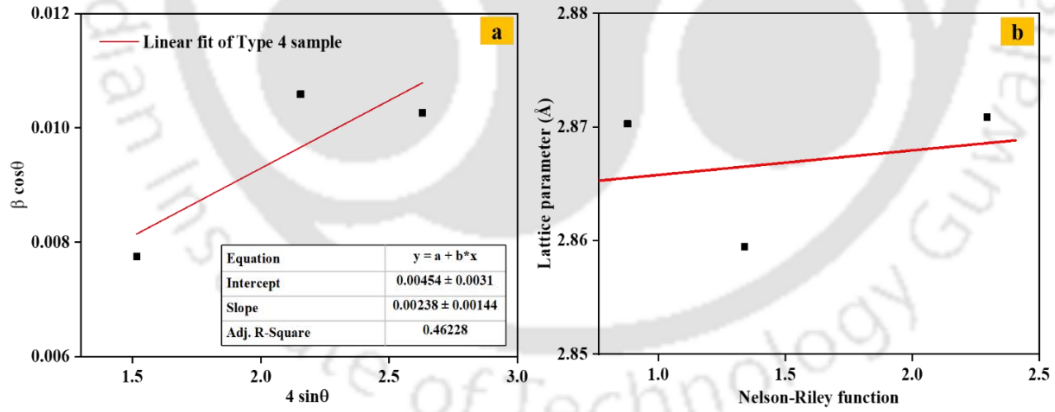

Figure 6.11 XRD analysis of Type 4 heat treated sample: (a) linear plot and (b) lattice constant from Nelson-Riley function

6.3.6 Hardness study

The Vickers microhardness value of the as-cladded sample and heat-treated sample are presented in Fig. 6.12. The variation of hardness in the Fe-based coating is due to the effects of strengthening mechanisms such as grain boundary strengthening, solid solution strengthening, precipitation strengthening, transformation strengthening and dislocation strengthening. Optical micrographs in Fig. 6.6 reveal that type of heat

treatment affects grain size. In general, the heat treatment involving high temperature results in grain coarsening. Type 4 heat treatment dealing with cryogenic temperatures results in refined grains. Grain size appears to be the most influencing factor on hardness. The highest value of hardness is 407 HV for Type 4 heat treated cladding layer with 20 μm grain size while the lowest value of hardness is 181 HV for Type 1 heat treated cladding layer with 30 μm grain size. The high density of grain boundaries in the fine-grained structure acts as a barrier to the motion of dislocations causing the rise in microhardness (Anijdan et al. 2018). The grain-boundary strengthening mechanism is captured by the Hall-Petch relation (Hall, 1955, Petch, 1955):

$$H = H_0 + \frac{k_H}{\sqrt{d}}, \tag{6.11}$$

where H_0 and k_H are material constants, H is the hardness, d is the average grain diameter. In order to assess the effectiveness of this relation, constants H_0 and k_H are obtained from the average grain size and hardness data of Type 1 and Type 4 heat treatment. These two types of heat treatment represent two extremes in terms of hardness. Hardness values in Type 2 and Type 3 heat treatment as well as in as-cladded case lie between the values obtained from Type 1 and Type 4. Any data-fitting technique predicts well in interpolation, but produces large error in extrapolation. Hence, the values of d and H were substituted in Eq. (12) to get two simultaneous linear equations based on the average values from Type 1 and Type 4 heat treatment. Accordingly, H_0=−783 MPa and k_H=5290. With these values, the calculated (interpolated) hardness values are 240 HV, 304 HV and 203 HV for as-cladded, Type 2 and Type 3 specimens, respectively. Corresponding measured hardness values are 237 HV, 331 HV and 204 HV, which show very good agreement with the calculated values. However, negative value of H_0 is untenable from the physics point of view because it represents the hardness of a highly coarse-grained material and should be a non-negative value. Despite this logical inconvenience, Hall-Petch relation is providing good estimate of hardness.

According to FESEM morphology (Fig. 6.4), the difference in microhardness value due to heat treatment is also caused by transformation strengthening. The maximum hardness value for Type 4 and Type 2 treated cladding layer owes to the strong and hard martensite structure compared to other types of specimens. Das, (2007) stated that cryogenic heat treatment increases the dislocation and twin boundary in the specimen and C atoms precipitates from the martensite matrix to produce fine carbides with other

alloying elements. However, due to presence of soft retained austenite and carbide at a few places and lower proportion of martensite transformation in the Type 2 treated cladding layer, the hardness value is low as compared to Type 4 treated cladding layer. The hardness value of Type 1 and Type 3 heat treated cladding layer is lower than that of the as-cladded layer due to ferritic transformation.

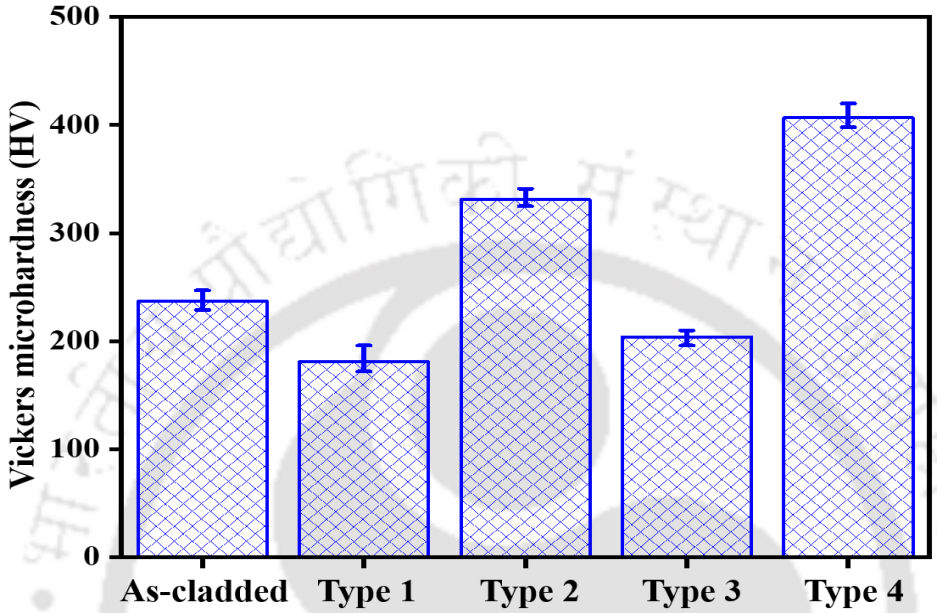

Figure 6.12 Variation of microhardness at the top surface of cladded (and milled) layer due to heat treatment

6.3.7 Effect on friction

The dry-sliding test was carried out against hardened steel at room temperature. The variation of coefficient of friction (CoF) of the heat-treated samples is shown in Fig. 6.13. The average CoF in the as-cladded layer was 0.23 under similar test condition (Chapter 4). The average CoF value increased to 0.26 in the Type 1 heat-treated sample and reduced to 0.20 in the Type 4 heat-treated sample. The high CoF in Type 1 heat treated samples is due to its low hardness. Furthermore, the contact surface becomes softer as a result of frictional heat developed between the Type 1 heat treated sample and hardened steel during the dry sliding wear. As a result, at the contact surface the debris forms, which increases the CoF value due to plowing and abrasion (Denape and Lamon, 1990). The development of coarse carbide also aids in increasing CoF for Type 1 and Type 3 heat treated sample. During Type 4 heat treatment the development of carbide is slow and uniformly distributed hard martensitic structure is formed (Fig. 6.4) leading to reduction in debris and consequently friction. Moreover, a harder surface encounters less

frictional resistance as it provides less adhesive contact area for a given load (Sun et al. 2008).

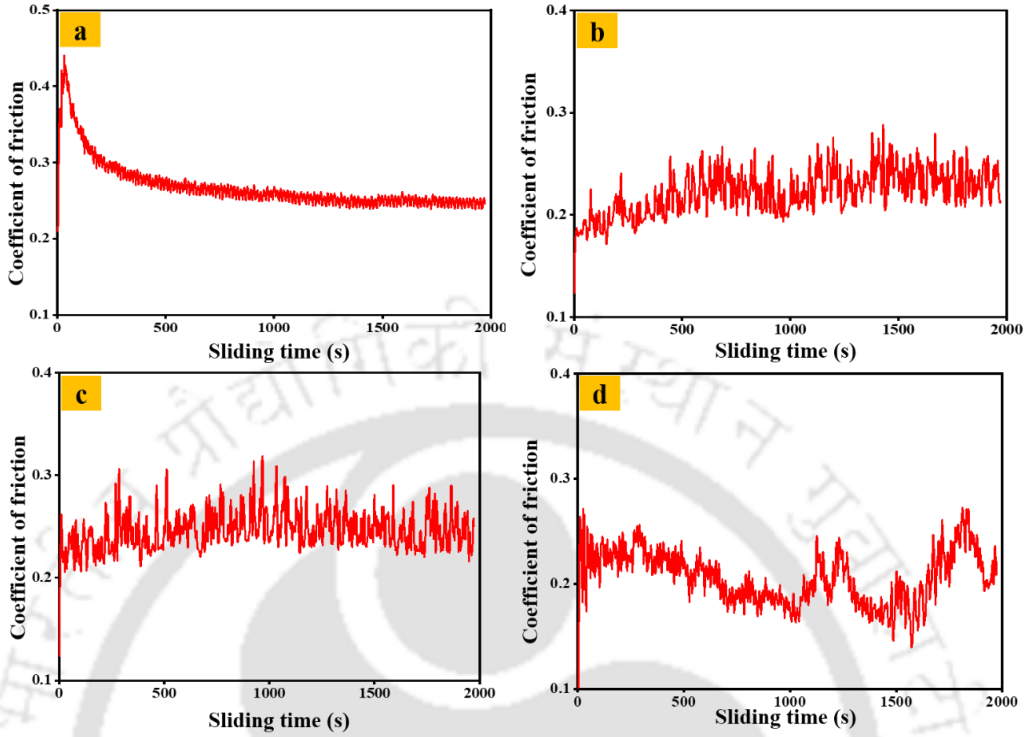

Figure 6.13 Coefficient of friction versus sliding time of the cladded (and milled) layer along the cladding direction after different heat treatment procedures: (a) Type 1 (b) Type 2, (c) Type 3 and (d) Type 4

The 3D AFM morphology of the worn surface is shown in Fig. 6.14. The wear tracks, debris, grooves and the pits are visible in the morphology. The sudden hike in the peak is due to wear debris and valleys are due to groove, pits and tracks. The morphology suggests that significant plastic deformation had occurred during wear. The Type 4 heat treated sample surface had smallest hike in peak-to-valley distance compared to all samples. The minimum average surface roughness (R_a) value of 76 nm was observed in Type 4 heat treated sample surface and the average maximum R_a was 126 nm in Type 1 heat treated sample surface compared to as-cladded sample surface, which was 94 nm. The greater increase in R_a value is related to the CoF. The smooth surface due to enhanced hardness and low plastic deformation in the Type 2 and Type 4 heat treated sample results in low R_a value. The surface roughness was measured in the scan surface area of 900 $(\mu m)^2$.

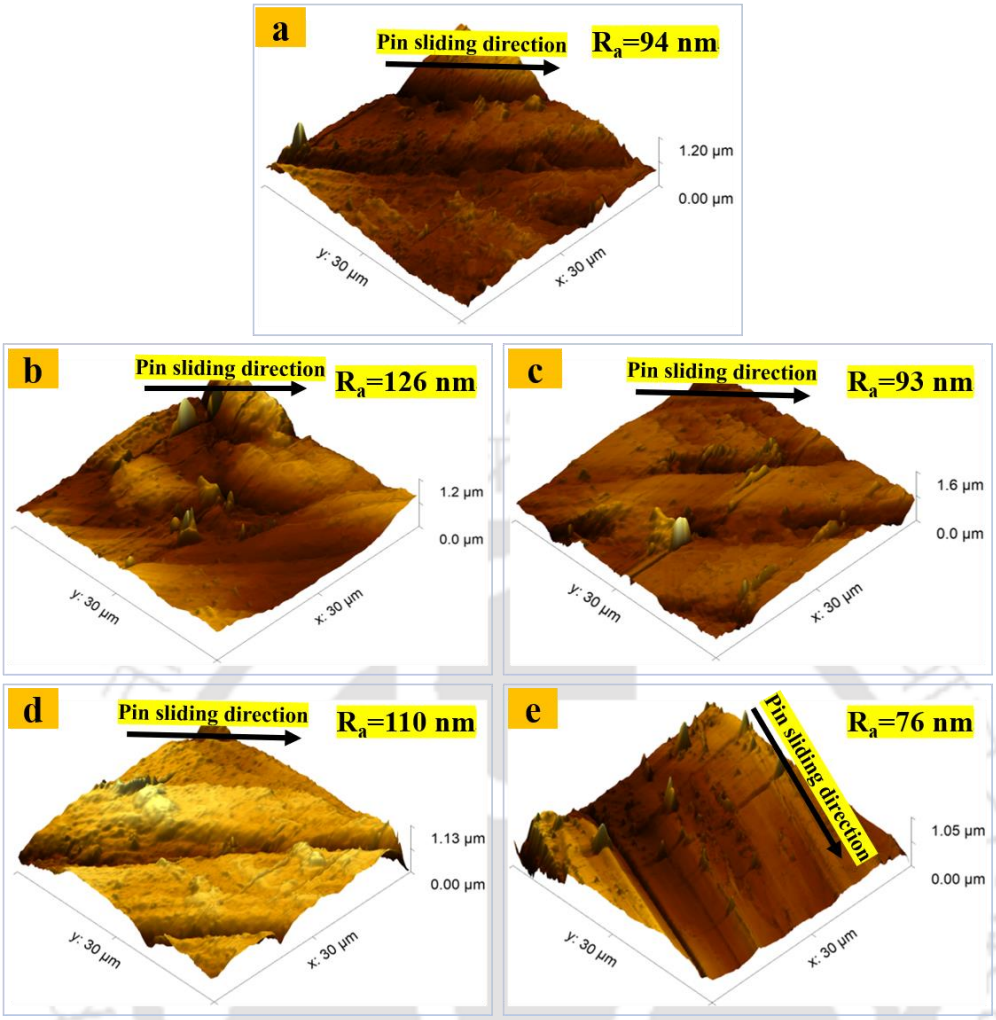

Figure 6.14 AFM 3D micrograph of worn-out surface: (a) as-cladded, (b) Type 1, (C) Type 2, (d) Type 3 and (e) Type 4

6.3.8 Wear study

The wear mass loss of the as-cladded sample and heat-treated sample is depicted in Fig. 6.15. The lower wear mass loss in the case of Type 2 and Type 4 heat treated sample is due to their enhanced hardness. The higher mass loss of Type 1 and Type 3 heat treated samples attributes to the softness of the surface, which caused significant plastic flow during sliding against steel surface. Increased mass loss is a result of increased pin (cladded layer) and disc (Hardened steel) contact area. The Type 4 heat treated samples surface comprises homogeneous and fine distribution of hard martensite and carbide, respectively. The hard debris in the worn surface behaves as an asperity and reduce the true contact between the sample surface and counter body. The reduced grain boundary and hard asperity acted as a strong barrier in material removal during dry-sliding. An oxide layer formed as a result of the micro thermal action during sliding

contact between the pin and disc. This oxide layer acted as a barrier, preventing true metal-to-metal contact.

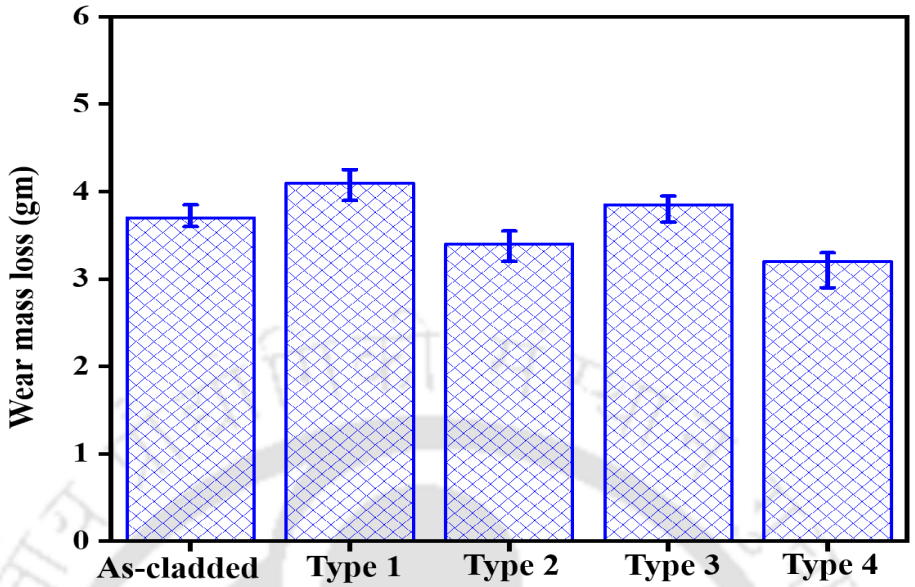

Figure 6.15 Wear mass loss of cladded layer due to heat treatment

The mean wear depth values of as-cladded and different heat-treated samples are given in Table 6.1. The strengthening mechanisms and grain refinement effects due to heat treatment of cladded layer are responsible for reducing the wear depth and wear volume. The XRD analysis indicated that additional dislocations were developed during Type 2 and Type 4 heat treatment. Dislocation mobility gets restricted with increasing dislocation density, thus increasing the hardness. In both adhesive and abrasive wear modes, the hardness is inversely correlated to the wear volume, which is also observed in Table 6.1. Table 6.1 shows that the harder is the material, the lesser is the wear volume. The Archard equation for wear (Archard, 1953) is given as

$$V = K\frac{F_n s}{H}, \tag{6.12}$$

where V represents the wear volume, s is the sliding distance, F_n is the applied load, H is the hardness and K is a coefficient. In this case, Archard's law is qualitatively satisfied; although V reduces as hardness increases, the product of VH is not constant for fixed F_n and s. The Lancaster wear coefficient, a measure of severity of the wear, as per equation 4.1 (Lancaster, 1967). The lesser the value of the k, the greater is the wear resistance. Table 6.1 shows that k is greater for softer material. The Lancaster wear coefficient of as-cladded samples was 1.01×10^{-5} mm^3/Nm, measured under similar test conditions (Chapter 4).

Table 6.1 Wear data of different heat-treated sample

Sample	Hardness (HV)	Mean wear depth (μm)	Wear volume (mm^3) $\times 10^{-3}$	Lancaster wear coefficient (mm^3/Nm) $\times 10^{-5}$
Type 1	181^{+9}_{-8}	51^{+3}_{-4}	$0.50^{+0.04}_{-0.03}$	$1.08^{+0.07}_{-0.09}$
Type 2	331^{+6}_{-4}	34^{+3}_{-2}	$0.43^{+0.02}_{-0.01}$	$0.93^{+0.05}_{-0.03}$
Type 3	204^{+5}_{-3}	42^{+2}_{-1}	$0.49^{+0.03}_{-0.02}$	$1.06^{+0.04}_{-0.02}$
Type 4	407^{+6}_{-7}	29^{+2}_{-3}	$0.40^{+0.02}_{-0.03}$	$0.86^{+0.05}_{-0.07}$

The worn surfaces identified by FESEM are shown in Fig. 6.16. The morphology is different for different types of heat treatment. Type 1 provides softer surface. Here the wear comprises plowing, spalling and deep grooves. Type 2 (water-quenching) has presence of some cracks. Type 3 morphology is similar to that of Type 1. However, here some delamination is observed. Type 4 offers the highest wear resistance, showing the absence of deep grooves. The line EDS analysis results at the worn surface of Type 4 heat treated sample is shown in Fig. 6.17. The hike in oxygen are marked by arrow in the micrograph. A significant amount of oxidation had occurred during the wear. The Fe oxide could be easily scraped off on the cladded worn surface and transferred as secondary abrasive particles, enhancing abrasive wear during sliding. Furthermore, as a result of the temperature rise from friction heat during dry sliding wear, the contact surface between the cladded surface and the counterpart became relative softer. As a result, there was more debris on the friction surface, which produced more visible micro-cut. The development of worn debris from adhesive wear may encourage three body abrasive wear (Qunshuang et al. 2016).

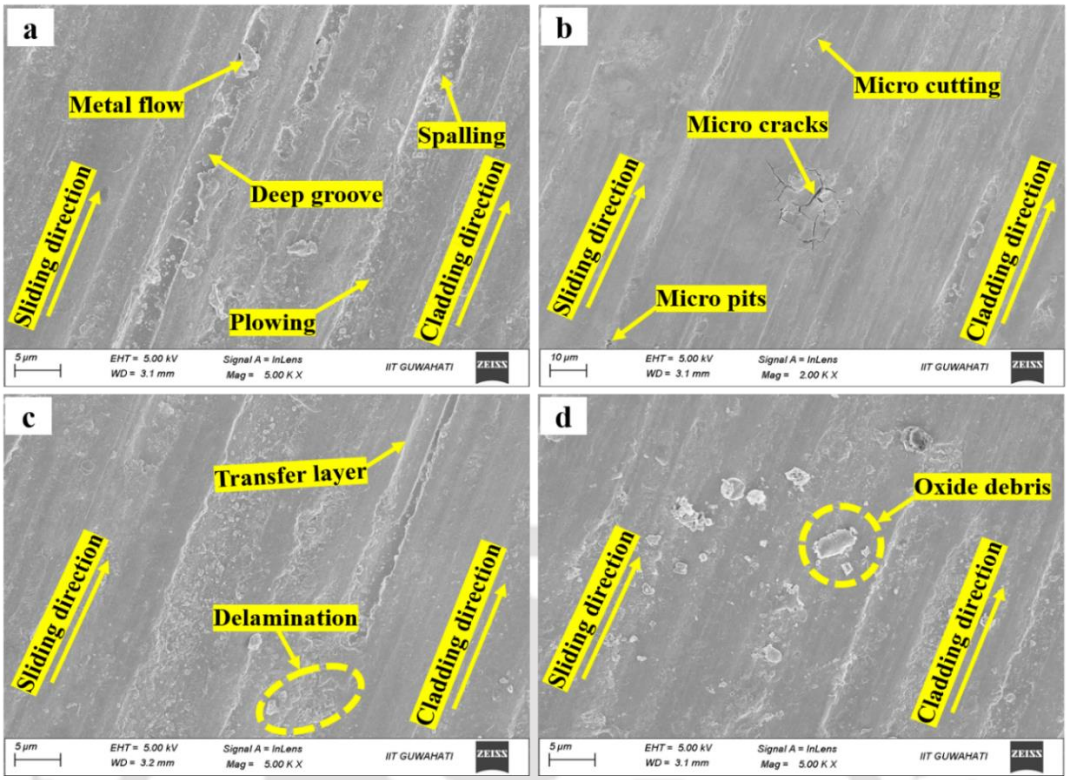

Figure 6.16 Worn out surface FESEM morphology of cladded layer: (a) Type 1 (b) Type 2, (c) Type 3 and (d) Type 4

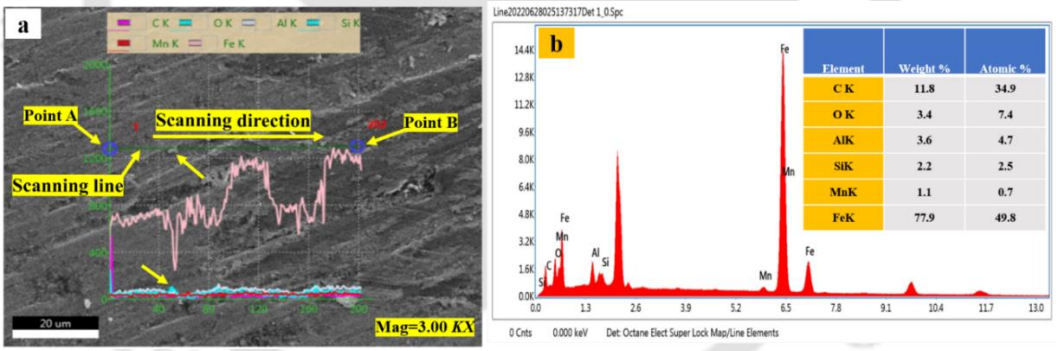

Figure 6.17 Line EDS analysis at the worn-out top surface of Type 4 heat treated sample: (a) elemental distribution graphs along the scanning line from point A to B and (b) corresponding elemental distribution

6.3.9 Wear debris analysis

The wear debris morphologies of different heat-treated samples are shown in Fig. 6.18. The irregular shape morphology of the debris in the Type 1 heat treated samples indicates that material was removed by severe sliding and fatigue. During severe sliding, the debris was produced by high adhesive forces and had parallel scratches or grooves on the surface (as seen in the enlarged Fig. 6.18(b)). This is mainly because of low surface hardness of Type 1 heat treated samples. The regular shape morphology of the debris in

the Type 2 heat treated samples indicates that material was removed by rubbing and mild adhesion. The debris is smaller in size having smooth surface and edges (Fig. 6.18(c, d)). The elongated and curl shape morphology of the debris in Type 3 heat treated samples indicates that material was removed by cutting and plowing action. Fig. 6.18(e, f) indicates that sharp edges of debris also contributed to cutting and plowing action.

The spherical shape morphology of the debris in Type 4 heat treated samples indicates that material was removed by sliding, welding and grinding (Fig. 6.18(g, h)). The parallel fringes are also observed on the debris serrated side, indicating the development of shear band (enlarged Fig. 6.18(h)). This type of wear mechanism is due to high hardness of Type 4 samples. The analysis of debris morphology can be used for condition monitoring (Peng and Kirk, 1998).

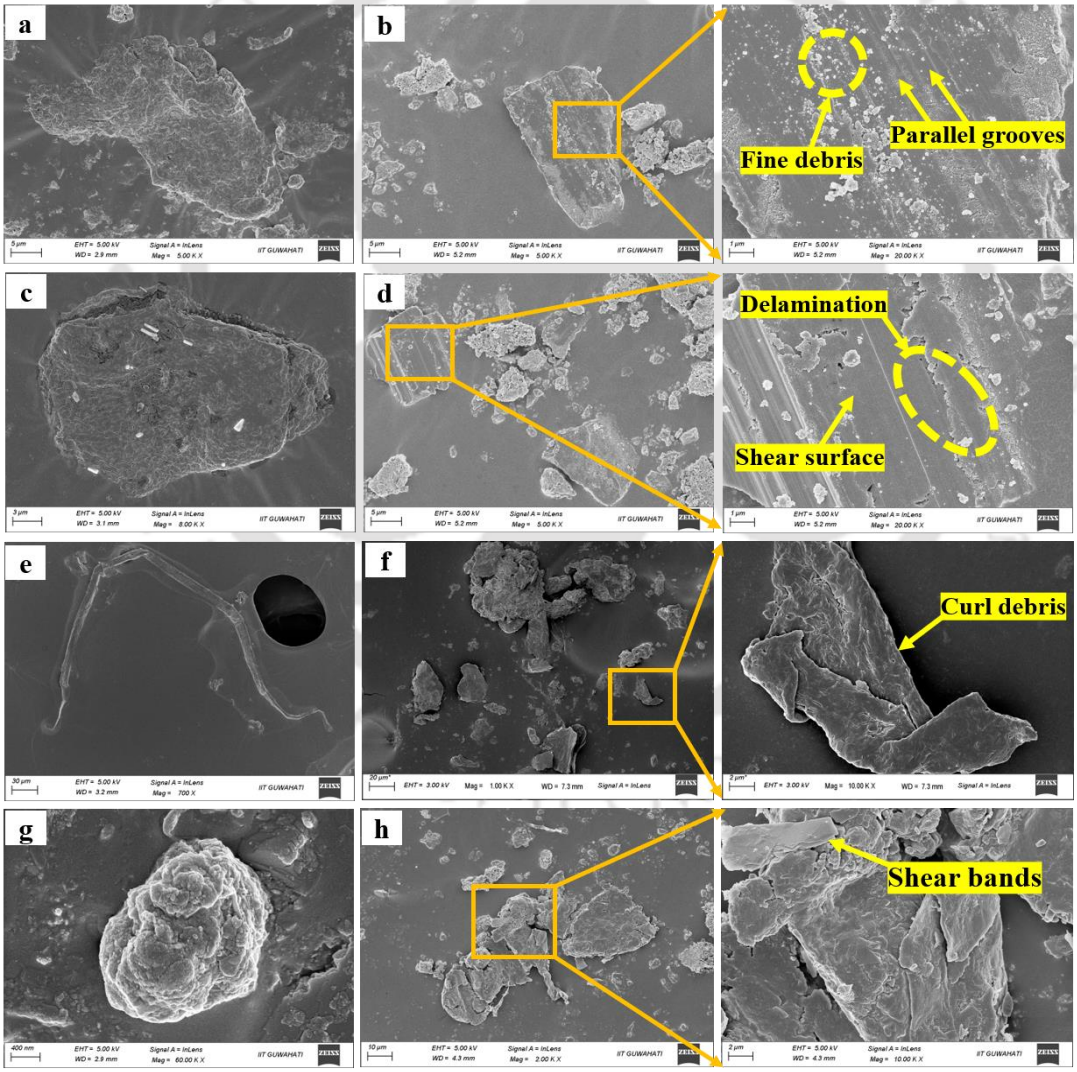

Figure 6.18 FESEM morphology of worn-out debris: (a, b) Type 1 (c, d) Type 2, (e, f) Type 3 and (g, h) Type 4

6.3.10 Tensile property and fracture behavior

The mechanical properties are shown in Table 6.2. The highest yield strength (YS) and ultimate tensile strength (UTS) of 336 MPa and 431 MPa, respectively, were observed in Type 4 heat treated sample; and the lowest YS and UTS of 232 MPa and 307 MPa, respectively, were observed in Type 1 heat treated sample. As-cladded (and milled) sample had YS and UTS as 300 MPa and 360 MPa, respectively (Chapter 4). The total elongation increased to 16% in Type 1 heat treated sample and reduced to 9% in Type 4 heat treated sample compared to as-cladded sample, which was 11% (Chapter 4). Increased strength in Type 4 and Type 2 heat treated samples is mainly due to Hall-Petch effect. Transformation of soft and ductile austenite to hard and brittle martensite during Type 2 and Type 4 heat treatment also contributed to strength enhancement. It was observed that the dislocation density was higher in case of Type 2 and Type 4 heat treated sample. This also enhanced the mechanical strength of the cladded layer. The findings of present tensile results match with the findings of Astaf'ev, (1997). According to Astaf'ev, the austenite grains in the steel microstructure can be refined to improve the material mechanical properties, including hardness, YS and UTS. The present report also explained that by refining austenite grain size, the YS is also enhanced. It can be justified based on Hall-Petch equation (Hall, 1955, Petch, 1955):

$$\sigma_{\mathrm{y}} = \sigma_i + \frac{k_{\mathrm{y}}}{\sqrt{d}} \tag{6.13}$$

where k_{y} is material constants, σ_{i} is the lattice friction stress, σ_{y} is the yield stress and d is the average grain diameter. In order to assess the effectiveness of this relation, constants σ_{i} and k_{y} are obtained from the average grain size and YS data of Type 1 and Type 4 heat treatment. Fitting the equation in this matter makes prediction for other cases in interpolation rather than in extrapolation. Hence, substituting the values of d and σ_{y} in Eq. (6.13), two simultaneous equations provided, σ_{i} =–218 MPa and k_{y} =2476. With these values, the calculated YS values are 260 MPa, 290 MPa and 243 MPa for as-cladded, Type 2 and Type 3 specimens, respectively. Corresponding measured YS values are 300 MPa, 305 MPa and 251 MPa, which show very good agreement with the calculated values, the maximum deviation being 13.33%. However, it is difficult to justify the negative value of lattice friction stress.

Table 6.2 Yield strength, ultimate tensile strength and elongation of various samples

Sample	Yield strength (MPa)	Ultimate tensile strength (MPa)	Elongation (%)
Type 1	232^{+6}_{-7}	307^{+9}_{-7}	16^{+1}_{-2}
Type 2	305^{+6}_{-5}	370^{+7}_{-6}	10^{+2}_{-1}
Type 3	251^{+5}_{-3}	329^{+7}_{-5}	13^{+2}_{-1}
Type 4	336^{+5}_{-6}	431^{+6}_{-7}	9^{+1}_{-2}

Fig. 6.19 shows the fracture morphology of different heat-treated sample. Fig. 6.19(a–d) shows the fracture surface of cladded portion. Fig. 6.19(e) shows the fracture surface of the substrate portion. The fracture morphology depicts the presence of both brittle and ductile behavior. The ductile section with dimple features and the brittle portion with characteristics of river patterns and rocky surface are visible at the fracture surface. The failure morphology of the Type 1 and Type 3 heat treated sample comprises mostly mixed ductile-brittle characteristics due to the presence of coarse carbide in the grain boundary and low martensitic phase. The Type 1 and Type 3 heat treatment lead to enhancement of ductility and austenitic phase.

From the fractography of Type 1 and Type 3, it can be seen that the morphology consists of large and deep dimples (~10 μm in diameter) on the major parts, which are typically caused by inclusions and undissolved precipitate phase. Only at small regions between the large dimples, small (<1 μm in diameter) or secondary dimples are observed. Secondary dimples are formed at the intersection of two major dimples. The presence of dimples in the Type 1 and Type 3 indicates gradual degradation of mechanical strength. Comparing Type 1 and Type 3, the Type 1 heat treated sample had large distribution of deep dimples that caused low mechanical strength.

The fractography of Type 2 and Type 4 heat treated sample comprises mostly brittle features as shown in Fig. 6.19(b, d), respectively. From the microstructure morphology in Fig. 6.4, it is observed that Type 2 and Type 4 heat treatment resulted in a great increase of brittle martensitic phase in the microstructure. This resulted in the reduction of plasticity in the austenite phase and enhancement of the brittle fracture.

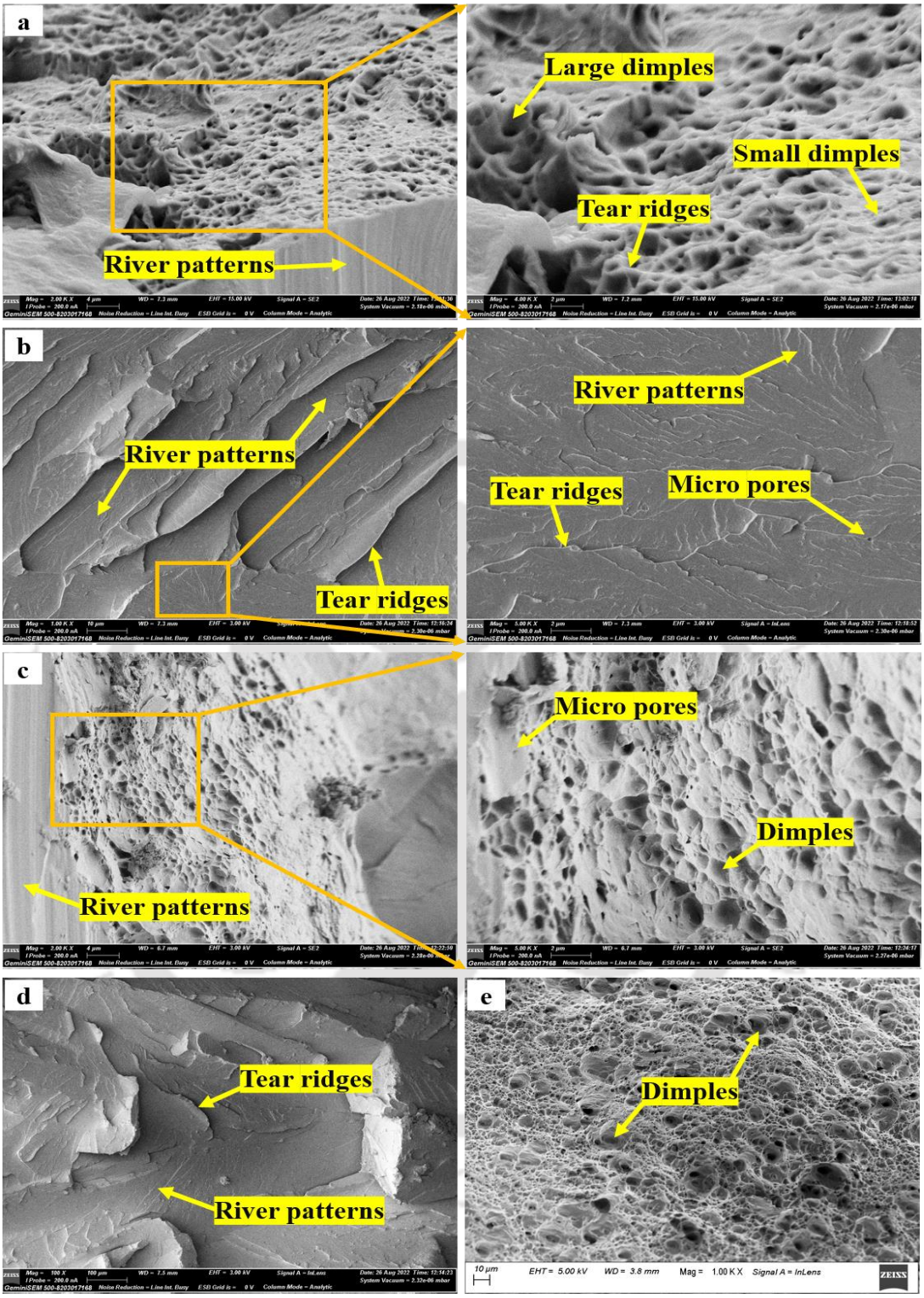

Figure 6.19 Fracture FESEM morphology of cladded layer region: (a) Type 1, (b) Type 2, (c) Type 3, (d) Type 4 and (e) substrate region of Type 4

6.3.11 Comparison of four heat treatment methods

Four different type of heat treatment methods, i.e., Type 1: furnace cooling, Type 2: water quenching, Type 3: artificial age hardening and Type 4: deep cryo-treatment, are compared in Table 6.3. It is clear that Type 4 heat treatment could make the maximum enhancement in the mechanical properties thanks to grain refinement and diffusion-less transformation to martensite. However, it causes some reduction in ductility. Next best treatment for the enhancement of mechanical properties is Type 2 heat treatment. Type 1 heat treatment also enhances the ductility but defeats the very purpose of cladding by weakening the tribological properties.

Table 6.3 Properties of different samples

Properties	As-cladded	Heat treated			
		Type-1	Type-2	Type-3	Type-4
Porosity (%)	2.56	1.35	1.51	1.72	2.08
Martensite phase (%)	32	20	43	26	56
Grain size (μm)	27	30	24	29	20
Roughness value (nm)	46	75	41	53	25
Crystallite size (nm)	38.94	47.16	32.77	40.77	30.53
Dislocation density ($10^{16}/m^2$)	6.08	4.15	8.47	5.67	10.78
Hardness (HV)	237	181	331	204	407
Coefficient of friction	0.23	0.26	0.22	0.24	0.20
Lancaster wear coefficient (mm^3/Nm)	1.01	1.08	0.93	1.06	0.86
Yield strength (MPa)	300	232	305	251	336
UTS (MPa)	360	307	370	329	431
Percentage elongation	11	16	10	13	9
Fracture behavior	Mostly brittle	Both ductile and brittle	Mostly brittle	Both ductile and brittle	Mostly brittle

6.4 Conclusions

In this chapter, various types of heat treatments were carried out on steel cladded aluminum alloy samples. Cladding was carried out with CMT technology. Four different types of heat treatment were carried out. Microstructural, tribological and mechanical characteristics were examined. The following are the salient observations:

- The porosity in the cladded samples decreased to approximately 0.48–1.21% after heat treatment process. The type of heat treatment and temperature significantly affects in the grain size. The average grain size increased to 30 μm after Type 1 heat treatment, compared to 27 μm in the as-cladded layer. However, during Type 4 heat treatement the average grain size reduced to 20 μm. Grain size is positively correlated with the yield and tensile strength.
- The minimum surface roughness was obtained in Type 4 heat treated sample (cryogenic treatment) due to the grain refinement and absence of oxidation. The martensite transformation was also observed to be high during Type 4 heat treatment with fine and homogeneous carbide precipitates at the grain.
- The maximum dislocation density of $10.78\times10^{16}/m^2$ was observed in case of Type 4 heat treatment, while the minimum was of $4.15\times10^{16}/m^2$ in the Type 1 heat treatment compared to $6.08\times10^{16}/m^2$ in the as-cladded layer.
- In terms of mechanical properties also, Type 4 heat treatment stands the best. The grain refinement, dense martensitic phase and enhanced dislocation density has resulted in enhanced hardness of 407 HV. Lancaster wear coefficient of 0.86×10^{-5} mm^3/Nm and tensile strength 336 MPa was observed in Type 4 heat treatment.

Thus, overall cryogenic treatment (Type 4) of steel cladded parts produced through CMT technology enhanced the properties of the cladded layer in a significant manner. The second-best heat treatment was water quenching (Type 2). Furnace cooling (Type 1) enhanced the ductility but had an adverse effect on the tribological properties.

Chapter 7

Effect of layer thickness in CMT cladding of ER70S-6 alloy on AA 6061-T6 aluminum alloy

7.1 Introduction

One of the important guiding principles of sustainable engineering is the minimization of the depletion of resources. By minimizing the consumption of material in a product, a designer also saves the energy in generating and operating the products. At the end of its lifecycle, a lighter product generates lesser waste than that generated by a heavier product. For optimum utilization of the material, often high strength steel and lightweight aluminum (Al) alloys are combined in a judicious way to make a composite structure. It is common to see such type of composite structures in automobiles, aircraft and ships. However, the different material properties of Al and steel make their joining a challenging task. Difference in melting temperature, heat conductivity and coefficients of thermal expansion of these materials produces residual stresses and many other defects. For joining Al to steel, a variety of welding techniques including laser beam welding, gas metal arc welding (GMAW), and friction stir welding were used, but quality of joint was poor in the most of the cases (Wang et al. 2016, Park et al. 20091). The mechanical characteristics of the finished product are impacted due to the fast oxidation of weld metal and subsequent development of a brittle intermetallic layer. To overcome the problems a few researchers used Cold Metal Transfer (CMT) welding technique to joint Al and sheet (Selvi et al. 2018, Feng et al. 2009).

Fundamentally, CMT technique operates in a short-circuit mode with low current and voltage, which generates very low heat input during the process (Lorenzin and Rutili, 2009). The metal transfer takes place with an extremely low current and the length of the arc is very small. With the support of complete computer control CMT produces a spatter-free and smoother weld bead than that produced in GMAW (Pickin et al. 2011). Selvi, (2018) outlined the working principle, tools, application and restrictions of CMT. With less heat input during the CMT process, distortion and residual stresses are also decreased in addition to the superior weld bead quality.

Aluminum (Al) and its alloys possess enhanced strength and high corrosion resistance. However, they have poor wear resistance and hardness, which could decrease the lifespan of products made of Al alloys. Surface cladding and coating of steel on

aluminum can improve the lifespan of products. Weld overlay is frequently used to combine similar materials, but it is also popular for mending damaged parts.

Several studies have investigated the use of steel powders to coat the surface of Al as a means to enhance its wear resistance and hardness. Sova et al. (2013) employed a cold spray technique to deposit 316 L stainless steel powder onto the Al surface, but encountered a notable presence of porosity between the deposited layers. Villa et al. (2013) deposited 316 L stainless powder onto the Al surface, and observed a significantly improved wear resistance at the coated surface compared to base Al surface. Zhou et al. (2020) utilized high-speed particle injection to deposit 316 L stainless powder onto an Al alloy sheet at a spraying temperature of approximately 400 °C. This resulted in a coating with a enhanced hardness (HV>400) and high wear resistance at elevated temperatures. Nevertheless, the thermal spray coating methods generally yield low deposition thickness in a single pass (Laha et al. 2005) and requires multiple passes to achieve a thick coating. In contrast, weld overlay process enables high deposition thickness in a single pass (Rajeev et al. 2019). Chapter 4, 5 and 6 discusses the cladding of Fe-based ER70S-6 alloy on Al substrates. The CMT cladding of Fe based alloy on Al substrate (Chapter 4) resulted in the enhancement of mechanical properties of Al substrate. A shear bond strength of 74 MPa was measured between the cladding layer and substrate. Following a 200 h corrosion test conducted on the cladded layer and substrate, the top surface layer exhibited pitting corrosion (Chapter 5). As a result, the hardness decreased by 10%, and the wear depth in the cladding layer increased by 39.5%. Different heat treatments were employed to enhance the mechanical characteristics of the deposited cladding layer (Chapter 6). The most enhanced mechanical properties were obtained after the deep cryo-treatment, thanks to the refined grain and dense martensite structure. On the other hand, the wear resistance and hardness reduced after the annealing treatment (heating up to 600 °C, soaking up to 1 h and then furnace cooling for a day).

Cladding layer thickness is an important decision variable. In the case of repair and reworking, it is dictated by finishing requirement. In the case of additive manufacturing, it influences total build time. When the cladding is used for surface protection, the layer thickness has a bearing on the life of the component. However, there is hardly any article on the effect of CMT cladding layer thickness on the bonding and mechanical characteristics. The effects of coating thickness on the microstructure and mechanical characteristics of Al alloys (Xiong et al. 2015, Moridi et al. 2014, Greving et

al. 1994) were studied for spray coating technology. Xiong et al. (2015) observed the reduction in shear adhesive bond strength of Al 7075 and 7050 cold sprayed coatings with increasing layer thickness due to residual stress. Moridi et al. (2014) also noted that thicker cold sprayed Al 6082 coatings on the similar material substrate resulted higher pores and defects. Thick coatings are typically accompanied by poor mechanical strengths in thermal spray as well (Greving et al. 1994). There is a strong need to carry out similar study for CMT cladding.

This chapter investigates CMT cladding of Fe-based ER70S-6 alloy on Al substrates with particular focus on the effect of cladding thickness. The chapter first discusses the effects of different cladding thickness on the bead contact angle, dilution and porosity level in the cladded samples. Subsequently, the effect of cladding thickness on the hardness and wear was reported.

7.2 Experimental details

This section provides the details of the experimental procedures as well as a characterization of the materials utilized to produce the cladded layer.

7.2.1 CMT cladding with ER70S-6 alloy

AA 6061-T6 alloy was used as a substrate material (120 mm × 40 mm × 6 mm). The substrate was properly cleaned with acetone and preheated to 400 °C in an electric furnace prior to cladding process. The 1.2 mm diameter filler wire of ER70S-6 was used for cladding using a Fronius TPS400i machine. The speed and path of the cladding layers were altered using the 6-axis FANUC Arc Mate 100iD robot. The process parameters used during the cladding process were controlled with the attached remote-controlled unit of CMT machine. For studying the effect of cladding layer thickness, ~1.5, ~2.5mm and ~3.5 mm cladded layer was deposited on the substrate. The thickness of ~ 0.5 mm was milled for getting a smooth surface for characterization purpose. Finally, cladded layers of 1, 2 mm and 3 mm thicknesses were obtained. The extracted samples for metallurgical characterization are shown in Fig. 7.1 (a). The process parameters are listed in Table 7.1. The current was a variable input parameter—90 A for ~1.5 mm, 100 A for ~2.5 mm and 110 A for ~3.5 mm. The stand-off distance was 10 mm. The design of the CMT power source includes an automatic adjustment feature for other welding parameters, including wire feed rate, pulse frequency, and arc voltage. This adjustment occurs seamlessly once the current input is established. The patterns of cladding layers are depicted in Fig. 7.1 (b). Each cladded layer was deposited one at a time, and the next

layer was deposited after a break of two minutes to allow the substrate to cool below 100 °C. The length of each layer was 140 mm.

Table 7.1 The CMT process parameters during the cladding process

Sample	Current (A)	Voltage (V)	Wire feed rate (m/min)	Welding speed (mm/min)
1.5 mm	90	8	8.3	400
2.5 mm	100	10	9.2	400
3.5 mm	110	12	10	400

7.2.2 Microstructural and phase characterization

For microstructure characterization purposes the samples were sectioned through a wire cut electric discharge machine. The sectioned samples underwent polishing using SiC papers ranging from 80 to 2000 mesh grits. The cloth and diamond polishing were also conducted to remove any scratches in the surface. In order to observe the microstructure, the polished samples were etched with Nital reagent for a duration of 15 s. The optical micrographs were obtained through upright optical microscopy (Model: Axiocam MRc; Make: Carl Zeiss). The surface roughness was measured using atomic force microscope (AFM) (Model: Cypher S; Make: Oxford Instruments) in tapping mode. The AFM measurements were conducted on the surface of the cladding layers before surface milling. The surface morphology milled cladded surface was obtained through Field emission electron microscope (FESEM) (Model: Sigma 300; Make: Zeiss). Furthermore, the detailed examination of grain size, grain distribution and grain misorientation was accomplished using electron backscatter diffraction (EBSD) (Model: Quanta 3D FEG; Make: FEI). Different phases and structure were observed using transmission electron microscopy (TEM) (Model: 2100F; Make: JEOL). The X-ray diffraction (XRD) was conducted using X-ray diffractometer machine (Model: SmartLab; Make: Rigaku) with Cu-$K_{\alpha 1}$ radiation (λ=1.54056). The development of different compounds was analysed using X-ray photoelectron spectroscopy (XPS) (Model: PHI 5000 Versa Probe III; Make: Φ Ulvac-PHI, Inc.).

7.2.3 Mechanical characterization

The Vickers microhardness test was conducted with 200 gf for 20 s using hardness tester (Model: MVH-II; Make: Omni Tech). The wear analysis was performed with a pin-on-disc machine (Model: TR-201, Make: Ducom). The parameters for wear

test were 20 N load, 350 rpm, 70 mm track diameter and 30 min sliding time. The calculated sliding distance was 2309 m, and the procedures are provided in Chapter 6. The cladding materials in the form of pin traversed on hardened steel disc (84 HRC), according to ASTM standard: G99. The porosity (%) was observed in the cladding layers according to Archimedes' principle and the procedure are provided in Chapter 3.

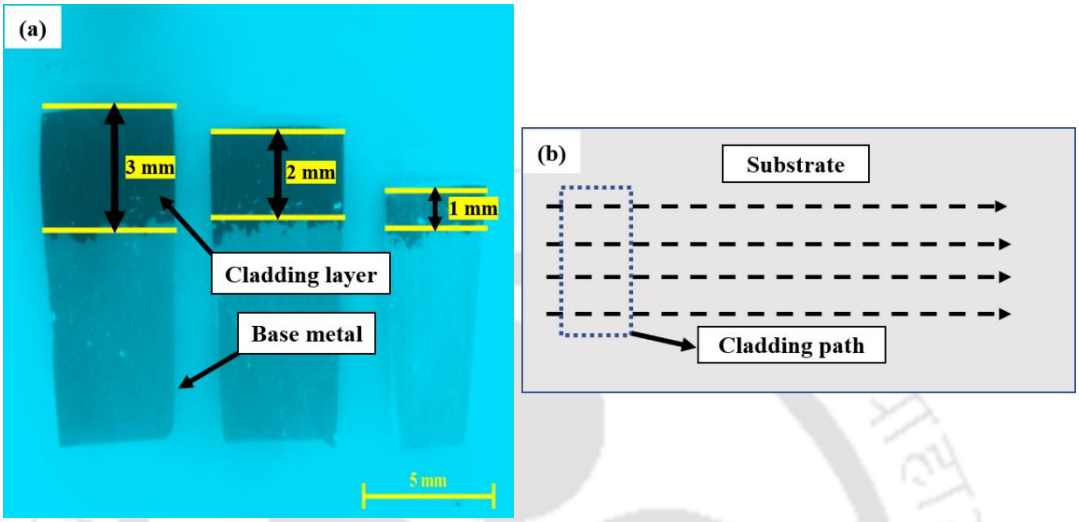

Figure 7.1 Cladding by CMT: (a) extracted samples of different layer thicknesses and (b) schematic of cladding path

7.3 Results and Discussion

This section discusses the results obtained during the experimental examination. First, the bead contact angle and dilution of the obtained cladded layer is discussed. Next, the microstructure, grain size, XRD and microhardness study are described. Finally, the results of tribological study is discussed.

7.3.1 Dilution and Bead contact angle

The dilution increases with increasing layer thickness. The dilution percentage was calculated as per equation 2.1. As the layer thickness is increased from 1 mm to 3 mm, the dilution increases from 4.01% to 6.6%. The dilution% for 2 mm thick bead was 5.04%. The calculated bead contact angles of different cladding layers are shown in Fig. 7.2 (a, b and c); the reported angles are average of angles at three locations; in each case difference between the maximum and minimum contact angle is less than 3°. The bead contact angle increases from 111° to 121°, when layer thickness increases from 1 mm to 3 mm; it was 117° for 2 mm. Thus, the contact bead angle and dilution have positive correlation with layer thickness. A few researchers also reported the similar observation. A lower bead contact angle is desirable to avoid lack of fusion when the surface is cladded by side-by-side overlapping beads (Rajeev et al. 2014, Zhou and Lin, 2014).

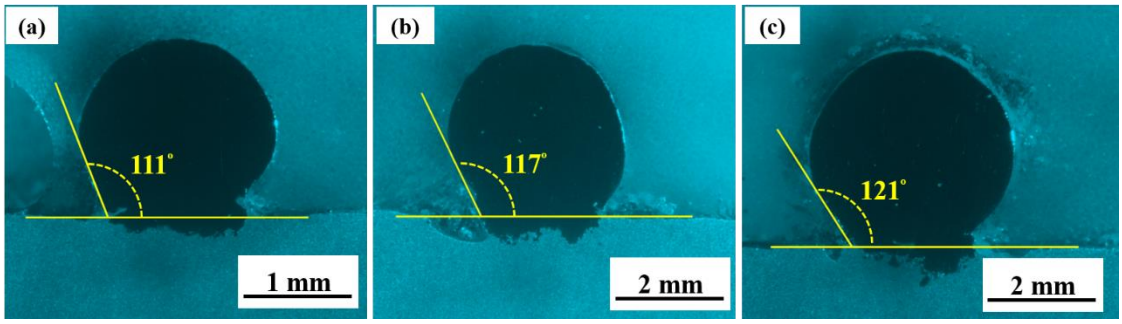

Figure 7.2 Contact angle micrograph of deposited cladding layer of different height: (a) 1-mm (20X), (b) 2-mm (10X) and (c) 3-mm (10X)

7.3.2 Cross-section and surface morphology

The micrographs of the cladding layer cross-sections are shown in Fig. 7.3 (a–f). None of the claddings display interface delamination or cracking. The microstructure depicts dilution of substrate by cladding material due to low melting temperature and density of the former. The positive aspect of it is a good metallurgical bonding between cladded layer and substrate. The maximum depth of cladding material into the substrate was 45 μm for the 3 mm thick cladding layer; the depth was 15 μm and 30 μm for 1 mm and 2 mm thick cladding layers, respectively. Thus, the depth of dilution of cladding material into substrate changed linearly with the layer thickness. The dilutions are related to heat input during the CMT process. The heat input for 1, 2 and 3 mm cladding layer was 102.6, 142.5 J/mm and 188.1 J/mm, respectively. The heat input was calculated as per equation 2.3. The elemental distributions observed through area EDS analysis across the cladded layer and substrate are shown in Fig. 7.3g. The increased wt.% of O in the distribution corresponds to oxidation during deposition of cladding layer.

Fig. 7.3 (h) shows the porosity % of three different cladding layers. The porosity was 1.75, 2.16% and 2.69% for 1, 2 mm and 3 mm cladding layers, respectively. The porosity % of CMT based ER70S-6 cladding produced in the present report were also low compared to a few studies (Bin-you et al. 2009). Bin-you et al. (2009) also reported a porosity of 2.1% for the fabrication of 1-mm Fe-based coating through spray technique.

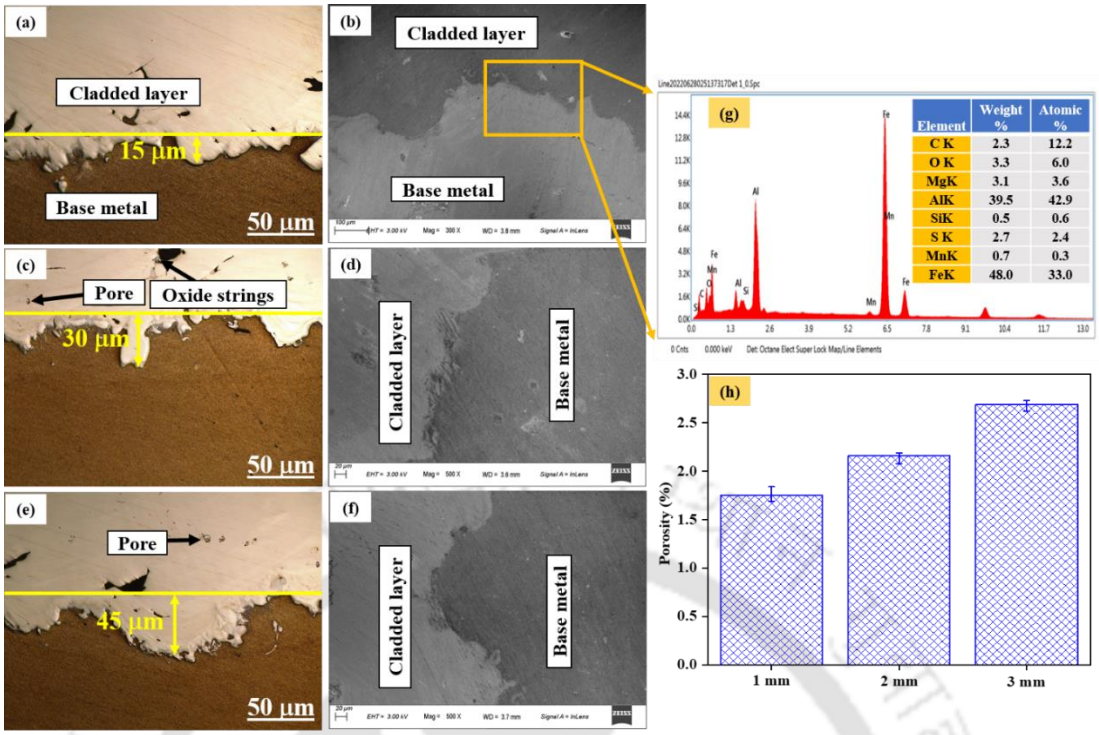

Figure 7.3 Micrographs and cross-section properties of deposited cladding layer of different thicknesses: (a, b) 1 mm, (c, d) 2 mm, (e, f) 3 mm, (g) EDS elemental distribution for 1 mm thickness and (h) porosity

The AFM 3D surface profile of different cladding layer thicknesses are shown in Fig. 7.4. The average minimum surface roughness (R_a) of 51 nm was observed in 1 mm thick layer, compared to 79 nm in the 3 mm cladding layer. The surface area affects the R_a value (Wen-Ruey et al. 2004). The scan surface area for present study was 400 $(\mu m)^2$. The increase in R_a value for 3 mm cladding layer is mainly due to the low cooling rate. Large grain size and the oxide layer's development at low cooling rates played a significant effect in raising the roughness value.

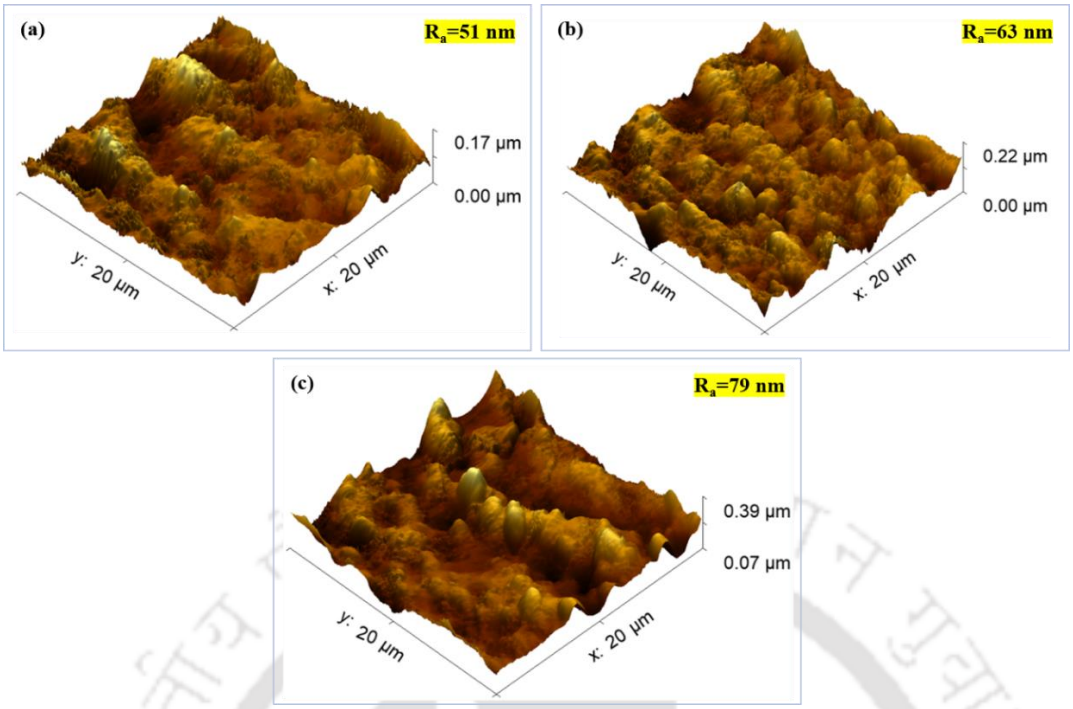

Figure 7.4 Surface roughness of deposited cladding layer of different thickness: (a) 1 mm, (b) 2 mm and (c) 3 mm

7.3.3 Microstructure study

7.3.3.1 EBSD observation

The EBSD analysis was conducted on the cross-section and top surface of different cladding layer thickness. The cross-sectional EBSD micrographs are shown in Fig. 7.5. The analysis areas (1000×1000 µm^2) of cross-sections are depicted in Fig. 7.5(a1). Figs. 5(b1, c1 and d1) show the band contrast (BC) maps of the grains near interface towards the top. In the cladding layers, the morphology of the grains changed from the bottom to the top of the layer owing to combined effect of the temperature gradient and the grain growth rate, as nicely explained by Li et al. (2021) for laser cladding process. At the beginning of CMT cladding, due to the developed arc electrode as well as substrate melted. Due to high thermal conductivity of Al alloy, the most of the heat transfer took place by conduction. The substrate served as the initial heterogeneous nucleation layer. At this point, the thermal gradient was high and grain growth rate was low; this provided high crystal nucleation speed. Therefore, nearer to the substrate in the cladding layer, some equiaxed grains were generated. After that grain growth and directional solidification promotes the formation of columnar grains. At this stage heat flows from bottom to top causing thermal gradient in vertical direction.

Figure 7.5(a2) shows the orientation along the three crystal planes of ferrite, {111}, {101}, and {001} in blue, green, and red colour, respectively. Figs. 7.5(b2, c2 and d2) show the inverse pole figure (IPF) maps of cladding layers. The different colours in IPF maps correspond to various grain orientations relative to the lattice structure. According to the colour distribution in IPF maps, the grain orientations from the bottom to top (towards the building direction) is non-uniform. There was no obvious preferred orientation and the grain orientations were randomly distributed.

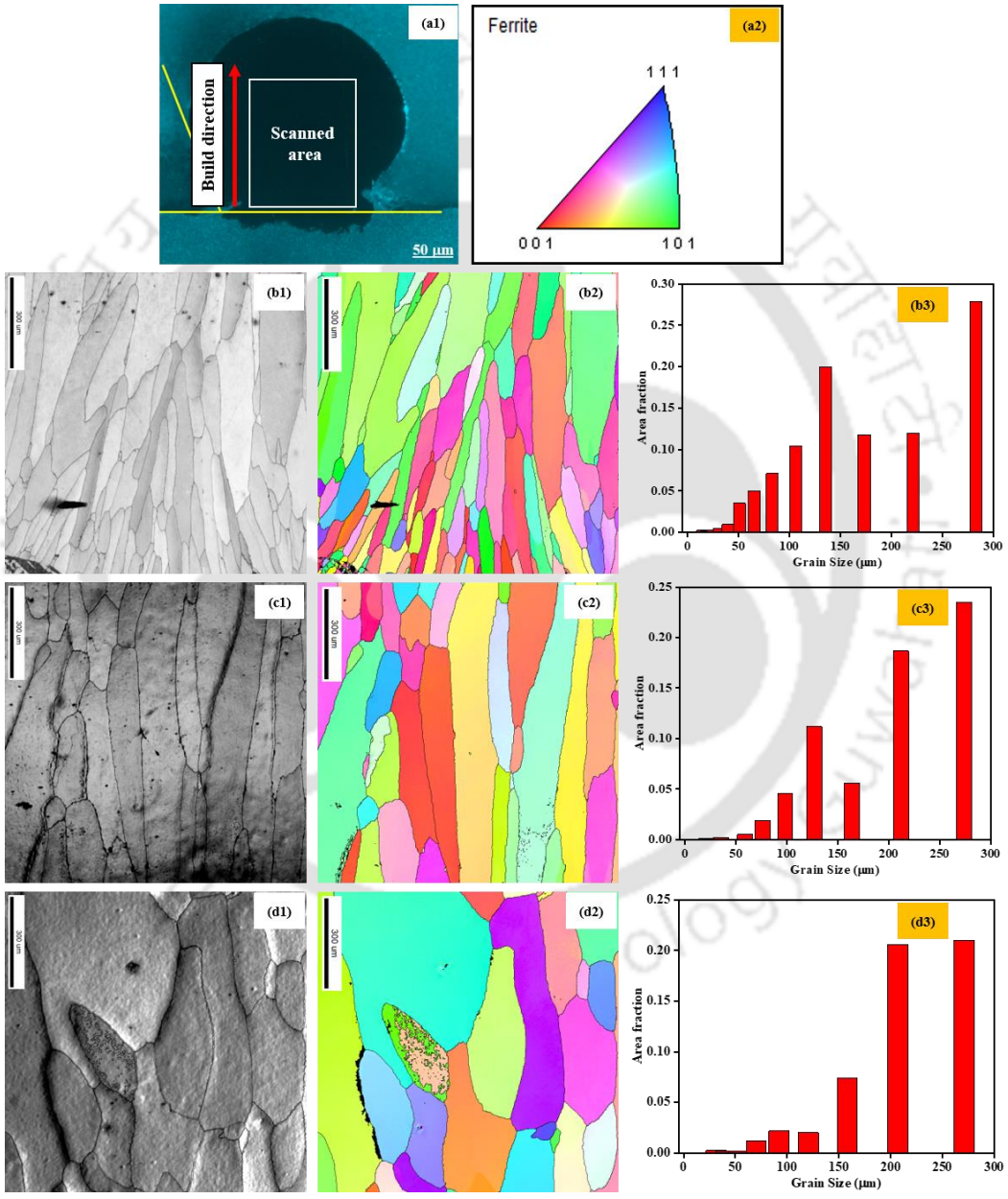

Figure 7.5 EBSD analysis of cross-section for different cladding layer thickness: (a1) sectioned evaluation surface for analysis and (a2) orientation maps; band contrast maps, IPF and grain size distribution: (b1, b2 and b3) for 1 mm thick layer, (c1, c2 and c3) for 2 mm thick layer and (d1, d2 and d3) 3 mm for thick layer, respectively

The BC and IPF maps depict that the grains in the cross-section of cladding layers were mostly coarse and grew along the structural direction. The similar observation was also reported by a few researchers (Guo et al. 2017). Peng et al. (2017), observed that the temperature gradient component perpendicular to the boundary of the molten pool was high compared to other directions. This temperature gradient discrepancy resulted in directional grain growth. Additionally, Fig. 7.5(b2, c2, and d2) illustrate the presence of columnar grains in the cladding layers, which exhibited growth along a direction perpendicular to the fusion line. This direction of grain growth coincided with the direction of the temperature gradient.

Figs. 7.5(b3, c3 and d3) show the grain size in cladding layers in the cross-sectional area. The grain size distribution of the full section was computed using EBSD post-processing software to determine the grain size. The average equivalent circle diameter of each grain served as the measure of grain size. From grain size analysis, the average minimum grain size of 65 μm was observed in the 1 mm cladding layer, compared to 78 μm and 98 μm in the 2 mm and 3 mm cladding layers, respectively.

The EBSD analysis of the top surface of the cladding layers are shown in Fig. 7.6. The BC and IPF maps of the grains of the top surface are shown in Figs. 6(a1, b1 and c1) and Figs. 7.6(a2, b2 and c2), respectively. The colour patterns of grains in different sizes are depicted in all the samples in the IPF maps in Figs. 7.6(a2, b2 and c2). Different cooling rates and solidification temperatures caused variations in the grain size and orientation in all of the cladding layers of the deposited specimens. Figs. 7.6(a3, b3 and c3) show the grain size of the top surface of cladding layer. The average smallest grain size of 40 μm was observed in 1 mm cladding layer, with more than 75 % of them below 50 μm grain size. In the 2 mm thick layer, 60% and in 3 mm layer 50% grains are less than 50 μm grain size. The average grain size of 2 mm and 3 mm cladding layer was of 69 μm and 87 μm, respectively.

Grain size of cladding metals is significantly influenced by cooling rate. In general, it is accepted that greater undercooling at higher cooling rates results in smaller grains. Higher cooling rates reduces the ferrite grain size and also aids high strength, hardness, dislocation density, and fine phases as it suppresses the atomic diffusion. On the other hand, slow cooling rates lead to transformation into soft, coarse, and less dislocated phases like polygonal ferrite, which is mostly observed in 3 mm cladding

layer. The development of different phases due to difference in cooling rates are briefly discussed in Section 7.3.3.2 and Section 7.3.3.4.

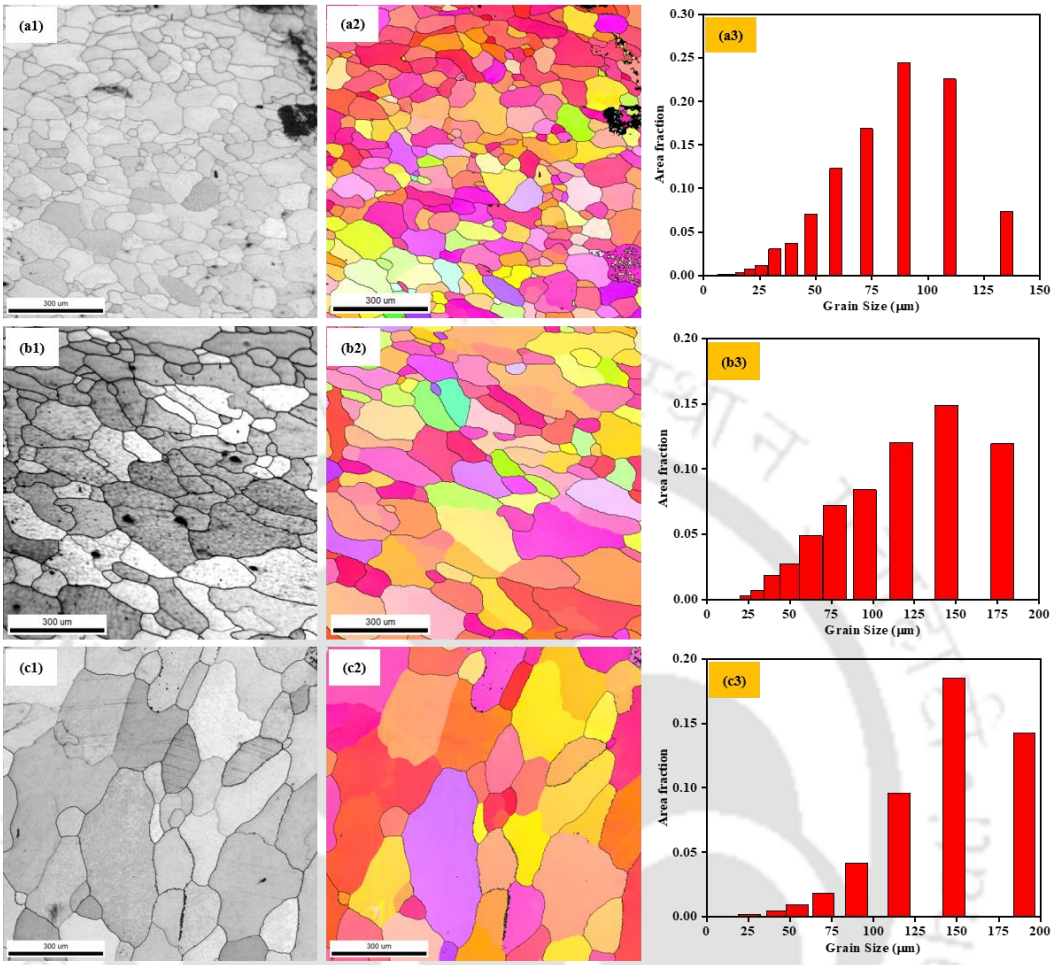

Figure 7.6 EBSD analysis of top surface for different cladding layer thickness: band contrast maps, IPF and grain size distribution: (a1, a2 and a3) 1 mm (b1, b2 and b3) 2 mm (c1, c2 and c3) 3 mm, respectively

The low-angle grain boundaries (LAGBs) and high-angle grain boundaries (HAGBs) in both cross-section and top surface of cladding layers are shown in Figs. 7.7(a1, b1 and c1) and Figs. 7.8(a1, b1 and c1), respectively. LAGBs are represented on colour maps in red and green, while HABs are represented on colour maps in blue. A misorientation angle ≥15° was used to distinguish HAGBs from LAGBs. In the cross-section of cladding layers, the proportion of LAGBs observed is 51% in 1 mm cladding layer (Fig. 7.7(a2)). The LAGBs % are of 44 and 38 on 2 mm (Fig. 7.7(b2)) and 3 mm (Fig. 7.7(c2)) cladding layer, respectively. In top surface of cladding layers, the proportion of LAGBs observed is 41% in 1 mm cladding layer (Fig. 7.8(a2)). The LAGBs % are 39 and 34 for 2 mm (Figs. 7.8(b2)) and 3 mm (Figs. 7.8(c2)) cladding layer, respectively. At the macro level, the presence of LAGBs contributed to the strengthening

of the material. The abundance of LAGBs impeded the motion of dislocations during the stretching process, leading to an increase in the overall strength of the sample. This strengthening effect is expected to be evident in subsequent mechanical performance tests.

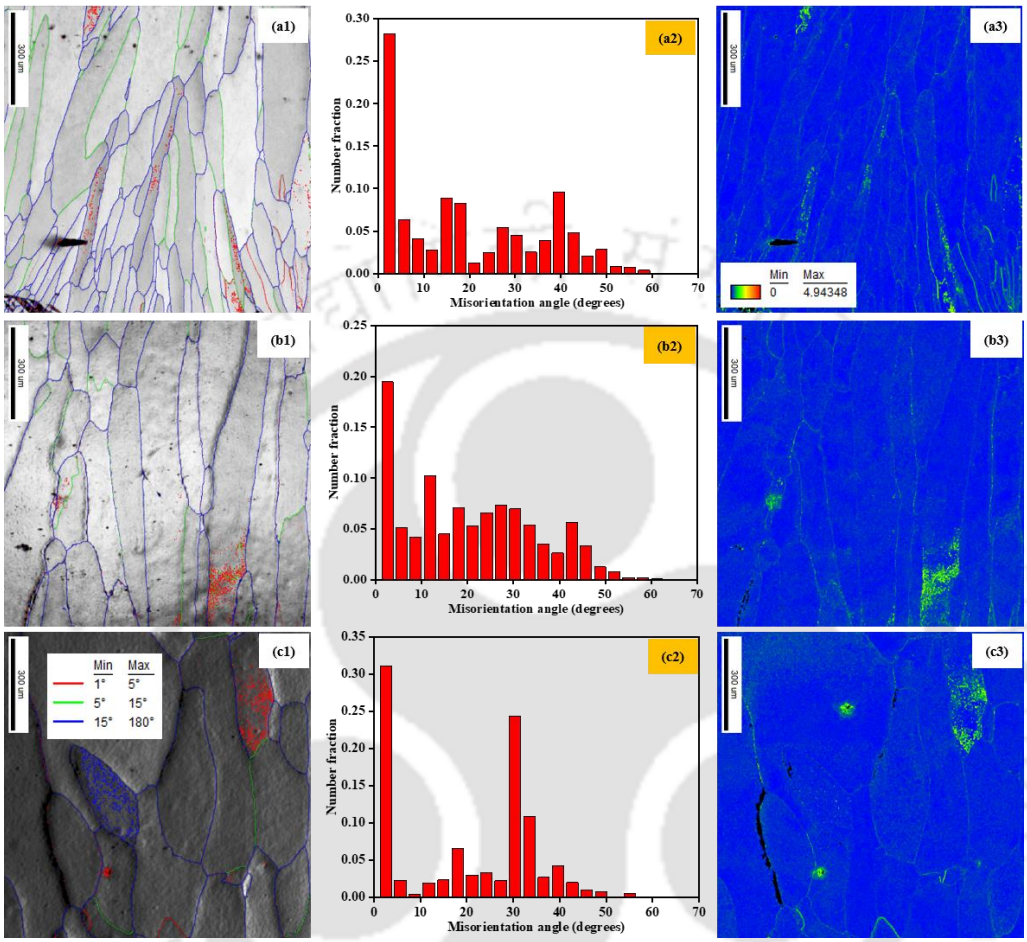

Figure 7.7 EBSD analysis of cross-section of different cladding layer thickness: grain boundary maps, misorientation angle distribution and KAM maps; (a1, a2 and a3) 1 mm (b1, b2 and b3) 2 mm (c1, c2 and c3) 3 mm, respectively

The kernel average misorientation (KAM) of cross-section and top surface of the deposited cladding layers derived from the EBSD data are shown in Figs. 7.7(a3, b3 and c3) and Figs. 7.8(a3, b3 and c3), respectively. The KAM diagrams depict the strain by calculating local grain misorientations. The green regions in Figs. 7.7(a3, b3 and c3) and Figs. 7.8(a3, b3 and c3) represents significant strain development, which are mainly distributed in the grain boundaries and sub-regions in the cladding layers. The average KAM values of all the cases were concentrated in <2°, with highest value reaching 4.9°. The average KAM value of a typically recrystallized structure is known to be <1° (Wright et al. 2011), suggesting the presence of minimal residual strains within the structure.

According to the current work, geometrically necessary dislocations (GNDs) have a positive correlation with KAM value, and their density may be calculated using the following formula (Lin et al. 2020):

$$\rho^{GND} = (\pi\theta)/(90\mu b), \tag{7.1}$$

where θ is the average local misorientation angle in degree, b=2.49 nm is the Burgers vector, μ=1 μm is the unit length (step size). The maximum dislocation density was of 1.65×10^{13} m^{-2} was observed in the top surface of 1 mm cladding layer (with θ=1.18°). The dislocation density of 1.59×10^{13} m^{-2} (θ=1.14°) and 1.55×10^{13} m^{-2} (θ=1.11°) was observed in the top surface of 2 mm and 3 mm cladding layer, respectively. The dislocation density was of 1.52×10^{13} m^{-2} (θ=1.09°), 1.50×10^{13} m^{-2} (θ=1.07°) and 1.40×10^{13} m^{-2} (θ=1.01°) was observed in the cross-section of 1, 2 mm and 3 mm, respectively.

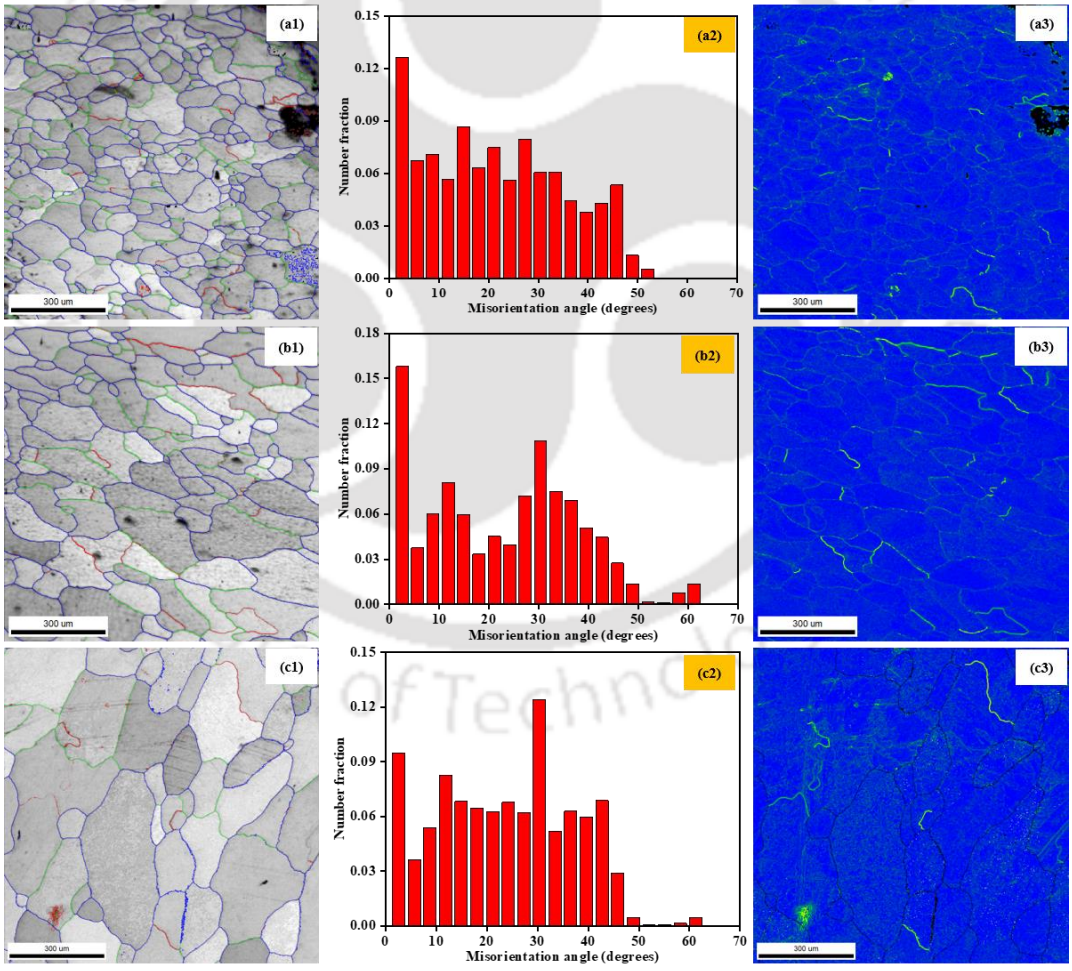

Figure 7.8 EBSD analysis of top surface for different cladding layer thickness: grain boundary maps, misorientation angle distribution and KAM maps; (a1, a2 and a3) 1 mm (b1, b2 and b3) 2 mm (c1, c2 and c3) 3 mm, respectively

Figs. 7.7(a3, b3 and c3) and Figs. 7.8(a3, b3 and c3) exhibits an inherent heterogeneity in the local misorientations throughout the structure, reflecting an uneven strains distribution. The cladding process involves rapid heating and cooling, causing localized expansion and contraction. This leads to the extrusion and collision of grains during the growth process, creating non-uniform stress and strain within the material. Thus, GNDs are generated as a mechanism to accommodate these differences and maintain continuity within the material (Huang et al. 2022). This helps to enhance the overall mechanical characteristics and structural integrity of the material, making it more resistant to failure.

7.3.3.2 FESEM observation

The schematic showing X-Y-Z-axes of the cladding layers are shown in Fig. 7.9(a). The FESEM morphology of the top surface and cross-section of different cladding layers are shown in Figs. 7.9(b1, c1 and d1) and Figs. 7.9(b2, c2 and d2), respectively. The observed morphology reveals the presence of distinct phases including ferrite, martensite, and acicular martensite. These different phases result due to rapid heating and cooling process employed in CMT cladding. The cooling of the cladding layers resembles a quenching process, leading to the formation of martensite at various locations within the structure. The extent of martensitic transformation during the cladding process was quantified using the image area method. The martensite phase at the top surface of 1 mm cladded layer was ~65%; it was ~49% and ~31% in 2 mm and 3 mm cladding layers, respectively. From the cross-sectional morphologies (Figs. 7.10(b2, c2 and d2)), the presence of acicular martensite phase is also densely distributed in the 1-mm cladding layer compared to all others. The proportion of higher % of martensite transformation in 1 mm cladding layer owns to rapid cooling and high surface area to volume ratio compared to 2 mm and 3 mm cladding layer. The microstructure also depicts the presence of intergranular chromium carbides precipitates in the cross-sectional morphology.

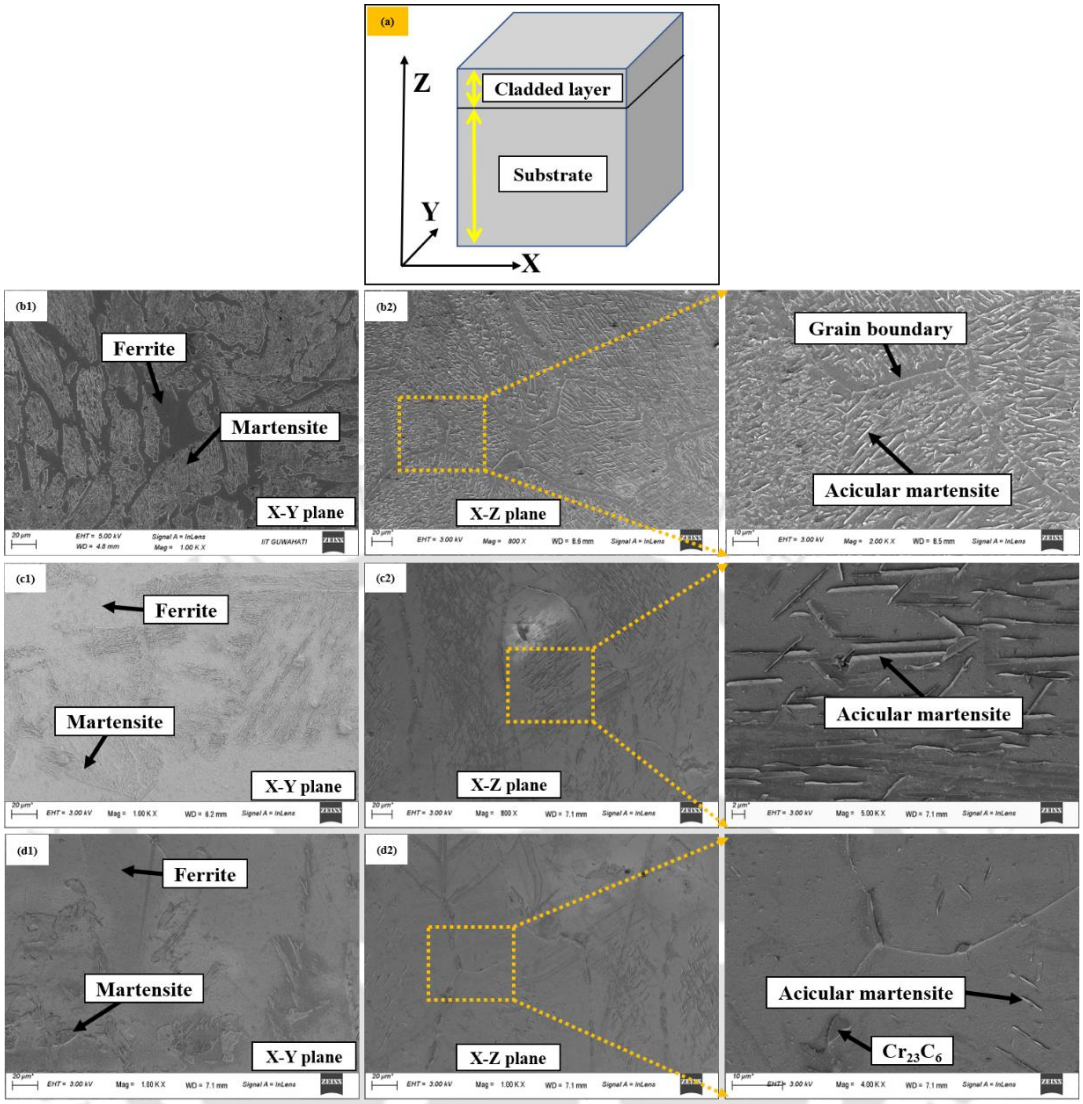

Figure 7.9 FESEM microstructure of top surface (X−Y plane) and cross-section (X−Z plane) of different cladding layer: (a) schematic of X-Y-Z-axes, (b1, b2) 1 mm, (c1, c2) 2 mm and (d1, d2) 3 mm

The EDS analysis of different cladding layers are shown in Fig. 7.10. The analysis depicts uneven distribution of present elements in the deposited cladding layers. The elemental mapping depicts clear segregation of elements corresponding to various phases in the micrographs. Fig. 7.10(b) illustrates the presence of secondary $Cr_{23}C_6$ and Cr_6C carbide networks in certain regions. The wt.% concentration of Cr was also observed to higher from the point EDS elemental distribution. In the elemental mapping, elevated levels of C and Cr in the concentrated Fe regions provide a clear indication of the existence of $Cr_{23}C_6$ and Cr_6C carbides particles. This finding aligns with the observations reported by Mohammadnezhad et al. (2018).

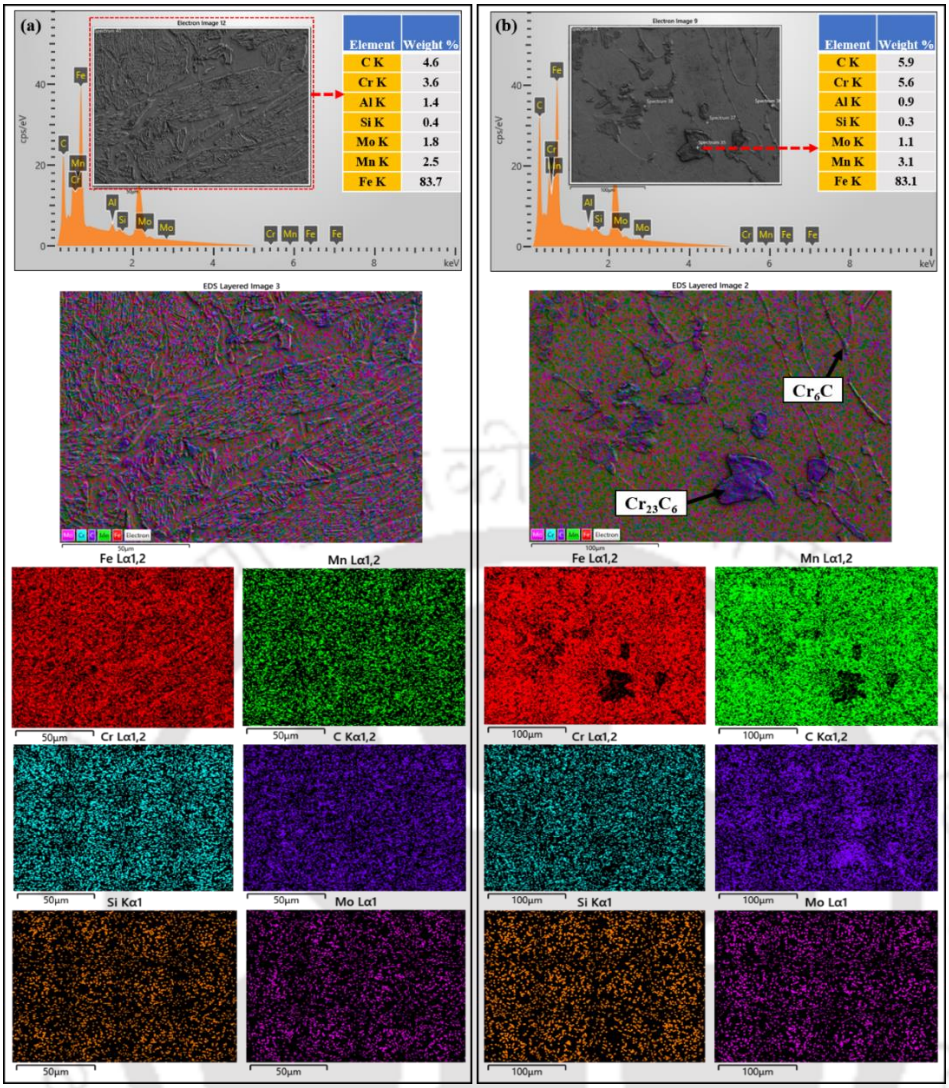

Figure 7.10 EDS analysis of different region: (a) top surface for 1 mm thick layer and (b) cross-section for 3 mm thick layer

7.3.3.3 Interface study and volumetric dilution rate

The elemental distribution of cladded samples along the cross-section plane near the interface region of different layers are shown in Fig. 7.11. Fig. 7.11(a1, b1 and c1) shows the EDS elemental mapping results across the interface region. EDS elemental mapping, especially the distribution of the Fe and Al, for the cladding joint (Fig. 7.11(a1, b1 and c1)) suggests that the diffusion was mostly directed into the aluminum. This is reasonable since the diffusion coefficient of Fe into Al is more than that of Al into Fe at higher temperature (Li et al. 2020). As a result, the intermetallic compounds (IMCs) layer was formed mainly on the aluminum side. The distribution of Cr across the interface in the EDS elemental maps also supports that diffusion occurred during cladding process. As a result of diffusion, effective joining occurred at the interface under the plastic deformation.

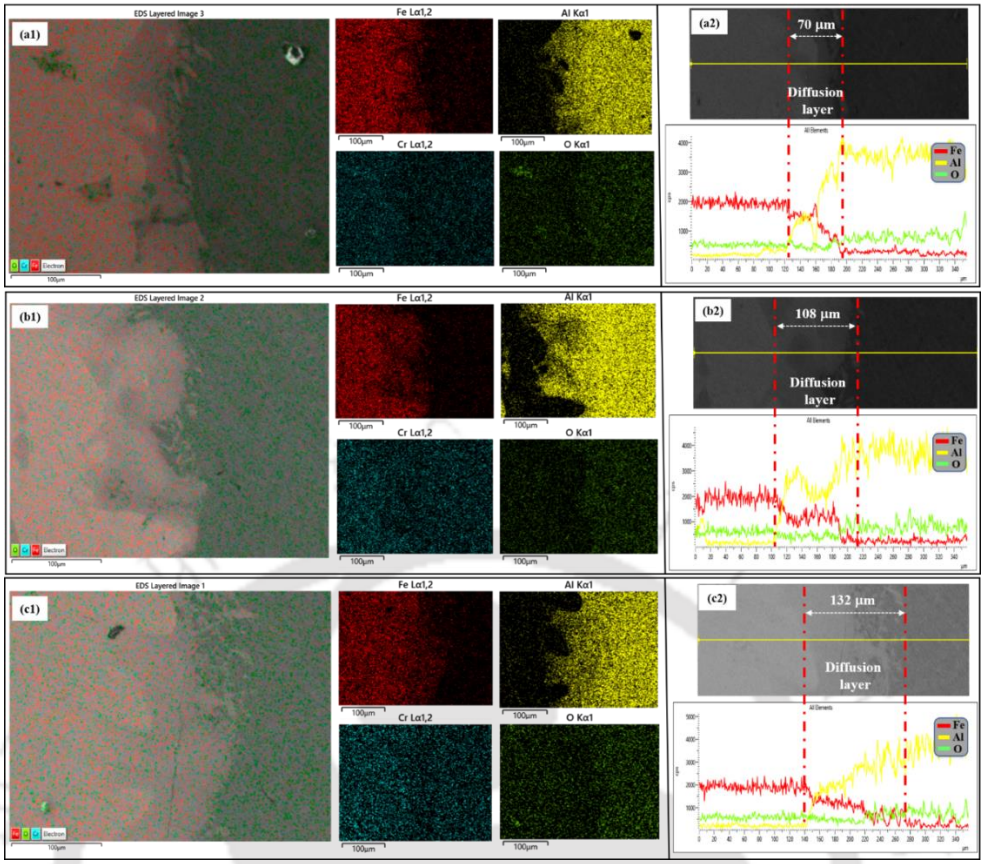

Figure 7.11 EDS analysis at the cross-sections of cladding layers: (a) 1 mm (b) 2 mm and (b) 3 mm

During cladding of dissimilar alloys, the primary melted zone is prone to liquation cracks but no such defect was observed in the cladding layer interfaces as depicted from the magnified SEM imaging of Fe/Al interfaces (Fig. 7.11(a2, b2 and c2)). The smooth and continuous interface indicates that a solid-state joining process occurred during cladding. Moreover, EDS line scan across the Fe/Al interfaces of the cladding layers (Fig. 7.11(a2, b2 and c2)) confirmed the atomic diffusion, indicating the formation of Fe/Al IMCs (Fereiduni et al. 2015). Metallurgical bonds were formed as a result of the atomic diffusion across the joint interface. Based on the elemental distribution of line scan across interface (marked by a dotted line in the figure), the thickness of the diffusion layers was determined. An average diffusion layer thickness of 70, 108 µm and 132 µm was observed at the 1, 2 mm and 3 mm cladding layers, respectively. The higher diffusion layer in the 3 mm cladding was due to combined effect of high heat input and compressive stress (Fereiduni et al. 2015). Based on the Al–Fe phase diagram (Sina et al. 2015) and EDS analysis, the possible IMCs formed at the interface were FeAl, $FeAl_3$, Fe_2Al_3 and Fe_2Al_5. The similar IMCs were also reported by a few researchers (Li et al. 2020, Fereiduni et al. 2015, Sina et al. 2015).

7.3.3.4 TEM observation

The TEM microstructural morphology at the top surface of cladding layers is shown in Fig. 7.12. The morphologies depict typical lath-type martensitic structure with dense dislocations and carbide precipitates. At a few locations merged lath martensite was also observed (Fig. 7.12(b1)). The dislocation density is higher near the lath boundaries. The maximum average size of the lath martensite was found to be ~205, ~240 nm and ~300 nm in 1, 2 mm and 3 mm cladding layers, respectively. The density of lath martensite was observed to be higher in 1 mm cladding layer.

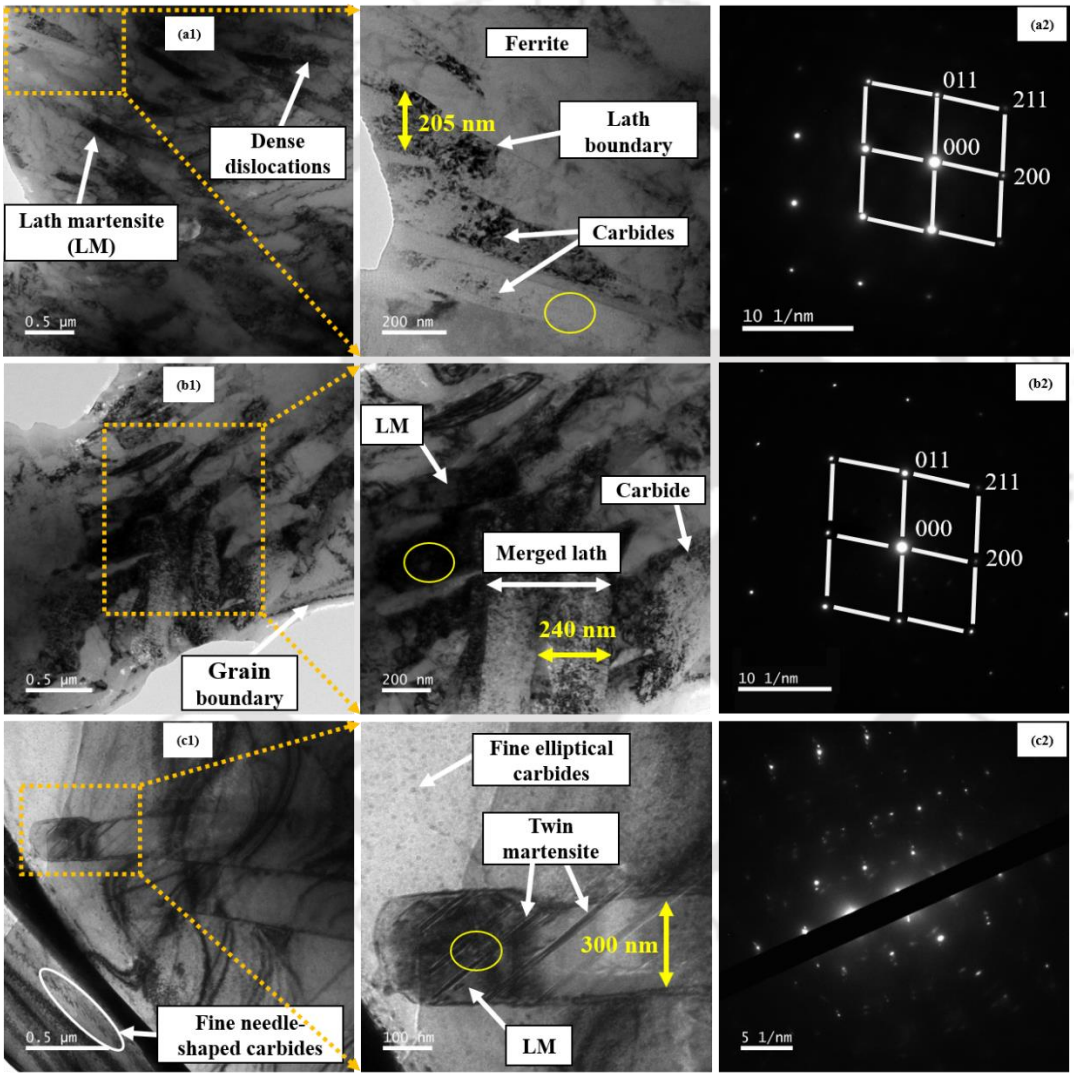

Figure 7.12 TEM microstructure of top surface and corresponding SAED patterns different cladding layers: (a1, and a2) 1 mm, (b1, and b2) 2 mm and (a1, and a2) 3 mm, respectively

The aligned needle-like carbides appear at some specific angles within the martensite laths, as shown in Fig. 7.12(a1 and c1), which are believed to be M_2C-type carbides enriched with Mo and V formed during cladding process (Ju et al. 2018, Chen et al. 2020). Fine elliptical carbides are also finely distributed in the structure (enlarged Fig. 7.12(c1)), similar observation is also reported by Ju et al. (2018). The selected area electron diffraction (SAED) pattern of the lath martensite is shown in Figs. 7.12(a2, b2). Distinct twin martensite is identified within the lath martensite as shown in the enlarged Fig. 7.12(c1) and the corresponding SAED pattern is shown in Fig. 7.12(c2).

The TEM morphology of cross-section of different cladding layers are shown in Fig. 7.13. The TEM bright field morphology depicts distribution of ferrite and acicular martensite (AM) in accordance with the FESEM morphology of cross-section (Fig. 7.9). The AMs densely surrounded by fine dislocation lines are clearly revealed in all the bright field images. Dislocation lines are more pronounced in 1 mm thick layer than in 2 mm and 3 mm layers. Each AM plate in the microstructure is composed of a high density of twinning substructure. Long and short twinned martensite structure is identified in (enlarged Figs. 7.13(a2, b2 and c2)) some locations in AM; these must have been formed during the final cooling, as the martensitic transformation in carbon steels often accompanies formation of twins to accommodate the transformation strains (Zhang et al. 2016).

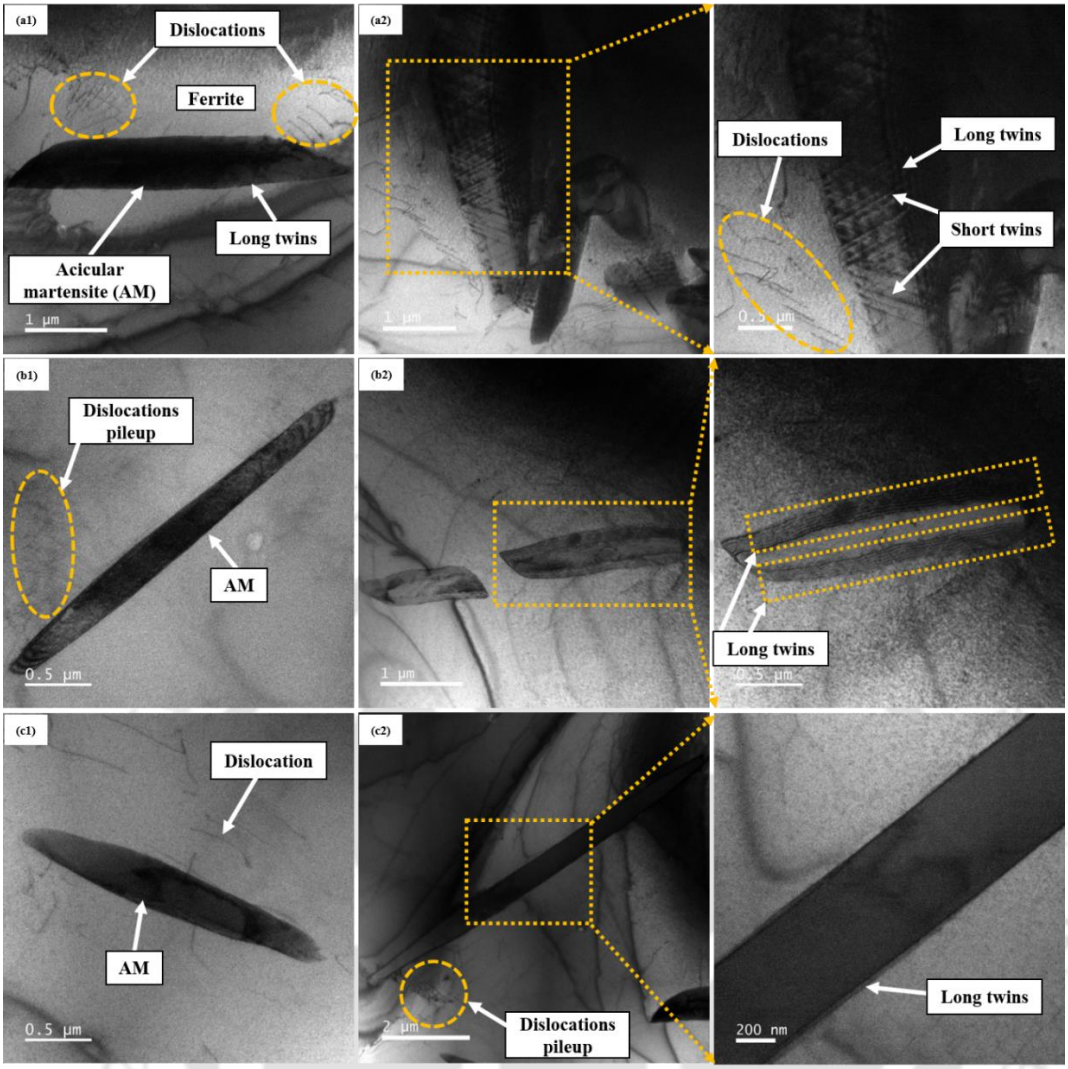

Figure 7.13 TEM cross-sectional microstructure of different cladding layers: (a1, and a2) 1 mm, (b1, and b2) 2 mm and (a1, and a2) 3 mm, respectively

7.3.4 Phase study

The phases and compounds developed in the different cladding layers has been analysed using XRD and XPS, respectively. The phases developed in the top surface of cladding layers are shown in Fig. 7.14. The XRD patterns reveals the presence of body-centred cubic (BCC, ferrite) lattice of α−Fe phase corresponding to 2θ value of 44.43º, 64.77º, 81.90º as per JCPDS-96-901-3477. The similar phases are observed in all the cladding layer. Since XRD could not detect the presence of compounds, further detection was carried out through XPS.

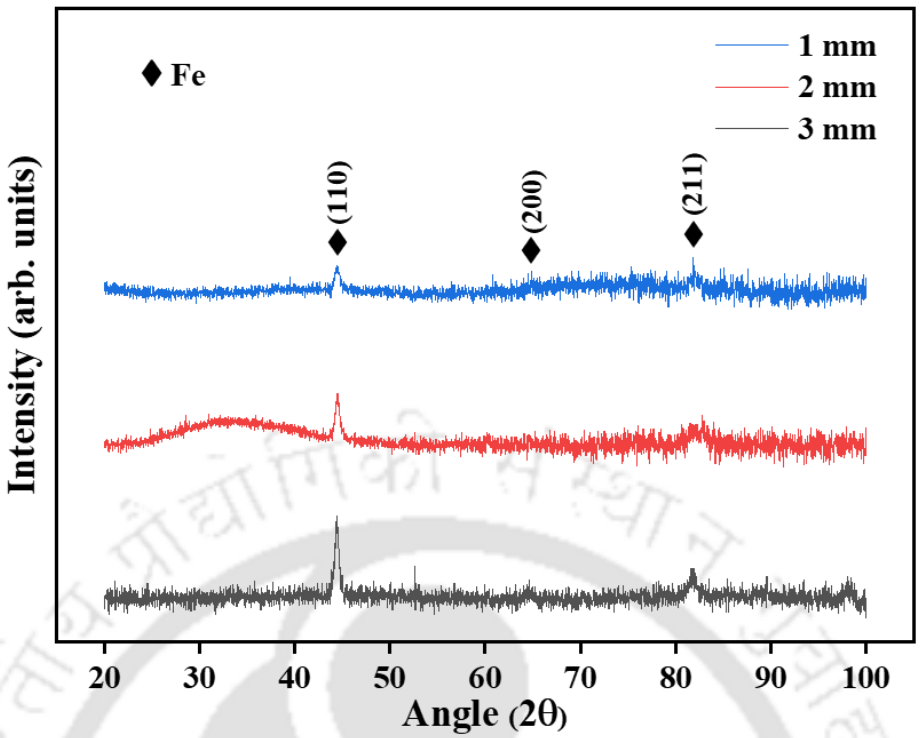

Figure 7.14 XRD plots at the top surface of different cladding layers

Figure 7.15 shows the XPS plots of different cladding layers. The plots depict the spectra of fabricated elements, bonding states and chemical structure. The survey spectrum in XPS plots show the presence of Fe 2p, Cr 2p, O 1s, C 1s, and Fe 3p in the cladding layers. The XPS spectra of the three different cladding layers depicts that the signal peak trend in the cladding layer is consistent. The high-resolution spectra of present elements (Fe 2p, Cr 2p, O 1s and C 1s) are shown in Figs. 7.16(a–d), which are obtained through curve fitting. The peak splitting depicts, the binding energy values of 706 eV, 711 eV and 717 eV correspond to Fe 2p (Fig. 7.16(a)), which represents the existence of metallic Fe at 706 eV and Fe_2O_3 at 711 eV and 717 eV in the cladding layer. The Fig. 7.16(b) depicts the splitting of Cr 2p into Cr_2O_3 at the binding energy values of 578 eV and 587 eV. Fig. 7.16(c) shows the O 1s energy spectrum constitutes binding energy peaks of 527 eV, 531 eV and 537 eV, which corresponding to O at 531 eV and O_2 at 527 eV and 537 eV. Finally, C-C, C-O, and O-C=O bond in the C1s peak (Fig. 7.16(d)), corresponding to binding energy values at 283 eV, 285 eV and 288 eV, respectively. Similar outcomes with insignificant variations in the binding energy values are also seen in the 2 mm and 3 mm cladding layers, as also reported by a few researchers (Wang et al. 2023, Tardio et al. 2015). According to Chen et al. (2019), the presence of Fe_2O_3 and Cr_2O_3 compounds in the steel acts as a protective film and aids in enhancement of different mechanical properties.

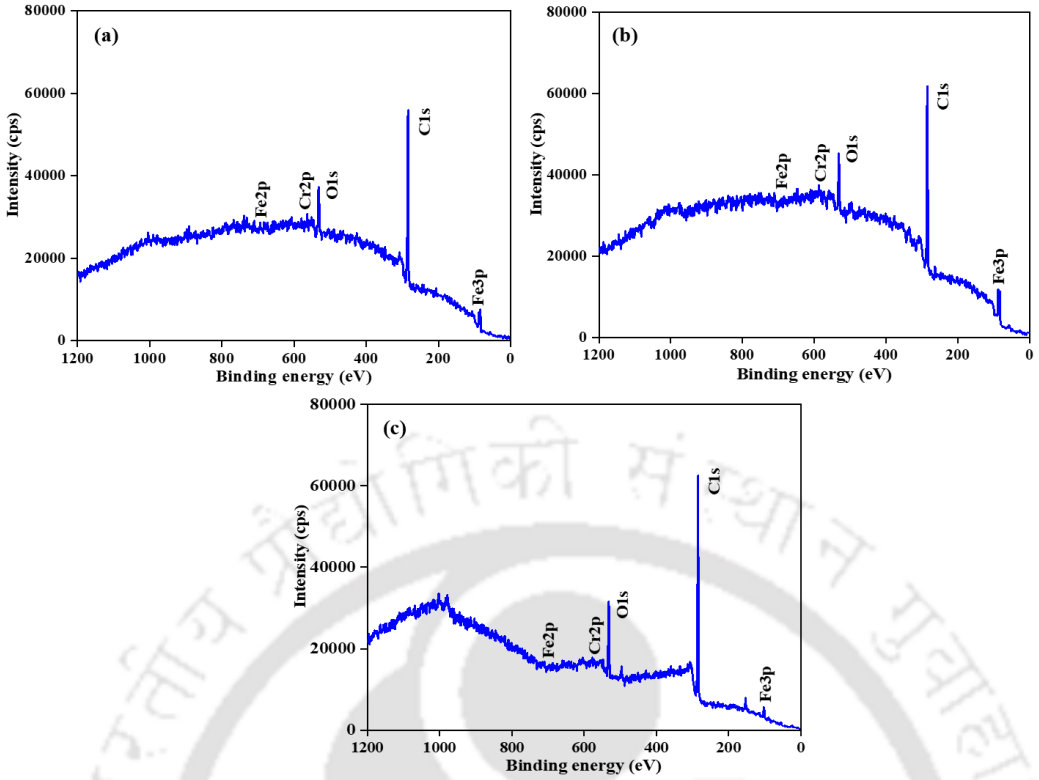

Figure 7.15 XPS spectra of cross-section of different cladding layers: (a) 1 mm, (b) 2 mm and (c) 3 mm

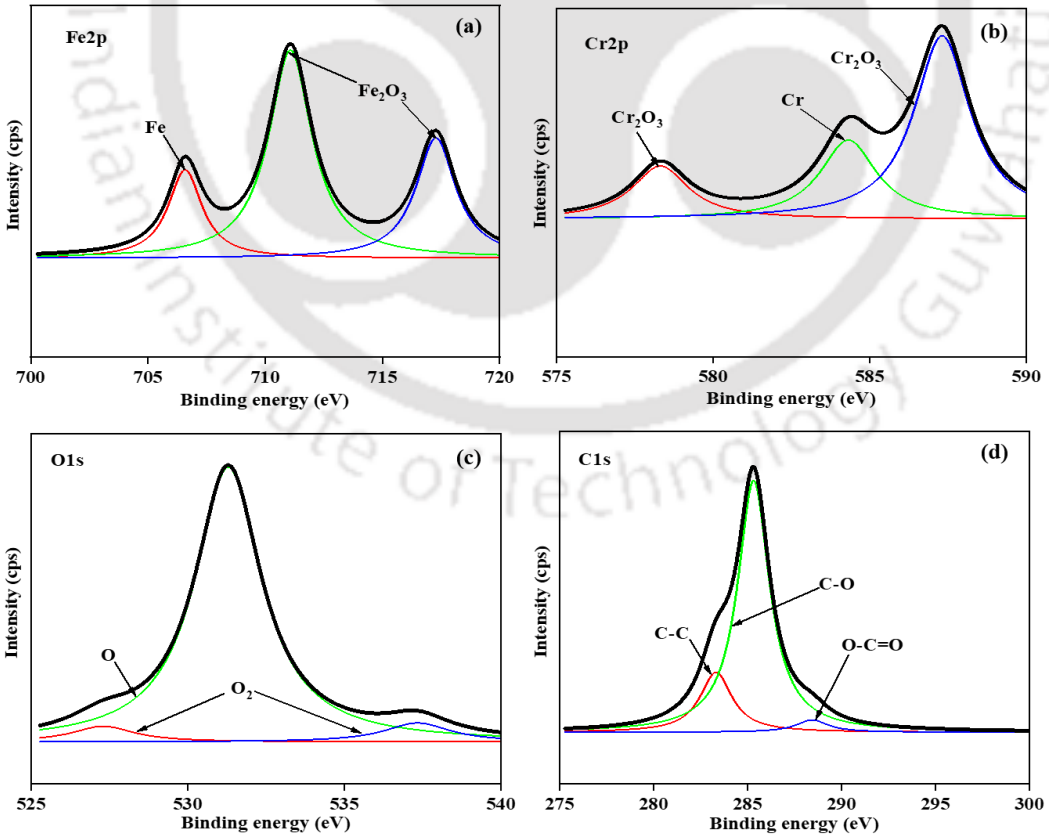

Figure 7.16 High resolution XPS spectra of different elements: (a) Fe 2p, (b) Cr 2p, (c) O 1s and (d) C 1s

7.3.5 Hardness study

Figure 7.17 shows the Vickers microhardness values of the different cladding layers. The variation of hardness in the cladding layers are because of strengthening mechanisms; grain boundary strengthening, dislocation strengthening, transformation strengthening and solid solution hardening. EBSD grain size analysis in Figs. 7.5(c1, c2 and c3) and Fig. 7.6(c1, c2 and c3) reveals that cladding thickness affects grain size. The 1 mm cladding thick cladding layer resulted in finer grains, thus increasing the microhardness. The greatest value of microhardness is 282 HV and 273 HV for 1 mm cladding layer on top surface and cross-section with 40 μm and 65 μm grain sizes, respectively. The lowest value of microhardness was 249 HV and 233 HV for 3 mm cladding layer on top surface and cross-section with 87 μm and 98 μm grain sizes, respectively. The presence of numerous grain boundaries in the fine-grained structure impedes the movement of dislocations, resulting in an increase in microhardness (Anijdan et al. 2018). The grain-boundary strengthening mechanism is effectively described by the Hall-Petch relation as per equation 6.11 (Hall, 1955, Petch, 1955). To evaluate the validity of relation, the H_0 and k_H are derived using the hardness and average grain size of two cladding layers: one with a 1 mm thickness and the other with a 3 mm thickness. These cladding layers represent the two extremes in terms of hardness. Although data-fitting techniques perform well in interpolation, they tend to yield significant errors when extrapolating. Therefore, the values of d and H were substituted into Eq. (6.11) to form two simultaneous linear equations based on the average measurements from the 1 mm and 3 mm cladding layers. Accordingly, for the top surface H_0=179 MPa, k_H=648 MPa√μm and for the cross-section: H_0=57 MPa, k_H=1738 MPa√μm. Using these values, the interpolated hardness values for 2 mm thick layer are determined to be 257 HV and 254 HV for the top surface and cross-section, respectively. The corresponding measured microhardness values are 261 HV and 256 HV, indicating a good agreement. This demonstrates that the Hall-Petch relation offers a reliable estimation of hardness.

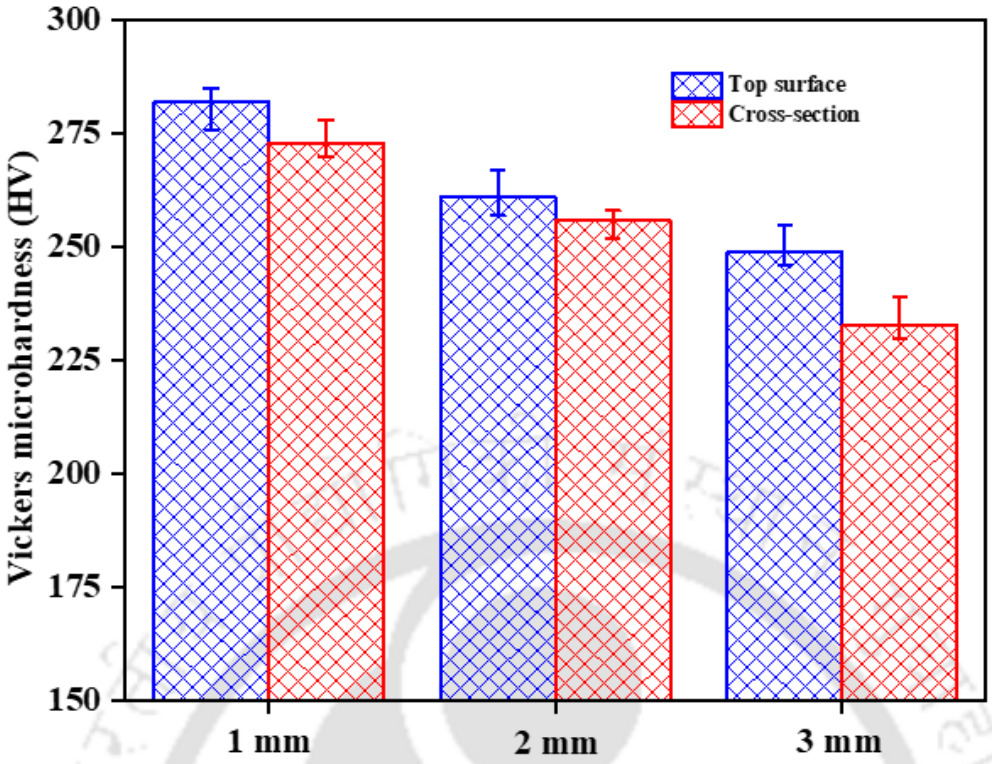

Figure 7.17 Microhardness of deposited cladding layer of different thickness

According to EBSD analysis, the difference in hardness is also caused by dislocation strengthening. The enhanced hardness in 1 mm thick cladding were also related to higher number of LAGBs (Figs. 7.7 and 7.8) compared to 2 mm and 3 mm cladding layer. From KAM maps, the higher number of dislocations were observed in LAGBs. Thereafter, the cladding layer with 1 mm thickness in both top and cross-section has higher dislocation density owns to higher number of LAGBs.

According to FESEM (Fig. 7.9) and TEM morphology (Figs. 7.12 and 7.13), the variation in microhardness values can be attributed to transformation strengthening. The enhanced microhardness in 1 mm cladding layer attributes to higher martensitic structure as compared to 2 mm and 3 mm cladding layer. The twins in the martensite structure are pronounced in 1 mm and 2 mm cladding layers (Fig. 7.13). Das et al. (2007) also stated that increase in the dislocations and twin boundaries in the sample enhances the hardness. However, due to presence of ferritic structure and low proportion of martensitic transformation in the 2 mm and 3 mm cladding layer, the hardness is low. Further, the cooling rate of 1 mm cladding was higher than that of 2 mm and 3 mm cladding layers. The relationship between microhardness and cooling rate as well as carbon content is well-known, where an increase in both parameters leads to solid solution hardening and subsequently higher microhardness (Ali et al. 2019).

7.3.6 Wear study

The wear mass loss of different cladding layer thickness is represented in Table 7.2. The reduced mass loss experienced by the 1 mm cladding layer can be attributed to its high hardness. On the other hand, the 2 mm and 3 mm cladding layers exhibit higher mass loss due to the surface's softness, which results in substantial plastic deformation during sliding against the steel surface. In contrast, the surface of the 1 mm cladding layer comprises a uniform and finely dispersed distribution of hard martensite. The presence of hard debris generated during sliding serves as asperities on the worn surface, reducing the actual contact between the surfaces of the cladding layer and the hardened steel. These debris and the reduced grain boundaries create a significant obstacle in the removal of material during dry-sliding. Furthermore, due to the heat generated by the sliding motion between the pin and disc, an oxide layer that which prevents direct metal-to-metal contact by acting as a barrier.

The mean wear depth, wear volume, coefficient of friction (CoF) and Lancaster wear coefficient values of different cladding layer thickness are represented in Table 7.2. The enhanced strengthening mechanisms and fine grain effects in 1 mm cladding layer are accountable for low wear depth and volume. The EBSD and TEM investigation showed higher dislocations in 1 mm thick cladding layer. As the dislocation density increases, the mobility of dislocations becomes restricted, resulting in an increase in hardness. Hardness and wear volume are inversely associated in both adhesive and abrasive wear modes, as evident in Table 7.2. The data presented in Table 7.2 confirms that materials with higher hardness demonstrate lower wear volumes. The wear equation proposed by Archard, (1953) as per equation 6.12. For each case K is obtained approximately as 2.5×10^{-5}.

The elevated CoF observed in the 3 mm cladding layer can be attributed to its relatively low hardness. Additionally, the frictional heat generated during dry sliding wear between the cladding layer and hardened steel causes the contact surface to become softer. Consequently, debris forms at the contact surface, leading to increase CoF values as a result of plowing and abrasion (Denape and Lamon, 1990). In 1 mm cladding layer due to enhanced hard martensitic structure the development of debris is less and consequently friction. Additionally, a harder surface experiences less friction resistance since it offers less adhesive contact area for a fixed load. The minimum Lancaster wear coefficient was observed in 1 mm cladding layer (0.88×10^{-5} mm^3/Nm) compared to 2

mm and 3 mm cladding layer. The Lancaster wear coefficient was calculated as per equation 4.1 (Lancaster, 1967). The lower the value of *k*, the higher is the wear resistance. Table 7.2 shows that *k* is higher for softer material.

Table 7.2 Wear values of different thickness cladding layer

Sample	Mass loss (g)	Mean wear depth (μm)	Wear volume ($mm^3 \times 10^{-3}$)	Hardness (HV)	Coefficient of friction	Lancaster wear coefficient ($mm^3/Nm \times 10^{-5}$)
1mm	$3.2^{+0.9}_{-0.8}$	31^{+4}_{-2}	$0.41^{+0.05}_{-0.03}$	282^{+3}_{-6}	$0.19^{+0.06}_{-0.05}$	$0.88^{+0.08}_{-0.05}$
2 mm	$3.6^{+1}_{-0.7}$	35^{+4}_{-2}	$0.46^{+0.05}_{-0.03}$	261^{+6}_{-4}	$0.21^{+0.03}_{-0.02}$	$0.99^{+0.09}_{-0.04}$
3 mm	$3.8^{+0.6}_{-1.5}$	41^{+3}_{-4}	$0.48^{+0.04}_{-0.03}$	249^{+6}_{-3}	$0.24^{+0.04}_{-0.02}$	$1.03^{+0.08}_{-0.03}$

The FESEM morphologies of worn-out surfaces are shown in Fig. 7.18. The morphologies are different for different cladding layer thicknesses. Evidence of the existence of pores, scratches, and grooves were observed in all morphologies. However, 3 mm cladding layer displayed a substantial degree of surface wear compared to 1 mm and 2 mm cladding layer, which could potentially result in crack development. The extensive wear of 3 mm cladding layer can be attributed to its low hardness, which causes an increase in wear volume, Lancaster wear coefficient, and abrasive wear compared to those in 1 mm and 2 mm thick cladding layers. Some areas of the wear track of the cladding exhibit localized peeling-off of layers, micro pits and delamination phenomena, which inferred to abrasive and adhesive wear mechanism. During the wear process, localized porosities aggregate, which accelerates cracking followed by wear loss. The higher grain boundary area and LAGBs in 1 mm cladding layer may resist deformation during wear, which in turn reduces wear loss. The presence of oxide debris observed on the worn surface indicates a substantial level of oxidation occurring during the wear process. On the cladded worn surface, the Fe oxide was found to be easily scraped off and transferred as secondary abrasive particles, which intensified the abrasive wear during sliding. Additionally, the frictional heat generated during dry sliding wear caused a rise in temperature, resulting in a relative softening of the contact surface between the cladding layer surface and its counterpart. This softening led to an increased

accumulation of debris on the friction surface, which produced more visible micro-cuts. The accumulation of worn debris from adhesive wear further facilitated three-body abrasive wear (Qunshuang et al. 2016). From the surface morphology of the wear track and Lancaster wear coefficient analysis, it is evident that enhanced hardness and LAGBs protects the surface from wear and improves the wear resistance in 1 mm cladding layer.

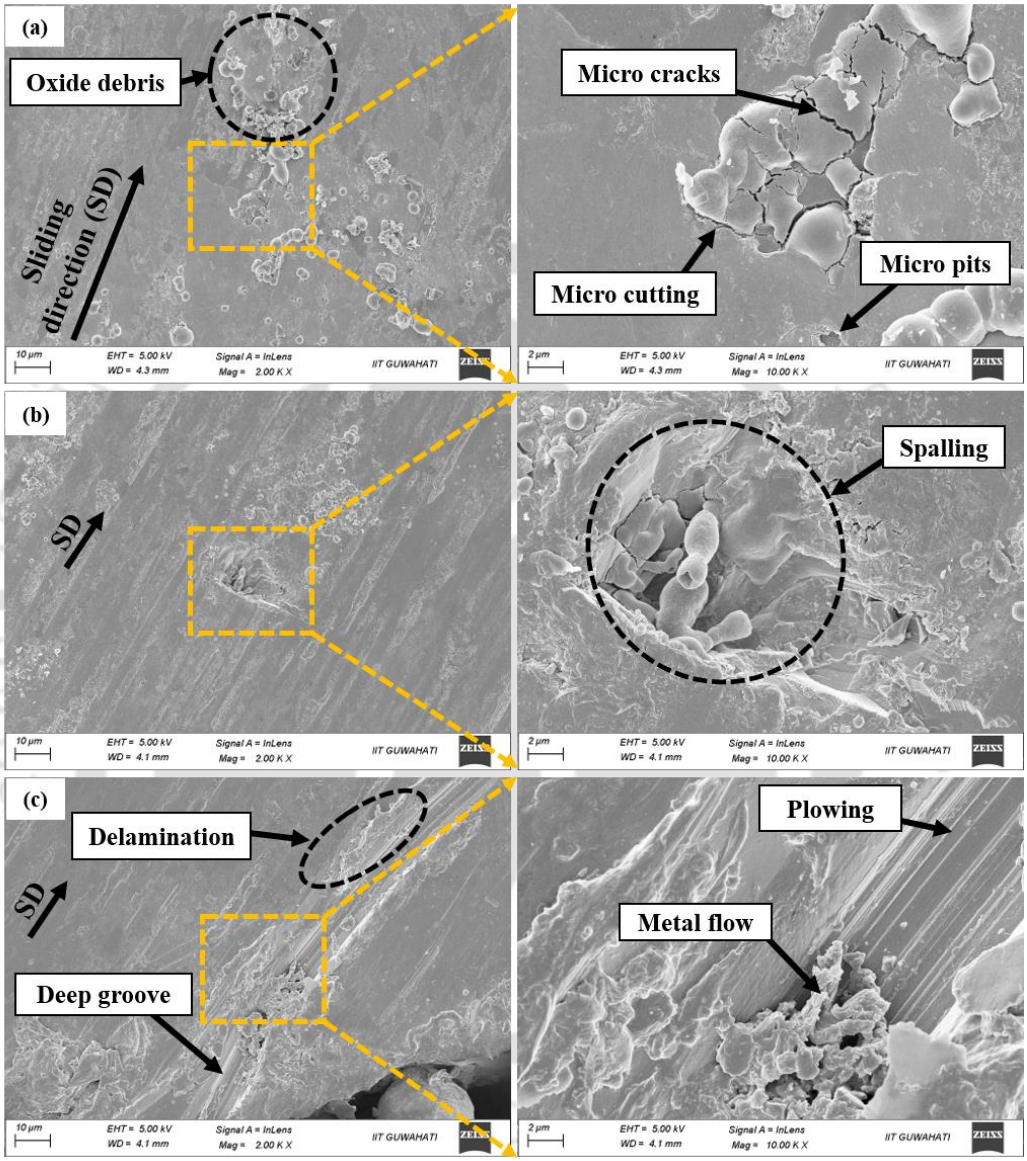

Figure 7.18 Surface roughness of deposited cladding layer of different thickness: (a) 1 mm, (b) 2 mm and (c) 3 mm

Figure 7.19 shows the 3D AFM morphology of the worn surface, depicts the presence of wear tracks, debris, grooves, and pits. The sudden rise in peak height can be attributed to wear debris, while the valleys correspond to grooves, pits, and tracks. This morphology indicates a significant amount of plastic deformation occurring during wear. Among the different cladding layer surfaces, the 1 mm cladding layer exhibited the

smallest increase in peak-to-valley distance compared to the 2 mm and 3 mm layers. The surface roughness was quantified using the average R_a value, which was found to be 30 nm for the 1 mm cladding layer, 37 nm for the 2 mm cladding layer, and 41 nm for the 3 mm cladding layer. The higher increase in R_a value is associated with the higher CoF. The 1 mm cladding layer, with its enhanced hardness and minimal plastic deformation, displayed a smoother surface and a lower R_a value. The surface roughness was measured within a scanned area of 400 μm^2.

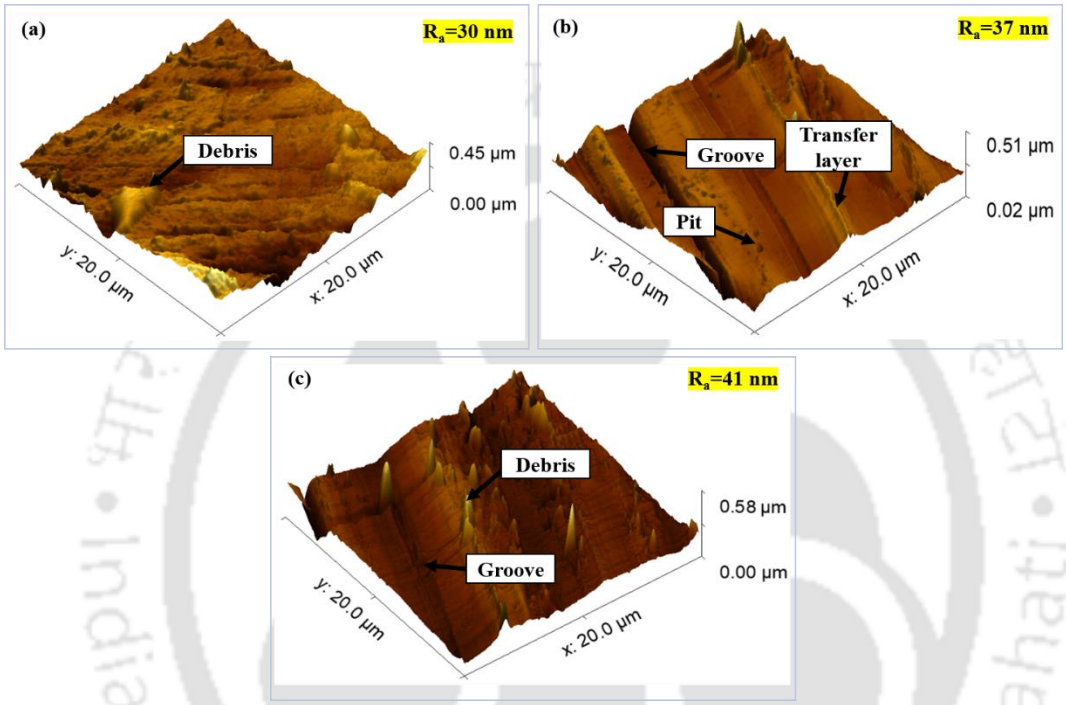

Figure 7.19 Surface roughness of deposited cladding layer of different thickness: (a) 1 mm, (b) 2 mm and (c) 3 mm

Figure 7.20 shows the morphologies of wear debris from different cladding layers. The micrograph exhibits a variety of shapes, including regular, irregular, spherical, elongated, and curled forms. The presence of regular-shaped debris in the 1 mm cladding layer suggests that material removal occurred through rubbing and mild adhesion. These smaller debris particles possess smooth surfaces and edges (Fig. 7.20(a1, a2)). In contrast, the irregular-shaped debris in the 2 mm cladding layer indicates material removal through severe sliding and fatigue. These larger debris possess rough surfaces and irregular sharp-edge (Fig. 7.20(b1, b2)). The elongated and curled shapes of the debris in the 3 mm cladding layer suggest material removal through cutting and plowing actions. Fig. 7.20(c1, c2) reveals that the sharp edges of the debris contributed to the cutting and plowing actions. The presence of irregular, elongated, and curled debris shapes in the cladding layers indicates lower hardness, as observed in the 2 mm and 3

mm layers. Furthermore, the spherical-shaped debris in the cladding layers signifies material removal through sliding and grinding. The investigation of debris morphologies can be used for condition monitoring (Peng and Kirk, 1998). Fig. 7.20(d1, d2 and d3) shows the point EDS analysis of the wear debris of 1 mm cladding layer. The elements distribution at two different points detected higher peak of oxygen, which depicts oxidation during the wear mechanisms. The higher amount of iron oxide and chromium oxide also had developed as they share the same peak with oxygen. The XPS analysis also reported the development of iron oxide and chromium oxide in the cladding layers. These oxide debris acted as an asperity in the worn surface, and lowered the wear mass loss by reducing the true contact between the cladding layers and counterpart.

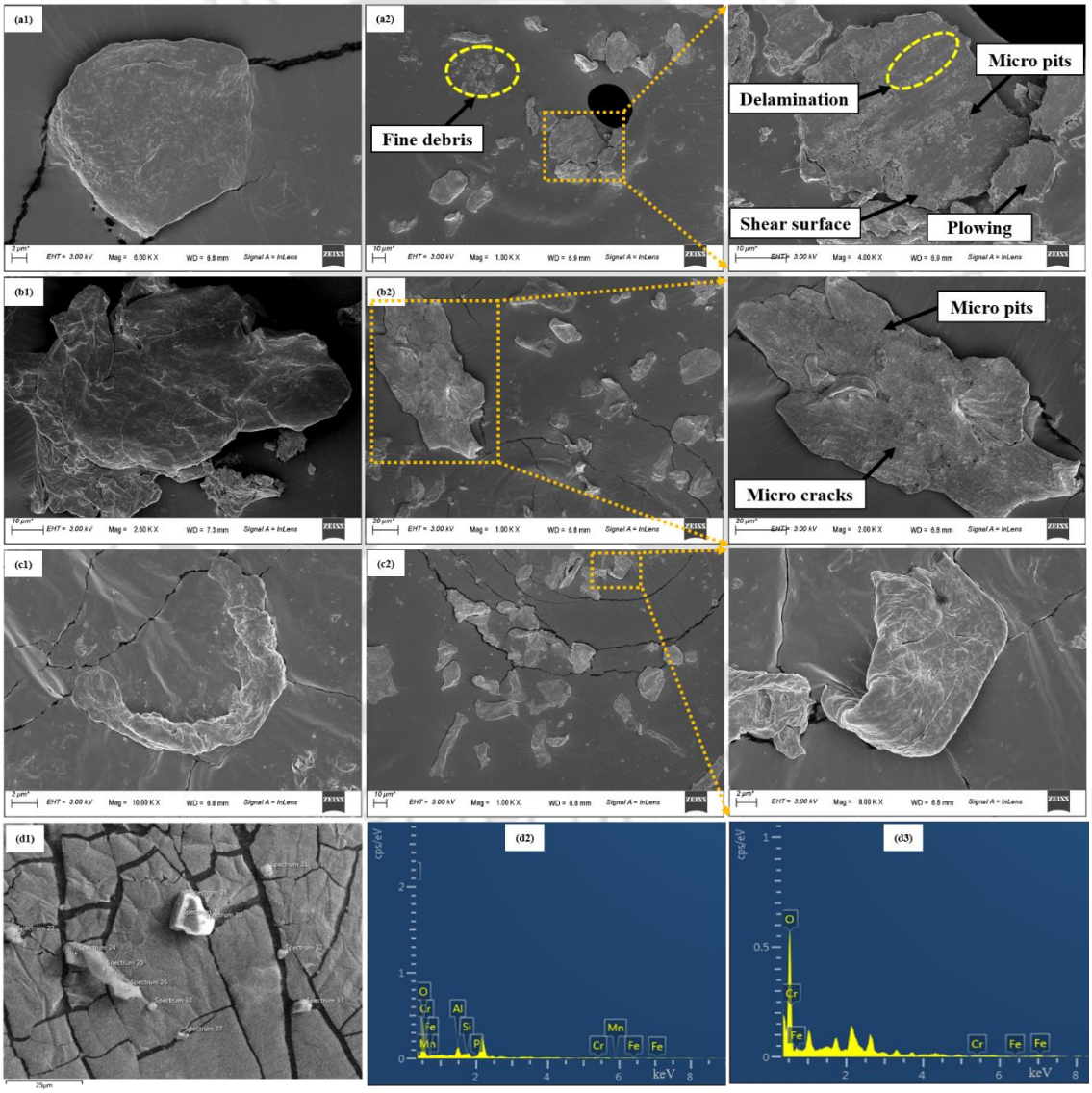

Figure 7.20 Morphology of wear debris of different cladding layers: (a1, a2) 1 mm, (b1, b2) 2 mm and (c1, c2) 3 mm; point EDS analysis of wear debris of 1 mm cladding layer: (d1) microstructure and (d1, d2) elemental distribution

7.4 Conclusion

In this Chapter, Fe-based cladding of different layer-thicknesses was fabricated on aluminum substrate with cold metal transfer technology. Microstructural, tribological and mechanical properties were obtained in each thickness and compared. The following are the salient observations:

- Among 1 mm, 2 mm and 3 mm thick cladding layers, the quality of bead in 1 mm thick layer was the best. It has the minimum dilution, reduced porosity, low bead contact angle and relatively smoother surface. This outcome attributes to the lower heat input associated with the 1 mm cladding layer, which resulted in a more controlled solidification process. The reduced dilution between the cladding material and the substrate, likely due to the thinner layer, contributed to the well-defined and high-quality bead. Furthermore, the lower heat input minimized the formation of porosity and irregularities, resulting in a smoother surface finish. The thin cladding layer provides fine grain structure and enhanced low angle grain boundaries. The presence of higher amount such boundaries in 1 mm cladding layer also resulted in the higher dislocation density. In general, this results in enhanced mechanical properties like hardness and wear resistance.
- Due to higher cooling rate in 1 mm cladding layer, a martensite structure was obtained that contributed to enhanced hardness. In other layers, the structure was largely ferrite.
- The fine grain, dense martensite phase and higher dislocation density has resulted in high microhardness of 282 HV and low Lancaster wear coefficient of 0.88 $\times 10^{-5}$ mm^3/Nm in 1 mm thick cladding layer. Corresponding values for 3 mm thick cladding layer were 249 HV and 1.03 $\times 10^{-5}$ mm^3/Nm; amounting to 12% and 17% deviations, respectively.

Considering these observations, the optimization of layer thickness in cladding as well as additive manufacturing is crucial. In additive manufacturing, a trade-off has to be made between productivity and mechanical properties; low layer thickness provides good mechanical properties but will require more time for fabrication. Developing the physics or database models of the cladding process using CMT will help in optimizing.

Chapter 8

Epilogue

8.1 Introduction

Cold metal transfer cladding, in fact, is an efficient additive manufacturing technology that finds application in various sectors such as automotive, defence, and power plants. Various industries, including aircraft, marine construction, automobile manufacturing, railways, and structural applications, heavily rely on welding to fabricate material joints. The preference for aluminum in welding has grown due to the increasing trend toward lighter materials and reduced fuel consumption. Welding enables the formation of joints between metallic plates through the application of heat, pressure, and, if necessary, filler material, without the requirement for complete melting of the metal surfaces. As additive manufacturing continues to advance, it has introduced innovative welding techniques that facilitate material joining and the gradual formation of surface layers. Among these techniques, the CMT method stands out as an advanced iteration of MIG welding, delivering superior performance with decreased spattering and minimal heat input. In the ever-evolving realm of additive manufacturing and welding, the CMT technique holds immense potential for the future of modern manufacturing. For this, the vastly available material steel-based alloy, has been cladded on aluminum to enhances the mechanical characteristics of aluminum.

As reported in Chapter 2, researchers have carried out several works in the domain of cladding using CMT process. However, the cladding of Fe-based alloy on aluminum is not addressed. This thesis utilizes the concept of low heat input using CMT process to address large difference in melting temperature between the former and latter. Based on a few parametric studies the best outcomes of the cladding process are reported. The content and outcomes of various subparts of the thesis are briefly summarized in the following sections. Finally, the overall conclusions and the scope of future work are highlighted.

8.2 Microstructure and mechanical properties of ER70S-6 alloy cladding on AA 6061-T6 aluminum alloy

The selection of Fe-based ER70S6 as cladding material was based on its suitability for automatic welding, offering excellent welding properties, stable arc, low sputtering, cost-effectiveness, and high deposition efficiency. While CMT has been studied for

cladding, no previous research has reported on cladding aluminum alloy with steel. Coating aluminum alloys using metallic powders through spray techniques resulted in porosity issues and high costs. Thus, this study focused on using CMT to clad AA6061-T6 aluminum alloy with ER70S-6 alloy in welding electrode form. ER70S-6, a mild steel with manganese and silicon, proved to be a more affordable alternative to steel powders. The comparison was made between CMT cladding and existing powder-based techniques. Remarkably, a single pass of CMT could achieve a 3 mm thick cladding layer, which is not typically possible with thermal spray processes.

8.3 Corrosion behavior and its effect on mechanical properties of ER70S-6 cladding on AA 6061-T6 alloy

The corrosion behavior of the Fe-based cladding on the Al substrate was investigated, revealing the importance of running longer-duration corrosion immersion tests. According to ASTM standard G31, test durations ranging from 48 to 168 h are typical, while corrosion rates below 0.5 mm/year may require tests lasting at least 200 h. It was observed that short-time testing on alloys generating passive films can lead to misleading results. Therefore, longer duration tests may be necessary to allow for the breakdown of the passive film and to assess borderline conditions accurately. The cladding layer showed significant surface damage primarily due to localized pitting corrosion. Notably, the growth of pits occurred more rapidly in the lateral direction compared to the depth direction. Additionally, the corrosion test resulted in reduced average micro-hardness due to the removal of hard materials and the introduction of porosity. This, in turn, reduced the load-bearing area at specific locations.

8.4 Heat treatment of ER70S-6 cladding on AA 6061-T6 aluminum alloy

The effect of heat treatment on the cladded layer was studied, employing four different methods. The first involved heating the sample to 600 °C, holding it for 1 h, and then furnace cooling over 24 h. The second method entailed water quenching after heating to 600 °C with a 1 h hold. The third approach included artificial age hardening, involving heating the sample to 175 °C, holding it for 24 h, and furnace cooling over 6 h. Lastly, deep cryo-treatment involved dipping the sample in liquid nitrogen (–196 °C) for 1 h, followed by returning to ambient temperature. Cryogenic treatment exhibited the most significant improvement in the properties of the steel cladded parts produced through CMT technology. Water quenching came in second, while furnace cooling showed enhanced ductility but had a detrimental impact on tribological properties.

8.5 Effect of layer thickness in CMT cladding of ER70S-6 alloy on AA 6061-T6 aluminum alloy

The CMT cladding of Fe-based ER70S-6 alloy on Al substrates with particular focus on the effect of cladding thickness. Cladding layers of approximately 1.5 mm, 2.5 mm, and 3.5 mm were deposited on the substrate for investigation. The cladding layer of 0.5 mm was milled to remove uneven surface. Among these thicknesses, the 1 mm cladding layer exhibited the most favourable results in terms of bead quality. It displayed minimal dilution, reduced porosity, a low bead contact angle, and a relatively smoother surface. The thin cladding layer at 1 mm provided a fine grain structure with enhanced low angle grain boundaries. The presence of a higher number of such boundaries in the 1 mm cladding layer resulted in a higher dislocation density, contributing to improved mechanical properties such as hardness and wear resistance. These findings indicate that cladding thickness significantly impacts the quality and properties of the cladded layer. The 1 mm thickness demonstrated the most promising performance, suggesting its potential use in various industrial applications to achieve superior mechanical characteristics.

8.6 Overall Conclusions

As the literature contains a number of studies on the deposition of cladding layer using CMT process, this work focused on steel-based filler wire deposition on AA 6061-T6 aluminum substrate. It also attempted to optimized parametric study by employing different voltage and current. Attempt was also made to enhance the mechanical characteristics of the cladding layer by employing different heat-treatment procedure. Study of mechanical bonding is also major contribution of the thesis. The cladding layer thickness towards to mechanical properties of cladded layer was also reported. Overall, this research emphasizes the potential of CMT technology for cladding applications, providing valuable insights into the influence of heat treatment and cladding thickness on the resulting properties. The findings have practical implications for industrial applications, paving the way for the optimization of cladding processes to achieve superior mechanical characteristics in various sectors.

8.7 Scope for future work

Here, an experimental study has been conducted on CMT cladding of aluminum by steel-based filler wire as a part of surface modification. The work done still now, confirms that CMT based cladding of steel alloys on aluminum is promising. The quality of the cladding layers can be controlled by optimum process parameters. There are several issues that need further investigations. Some of these are as follows:

- The influence of deposition directions on microstructural and mechanical characterization of CMT cladding.
- Development of a finite element based thermomechanical model to analyse the induced residual stress and microstructural changes during CMT based cladding process.
- Utilizing CMT cladding process for building functionally graded components by additive manufacturing.

References

- Ahmad R. and Bakar, M.A., 2011, Effect of a post-weld heat treatment on the mechanical and microstructure properties of AA6061 joints welded by the gas metal arc welding cold metal transfer method, Materials & Design, 32(10), pp. 5120–5126.
- Ahsan, M., Kim, Y.R., Kim, C.H., Kim, J.W., Ashiri, R. and Park, Y.D., 2016, Porosity formation mechanisms in cold metal transfer (CMT) gas metal arc welding (GMAW) of zinc coated steels, Science and Technology of Welding and Joining, 21, pp. 209–15.
- Ali, M., Porter, D., Kömi, J., Eissa, M., Faramawy, H.E. and Mattar, T., 2019, Effect of cooling rate and composition on microstructure and mechanical properties of ultrahigh-strength steels. Journal of Iron and Steel Research International, 26, pp. 1350–1365.
- Aluminum Association (1998), Aluminum Alloy Selection and Applications, The Aluminum Association, Inc. New York.
- Anijdan, S.H.M., Sabzi, M., Ghobeiti-Hasab, M. and Roshan-Ghiyas, A., 2018, Optimization of spot-welding process parameters in dissimilar joint of dual phase steel DP600 and AISI 304 stainless steel to achieve the highest level of shear-tensile strength, Materials Science and Engineering: A, 726, pp. 120–125.
- Archard, J., 1953, Contact and rubbing of flat surfaces, Journal of Applied Physics, 24, pp. 981–988.
- Astaf'ev, A.A., 1997, Effect of grain size on the properties of manganese austenite steel 110G13L, Metal Science and Heat Treatment, 39, pp. 198–201.
- Bakshi, S.R., Singh, V., Balani, K., McCartney, D.G., Seal S. and Agarwal, A., 2008, Carbon nanotube reinforced aluminum composite coating via cold spraying, Surface and Coatings Technology, 202, pp. 5162.
- Benoit, A., Jobez, S., Paillard, P., Klosek, V. and Baudin, T., 2011, Study of Inconel 718 weldability using MIG CMT process, Science and Technology of Welding and Joining, 16, pp. 477–482.
- Bergsdal, H., Stromman, A.H. and Hertwich, E.G., 2004, The Aluminium Industry - Environment, Technology and Production, Industrial Ecology Programme (IndEcol), 8, pp. 1501–6153.

- Bin-you F., Ding-yong H. and Li-dong, Z., 2009, Effect of heat treatment on the microstructure and mechanical properties of Fe-based amorphous coatings, Journal of Alloys and Compounds, 480(2), pp. 422–427.
- Bowen, Z., Chao, W., Zhaohui, W., Laiqi Z. and Qiang, G., 2019, Microstructure and properties of Al alloy ER5183 deposited by variable polarity cold metal transfer, Journal of Materials Processing Technology, 267, pp. 167–176.
- Cao, R., Sun J.H. and Chen, J.H., 2013, Mechanisms of joining aluminum A6061-T6 and titanium Ti–6Al–4V alloys by cold metal transfer technology, Science and Technology of Welding and Joining, 18, pp. 425.
- Cao, R., Sun, J.H., Chen, J.H. and Wang, P., 2014, Cold Metal Transfer Joining of Aluminum AA6061-T6-to-Galvanized Boron Steel, Journal of Manufacturing Science & Engineering,136(5), pp. 051015.
- Chen, R.C., Hong, C., Li, J.J., Zheng Z.Z. and Li, P.C., 2017, Austenite grain growth and grain size distribution in isothermal heat-treatment of 300M steel, Procedia Engineering, 207, pp. 663–668.
- Chen, X., Li, Y., Zhu, Y., Bai, Y. and Yang, B., 2019, Improved corrosion resistance of 316LN stainless steel performed by rotationally accelerated shot peening, Applied Surface Science, 481, pp. 1305–1312.
- Chen, K., Jiang, Z., Liu, F., Li, H., Ma, X., Zhao, B., Kang, C. and Li, Y., 2020, Enhanced mechanical properties by retained austenite in medium–carbon Si-rich micro-alloyed steel treated by quenching–tempering, austempering and austempering–tempering processes, Materials Science and Engineering: A, 790, pp. 39742.
- Chiareli, A.O.P., Huppert H.E. and Worster, M.G., 1994, Segregation and flow during the solidification of alloys, Journal of Crystal Growth, 139(1–2), pp. 134−146.
- Cong, B., Ouyang, R., Qi, B. and Ding, J., 2016, Influence of cold metal transfer process and its heat input on weld bead geometry and porosity of aluminum-copper alloy welds. Rare Metal Materials and Engineering, 45(3), pp. 606–611.
- Das, D., Dutta, A.K., Toppo, V. and Ray, K.K., 2007, Effect of Deep Cryogenic Treatment on the Carbide Precipitation and Tribological Behavior of D2 Steel, Materials and Manufacturing Processes, 22, pp. 474–480.

- Dearnley, P. A., 1988, Wear Resistant Surfaces in Engineering – A Guide to their Production Properties and Selection, Surface Engineering, 4(1), pp. 28–29.
- Denape, J. and Lamon, J., 1990, Sliding friction of ceramics: Mechanical action of the wear debris, Journal of Materials Science, 25, pp. 3592–3604.
- Deng, D., Chen, R., Sun Q. and Li, X., 2015, Microstructural Study of 17-4PH Stainless Steel after Plasma-Transferred Arc Welding, Materials, 8, pp. 424–434.
- Dong, L., Shi, Z., Zhang, Y., Wang, S., Wang, Q. and Liu, L., 2022, Microstructure and sulfide stress corrosion cracking of the Inconel 625/X80 weld overlay fabricated by cold metal transfer process, International Journal of Hydrogen Energy, 47, pp. 29113–29130.
- Elrefaey A., 2015, Effectiveness of cold metal transfer process for welding 7075 aluminum alloys, Science and Technology of Welding and Joining, 20(4), pp. 280−285.
- ESAB MW1, 2023, accessed on May 5, 2023, <https://esab.com/mv/ind_en/products-solutions/product/filler-metals/mild-steel/mig-wires-tig-rods-gmaw-gtaw/esab-mw1/> .
- Ermakova, A., Mehmanparast, A., Ganguly, S., Razavi J. and Berto F., 2022, Fatigue crack growth behaviour of wire and arc additively manufactured ER70S-6 low carbon steel components. International Journal of Fracture, 235, pp. 47–59.
- Evangeline A. and Sathiya, P., 2019, Cold metal arc transfer (CMT) metal deposition of Inconel 625 superalloy on 316L austenitic stainless steel: microstructural evaluation, corrosion and wear resistance properties, Materials Research Express, 6, pp. 066516.
- Feng, J., Zhang H. and He, P., 2009, The CMT short-circuiting metal transfer process and its use in thin aluminum sheets welding, Materials & Design, 30, pp. 1850–1852.
- Fouad, M.A., Zewail, T.M., Amine, N.A. and El-Tawail, Y.A., 2017, Comparison between corrosion behavior of copper and stainless steel 90_ elbow and failure investigation of 90_ copper elbow, Journal of The Institute of Engineers (India) Series C, 98(2), pp. 141–145.
- Furukawa, K., 2006, New CMT arc welding process – welding of steel to aluminium dissimilar metals and welding of super-thin aluminium sheets, Weld International, 20(6), pp. 440–445.

- Gärtner, F., Stoltenhoff, T., Voyer, J., Kreye, H., Riekehr S. and Koçak, M., 2006, Mechanical properties of cold-sprayed and thermally sprayed copper coatings, Surface and Coatings Technology, 200 (24), pp. 6770–6782.
- Gejendhiran, S., Karpagaraj, A., Kumar, D.V., Dhanusuraman, R. and Annamalai, N., 2023, Experimental investigations on Inconel 718 hard-faced layer deposited over SS304 using cold metal transfer, Surface and Coatings Technology, 468, pp. 129739.
- Ghelichi, R., Bagherifard, S., MacDonald, D., Pariente, I., Jodoin B. and Guagliano, M., 2014, Experimental and numerical study of residual stress evolution in cold spray coating, Applied Surface Science, 288, pp. 26–33.
- Gornikowska, M.R., Cieniek, L., Blicharski, M. and Kusinski, J., 2014, Microstructure and microsegregation of an Inconel 625 weld overlay produced on steel pipes by the Cld Metal Transfer technique, Archives of Metallurgy and Materials, 59, pp. 1081–1084.
- Gornikowska, M.R., Dymek, S., Blicharski, M., Cieniek, L. and Kusinski, J., 2021, Microstructure of 309 and 310 austenitic stainless steel CMT overlays on the 16Mo3 pressure vessel steel, Archives of Metallurgy and Materials, 66, pp. 645–649.
- Gornikowska, M.R., Kusinski, J., Cempura, G. and Morgiel, J., 2023, Microstructure and phase composition of transition zone between low alloyed steel boiler tube and an austenitic stainless-steel weld overlay produced by cold metal transfer method, International Journal of Pressure Vessels and Piping, 203, pp. 104951.
- Greving, D.J., Shadley, J.R., Rybicki, E.F., Greving, D.J., Shadley, J.R. and Rybicki, E.F., 1994, Effects of coating thickness and residual stresses on the bond strength of ASTM C633-79 thermal spray coating test specimens, Journal of Thermal Spray Technology, 3, pp. 371–378.
- Guo, P., Zou, B., Huang, C. and Gao, H., 2017, Study on microstructure, mechanical properties and machinability of efficiently additive manufactured AISI 316L stainless steel by high-power direct laser deposition, Journal of Materials Processing Technology, 240, pp. 12–22.
- Gurumoorthy, K., Kamaraj, M., Rao K.P. and Venugopal, S., 2006, Microstructure and wear characteristics of nickel based hardfacing alloys deposited by plasma transferred arc welding, Journal of Materials Science & Technology, 22, pp. 975−980.

- Hasson, J.T.M.D and Otterloo, L.D.M.V., 1997, Surface engineering with lasers: application to Co based materials, Surface Engineering, 13, pp. 471–482.
- Hadad, M., Marot, G., Demarecaux, P., Chicot, D., Lesage, J., Rohr, L. and Siegmann, S., 2007, Adhesion tests for thermal spray coatings: correlation of bond strength and interfacial toughness, Surface Engineering, 23(4), pp. 279–283.
- Hall, E.O., 1951, Proceedings of the Physical Society, Series B, 64, pp. 747.
- Han, Y., Zhong, S., Peng, C., Tian, L., Sun, Y., Zhao, L. and Xu, L., 2022, Fatigue behavior of X65 pipeline steel welded joints prepared by CMT/GMAW backing process, International Journal of Fatigue, 164, pp. 107156.
- Harish, S., Bensely, A., Lal, D.M., Rajadurai A. and Lenkey, G.B., 2009, Microstructural study of cryogenically treated En 31 bearing steel, Journal of Materials Processing Technology, 209(7), pp. 3351–3357.
- Hatch, J.E., 1984, Aluminum Properties and Physical Metallurgy, American Society for Metals, Metals Park, Ohio.
- He, J.Y., Wang, H., Huang, H.L., Xu, X.D., Chen, M.W., Wu, Y., Liu, X.J., Nieh, T.G., An, K. and Lu, Z.P., 2016, A precipitation-hardened high-entropy alloy with outstanding tensile properties, Acta Materialia, 102, pp. 187–196.
- Hengyong, B., Mohammed, Y., Chen L. and Bertrand, J., 2011, Effect of heat treatment on the intermetallic layer of cold sprayed aluminum coatings on magnesium alloy, Surface and Coatings Technology, 205(19), pp. 4665–4671.
- Hou, X., Gao, L., Cui, Z. and Yin, J., 2018, Corrosion and Protection of Metal in the Seawater Desalination, IOP Conference Series: Earth and Environmental Science, 108, pp. 022037.
- Hu, J., Zhang, W., Fu, D., Teng J. and Zhang, H., 2019, Improvement of the mechanical properties of Al–Mg–Si alloys with nano-scale precipitates after repetitive continuous extrusion forming and T8 tempering. Journal of Materials Research and Technology, 8(6), pp. 5950–5960.
- Huang, J.Y., Zhu, Y.T., Liao, X.Z., Beyerlein, I.J., Bourke, M.A. and Mitchell, T.E., 2003, Microstructure of cryogenic treated M2 tool steel, Materials Science and Engineering: A, 339, pp. 241–244.
- Huang, J., Li, W.P., He, J.Y., Zhou, R., Chou, T.H., Yang, T., Liu, C.T., Zhang, W.D., Liu, Y. and Huang, J.C., 2022, Dual heterogeneous structure facilitating an

excellent strength-ductility combination in an additively manufactured multi-principal-element alloy, Materials Research Letters, 10, pp. 575–584.

- Jenkins R., and Snyder, R.L., 1996, Introduction to X-Ray Powder Diffractometry, J Wiley & Sons Inc, New York.
- Jiru, W.G., Sankar, M.R. and Dixit, U.S., 2019, Laser Surface Alloying of Aluminum for Improving Acid Corrosion Resistance. Journal of the Institute of Engineers (India): Series C, 100, pp. 481–492.
- Joydip, S., Sahoo, R.K., Bardhan K.K. and Mukherjee, C.D., 2011, Influence of annealing temperature on the structural, topographical and optical properties of sol–gel derived ZnO thin films, Materials Letters, 65, pp. 2572–2574.
- Ju, Y., Goodall, A., Strangwood, M. and Davis, C., 2018, Characterisation of precipitation and carbide coarsening in low carbon low alloy Q&T steels during the early stages of tempering, Materials Science and Engineering: A, 738, pp. 174–189.
- Kah, P., Suoranta, R. and Martikainen, J., 2013, Advanced gas metal arc welding processes, The International Journal of Advanced Manufacturing Technology, 67, pp. 655–674.
- Kahyarian, A., Schumaker, A., Brown, B. and Nesic, S., 2017, Acidic corrosion of mild steel in the presence of acetic acid: Mechanism and prediction. Electrochimica Acta, 258, pp. 639–652.
- Kumar, N.P., Vendan S.A. and Shanmugam, N. S., 2016, Investigations on the parametric effects of cold metal transfer process on the microstructural aspects in AA6061, Journal of Alloys and Compounds, 658, pp. 255–264.
- Kumar, S., Manjunatha, L.H., Lokesha, M. and Ajaykumar, B., 2018, A review: Mechanical Properties of HSS Steel by deep Cryo-Treatment, IOP Conference Series: Materials Science and Engineering, 376, pp. 012098.
- Kun, H., Lijin, D., Qinying, W., Huali, Z., Yufei, L., Li L. and Zhi, Z., 2022, Comparison on the microstructure and corrosion behavior of Inconel 625 cladding deposited by tungsten inert gas and cold metal transfer process, Surface and Coatings Technology, 435, pp. 128245.
- Laha, T. Agarwal, A., McKechnie, T., Rea K. and Seal, S., 2005, Synthesis of bulk nanostructured aluminum alloy component through vacuum plasma spray technique, Acta Materialia, 53, pp. 5429.

- Lancaster, J.K., 1967, The influence of substrate hardness on the formation and endurance of molybdenum disulphide films, Wear, 10, pp. 103–117.
- Lee, K.J., Kumai, S., Arai, T. and Aizawa, T., 2007, Interfacial microstructure and strength of steel/aluminum alloy lap joint fabricated by magnetic pressure seam welding, Materials Science and Engineering: A, 471, pp. 95–101.
- Li, W., Sugio, K., Liu, X., Yamamoto, M., Guo, Y., Zhu, S. and Sasaki, G., 2021, Microstructure evolution and mechanical properties of 308L stainless steel coatings fabricated by laser hot wire cladding, Materials Science and Engineering: A, 824, pp. 141825.
- Li, W.Y., Li, C.J. and Liao, H., 2006, Effect of annealing treatment on the microstructure and properties of cold-sprayed Cu coating, Journal of Thermal Spray Technology, 15, pp. 206–211.
- Li, Z., Chai, L., Tang, Y., Zhang, C., Qi, L., Zhang, K., Peng, C. and Huang, C., 2023, 316L stainless steel repaired layers by weld surfacing and laser cladding on a 27SiMn steel: A comparative study of microstructures, corrosion, hardness and wear performances, Journal of Materials Research and Technology, 23, pp. 2043–2053.
- Liang, Y., Hu, S., Shen, J., Zhang, H. and Wang, P., 2017, Geometrical and microstructural characteristics of the TIG-CMT hybrid welding in 6061 aluminum alloy cladding, Journal of Materials Processing Technology, 239, pp. 18–30.
- Liao, J., Yamamoto, N. and Nakata, K., 2014, Gas tungsten arc welding of fine-grained AZ31B magnesium alloys made by powder metallurgy, Materials & Design, 56, pp. 460–467.
- Lin, D.Y., Xu, L.Y., Han, Y.D., Zhang, Y.K., Jing, H.Y., Zhao, L. and Minami, F., 2020, Structure and mechanical properties of a FeCoCrNi high-entropy alloy fabricated via selective laser melting, Intermetallics. 127, pp. 106963.
- Liu, L., Ren, D. and Liu, F., 2014, A Review of Dissimilar Welding Techniques for Magnesium Alloys to Aluminum Alloys, Materials (Basel), 7(5), pp. 3735–3757.
- Lorenzin G. and Rutili, G., 2009, The innovative use of low heat input in welding: experiences on ‘cladding’ and brazing using the CMT process, Welding International, 23(8), pp. 622−632.
- Luchtenberg, P., Campos, P.T., Soares, P., Laurindo, C.A.H., Maranho O. and Torres, R.D., 2019, Effect of welding energy on the corrosion and tribological

properties of duplex stainless-steel weld overlay deposited by GMAW/CMT process, Surface and Coatings Technology, 375, pp. 688–693.

- Luzin, V., Spencer K. and Zhang, M.X., 2011, Residual stress and thermo-mechanical properties of cold spray metal coatings, Acta Materialia, 59(3), pp. 1259–1270.
- Mathieu, A., Viala, J., Cicala, E., Matte, S. and Grevey, D., 2006, Laser brazing of a steel /aluminium assembly with hot filler wire (88% Al, 12% Si), Materials Science and Engineering: A, 436, pp. 19–28.
- Mangour, B., Phuong, V., Rosaire, M., Eric I. and Stephen, Y., 2014, Effect of Heat Treatment on the Microstructure and Mechanical Properties of Stainless Steel 316L Coatings Produced by Cold Spray for Biomedical Applications, Journal of Thermal Spray Technology, 23, pp. 641–652.
- Meco, S., Pardal, G., Eder, A. and Quintino, L., 2013, Software development for prediction of the weld bead in CMT and pulsed-MAG processes, The International Journal of Advanced Manufacturing Technology, 64, pp. 171–178.
- Meng, W., Lei, Y., Wang, X., Ma, Q., Hu, L., Xie, H. and Yin, X., 2022, Interface characteristics and mechanical properties of wire-arc depositing Inconel 625 superalloy on ductile cast iron, Surface and Coatings Technology, 440, pp. 128493.
- Meng, W., Lei, Y., Wang, X., Ma, Q., Yin, X. and Hong, Y., 2023, Interface characteristics and properties of nickel-based alloy coatings on cast iron fabricated by plasma and cold metal transfer wire-arc deposition. Welding in the World, 67, pp. 1967–1983.
- Mindivan, H., 2010, Wear behavior of plasma and HVOF sprayed WC-12Co + 6% ETFE coatings on AA2024-T6 aluminum alloy, Surface and Coatings Technology, 204, pp. 1870.
- Ming, M., Bao, Z., Wei, H., Jie Z. and Li, L., 2011, Influence of annealing treatment on the microstructure and mechanical performance of cold sprayed 304 stainless steel coating, Applied Surface Science, 258(2), pp. 700–704.
- Mishra, R.K., Kumar, H., Harmain G. and Albert, S., 2022, Wear performance of Ni-Cr-B-Si hardface coatings fabricated by cold metal transfer welding. Proceedings of the Institution of Mechanical Engineers, Part C: Journal of Mechanical Engineering Science, 236(3), pp. 1850–1860.

- Mishra, R.K., Kumar, H., Harmain, G. and Albert, S.K., 2023, Comparative wear behaviour of Ni-Cr-B-Si hardface coatings made by cold metal transfer and plasma transfer Arc welding processes. Proceedings of the Institution of Mechanical Engineers, Part L, 237(1), pp. 92–106.
- Mohammadnezhad, M., Javaheri, V., Shamanian, M., Rizaneh, S. and Szpunar, J., 2018, Insight to the Microstructure Characterization of a HP Austenitic Heat Resistant Steel after Long-term Service Exposure. Acta Metallurgica Slovaca, 24, pp. 296.
- Molak, R.M., Araki, H., Watanabe, M., Katanoda, H., Ohno N. and Kuroda, S., 2017, Effects of Spray Parameters and Post-spray Heat Treatment on Microstructure and Mechanical Properties of Warm-Sprayed Ti-6Al-4V Coatings, Journal of Thermal Spray Technology, 26, pp. 627–647.
- Moorthy, C.V. and Srinivas, V., 2016, Corrosion and heat transfer characteristics of water dispersed with carboxylate additives and multi-walled carbon nano tubes. Journal of The Institute of Engineers (India) Series C, 97(4), pp. 569–577.
- Moridi, A., Gangaraj, S.M.H., Vezzu, S. and Guagliano, M., 2014, Number of Passes and Thickness Effect on Mechanical Characteristics of Cold Spray Coating, Procedia Engineering, 74, 449–459.
- Murakami, T., Nakata, K., Tong, H. and Ushio, M., 2003, Dissimilar metal joining of aluminum to steel by MIG arc brazing using flux cored wire, ISIJ International, 43, pp. 1596–1602.
- Murugan N. and Parmar, R.S., 1994, Effects of MIG process parameters on the geometry of the bead in the automatic surfacing of stainless steel, Journal of Materials Processing Technology, 41, pp. 381.
- Ni, X., Zhang, L., Wu, W., Zhu, D., Kong, D., Dong, C., and Zhu, G., 2019, Functionally Nb graded Inconel 718 alloys fabricated by laser melting deposition: mechanical properties and corrosion behavior, Anti-Corrosion Methods and Materials, 67, pp. 16–23.
- Ning, J., Yu, Z.S., Sun, K., Hu, M.J., Zhang, L.X., Zhang, Y.B. and Zhang, L.J., 2021, Comparison of microstructures and properties of X80 pipeline steel additively manufactured based on laser welding with filler wire and cold metal transfer, Journal of Materials Research and Technology, 10, pp. 752–768.

- Ola O.T. and Doern, F.E., 2014, A study of cold metal transfer clads in nickel-base INCONEL 718 superalloy, Materials & Design, 57, pp. 51–59.
- Panossian, Z., Almeida, N.L.D., Sousa, R.M.F.D., Pimenta, G.D.S. and Marques, L.B.S., 2012, Corrosion of carbon steel pipes and tanks by concentrated sulfuric acid: A review, Corrosion Science, 58, pp. 1–11.
- Park, H.J., Rhee, S., Kang, M.J. and Kim, D.C., 2009, Joining of Steel to Aluminum Alloy by AC Pulse MIG Welding, Materials Transactions, 50, pp. 2314–2317.
- Pawel, P., Blicharski, M., Dymek, S. and Solecka, M., 2015, Electron Microscopy Investigation of Inconel 625 Weld Overlay on Boiler Steel. Solid State Phenomena, 231, pp. 113–8.
- Peng Z. and Kirk, T.B., 1998, Computer image analysis of wear particles in three-dimensions for machine condition monitoring, Wear, 223, pp. 157–166.
- Petch, N.J., 1955, Proceedings of Swampscott Conference, MIT Press, pp. 154.
- Pickin, C.G., Williams S.W. and Lunt, M., 2011, Characterization of the cold metal transfer (CMT) process and its application for low dilution cladding, Journal of Materials Processing Technology, 211, pp. 496.
- Pirso, J., Viljus M. and Letunovits, S., 2004, Sliding wear of TiC–NiMo cermets, Tribology International,37, pp. 817–824.
- Pirso, J., Viljus M., Juhani K. and Letunovits, S., 2009, Two-body dry abrasive wear of cermets, Wear, 266, pp. 21–29.
- Ponomareva, T., Ponomarev, M., Kisarev A. and Ivanov, M., 2021, Wire Arc Additive Manufacturing of Al-Mg Alloy with the Addition of Scandium and Zirconium. Materials, 14, pp. 3665.
- Prakash, S., John F. K. R. and Jerome, S., 2018, Effect of heat treatment on microstructure and mechanical properties of CMT welded Aluminium alloy 2024, Materials Today: Proceedings, 5(13), pp. 26997–27003.
- Qunshuang, M., Yajiang, L., Juan, W. and Kun, L., 2016, Microstructure evolution and growth control of ceramic particles in wide-band laser clad Ni60/WC composite coatings. Materials & Design, 92(15), pp. 897–905.
- Rajeev, G.P., Kamaraj M. and Bakshi, R. S., 2014, Al-Si-Mn Alloy Coating on Aluminum Substrate Using Cold Metal Transfer (CMT) Welding Technique, The Journal of The Minerals, Metals & Materials Society, 66, pp. 1061–1067.

- Rajeev, G.P., Kamaraj M. and Bakshi, R. S., 2017, Hardfacing of AISI H13 tool steel with Stellite 21 alloy using cold metal transfer welding process, Surface and Coatings Technology, 326, pp. 63–71.
- Rajeev, G.P., Kamaraj M. and Bakshi, R. S., 2019, Comparison of microstructure, dilution and wear behavior of Stellite 21 hardfacing on H13 steel using cold metal transfer and plasma transferred arc welding processes, Surface and Coatings Technology, 375, pp. 383–394.
- Rashidi A.M. and Amadeh, A., 2009, The effect of saccharin addition and bath temperature on the grain size of nanocrystalline nickel coatings, Surface and Coatings Technology, 204(3), pp. 353–358.
- Ron, T., Levy, G.K., Dolev, O., Leon, A., Shirizly A. and Aghion, E., 2019, Environmental Behavior of Low Carbon Steel Produced by a Wire Arc Additive Manufacturing Process, Metals, 9(8), pp. 888.
- Selvi, S., Vishvaksenan A. and Rajasekar, E., 2018, Cold metal transfer (CMT) technology - An overview, Defence Technology, 14(1), pp. 28−44.
- Shang, J., Wang, K., Zhou, Q., Zhang, D., Huang J. and Li, G., 2012, Microstructure characteristics and mechanical properties of cold metal transfer welding Mg/Al dissimilar metals, Materials & Design. 34, pp. 559.
- Shanglu, Y., Jing, Z., Jin L. and Yongpin, L., 2013, Welding of aluminum alloy to zinc coated steel by cold metal transfer, Materials & Design, 49, pp. 602–612.
- Shanthi, M., Lim C.Y.H. and Lu, L., 2007, Effects of grain size on the wear of recycled AZ91 Mg, Tribology International, 40, pp. 335–338.
- Solecka, M., Petrzak, P. and Radziszewska, A., 2015, The Microstructure of Weld Overlay Ni-Base Alloy Deposited on Carbon Steel by CMT Method. Solid State Phenomena, 231, pp. 119–124.
- Solecka, M., Kopia, A., Radziszewska, A. and Rutkowski, R., 2018a, Microstructure, microsegregation and nanohardness of CMT clad layers of Ni-base alloy on 16Mo3 steel, Journal of Alloys and Compounds, 751, pp. 86–95.
- Solecka, M., Kopia, A., Petrzak, P. and Radziszewska, A., 2018b, Microstructure, chemical and phase composition of clad layers of Inconel 625 and Inconel 686, Archives of Metallurgy and Materials, 63. pp. 513–518.

- Sova, A., Grigoriev, S., Okunkova A. and Smurov, I., 2013, Cold spray deposition of 316L stainless steel coatings on aluminum surface with following laser post-treatment, Surface and Coatings Technology, 235, pp. 283–289.
- Sudharshan, P., Srinivasa, R.D., Joshi S.V and Sundararajan, G., 2007, Effect of Process Parameters and Heat Treatments on Properties of Cold Sprayed Copper Coatings. Journal of Thermal Spray Technology, 2007, 16, pp. 425–434.
- Sun, H.Q., Shi Y.N. and Zhang, M.X., 2008, Wear behaviour of AZ91D magnesium alloy with a nanocrystalline surface layer, Surface and Coatings Technology, 202, pp. 2859–2864.
- Tang, X., Zhang, S., Cui, X., Zhang, C., Liu Y. and Zhang, J., 2020, Tribological and cavitation erosion behaviors of nickel-based and iron-based coatings deposited on AISI 304 stainless steel by cold metal transfer, Journal of Materials Science and Technology, 9, pp. 6665–6681.
- Tapiola, J., Tuominen, J., Vihinen, J., Vuoristo, P., 2023, Sliding wear behavior of cold metal transfer cladded Stellite 12 hardfacings on martensitic stainless steel, Welding in the World, 67, pp. 573–584.
- Tardio, S., Abel, M.L., Carr, R.H., Castle, J.E. and Watts, J.F., 2015, Comparative study of the native oxide on 316L stainless steel by XPS and ToF-SIMS. Journal of Vacuum Science & Technology A, 33, pp. 05E122.
- Thiagarajan T.B. and Ponnusamy, S., 2021, Effect of cladding of stellite-6 filler wire on the surface of ss316l alloy through cold metal arc transfer process, Journal of Metals, Materials and Minerals, 31(3), pp. 70–84.
- Toguyeni, G., Pepe, N., Barritte, G., Banse, J., Schmidt, T., Jones, R. and Mair, J., 2013, High Strength Carbon Steel and CRA Lined Pipe for Reel-lay Installation, Offshore Technology Conference.
- Varghese, P., Vetrivendan, E., Dash, M.K., Ningshen, S., Kamaraj M. and Mudali, U.K., 2019, Weld overlay coating of Inconel 617M on type 316 L stainless steel by cold metal transfer process, Surface and Coatings Technology, 357, pp. 1004–1013.
- Villa, M., Dosta, S. and Guilemany, J.M., 2013, Optimization of 316L stainless steel coatings on light alloys using Cold Gas Spray, Surface and Coatings Technology, 2013, 235, pp. 220–225.

- Wang, P., Chen, X., Pan, Q., Madigan, B. and Loag, J., 2016, Laser welding dissimilar materials of aluminum to steel: an overview, The International Journal of Advanced Manufacturing Technology, 87, pp. 3081–3090.
- Wang, J., Cui, X., Jin, G., Zhao, Y., Wen, X. and Zhang, Y., 2023, Effect of in-situ Ni interlayer on the microstructure and corrosion resistance of underwater wet 316L stainless steel laser cladding layer, Surface and Coatings Technology, 458, pp. 129341.
- Wen-Ruey, C., Mikko, H. and Raoul, G., 2004, The effects of cut-off length on surface roughness parameters and their correlation with transition friction, Safety Science, 42, pp. 755–769.
- Wong, W., Irissou, E., Vo, P., Sone, M., Bernier, F., Legoux, J.G., Fukanuma H. and Yue, S., 2013, Cold Spray Forming of Inconel 718, Journal of Thermal Spray Technology, 22, pp. 413–421.
- Wright, S.I., Nowell, M.M. and Field, D.P., 2011, A Review of Strain Analysis Using Electron Backscatter Diffraction, Microscopy and Microanalysis, 17, pp. 316–329.
- Wu, S., Feng, J., Cheng, F., Wang, Z. and Wang, D., 2023, Research on root appearance and fatigue life of steel catenary riser (SCR) using GMAW/GTAW-P double-sided root welding process, International Journal of Pressure Vessels and Piping, 201, pp. 104866.
- Xiong, Y., Zhuang, W. and Zhang, M., 2015, Effect of the thickness of cold sprayed aluminium alloy coating on the adhesive bond strength with an aluminium alloy substrate, Surface and Coatings Technology, 270, pp. 259–265.
- Yang, S., Zhang, J., Lin, J. and Lei, Y., 2013, Welding of aluminum alloy to zinc coated steel by cold metal transfer, Materials & Design, 49, pp. 602–612.
- Yuhua, L., Yongli, C. and Xuejiao, Z., 2020, Effects of Cryogenic Treatment and Tempering on Mechanical Properties and Microstructure of 0.25C-0.80Si-1.6Mn Steel, Advances in Materials Science and Engineering, 2020, pp. 8.
- Zhang, H.T., Feng, J.C., He, P., Zhang, B.B., Chen J.M. and Wang, L., 2009, The arc characteristics and metal transfer behaviour of cold metal transfer and its use in joining aluminum to zinc-coated steel, Materials Science and Engineering: A, 499, pp. 111–113.

- Zhang, H., Hu, S., Wang, Z. and Liang, Y., 2015, The effect of welding speed on microstructures of cold metal transfer deposited AZ31 magnesium alloy clad, Materials & Design, 86, pp. 894–901.
- Zhang, P., Chen, Y., Xiao, W., Ping, D. and Zhao, X., 2016, Twin structure of the lath martensite in low carbon steel. Progress in Natural Science: Materials International. 26, pp. 169–172.
- Zhang, B., Wang, C., Wang, Z., Zhang L. and Gao, Q., 2019, Microstructure and properties of Al alloy ER5183 deposited by variable polarity cold metal transfer, Journal of Materials Processing Technology, 267, pp. 167–176.
- Zhao, Y.H., Sheng H.W. and Lu, K., 2001, Microstructure evolution and thermal properties in nanocrystalline Fe during mechanical attrition, Acta Materialia, 49(2), pp. 365–375.
- Zhao, T., Zhang, S., Wang, Z.Y., Zhang, C.H., Liu, Y. and Wu, C.L., 2022a, Modulating heat input to optimize corrosion and synergistic cavitation erosion-corrosion behavior of Ni201 cladding layer by cold metal transfer, Surface and Coatings Technology, 443, pp. 128595.
- Zhao, T., Zhang, S., Wang, Z.Y., Zhang, C.H., Zhang, D.X., Wang, N.W. and Wu, C.L., 2022b, Cavitation erosion/corrosion synergy and wear behaviors of nickel-based alloy coatings on 304 stainless steel prepared by cold metal transfer, Wear, 510–511, pp. 204510.
- Zhao, T., Zhang, S., Zhang, C.H., Sun, X.Y., Bai, X.L. and Wu, C.L., 2023, The effect of Ni201 transition layer on the corrosion, wear and synergetic cavitation erosion-corrosion behavior of CMT-Monel K500 coating, Surface and Coatings Technology, 463, pp.129507.
- Zhou Y. and Lin, Q., 2014, Wetting of galvanized steel by Al 4043 alloys in the first cycle of CMT Process, Journal of Alloys and Compounds, 589, pp. 307–313.
- Zhou, J., Ma, K., Li, C.X., Yasir, M., Luo, X.T. and Li, C.J., 2020, Microstructures of aluminum surfaces reinforced with 316L stainless steel particles via high-speed particle injection and the resulting double strengthening mechanism, Surface and Coatings Technology, 385, pp. 125380.
- Zhu, T., Chen, Z.W. and Gao, W., 2006, Incipient melting in partially melted zone during arc welding of AZ91D magnesium alloy, Materials Science and Engineering: A, 416, pp. 246–252.

Appendix A

Important specifications of CMT machine

Make	Fronius
Model	TPS 400i
Current	5–400 A
Mains voltage	3×400 V
Weight	36,45 kg

Important specifications of Fanuc robot ARC mate 100iD

Make	Fanuc
Model	100iD
Controlled axis	6
Speed	260–720 °/s
Repetitive accuracy	±0.02 mm
Weight	145 kg
Maximum reach	1441 mm
Maximum load capacity at wrist	14 kg

Appendix B

Important specifications of Optical microscope

Make	Nikon Corporation
Model	Nikon SMZ25
Zooming	Right/left single axis knob
Zoom ratio	25:1
Magnification	0.75 to 13.75X

Appendix C

Important specifications of scanning electron microscopes

Make	Zeiss
Model	Sigma
Specific Chamber	330 mm inner diameter, 270 mm height
Specimen weight	up to 500 g tilted, up to 200 g not tilted
Movement	X=125 mm, Y=125 mm, Z=50mm
	T= -10° to +90°, R=360°
Specific stage	5-axis motorized Cartesian
Chamber detector	Inlense, SE-2, NEBSD
Magnification range	300 X to 1000kX

Appendix D

Important specifications of non-contact profilometer

Make	Taylor Hobson
Model	CCI-Lite
Magnification	20X
Precision (megapixel)	1
Power supply	220 V
Focal distance	4.7 mm
Field of view	0.825 mm×0.825 mm

Appendix E

Important specifications of microhardness tester

Make	Omni Tech
Model	MVH-II
Test load	10 gf to 1000 gf
Dwell time	1 to 99 s
Magnification range	100X to 400X
Measurement of indentation	Digital filler micrometer eyepiece (10X) with 0.025 Micron accuracy
Maximum height of specimen	65 mm
Maximum depth of specimen	85 mm
Stage dimension	100 ×100 mm
Camera port	With optical diversion knob (For computer attachment)
Power supply	AC 230V

Appendix F

Important specifications of universal testing machine

Make	Instron
Model	881J4051
Capacity	±100 kN
Actuator stroke	±75 mm (±3 in)
Load cell height	97 mm (308 in)
Maximum day light	1480 mm (58.3 in)
Column spacing	652 mm (22.1 in)
Column diameter	70 mm (2.1 in)
Table height	890 mm (35 in)
Overall width	920 mm (36.2 in)
Overall depth	546 mm (21.5 in)
Overall height (maximum)	2778 mm (109.4 in)
Weight	625 kg (1375 lb)

Publications

Journal papers

1. B. Das, B.N. Panda and U.S. Dixit, Microstructure and Mechanical Properties of ER70S-6 Alloy Cladding on Aluminum Using a Cold Metal Transfer Process. Journal of Materials Engineering and Performance, 31, 9385–9398 (2022). https://doi.org/10.1007/s11665-022-06937-8
2. B. Das, B.N. Panda and U.S. Dixit, Effects of heat-treatment on the mechanical properties of Fe-based ER70S-6 cladding on aluminum substrate using CMT process. Journal of Materials Engineering and Performance, 33, 173–193 (2024). https://doi.org/10.1007/s11665-023-07975-6
3. B. Das, F. Sharma, B.N. Panda and U.S. Dixit, Recent developments in cladding and coating using cold metal transfer technology. Journal of Materials Engineering and Performance, 2023. https://doi.org/10.1007/s11665-023-08940-z
4. B. Das, B.N. Panda and U.S. Dixit, Effect of cladding thickness on microstructure and mechanical properties of cold metal transfer cladding of Fe-based ER70S-6 alloy on aluminum alloy. Journal of Materials Engineering and Performance. (Under revision)

Book chapters

1. B. Das, B.N. Panda and U.S. Dixit, Corrosion Behavior and its Effect on Mechanical Properties of ER70S-6 Cladding on AA 6061-T6 Alloy Using a Cold Metal Transfer Process. In: Joshi, S.N., Dixit, U.S., Mittal, R.K., Bag, S. (eds) Low Cost Manufacturing Technologies. NERC 2022. Springer, Singapore, (2023). https://doi.org/10.1007/978-981-19-8452-5_2

Conferences

1. B. Das, B.N. Panda and U.S. Dixit, Corrosion behavior and its effect on mechanical properties of ER70S-6 cladding on AA 6061-T6 alloy using a cold metal transfer process. North-East Research conclave, Indian Institute of Technology Guwahati, India, 2022. (Published as Book Chapter # 1)